PART I

STUDY OF SOME BETA DECAYS IN THE SD SHELL

PART II

COMPARISON OF EXPERIMENTAL REACTION CROSS SECTIONS WITH THE HAUSER-FESHBACH MODEL

Thesis by

Frederick M. Mann

In Partial Fulfillment of the Requirements

for the Degree of

Doctor of Philosophy

California Institute of Technology

Pasadena, California

1975

(Submitted January 7, 1975)

ACKNOWLEDGMENTS

I wish to express my sincere gratitude to the members of the Kellogg Radiation Laboratory who have created such a stimulating and pleasant atmosphere. I would particularly like to thank Professor R. W. Kavanagh for his guidance and useful comments which are evident throughout this study.

The help of Dr. Zygmunt E. Switkowski and Dr. Dennis W. Kneff in the study of the cross section for $^{23}Na(p,n)^{23}Mg$ is very much appreciated.

Special thanks are due to Ms. Barbara A. Zimmerman whose knowledge of programming was invaluable, to Mr. Lawrance J. Graham whose knowledge of electronic circuits and instrumentation quickened the pace of these experiments, and finally to Mr. M. L. "Bud" Warrick whose knowledge of the tandem accelerator and all the equipment associated with the Tandem Laboratory was necessary for the success of the experiments.

This research was supported in part by the National Science Foundation (GP-28027).

ABSTRACT

Part One

The beta decays of ^{19}Ne, ^{23}Mg, ^{27}Si, ^{37}K, ^{38}K, and ^{39}Ca have been studied by observing the delayed gamma radiation with large volume Ge(Li) detectors. A pneumatic shuttle was used so that weak beta transitions could be observed. Two previously unobserved allowed transitions have been found, and the uncertainty for most of the previously known transitions has been reduced. Limits for unobserved transitions have been strengthened. A comparison is made between the predictions of various nuclear models, particularly the many-particle shell model, and observed values.

Part Two

Cross sections have been measured by the activation method for $^{23}Na(p,n)^{23}Mg$, $^{35}Cl(\alpha,n)^{38}K$, and $^{63}Cu(p,n)^{63}Zn$ from threshold to 11 MeV and for $^{59}Co(\alpha,n)^{62}Cu$, $^{63}Cu(\alpha,n)^{66}Ga$, and $^{65}Cu(\alpha,n)^{68}Ga$ from threshold to 19 MeV. The excitation functions are compared with the predictions of the Hauser-Feshbach model of nuclear reactions. If resonance effects are averaged, then using established parameters for the nuclear potentials and for the nuclear level densities, the predicted values are within a factor of 2 of the experimental values for practically all cross sections measured. For cases where direct reactions are not important, agreement to within 20% is obtained.

TABLE OF CONTENTS

PART I. STUDY OF SOME BETA DECAYS IN THE SD SHELL

PART I

STUDY OF SOME BETA DECAYS IN THE SD SHELL

I. INTRODUCTION

One of the main goals of nuclear physics is to be able to explain the properties of the various states occurring in nuclei. It is generally believed that if one knows the fundamental interactions and the appropriate wavefunctions describing the levels, then the desired properties can be calculated. Thus much effort has gone into the study of interactions and into the production of accurate wavefunctions.

In recent years nuclear beta decay has been one of the best tests for determining the accuracy of wavefunctions. For the case of nuclear beta decay, the weak interaction is believed to be well understood. Thus given the wavefunctions of various levels, it is straightforward to calculate unambiguously a quantity (known as ft) which can be compared with experimental results.

As the ability to predict wavefunctions becomes better, one wants to be able to test smaller parts of the wavefunctions. Almost any theory can predict the ft value for the decay of a level to its mirror level; as apart from a known correction factor, the value is that obtained from the decay of a free neutron. Rather it is those decays which are not to mirror levels that test the small components and differences in the wavefunctions.

This part of the thesis will describe the search for these transitions which, because they compete against mirror transitions and are energetically unfavored, are usually quite weak. The second section of this part will describe the weak interaction Hamiltonian that is normally used and the formulae that are used to calculate ft values

for the strongest (that is, for the allowed) transitions. Also in the second section the current status of theories predicting nuclear wavefunctions is reviewed, with particular emphasis on those theories which derive ft values for transitions studied in this work. The third section describes the experimental procedures used in this study. The types of analysis and corrections made and a general overview of the experiments are given in the fourth section. The fifth section treats in detail the results for the decays studied, viz., ^{19}Ne, ^{23}Mg, ^{27}Si, ^{37}K, ^{38}K, and ^{39}Ca. Also in this section are further details about the wavefunctions predicted for levels populated in these decays. In the sixth and final section of this part, comparisons between theory and experiment are made, and the status of the ability to predict accurate wavefunctions is discussed.

II. THEORETICAL CONSIDERATIONS

A. Nuclear Beta Decay Theory

This subsection lays the theoretical groundwork underlying the connection between the wavefunctions calculated by theorists and the branching ratios and lifetimes measured by experimentalists. Since all the decays observed in this work are of the allowed type (that is, they appear in the first order of the theory), approximations will be made whenever the omitted or excluded term is small compared to the remaining terms. It should be noted, however, that whenever either very high accuracy is desired (as in the case of superallowed transitions used to determine beta decay coupling constants) or when forbidden (at least in the sense of the allowed theory) transitions are studied, then a more complete treatment is necessary. For example, Stech and Schülke (1964), Schülke (1964), Buhring (1963a and 1963b), and Behrens and Buhring (1971) have provided a formulation in which the kinematical structure, the effect of electromagnetic interactions between the charged lepton and the nucleus, and model dependent nuclear effects are clearly separated. Furthermore, approximations, when necessary, are made only at a late stage where their implications can easily be recognized. In the treatment given here, emphasis will be given more to physical insight than to mathematical details.

It should be noted that although the Hamiltonian involved in nuclear beta decay is believed to be well known, the weak interactions from which the Hamiltonian is derived are not well understood, particularly at the highest energies. In fact, using current weak-

interaction theory (Feynman and Gell-Mann 1958), certain reactions, such as electron-neutrino scattering, are predicted to have unbounded cross sections, thus violating unitarity. Weinberg (1967) and others have proposed merging weak interactions and electromagnetic interactions into one unified theory by the introduction of an intermediate vector boson which would act as the propagator of the weak interactions, just as the photon (also a vector boson) acts in electromagnetic interactions. This unification could solve the problem of unbounded cross sections. It should be noted that since the proposed intermediate vector boson is so massive (greater than 37 GeV) as compared with energies involved in nuclear beta decay, the existence of this massive boson and its precise mass have no measurable effect on nuclear beta-decay predictions.

Enrico Fermi (1934) set the stage for merging the two interactions by describing the nuclear beta-decay Hamiltonian density in exact analogy with the density associated with electromagnetic interactions,

$$\mathcal{H}_{em} = \sum_n \sum_\mu e\, J_\mu^+(r_n) \cdot A_\mu(r_n) \qquad (1)$$

Here e is the electric charge (or strength of the interaction), J_μ is the current density, A_μ is the vector potential describing the radiation field, and r_n is the position coordinate of the nth particle. Thus Fermi's proposal for beta decay was

$$\mathcal{H}_\beta = \sum_n \sum_\mu g\, J_\mu^+(r_n) \cdot L_\mu(r_n) \qquad (2)$$

where J_μ is the current density associated with the proton-neutron transition, L_μ is the "vector potential" of the lepton field, and g is the elementary charge of weak interactions. Although this Hamiltonian density has changed slightly in details since Fermi first proposed it, it still forms the starting point for all discussions of nuclear beta decay.

Assuming that equation 2 is the proper form for the Hamiltonian density, the question arises as to what form the representations of the currents and potentials should take. The form of the representations can be limited by making some physically reasonable assumptions and then using experimental results to determine the values of the parameters remaining in the theory. The assumptions which are normally used are:

1) Special relativity is valid, and therefore invariance with respect to the proper Lorentz group is required. As shown by Wu et al (1957) and others, parity (invariance with respect to mirror reflection) is violated.

2) The interaction is at a point. Although this assumption implies violation of unitarity at high energies, the energies involved in nuclear beta decay are so small compared with any proposed propagator that the error introduced with this assumption is small.

3) Quantum mechanics is valid, thus requiring the Hamiltonian to be Hermitian.

4) Charge, baryon number, and lepton number are conserved, thus requiring creation and annihilation operators to appear as pairs.

5) The operators of the particles enter only linearly into the Hamiltonian.

6) No derivatives appear in the Hamiltonian. Again an appeal can be made to the low energies and hence low momenta available in nuclear beta decay.

Using these assumptions it can be shown (Pauli 1958) that the most general form of the Hamiltonian density is

$$\mathcal{H} = \frac{g}{\sqrt{2}} \sum_i (\bar{\psi}_p \theta_i \psi_n) [\bar{\psi}_e \theta_i (C_i + C_i' \gamma_5) \psi_\nu] \qquad (3)$$

+ Hermitian conjugate

where $\sum_i (|C_i|^2 + |C_i'|^2) = 1$, the θ_i are operators which are formed from the products of Dirac gamma matrices, γ_μ , and ψ_X is the creation operator for particle X . For historical reasons, $2^{1/2}$ is introduced so that the value of g is the same as would have been obtained before the discovery of parity violation. The operators θ_i can be grouped into five classes depending upon their transformation under the proper Lorentz group,

a)	scalar (S)	$\theta_i = 1$
b)	vector (V)	$\theta_i = \gamma_\mu$
c)	axial vector (A)	$\theta_i = \gamma_\mu \gamma_5$
d)	pseudo-scalar (P)	$\theta_i = \gamma_5$
e)	antisymmetric tensor of rank 2 (T)	$\theta_i = \gamma_\mu \gamma_\nu$

The pseudo-scalar form is thought to be zero, but as it does not play

a role in the theory of allowed transitions, its exact value is unimportant for this study. Paul (1970) has performed a least-squares adjustment on the remaining coupling constants (which can be involved in allowed transitions) with the following results:

1) $C_V'/C_V = 0.82\ ^{+0.40}_{-0.13}$

$C_A'/C_A = 1.10 \pm 0.06$

2) If one assumes that $C_V = C_V'$ and $C_A' = C_A$ (which is equivalent to assuming that the neutrino is massless and has a definite helicity) one obtains

$C_A/C_V = 1.262 \pm 0.008$

3) If it is further assumed that $C_S' = C_S$ and $C_T' = C_T$, then

$C_S/C_V = -0.001 \pm 0.006$

$C_T/C_A = -0.0004 \pm 0.0003$

However, if equality is not assumed between the primed and unprimed quantities, then the results become very uncertain,

$C_S/C_V = 0.08 \pm 1.2$

$C_S'/C_V = -0.07 \pm 1.0$

$C_T/C_A = 0.006 \pm 0.2$

$C_T'/C_A = -0.006 \pm 0.2$

In practically all studies involving allowed decays, the neutrinos are treated as massless and the scalar and the tensor parts of the beta interaction are ignored. This results in the V-A theory, first proposed by Feynman and Gell-Mann. Thus the Hamiltonian density becomes

$$\mathcal{H}_\beta = \frac{g}{\sqrt{2}} [\bar{\psi}_p \gamma_\mu (1 - \lambda\gamma_5)\psi_n][\bar{\psi}_e (1 - \gamma_5)\psi_\nu] \cdot$$

$$+ \text{Hermitian conjugate} \qquad (4)$$

where $\lambda = |C_A|/|C_V|$. It is felt that the inequality between C_V and C_A is due to the renormalization of C_A due to exchanges with the meson cloud surrounding the baryons, while C_V experiences no such renormalization (the conserved-vector current theory). As to further renormalization due to the many nucleons within a nucleus, Mukhopadhyay and Miller (1973) state that after all corrections are included, no evidence exists for further renormalization. Finally Towner and Hardy (1973) after performing extended analyses of superallowed Fermi decays have determined the beta coupling constant g , to be

$$g = (1.4129 \pm 0.0005) \times 10^{-49} \text{ erg-cm}^3$$

Since the coupling constant is so small, the relationship between the Hamiltonian density and the rate of nuclear beta decay can be made by using first-order perturbation theory (Fermi's (1949) Golden Rule). Thus the probability, w_{12}, for a transition from an initial state 1 to a final state 2 which involves a neutrino with energy E_r , is

$$w_{12} = 2\pi |H_{12}|^2 \, (dn/dW_r) \, m_e c^2/\hbar \qquad (5)$$

where $|H_{12}|^2$ is the transition matrix element found by integrating the Hamiltonian density over space and summing over all nucleons in the initial (or final) nucleus, and where $(dn/dW_r)\, m_e c^2$ is the number of final states per unit energy at an energy equal to the normalized total neutrino energy $W_r = E_r/(m_e c^2)$.

The transition matrix element H_{12} can be expanded in a series, and for allowed decays the first term is sufficient. First consider the term in H_{12} involving the baryons. As there is so little kinetic energy in the nucleus relative to the total energy contained in the nucleus (less than 1%), the nucleons are moving non-relativistically, and hence the Dirac matrices can be reduced to their Pauli matrix equivalents which now operate on wavefunctions rather than on state vectors. Thus the baryon current term reduces to the nuclear matrix element, M_{if},

$$\begin{aligned} &\langle i | \, \psi_n (1 + \lambda \gamma_5) \psi_p) \, | f \rangle \\ &\qquad \rightarrow \langle T_f \, | T^- | \, T_i \rangle \int \phi(n_f)(1 + \lambda \vec{\sigma}) \, \phi(n_i) \qquad (6) \\ &\qquad = M_{if} \end{aligned}$$

where ϕ is the many-particle wavefunction describing the nucleons inside the nucleus, σ is the Pauli spin matrix, and where $\langle T_f \, | T^- | \, T_i \rangle$ is the isospin term, where T^- is the isospin lowering operator for the nucleus and T_f and T_i are isospin quantum numbers.

The reduction of the lepton-current term depends upon which beta-decay process occurs. For electron or positron emission, the wavefunc-

tions involved are the solutions of the Dirac equation in a Coulomb field, while for electron capture, the wavefunction of importance is that of the bound electron that will be captured. It should be noted that the effect of the other electrons on the beta-decay process is neglected except insofar as they modify the Coulomb field. The remainder of the lepton-current term is easily evaluated. Since the neutrino interacts so slightly with matter, it can be represented by a plane wave, normalized to unity in some volume V. Also, since the wavelengths associated with the emitted neutrino and electron are quite large compared to the nuclear volume, their wavefunctions can be expanded in a power series. Following the convention of Kotani and Ross (1958), the neutrino wavefunction is expanded about the nuclear origin, while the electron or positron wavefunction is expanded about the nuclear radius. In cases studied in this work, the zero order terms are much larger than the succeeding terms and thus only they need be kept since the nuclear matrix element, M_{if}, is non-zero.

For electron capture, the same arguments cannot be made, since except for s-wave electrons, the wavefunctions of bound electrons are zero at the nuclear center and increase to a finite value at the nuclear radius, hence changing greatly over the nuclear volume. However, since it is the s-wave (or K-shell) electrons which have the largest overlap with the nucleus, the other electrons can usually be neglected or be included only in an approximate manner. For example, the L-shell electrons usually contribute about 10%of the rate. For the case of K-shell electron capture, the bound-electron wavefunction is nearly constant over the nuclear volume, and hence like the emitted electron or positron

wavefunction, it too can be expanded in a series. For similar reasons as outlined above, only the zero order term need be kept.

The density of states, (dn/dW), which results just from kinematic considerations, also depends upon which beta-decay process occurs. For particle emission, there are three bodies in the final state. Thus all neutrino energies up to a maximum energy determined by the mass difference of the parent and daughter nuclei are available. Neglecting the small amount of kinetic energy in the recoiling nucleus, the density of states for electron or positron emission is

$$dn/dW_r = V\, m_e^4\, c^2 W_r^2 (W_e^2 - 1)^{1/2}\, W_e/(4\pi^4\, \hbar^6) \qquad (7)$$

where W_e is the normalized total electron energy, $W_e = (E_e + m_e c^2)/m_e c^2$. In the case of electron capture, there are only two bodies in the final state, and hence only one neutrino energy is available,

$$dn/dW_r = nV\, W_r^2\, \delta(E_e - \varepsilon_B)/(2\pi^2 c^3 \hbar^3) \qquad (8)$$

where ε_B is the electron binding energy and n is the number of electrons in the shell, which for K-shell capture is 2.

Thus using equations 5, 6, 7, and 8, one obtains for the probability for transition from initial state 1 to final state 2 which includes a neutrino having a definite energy

$$w_{12} = |M_{if}|^2\, W_r^2/\tau_o \; * \left\{ \begin{array}{l} F_z(W_e,R)\; W_e(W_e^2 - 1)^{1/2} \\ \\ + G_z(R)\; (E_e - \varepsilon_B) \end{array} \right\} \qquad (9)$$

where τ_o is the universal beta-decay time constant ($\tau_o = (2\pi^3\hbar^7) / (g^2 m_e^5 c^4) \simeq 8890$ sec), $F_z(W_e,R)$ is the solution to the Dirac equation evaluated at the nuclear radius R, and $G_z(R)$ is the bound state wavefunction of the K-electron to be captured, again evaluated at the nuclear radius. However, since no attempt is made to observe the neutrinos, much less to measure their energy, the quantity of interest is the probability for decay regardless of neutrino energy. Thus by integrating equation 9 over all neutrino energies, the decay probability is

$$\int w_{12}\, dW_r = \frac{1}{\tau} = \frac{|M_{if}^2|^2}{\tau_o} (f_{e\pm} + f_K) \qquad (10)$$

where W_o is the normalized total energy of the decay, and the f's are the Fermi functions for beta decay,

$$f_{e\pm} = \int W_r^2 (W_e^2 - 1)^{1/2} W_e F_z(W_e,R)\, dW_r$$

$$f_K = (W_o - \varepsilon_B/m_e c^2)^2 \; G_z(R) \qquad (11)$$

Traditionally, instead of the mean life of the decay, τ, the half-life of the decay is used. If $t_{1/2}$ is multiplied by the appropriate Fermi functions, the "comparative half-life" or ft value is formed,

$$ft \equiv (f_{e\pm} + f_K) t_{1/2} = \tau_o (\ell n\, 2)/|M_{if}|^2 \qquad (12)$$

For electron emission, the capture term is of course absent. It will be noted that the ft value is independent of the energy of the decay and hence indicates only nuclear properties, the overlap between the

initial and final nuclear states.

Three types of corrections are sometimes applied to the above results: (1) an electron-screening correction, (2) a finite nuclear-size correction, and (3) electromagnetic corrections. Each of these tries to correct for approximations made in obtaining $F_z(W_e,R)$, the solution to the Dirac equation for a point-source Coulomb field. The electron-screening correction attempts to correct for the effect of screening electrons by replacing $F_z(W_e,R)$ with $(1-V_o/W_e) * F_z(W_e-V_o,R)$ where V_o is the shift in potential energy at the nucleus caused by the screening. This correction was proposed by Rose (1936). The finite nuclear-size correction of Rose and Holmes (1951) attempts to correct for the nucleus not being a point charge. This effect is small for the low-Z decays studied in this work. The various electromagnetic corrections are quite complicated (see Kallen (1967) for a discussion). These corrections attempt to include those electromagnetic interactions involving the electron or positron with the decaying nucleon which are neglected in this simple treatment.

By using equation 12, the results of experiment ($t_{1/2}$, remembering that this is the half-life to decay to a certain state and not the half-life for decay to any of the several available levels) can be compared with the predictions of theory (M_{if}). The nuclear matrix element is quite simple in form (see equation 6), involving only the simple overlap of wavefunctions and overlap after a spin flip operation. Since the Pauli spin matrices transform as vectors, the Wigner-Eckart theorem (Wigner 1927, and Eckart 1930) holds that the spin difference between the initial and final nuclear states cannot be

greater than 1. Also since neither the Pauli spin matrices nor the unit operator change parity, the initial and final nuclear states must have the same parity. By using the Wigner-Eckart theorem on the isospin term of equation 6, additional selections can be obtained. Thus the selection rules for allowed beta decay are

$$\begin{aligned} &\Delta J = 0,1 \\ &\Delta \pi = \text{no} \\ &\Delta T = 0,1 \\ &\text{only one } J = 0 \rightarrow 0 \text{ decay (if isospin is a good quantum number)} \end{aligned} \tag{13}$$

As can be seen from the expression for ft (equation 12), the smaller the overlap, the higher the value for ft. Experimentally it has been found that ft values cover many orders of magnitude. Thus it is customary to refer to $\log_{10} ft$ rather than to ft. Figure 1 shows the distribution of $\log ft$ for $A \leq 44$ (the data being taken from Ajzenberg-Selove and Lauritsen 1968,1974, Ajzenberg-Selove 1970, 1972, and Endt and van der Leun 1973). The distribution is doubly humped. The first hump (at $\log ft \sim 3.5$) contains those decays where the overlap is near unity, the superallowed decays. The second hump (at $\log ft \sim 5.1$) are those decays where the initial and final nuclear states are quite different, but yet still have appreciable overlap ($\sim 10\%$). The tail consists of decays which involve gross mismatches in the nuclear wavefunctions or accidental cancellations in the nuclear matrix elements.

B. Nuclear-Structure Models

Most of the theoretical work performed in constructing wavefunctions and nuclear matrix elements for nuclei in the s-d shell ($17 \leq A \leq 40$) has been done using the shell model. In this model, one or more nucleons are active outside an inert core. Any transitions which occur are described by changes in the valence nucleons, the core remaining unchanged.

In the simplest treatment, only one particle is considered active. The wavefunction is expressed as a linear combination of available shell wavefunctions. The coefficients in the resultant sum are determined by calculating various transition probabilities and static moments and requiring agreement with experimental values. These wavefunctions are then used to predict other properties and transitions. An example of this method, known as the weak coupling model, is the beta decay of ^{27}Si to ^{27}Al; ^{27}Si is considered to be a neutron hole in an inert ^{28}Si core. The beta decay changes the neutron hole into a proton hole, thus forming ^{27}Al.

It has long been recognized that the weak-coupling model is an over-simplification, but to include more than a few nucleons outside the inert core was computationally impractical. In recent years, however, with the increase in memory size and computational speed, large computers have enabled theorists to treat many-valence-nucleon cases (see McGrory (1973) for a review of these calculations.) In this approach, the nuclear Hamiltonian, H_N , is broken into three parts:

$$H_N = H_c + H_{cs} + H_s \tag{14}$$

where H_c is the Hamiltonian describing the core, H_s is the Hamiltonian describing the interaction between the valence nucleons, and H_{cs} is the Hamiltonian describing the interaction between the core and the valence nucleons. Since the core is assumed not to partake in the transitions, the Hamiltonian describing the core can be removed from the calculations. Matrix elements of the form $\langle core|H_{cs}|\alpha\rangle$ and $\langle B|H_s|\gamma\rangle$ must still be calculated or derived from experiment. These matrix elements can depend on many quantum numbers, especially important are the ℓ and j values of the valence nucleons.

Harmonic oscillator wavefunctions are taken as the basis and some form of "realistic" (i.e., physically reasonable extrapolation from nucleon-nucleon) potentials is used. Usually there are adjustable parameters in the potential so that agreement between experimental values and theoretical predictions can be optimized. In the case of the Rochester-Oak Ridge computer code (French et al 1966), the energy matrix $\langle i|(H_{cs} + H_s)|j\rangle$ is formed and then diagonalized. Even though computers with large memory units are used, very often restrictions on the set of possible shell configurations are imposed in order that the matrices can fit inside the computer. For the calculation of ^{28}Si, matrices which have dimensions of $\sim$3800 are needed if the full s-d shell is used; no computer exists which is capable of keeping this much data in core. Whitehead (1972) has devised another method of diagonalization which takes less core, but the results for the decays studied in this work have not yet been published. However, calculations covering the entire s-d shell have been performed with the Rochester-Oak Ridge program and these will form the major theoretical predictions

with which experimental values will be compared (see Lanford and Wildenthal (1973) for a compilation of the predicted log ft values).

III. EXPERIMENTAL DETAILS

A. Introduction

As the beta decays of interest in this work are quite difficult to observe in the presence of the much stronger superallowed transitions, a system was developed which rendered the delayed gamma transitions which followed the beta decay more easily observable by using high resolution Ge(Li) detectors. Preferential absorption through the use of lead attenuators optimized the relative photopeak efficiency of the gamma ray detectors.

To obtain maximum yield the energy and intensity of the bombarding beams were at the limits of CIT-ONR tandem accelerator. Use of such high energy (10 MeV and greater) and high current ($\frac{1}{2}$ μA and greater) beams caused large yields of prompt neutrons (greater than 2000 neutrons per cm^2-sec at a detector 7 m from the target) which would quickly destroy any Ge(Li) detector near the target during bombardment. A shuttle system was thus used to carry the activated target material from the target room to the control room for remote counting.

To insure that gamma rays observed by the Ge(Li) detector resulted from the beta decay under study, the yield of gamma rays was studied as a function of time after bombardment. Often further checks such as using different target materials and different lead attenuators were performed, and these are further described below.

B. Shuttle (Rabbit) System

Since the activities under study, except for the decay of the ground state in ^{38}K, had half-lives less than 20 s, a human shuttle

system could not be used. Instead the shuttle system used by Kavanagh and Goosman (1964) to study the beta decay of ^{37}K was modified for the present requirements.

Figure 2 shows a block diagram of the rabbit system. The solenoid valves control the admission of propelling gas and the connection to the roughing pump, and hence control the direction of the rabbit's motion. The pump used was a Beach-Russ Co. rotary pump, model #2HVRC, circa 1930. This pump was capable of 5 mm Hg vacuum and had a capacity of 7 liter/s. The tubing through which the rabbit passed is Eastman Imperial Poly-Flo plastic tube, having an inner diameter of 3/8 inch and a length of 17 meters. Typical transit time was 0.5 to 1.0 sec, depending upon the timing of the opening of the solenoid valves. The tubing was replaced whenever large amounts of carbon (probably from cracked roughing pump oil) settled in the tubing and retarded the rabbit's movement.

The Ansco 2-way solenoid valves were powered by Clare mercury-wetted-contact relays which were in turn controlled by electronic sequence timers which will be described in part D (electronics) of this section.

Figure 3 shows in detail the hutch, or rabbit holder, at the beam end of the shuttle system. A thin foil of Al, approximately 25 microns thick, was used to separate the low pressure system associated with the tandem beam lines (10^{-5}torr) and the pressure in the rabbit tubing. Under favorable conditions these foils would last for more than ten running days subjected to 1 μA of 10-MeV protons. Aluminum was

chosen as the foil material because for the thickness needed to separate the two systems, Al degraded the beam energy as little as possible (about 250 keV for a 10 MeV proton beam) and the radioactive products of Al from beam bombardment have been well studied. It is possible for recoiling products of the Al + beam reaction to stick onto the rabbit and then be shuttled to the counting station.

The beam rabbit hutch was a piece of heat-treated 4340 stainless steel. This material was required in the present series of experiments since it soon became apparent that the deceleration of the rabbit put too much stress on the previously designed hutch of Kavanagh and Goosman. The hutch was contained within a brass holder which served to connect the hutch to the gas-handling system, to the beam pipe of the accelerator, and to the poly-flo tubing. To soften the rabbit's landing, Viton O-rings were placed at the end of the hutch. Viton O-rings were used as they absorb a blow with minimal bounce, while standard butyl O-rings can produce large bounces.

Figure 4 shows the rabbit hutch located in the control room, as well as the gamma-ray detection system (which will be described in part B). The control-room hutch was a cylindrical piece of lucite 8.9 cm long and 7.5 cm in diameter. A flat face was cut into the cylinder 2.0 cm from the axis, leaving just enough low-Z material to stop the beta rays with reasonable minimization of bremsstrahlung. Since a low-Z material is used to stop the beta rays, the positrons do not annihilate at the target, at a point, but rather annihilate some distance from the rabbit, creating a distributed source for 511-keV annihilation radiation.

The construction of the rabbit is shown in Figure 5. The rabbit consists of three pieces, the Be front shell, the target material, and the nylon tail. Beryllium was chosen for the front shell because it is extremely light and bombardment by most beams does not produce any activity that would hamper these experiments (see Table 1). The activities have either very short or very long half-lives. The only exception results from bombardment of ^{3}He which produces ^{11}C in large quantities by the $^{9}Be(^{3}He,n)^{11}C$ reaction. A tail plug was needed to keep the target material inside the Be front shell. Nylon was chosen for the tail plug because of its low density and atomic number and high resilience. Weight is important in rabbit construction, as transit times are dependent upon the mass of the rabbit. High resilience is important because of the mechanical shock the rabbit receives on impact with the hutches. The target material itself was usually a three-part system. Since most of the targets were powders, a foil was needed to retain the target inside the rabbit. This foil had to be strong so that repeated impacts by the powder did not pierce it, yet thin so that energy loss of the bombarding beam was small. Also the foil could not produce any activity of its own. Because of this last requirement high-Z materials whose products had long half-lives were considered. Both 25 micron Ta and Re foils were used. Neither foil produced any measurable activity and would usually remain intact for a full day's run. Behind the target powder, 500 microns of Ta were placed so that if the foil did break and the powder leave the rabbit, the bombarding beam would stop in Ta rather than in nylon which because of the carbon, nitrogen, and oxygen in it produces large amounts of radioactivity when

bombarded.

Although the shuttle system is extremely convenient for measuring relative intensities of delayed radiations, as is done in the first part of this thesis, reliable measurement of absolute yields is much more difficult. Because of the poor vacuum at the bombarded target, the use of a moving target, and the need to use collimators which form part of the Faraday cup, electronic measurement of the beam current is unfeasible and other means must be employed to obtain absolute production rates.

C. Detection Systems

No attempt was made to observe the emitted positrons directly. Rather the observation of beta branches depended upon detection of the gamma rays which de-excited the nuclear levels populated in the beta decay. Since all the beta decays studied decay predominantly by positron emission (more than 99% of the decays), two 511-keV annihilation gamma rays also follow each decay.

Although NaI detectors have higher detection efficiencies, particularly for high-energy gamma rays, Ge(Li) detectors were preferred because of their excellent energy resolution. Ge(Li) detectors are now standard laboratory equipment, and their properties will not be described here. (For a review, see French et al 1969). Figure 6 shows the detection efficiency for a 73cc Ge(Li) in the geometry of Figure 4. Three curves are shown: 0 cm of lead between the hutch and the detector, 2.5 cm of lead, and 5.0 cm of lead. Since in all cases studied, the 511-keV gamma ray was by far the most intense, steps were taken to lower

its efficiency relative to the higher-energy gamma rays of the weak branches. As can be seen from Figure 6, the addition of a few cm of lead between the hutch and the detector makes high-energy gamma rays much more likely to produce a photopeak event in the Ge(Li) than the 511 keV gamma rays. However, the presence of lead results in much lower absolute detection efficiency.

The introduction of lead attenuator has one other minor benefit. Since the probability for detecting two gamma rays is so low when even a small amount of lead is used, corrections for summing of gamma rays become unimportant. To reduce detection of X-rays produced in the lead shielding, an X-ray filter of Ta and Sn is placed between the Pb attenuator and the Ge(Li) detector.

In most of the experiments described the count rate was lower than desired, being about 10^4 counts/sec. It was felt, however, that to increase the rate by reducing the amount of Pb attenuator would not help sufficiently for the loss of resolution in the Ge(Li) detector. Consequently counting periods, although not intolerably long, often lasted a full running day. In order to keep the detected room background as low as possible for such long runs, 5 cm of Pb surrounded the Ge(Li) detector. With this arrangement, the integral count rate for pulses greater than .511 MeV was 1.5/sec.

Two different Ge(Li) detectors were used in these experiments. Both detectors were purchased from Princeton Gamma-Tech and were of coaxial design with one end open as shown in Figure 4. The smaller of the two detectors (#503) originally had a nominal active volume of 55 cm^3 and a photopeak efficiency relative to a 3"x3" NaI of 12%.

However, before these experiments started, the detector was sent back to the manufacturer for lithium redrifting because of neutron radiation damage. Through redrifting, the active volume was reduced by about 10%. The resolution of the redrifted detector for the 1.33 MeV gamma ray of ^{60}Co is about 3 keV and the peak-to-Compton ratio is 25:1. The larger of the detectors (#909) arrived after the start of these experiments. It has a nominal volume of 73 cm^3 and an efficiency relative to NaI of 16%. The resolution for this detector at 1.33 MeV is 2 keV and the peak-to-Compton ratio is 35:1.

D. Electronics

A block diagram of the electronic equipment used in these experiments is shown in Figure 7. The electronics associated with the treatment of the charge pulse from the Ge(Li) detector is standard, consisting of a preamplifier, a main amplifier, and an analog-to-digital converter. For all experiments a Tennelec TC-200 amplifier was used with 3.2 μsec double differentiation pulse shaping. This shaping time was determined to give best resolution under actual counting conditions. The preamplifiers were charge-sensitive and were an integral part of the Ge(Li) detectors. The ADC's were integral parts of the multi-channel analyzers of which three were used, a Nuclear Data ND160 with ND2200 ADC's, RIDL Model 34-27, and the Nuclear Data ND4420 computer system.

In the earliest investigations, the timing signals for bombardment, transfer of the rabbit, and counting were obtained from a pre-existing analog sequence timer (Kellogg drawing #101B). Then, to achieve superior precision and facility in setting required timing

intervals, a digital sequence timer was constructed. A description of the operation of this sequence timer is given in Appendix A. The unit consists of a basic oscillator, a frequency divider, and 14 preset scalers. The basic oscillator is a multi-vibrator whose frequency is controlled by a quartz crystal. The frequency is stable to 10 ppm and can be adjusted over a small range, ±30 ppm. The frequency divider is a set of synchronous divide-by-ten circuits which can be gated into or out of the circuit by means of a thumbwheel switch. The frequency following the divider circuit is as accurate as the basic clock and can range (when the standard 1 MHz crystal is used) from 1 MHz to 0.1 Hz. The preset scalers are set by use of four-decade thumbwheel switches. The precision of the timer is limited by the range (1 to 9999) of these scalers. Because the times are digitally set through the use of thumbwheel switches, the time necessary for set up is small. The unit also has provision to act as a free-run oscillator so that signals from an ADC can be digitally routed into various sections of memory depending upon the amount of time since a given event. This sequence timer was used for all measurements except those of the ^{27}Si and ^{23}Mg decays.

E. Timing

The selection of the timing sequence was determined so that bombardment is long enough to obtain maximum yield, yet not so long that long-lived contaminant radiation will be significantly produced. Also since many cycles are necessary, the total bombarding time, not just the length of an individual bombardment, is important. Normally, in

view of the limited available beam current, the best compromise was to bombard for a mean life of the activity under study. This usually produced sufficient yield per cycle and kept long-lived contaminants to a tolerable level.

If the half-life of the decay under study was comparable to the rabbit transit time, as in the case of ^{39}Ca, then the counting periods needed to start as soon as possible. For longer-lived activities, the start of the counting periods could be delayed somewhat so that any short-lived activity could decay.

Since positive identification of the source of the delayed gamma radiation was desired, the gamma rays were stored into different areas of the analyzer's memory depending upon the length of time since bombardment. This procedure gave valuable information about the half-life of the parent nuclei. Usually two time periods, each either a half-life or a mean-life in length, were sufficient as the energy of the gamma ray narrowed the possible parents to a few nuclei. Since there are so many sources of 511-keV annihilation radiation, the energy signal is not useful. Therefore, four or more counting periods were used whenever the intensity of the 511-keV gamma radiation was desired. This allowed an adequate determination of the strength of the 511-keV radiation produced by the decay of interest, which was always the most intense source.

IV. METHODS OF DATA ANALYSIS

A. General Features of Spectra

As all but one of the experiments involved a rabbit bombarded by a high energy proton beam, many common background features are present in the spectra independent of the target material used. These features can be divided into three categories, room-background radiation, beam-produced background radiation, and gamma-ray processes from high energy positrons.

Although the Ge(Li) detector was heavily shielded with lead, peaks nevertheless appear in the spectra that can be ascribed to room background. The photopeaks at 1461 keV (^{40}K) and 2614 keV (^{232}Th) arise from radioactivity in the concrete walls of the control room. Lower energy gamma rays from the decay of ^{232}Th are not seen because they are much more severely attenuated by the lead shielding than the 2614-keV gamma ray. These two photopeaks (and the escape peaks from the Th 2614-keV gamma ray) did not coincide with any gamma-ray transition sought, and the Compton events from this room-background radiation were always much less than the background produced by the other two processes in the areas of interest.

The gamma ray from the beta decay of ^{14}O, 2313 keV, is seen in most spectra, the ^{14}O being produced by the $^{14}N(p,n)^{14}O$ reaction. Although neither the photopeak nor the escape peaks from this gamma ray interfere with any of the experiments, the Compton events sometimes did. To reduce the activities attributable to beam bombardment of air, argon was used as the propellant gas whenever this background was severe.

When bombarded by 10-MeV protons, ^{40}Ar (which makes up 99.6% of natural Ar) produces only activities which have very long half-lives (269 days and longer) or decay without producing any gamma radiation (^{33}P and ^{36}Cl). Beam on the beryllium rabbit produced no discernible radioactivity, but in certain long runs which had low yield of high-energy gamma rays, photopeaks ascribed to the decay of ^{66}Ga, ^{52}Mn, and ^{60}Cu were noted. These are attributed to beam bombardment of the stainless steel beam hutch and the brass hutch holder. This activity was picked up by the rabbit and carried to the detector station. These gamma rays were extremely weak and never bothered the experiment.

The most serious background problems arose from the activity of interest, radiation produced by moving positrons, viz., bremsstrahlung and annihilation in flight. Annihilation in flight is important not only as a background problem but as a correction needed to determine accurately the positron yield. It is thus treated extensively in the next section. Like bremsstrahlung, annihilation in flight increases with positron energy and with the Z of the stopping medium. Also like thick-target bremsstrahlung, its intensity drops quickly as a function of gamma-ray energy. These properties can be seen in Figure 8. Bremsstrahlung is a well known process, its important properties having already been described. (For derivation see, e.g., Heitler 1954). These background problems were minimized by using materials with as low an atomic number as possible to stop the emitted positrons. However, as in previous arrangements chosen to improve signal-to-noise, the absolute efficiency for detecting gamma rays is reduced, as the thickness of

lucite needed to stop a given energy positron is more than that of a dense material, hence increasing the source-to-detector distance.

The sensitivity of this detection method is limited by the bremsstrahlung and the annihilation in flight.

B. Correction to Gamma-Ray Yields

1. Introduction

After the gamma-ray spectra have been obtained, the observed photopeak intensities must be corrected to determine the true yield. The lead-shielded Ge(Li) detector, as can be seen from Figure 6, does not have the same efficiency for each gamma-ray energy. Indeed, the detection system was designed so that 511-keV gamma rays would be detected far less efficiently than higher energy gamma rays.

When annihilation radiation is observed, two further corrections are necessary. Since the annihilation gamma rays do not originate from a point, the point-efficiency measurements used for nuclear gamma rays must be corrected for a distributed source. Also because of annihilation in flight, two 511-keV gamma rays are not necessarily emitted for each positron. In most cases, these last two effects tend to cancel.

2. Gamma-Ray Detection Efficiency

Although gamma-ray attenuation coefficients are known for lead, for the best precision the relative-efficiency functions for each of the two Ge(Li) detectors and for each thickness of lead attenuator is determined experimentally. Standard well-known gamma-ray sources were placed inside the detector hutch at the position of the rabbit or were

otherwise separated from the lead attenuator by the appropriate amount of lucite. For large thicknesses of lead, the amount of room-background radiation could not be neglected, and backgrounds were subtracted.

The two calibration sources most often used, ^{56}Co and ThB, were produced at the Kellogg Radiation Laboratory. Thorium B was produced by milking a ^{228}Th source. Before use, the source was allowed to decay for more than 10 hours so that the daughters of ThB would be in transient equilibrium with the parent. Branching ratios were taken from Nuclear Data Sheets (Pancholi 1972, and Lewis 1971). Cobalt-56 was made by 11-MeV proton bombardment on 'Netic' magnetic shielding foil. After allowing time for the short-lived activities to decay (about a month), no gamma radiation appeared except that which could be ascribed to ^{56}Co. The branching ratios for this source were taken from the adopted values of Camp and Meredith (1971).

After obtaining relative-efficiency measurements at energies present in the radioactive sources, relative-efficiency values had to be determined for the energies actually seen in the decay measurements. Usually interpolation with the logarithm of the gamma-ray energy versus the logarithm of the relative efficiency was found to give the simplest fit for the measured efficiencies and so was used for the unmeasured gamma-ray energies.

A correction needed only in the study of the beta decay of ^{23}Mg was that for coincidence summing. (Random summing was negligible in all cases studied.) This correction depends on the cascade structure of the decay and will be explained in the description of the experimental results for the ^{23}Mg decay.

3. Annihilation in Flight

When a positron at rest annihilates with an electron at rest, two 511-keV gamma rays are emitted. (The case of three-photon emission can be neglected.) However, the positrons are not at rest when they leave the nucleus, and there is a non-negligible probability that they will annihilate while moving. This process will yield gamma rays having energies different from 511 keV. Since in these experiments the number of positron decays is deduced from the number of 511-keV gamma rays observed, the number of positrons which annihilate in flight and hence do not produce 511-keV gamma rays must be known.

The treatment given here follows that of Gerhart et al (1954); an alternative derivation can be found in Heitler (1954). There are two important processes, two-quanta annihilation and one-quantum annihilation (which is important at high energies and for high-Z stopping materials). Using the probability for two-quanta annihilation when the positron is at rest, first derived by Dirac (1930), Bethe (1933) obtained the cross section for annihilation when the positron is moving,

$$\frac{dw_2}{dk} = \frac{\pi r_0^2}{E^2 - 1} \frac{1}{kk'} \left\{ k^2 + k'^2 + 2(E+1) - \frac{(E+1)^2}{k'k} \right\} \qquad (15)$$

where $r_0 = e^2/(m_e c^2)$ is the classical electron radius, $Em_e c^2$ is the energy of the positron (including the rest mass), and $km_e c^2$ and $k'm_e c^2$ are the energies of the gamma radiation emitted. The conservation of energy and momentum requires $k + k' = E + 1$ and that the gamma-ray energies lie between

$$(E+1) - (E^2-1)^{1/2} \leq 2k \leq (E+1) + (E^2-1)^{1/2} \tag{16}$$

The probability that a positron will annihilate with a gamma ray having energy in the range dk while traversing a distance dx is then just

$$NZ\ dw\ dx = NZ\ dw(dE/dx)^{-1}\ dE \tag{17}$$

where N is the number of atoms per unit volume having Z electrons per atom, and dE/dx is the stopping power. The stopping power has two sources, collisions and bremsstrahlung. Using the Bhabha (1936) cross section for positron-electron scattering, Rohrlich and Carlson (1954) derived the stopping power for positrons due to collisions,

$$-\frac{dE}{dx} = NZ\ \frac{2\pi r_o^2}{\beta^2}\ \{\ell n\ \frac{2T^2(E+1)}{I^2} - \frac{\beta^2}{12}\left[23 + \frac{14}{(E+1)} + \frac{10}{(E+1)^2} + \frac{4}{(E+1)^3}\right]\} \tag{18}$$

where T is the kinetic energy of the positron, β is v/c of the positron, and I is the ionization potential of the stopping material. This stopping power differs by about 5% at 100 keV, and less at higher energies, from the Bethe (1932 and 1930) formula. The stopping power due to radiation emission was taken from Jackson (1962)

$$\frac{dE_{rad}}{dE_{col}} = \frac{4}{3\pi}\ \frac{m_e}{M}\ \beta^2\ \alpha Z[\ell n(2T^2(E+1)/I^2]^{-1} \tag{19}$$

where (m_e/M) is the mass of the electron relative to the mass of the average atom in the stopping material.

If every positron started with the same energy, then the number of annihilating photons could be obtained by integrating equation 17 over the positron energy from the starting energy E_1 to the minimum energy needed to produce a photon in the range dk,

$$E_{min} = k - (k-1)/(2k-1) \tag{20}$$

There is a small correction to equation 20 since the positrons which annihilate should not be included in the integral after annihilation. However, this correction is small and will be neglected. Also the positrons do not start with the same energy but rather with a distribution $D(E_1,E_o)$ of energies as determined by the phase space available to the decay. This distribution is related to equation 7. In addition, since the energy of the annihilation photon is not important in this experiment (except as a source of background), an integration over photon energies is required from the maximum gamma energy to that energy for which the gamma ray is indistinguishable from a 511-keV gamma ray (i.e., $E_{min} = 511 + \Delta$, where Δ is the resolution of the gamma detector). Thus the number of positrons lost due to two-quanta annihilation in flight per positron is

$$L_2 = \int_{\gamma_{min}}^{\gamma_{max}} dk \int_{E_{min}}^{E_o} dE\ NZ \frac{dw_2}{dk} \left(\frac{dE_e}{dx}\right)^{-1} D(E,E_o) \tag{21}$$

One-quantum annihilation in flight is not important in these experiments except as a source of background. However, when stopping materials with a high atomic number are used, the correction can be significant. The cross section per K electron for single-quantum

annihilation was given by Bethe (1933),

$$w_1 = \alpha^4 Z^5 \, 2\pi r_o^2 (E+1)^{-2} \, (E^2-1)^{-1}$$

$$* \, [(E^2-1)^{1/2} \, (E^2+ 2E + 4)/3 - (E+2) \cosh^{-1} E] \qquad (22)$$

where the symbols have the same meaning as for two-quanta emission. The energy of the emitted photon is given to sufficient accuracy by $k = E + 1$ (i.e., the binding energy of the annihilated electron and the recoil of the spectator atom can be neglected). Again integrals over initial positron energy and over the energy of the annihilating positron must be performed. The probability that a positron will annihilate by one-quanta emission is

$$L_1 = 2N \iint w_1 (dE_e/dr)^{-1} \, D(E,E_o) \, dE \, dE_o \qquad (23)$$

where the factor of 2 represents the two K electrons per atom. In Figure 8, the number of photons emitted per positron per keV gamma-ray energy is shown for the positron decay of ^{27}Si, both for a tantalum and a lucite absorber. Since the only Z dependence for two-quanta annihilation in flight appears in the stopping power , there is little difference in intensity between the two absorbers for the low-energy gamma rays where the two-quanta process is important. At higher energies, the single-quantum becomes important and its Z^5 dependence separates the curves for the two absorbers. In Figure 9, the percentage of positrons which annihilate in flight is shown as a function of positron endpoint energy for a detector resolution of 2 keV. As can be seen from Figure 8, the gamma-ray cutoff energy is relatively

unimportant since the added contribution near 511 keV is small.

Experimental tests of these predictions are difficult because in addition to annihilation in flight, inner and outer bremsstrahlung are present. Added experimental complications are the difficulty of normalization and the response function of the gamma detector. Kendall and Deutsch (1956) obtain agreement to about 5% for low energy positrons in anthracene, while Gerhart et al find larger disagreements, particularly for positrons from the decay of ^{35}Ar (E_o = 4.4 MeV, the highest endpoint energy for the decays they studied). Therefore, the uncertainty in the annihilation in flight correction is taken equal to the correction for the decays studied in this work. If the correction is too small, as found by Gerhart et al, then the branching to the non-mirror states would be decreased from the values stated in this thesis. Many experimenters neglect the correction for annihilation in flight and hence their branchings to non-ground-state decays will be systematically high. This systematic error increases if high-Z material is used to contain the positrons near the decaying nucleus.

4. Spatial Distribution

Because the efficiency of the gamma-ray detector was obtained for point sources and since the 511-keV annihilation radiation is not a point source, a correction for a distributed source must be made. A ^{22}Na source enclosed in steel was placed at various distances from the crystals, both on and off axis. Because of the cylindrical symmetry of the detector system, only a two-dimensional grid is required. Lucite

and lead were placed between the source and the detector, so that the proper amount of attenuation was included. Knowing the point efficiencies and the range for a given energy positron (obtained from a linear interpolation from the data given in Nelms 1956 and 1958), integrals over space and positron energy were performed to obtain the efficiency of the distributed source relative to a point source. For the positron energies and distances used in these experiments, the correction was usually less than 10%.

C. Calculation of the Fermi Function

Once the partial half-life of a beta transition is known (by dividing $t_{1/2}$ of the parent nucleus by the branching ratio for the transition), the Fermi function, f , must be calculated in order to obtain log ft . Both positron and electron capture must be considered.

The calculation of the Fermi function for positron emission is straightforward although some exotic mathematical functions are used. The computer program of Bahcall (1966) was used to calculate the positron f values. This program includes the nuclear-size corrections and atomic screening corrections as described in Section 2. Electromagnetic corrections are not included.

The calculation for electron capture is more difficult as bound-state wavefunction must be calculated. The values for the Fermi function for electron capture were derived from the tables of Gove and Martin (1971). The bound-state wavefunctions and the exchange and overlap corrections were calculated from solutions of the Dirac equation with a Hartree self-consistent potential (Lu et al 1971). The

electron exchange is included in the Slater (1951) approximation.

V. EXPERIMENTAL RESULTS

A. Introduction

This section will separately treat each of the decays studied. The expected beta branches will be discussed based upon the spectroscopic information in Ajzenberg-Selove (1972) and Endt and van der Leun (1973). Also earlier attempts to measure the beta branches will be described. Since each decay involves slightly different experimental details, these details will be reviewed. The actual experimental data and its interpretation follows. Finally, the various theoretical models used to calculate the beta decay studied will be considered.

B. Neon-19 Decay

1. Previous Knowledge

The decay of ^{19}Ne to its mirror, the ground state of ^{19}F, is well known. The energy level diagram for ^{19}F - ^{19}Ne is shown in Figure 10, the data being taken from Ajzenberg-Selove (1972). As can be seen, the only allowed decays of the $1/2^+$ ground state of ^{19}Ne are to its mirror and to the $3/2^+$ level at 1554 keV. Jones et al (1954), the first group to study the ^{19}Ne decay, observed no indication of gamma rays other than the 511-keV annihilation radiation. Other investigators have looked at various aspects of the decay, but none have sought the decay to the 1554-keV level.

The most precise values for the ^{19}Ne half-life come from Earwaker et al (1962) ($t_{1/2}$ = 17.43 ± 0.06 sec) and from Goss et al (1968) ($t_{1/2}$ = 17.36 ± 0.06 sec). The earlier measurement of Janecke

(1960) disagrees with the more recent results and was not used.

2. Experimental Details

Because the decay to the 1554-keV level was expected to be the weakest of the beta branches that we would try to observe (on the basis of the many-particle shell model; see the compilation of Lanford and Wildenthal 1973), the greatest amount of lead attenuator, 5.1 cm, was used in this experiment. Since so much lead is needed to increase the efficiency for detecting the 1357-keV gamma cascade from the 1554-keV level relative to the annihilation radiation, other attenuators were investigated. Denser materials which have a lower atomic number than lead, such as Ta, were unsatisfactory as the attenuation coefficient for 511-keV radiation relative to 1357-keV radiation is not as high as for lead. For denser materials than lead which also had a higher atomic number, radioactivity becomes a serious problem. For example, depleted U (which is also totally ^{238}U $t_{1/2} = 4.5 \times 10^9 yr$) produces large amounts of gamma radiation, primarily due to the beta decay of ^{234}Pa.

Since the delayed gamma yield is greatly reduced by the Pb attenuator, thick targets of fluorine are required to obtain sufficient yield. Teflon, $(CF_2)_n$, was tried but the bombarding proton beam quickly drilled a hole through the teflon rabbit. Since no other solid, non-powder form of fluorine-containing compound was available, compounds of fluorine, LiF and PbF_2 were used. The powders were held in the rabbit by either a Ta or Re foil.

Using the LiF salt, a 1357-keV gamma ray was observed having the approximate half-life of ^{19}Ne. However, when the experiment was repeated, using slightly different beam currents and energies, the intensity relative to the annihilation radiation differed by a factor of 3. It is believed that the gamma ray observed originates not from the decay of ^{19}Ne but rather from ^{19}O. Oxygen-19 decays through the 1554-keV level, the same level as that sought in ^{19}Ne decay. Oxygen-19 has nearly the same half-life ($t_{1/2}$ = 29 sec) as ^{19}Ne. It is presumed that ^{19}O was produced from the $^{19}F(n,p)$ reaction, the neutrons coming from the prolific $^{7}Li(p,n)$ reaction. Evidence for a high neutron flux came from the observation of 1634-keV gamma rays produced from $^{19}F(n,\gamma)^{20}F(\beta^+,\gamma)^{20}Ne$ and of ~6-MeV gamma rays produced from $^{19}F(n,\alpha)^{16}N(\beta^-,\gamma)^{16}O$. When PbF_2 was used instead of the LiF, these gamma rays, including the 1357-keV gamma ray, were absent, consistent with this interpretation.

The main background problems were annihilation in flight and the Compton events from the 2313-keV gamma ray following decay of ^{14}O. This latter source of background was greatly reduced by use of argon gas as the propellant in the rabbit system.

3. Experimental Results

As can be seen from Figure 10, if a beta branch feeds the 1554-keV level, a 1357-keV gamma ray should be observable. In Figure 11 is the 4096-channel spectrum obtained during the first 17.5 sec counting period with PbF_2 as the target material. No evidence of a 1357-keV gamma ray is seen, although many gamma ray peaks appear. In

Figure 12, the region around 1357-keV is shown in more detail. The gamma rays (other than 511-keV) come from various parts of the rabbit system or from lead in the PbF_2 target material. For example, the 1291-keV peak seen in Figure 12 is the second escape peak of the 2313-keV gamma ray following ^{14}O decay. The peak at 1434 keV results from $^{52}Mn^*$ beta decay. Oxygen-14 is produced by proton bombardment on nitrogen trapped in the powder, while $^{52}Mn^*$ is from proton bombardment of the stainless steel rabbit hutch (which contains chromium), the recoil nuclei sometimes being implanted into the rabbit.

Only an upper limit for the decay of ^{19}Ne to the 1554-keV level can be assigned, as no gamma ray from the 1554-keV level has been observed. Using the gamma decay scheme for the 1554-keV level given in Ajzenberg-Selove, viz., $(92.5 \pm 0.1)\%$ cascading via the 197-keV level, one finds the beta branch to be less than 3×10^{-5} with a confidence level at 90% (2σ level). This corresponds to a log ft > 5.7 .

4. Theoretical Work

Although much theoretical work has been performed for A = 19 , particularly using the shell model, only two predictions for the strength of the beta branch to the 1554-keV level are available.

In the compilation of Lanford and Wildenthal (1973), the results for a many-particle shell-model calculation of Wildenthal are included. The work has not otherwise been published. Using an unrestricted s-d shell basis and an inert ^{16}O core, Wildenthal calculated the allowed beta branches from the ^{19}Ne ground state, predicting the

branch to the 1554-keV state to have a log ft of 10.5 . For comparison, the well-known highly retarded allowed decay of ^{14}C has a lot ft of 9.0 .

Although all the particles in the s-d shell were considered active in the calculations by Wildenthal, the configuration space may have been too restricted. If only s-d particles are active, then only positive parity states can be formed. Yet the first excited state of ^{19}F, at 110 keV, has negative parity as do three of the five states below the level at 1554-keV. According to the calculation of Zucker et al (1968), if a ^{12}C core of $(1s)^4(1p_{3/2})^8$ is used, then there is a sizable component of $(1p_{1/2})^2(1d_{5/2})^2$ in the ground state of ^{16}O as well as $(1p_{1/2})^4$. According to this calculation, ^{16}O cannot be treated as just an inert $(1s)^4(1p)^{12}$ core, but core excitations from this configuration must be included. Consequently if the configuration space is enlarged, the calculations may show that the beta transition from ^{19}Ne to the 1554-keV level is not so extremely retarded as now predicted by Wildenthal.

Donnelly et al (1974) in an article suggesting the possibility of studying neutral weak currents by inelastic neutrino scattering from nuclei, predict log ft = $5.0\ ^{+1.0}_{-0.3}$ for the branch to the 1554-keV level. They used the single particle Nilsson model with a K = 1/2 band and four adjustable parameters, which predict various gamma strengths and energies in good agreement with experimental values. Donnelly et al note that the use of this simple model is justified

through extensive intermediate-coupling calculations of Benson and Flowers (1969).

The upper limit obtained in this experiment cannot rule out either prediction. However, the strength of this transition is not near the middle value of Donnelly et al, as then the strength of the 1357-keV gamma ray shown in Figure 12 would be as large as the 1434-keV to its right. Because of the large uncertainty assigned to the Nilsson-model prediction, $(1.0 \pm 0.9) \times 10^{-5}$, it is difficult to prove it too low. On the other hand, until the branch to the 1554-keV level can be actually seen, the prediction or the many particle shell model must remain unchallenged.

C. Magnesium-23 Decay

1. Previous Work

As the beta decay of ^{23}Mg to the first excited state of ^{23}Na is quite strong (about 10% of the mirror transition), the mirror decay and the decay to the first excited state have been well studied. Table 2 shows the results of previous investigations.

The energy level diagram for ^{23}Na-^{23}Mg is shown in Figure 13, based on the data from Endt and van der Leun (1973). Besides the decays to the ground and first excited state of ^{23}Na, there are three other possible allowed ^{23}Mg decays, to the $1/2^+$ level at 2391 keV, to the $3/2^+$ level at 2982 keV, and to the $5/2^+$ level at 3915 keV. The last two decays lack sufficient energy for positron decay but may decay by electron capture.

Only Détraz et al (1971) have searched for these weak branches. They did not find them but placed an upper limit of 8×10^{-5} for the transition to the 2391-keV level. This limit corresponds to a log ft of 4.9, comparable to typical allowed transitions. Détraz et al did not place limits on other allowed transitions.

The value for the half-life of ^{23}Mg is the weighted average from Goss et al (1968) 11.40 ± 0.05 sec, Alburger (1974), 11.36 ± 0.05 sec, and Azuelos et al (1974), 11.26 ± 0.08 sec. This weighted average, 11.36 ± 0.04 sec, is considerably smaller than older values. All gamma-ray branching information was taken from the compilation of Endt and van der Leun.

2. Experimental Details

The measurement was performed in two separate stages. First, the strengths of gamma rays depopulating levels in ^{23}Na were measured relative to the 440-keV gamma ray. Then the strength of the first excited state branch was measured by comparing the strength of the 440-keV gamma ray to the amount of annihilation radiation.

For the first stage, two salts, NaF and NaBr, were used as target materials. Gamma radiation from the beta decay of ^{79}Kr, produced from the ^{79}Br(p,n) reaction, was observed but did not interfere with the study of the ^{23}Mg decay. Proton bombardment of ^{19}F produced only annihilation radiation. In order to increase the relative efficiency of high-energy gamma rays to the normalizing 440-keV gamma rays, 2.5 cm of lead separated the rabbit hutch from the 50 cc Ge(Li) detector. Although the lead attenuates the 440-keV gamma rays more

strongly than annihilation radiation, the photopeak was still quite visible in the hollow between the Compton edge and the annihilation photopeak.

Since in the second stage of the study, the amount of annihilation radiation was the primary concern, the target powder, Na_2WO_4, was used to avoid extraneous production of annihilation radiation under proton bombardment. Both NaF and NaBr produce significant amounts of 511-keV annihilation radiation from non-^{23}Mg decays. Using Na_2WO_4 the only contaminant source of 511-keV radiation is from (p,n) reactions on the less abundant isotopes ^{17}O and ^{18}O whose products are relatively long-lived. No lead attenuator was placed between the detector and the lucite hutch in this case.

Gamma-ray efficiencies for point and distributed sources were measured as described above. Furthermore, since there is a substantial probability that the 440-keV gamma ray will be detected in coincidence with one of the 511-keV gamma rays, a summing correction was applied. From the observed sum peak in the spectrum of the ^{23}Mg decay and the photofraction of 511-keV radiation (obtained by using a radioactive source of ^{68}Ge, which decays predominantly by positron emission and has no low energy gamma rays), the summing correction was calculated to be $(12 \pm 1)\%$.

3. Experimental Results

The spectrum of the delayed gamma rays following 10-MeV proton bombardment of NaF is shown in Figure 14. The photopeak corresponding to the 2391-keV transition to the ground state is observed as is the

photopeak corresponding to the cascade through the 440-keV level. No indication (less than 7×10^{-5} of the strength to the 440-keV level) was found for any gamma ray depopulating the 2981-keV level. No special attempt was made to see the gamma rays, if any, depopulating the 3915-keV level as the available energy for electron capture is only 142 keV, making the phase space very small. Besides the checks provided by measuring the half-life of the gamma-rays at 2391 and 1951 keV and the energies of these two gamma rays, a confirmation that these gamma rays correspond to the decay of ^{23}Mg to the third excited state of ^{23}Na is the ratio between the ground-state gamma-ray branch and the branch to the 440-keV level. From the data obtained in this experiment, the 2391-keV level decays $(64 \pm 7)\%$ of the time directly to the ground state, consistent with the value $(65 \pm 1)\%$ appearing in the compilation of Endt and van der Leun.

For the measurement of the intensity of the beta branch to the 440-keV level, two runs were taken, each having four counting periods, each period lasting a ^{23}Mg mean life. There was no evidence of any troublesome amount of long-lived 511-keV radiation. One of the spectra obtained while determining the absolute branch to the first excited state appears in Figure 15.

Table 3 lists the beta branching of ^{23}Mg to various states of ^{23}Na relative to the first excited state branch. The results for the branch to the state at 2391 keV, $(8.1 \pm 1.2) \times 10^{-4}$ is consistent with the limit of Détraz et al, 9×10^{-4}. The limit for the transition to the 2077-keV level is one-half the value given by Détraz et al.

After making corrections, the branch to the first excited state of ^{23}Na is (8.1 ± 0.4)%. When this value is averaged with previous values, which are slightly higher (see Table 2), the strength of the beta branch from ^{23}Mg to the first excited state of ^{23}Na is (8.7 ± 0.2)%.

Using the weighted average for the strength of the beta branch to the 440-keV state, the absolute strengths to the other levels are calculated as listed in Table 4. It can be seen that the branch to the 440-keV level is quite strong, having a log ft value of 4.39, and that the branch to the 2391-keV level is not retarded, having a log ft of 5.0. The limits for transitions to other levels are not stringent. Even for the allowed decay to the 2981-keV level, which has a branching ratio of 5×10^{-6}, the limit for log ft is only 4.6, a value smaller than most non-mirror allowed decays.

4. Theoretical Work

Only two papers have appeared which contain predictions concerning non-mirror decays of ^{23}Mg. Gunye (1973), using projected multishell Hartree-Fock wavefunctions, predicted the branch to the ground and first excited states. He modified the NN interaction obtained by Elliott et al (1968) so that reasonable binding energies and rms radii are obtained for s-d shell nuclei. The calculation is restricted to axially symmetric deformations and does not include pairing corrections. Band mixing, however, is included. Gunye obtains a log ft for the transition to the ground state of 3.92, as contrasted with 3.67 obtained experimentally, and 4.15 for the log ft for the branch to the 440-keV level, compared with 4.39 obtained experimentally. Gunye comments that

this disagreement, which he calls "semiqualitative agreement" is due to the use of states which are not invariant under time reversal. It must be noted, however, that the ground-state branch is a mirror decay and hence should be accurately calculable.

The other calculation is a many-particle shell-model calculation by McGrory and Wildenthal (1971). However, unlike the calculation for the ^{19}Ne decay, the model space is truncated to a subset of s-d shell orbits. An inert core of ^{16}O is assumed and the configurations outside this core are restricted to

$$(d_{5/2})^{n_1} (s_{1/2})^{n_2} (d_{3/2})^{n_3}$$

where $3 \leq n_1 \leq 7$, $n_2 \leq 4$, and $n_3 \leq 2$. That is, they allow no more than 4 particles outside the $d_{5/2}$ shell and no more than two particles in the $d_{3/2}$ shell. The configuration space is restricted so that computer computations would not take inordinate time or computer memory. McGrory and Wildenthal used "realistic" matrix elements by Kuo (1967) but modified them to improve the agreement between calculated and observed energy levels for $A = 18$ to 22, but not for $A = 23$. They report that they found no significant difference between the spectra of low-lying states for $A = 20$ to 22 when calculated in the full space or in the truncated space. They note, however, that although this is certainly a necessary test, it is hardly sufficient, since the percentage of states truncated is larger for $A = 23$ than for lighter nuclei. Also McGrory (1970) has shown that both M1 gamma rays and beta decays for $A = 17$-22 depend strongly on the size of the model space. Even so, the

model does very well, as shown in Table 5. McGrory and Wildenthal accurately predict the mirror decay and disagree with experimental values for the two lowest non-mirror decays by a factor of only two. Again, like Gunye, values for the decays obtained theoretically differ in opposite directions from the experimental values for the two states. Although the necessary wavefunctions have been calculated, McGrory and Wildenthal do not report predictions for other allowed transitions. All their reported values appear in the compilation of Lanford and Wildenthal and not in the original paper.

D. Silicon-27 Decay

1. Previous History

The mirror decay of ^{27}Si to ^{27}Al has been studied by many investigators as noted by Endt and van der Leun (1973). Using the information from their compilation, Figure 16 displays the energy level diagram for ^{27}Al-^{27}Si. Allowed decays should be present to the states at 1014, 2211, 2734, 2981, 3956, 4409, and 4580 keV.

Table 6 presents the work which has been performed on the intensity of the beta branch to the 2211-keV level. There are serious discrepancies. Vasil'ev and Shavtvalov (1961) used a magnetic spectrometer to observe emitted positrons. Talbert and Stewart (1960), Paul et al (1961), and Gorodetzky et al (1964) used NaI counters to detect the delayed gamma rays following the beta decay of ^{27}Si. Détraz et al (1971) and Berenyi et al (1971) used Ge(Li) detectors to observe the delayed gamma rays.

There is much less information for the other allowed transitions. Détraz et al observed transitions to levels at 1014 and 2981 keV, as well as to the 2211-keV level. They did not see a transition to the 2734-keV level or to any of the levels above 3 MeV. For allowed transitions to levels above 3 MeV, the decay of ^{27}Si can proceed only by electron capture, thus making the branching to these levels very small.

The value for the half-life of ^{27}Si is taken from Goss et al (1968) to be 4.17 ±0.01 sec, which is in good agreement with earlier measurements summarized in Endt and van der Leun.

2. Experimental Details

As for the study of the ^{23}Mg decay, the ^{27}Si decay study was carried out in two distinct stages. However, the study of ^{27}Si was facilitated by the use of an aluminum cylinder of 99.999% purity as a rabbit. This alleviated concern about the breakage of foils and contaminants in the rabbit while providing a stopping target to the beam producing ^{27}Si via the ^{27}Al(p,n) reaction.

For the relative measurements two runs were made, both having 3.3 cm of lead separating the lucite hutch from the detector. For the absolute measurements of the branch to the 2211-keV level, 0.6 cm of lead separated the hutch and the detector. It should be noted that at the bombarding energies used (about 10 MeV), no proton induced activity other than ^{27}Si can be produced on a pure aluminum target.

3. Experimental Results

The spectrum of gamma rays following the beta decay of ^{27}Si is shown in Figure 17. Background photopeaks, at 1461, 2313, and 2614 keV are quite evident. Also present are gamma rays depopulating levels in ^{27}Al. The gamma ray corresponding to the ground-state decay of the 2734-keV level is seen as well as the cascade through the 1014-keV level. According to the compilation of Endt and van der Leun, $(76 \pm 2)\%$ of the 2734-keV level decays proceed through the 1014-keV state, while in this experiment the value is $(79 \pm 2)\%$, an acceptable agreement. In Table 7 are shown the relative intensities for the beta branches of ^{27}Si allowed decays obtained in this experiment and by Détraz et al. Although there is agreement concerning the relative strength of the branch to the 2981-keV level, the strengths of the branches to the 1014- and 2734-keV levels are in disagreement. In a private communication, Détraz (1972) stated that the strength of the 1014-keV gamma ray depopulating the 3/2+ level was difficult to measure because of the presence of summing 511-keV annihilation radiation. Détraz et al used no attenuator between the target and the detector. In the spectra sent by Zaidins (1973) for the gamma rays following ^{27}Si decay as observed by Détraz et al, a 2754-keV gamma ray is clearly present. This gamma ray results from the beta decay of ^{24}Na and is seen because the rabbit facility at the University of Colorado is in a target room rather than in a shielded area. Both Détraz and Zaidins conclude that their upper limit for the branch to the 2734-keV level is realistic. However, the signature of the gamma rays observed in this experiment is too clear to mistake the branch to the 2734-keV level in ^{27}Al for some other decay.

If the branch to the 2734-keV level is accepted, then the discrepancy concerning the 1014-keV level can be explained. Since the 2734-keV level decays most of the time to the 1014-keV level, much of the strength Détraz et al ascribe to the branch to the 1014-keV level should be ascribed to the 2734-keV level. If the relative intensities of the 1014- and 2211-keV gamma rays observed by Détraz et al and in this experiment are compared (0.142 ± 0.048 and 0.093 ± 0.012, respectively), then the disagreement becomes much less.

After making small corrections for the various effects already mentioned in the ^{23}Mg decay study, the absolute strength to the 2211-keV state is $(0.181 \pm 0.014)\%$. This is in excellent agreement with the result of Berenyi et al $(0.18 \pm 0.05)\%$ but in disagreement with the precise measurement of Gorodetzky et al $(0.10 \pm 0.02)\%$. No reason for this disagreement is apparent, except perhaps that the poorer resolution of the NaI detector (as compared to a Ge(Li)) was insufficient to separate adequately the gamma ray peak from the large amount of bremsstrahlung.

From the weighted average of the strength of the beta branch to the 2211-keV level, the beta-branching ratios for ^{27}Si are calculated as listed in Table 8. It can be seen that the transitions to the 2211-, 2734-, and 2981-keV levels are strong, each having log ft values less than 5.1. However, the transition to the 1014-keV level ($\log ft = 7.4 \pm 0.2$) is substantially retarded. As can be seen from Figure 1, there are few allowed beta decays in the s-d shell having higher log-ft values.

4. Theoretical Work

Two different models, the weak-coupling model and the many-particle shell model, have been used to describe beta transition strengths of ^{27}Si. Because the branch to the 1014-keV level is so retarded, it probes the smallest parts of the wave functions and is a sensitive test of the models.

The weak-coupling model is the single particle shell model built upon two inert cores, in this case the ground and first excited states of ^{28}Si. Silicon-27 is viewed as a neutron hole coupled partially to the 0^+ ^{28}Si ground state, and partially to the 2^+ ^{28}Si level at 1779 keV. Aluminum 27 is hence considered as a proton hole coupled to the two states. Using the wave functions of Thankappan (1966) who considered the hole to be in the $d_{5/2}$ subshell, Berenyi et al predict the various decay strengths, which appeared in Table 9 along with the experimental values. It can be seen that except for the mirror transition, the model's predictions are about an order of magnitude in disagreement with the data. It even predicts the transition to the 2734-keV level to be weaker than the retarded transition to the 1014-keV level. Part of the reason for this disagreement may be in neglecting the other two subshells, the $s_{1/2}$ and the $d_{3/2}$. If only the $d_{5/2}$ subshell is used, then only one $3/2^+$ state is predicted, yet two exist below 3 MeV. Another source of error may be in neglecting higher states in ^{28}Si, but since the second excited state of ^{28}Si is at 4.6 MeV, the neglect of this and higher states is probably valid.

DeVoigt et al (1972) have used the many-particle shell model to predict beta decay strengths. They used an inert ^{16}O core and confined

the active configurations to

$$(1d_{5/2})^{n_1} (2s_{1/2})^{n_2} (1d_{3/2})^{n_3}$$

where $n_1 + n_2 + n_3 = 9$ and $n_1 \geq 8$. This restriction is necessary because of computer memory size. For the nucleon-nucleon interaction, DeVoigt et al used a surface delta interaction (Glaudemans 1967). Also, in order to save computer time, DeVoigt et al included in the transition strengths only those contributions for which the product of the amplitudes of the initial and final states is greater than 5×10^{-4}. This truncation, although not important in E2 transitions, is important for M1 transitions (and hence, since the operators are similar, for beta decay) as the predicted strength oscillates as the number of included components is increased. The values predicted by DeVoigt et al also appear in Table 9. Except for the transition to the 1014-keV level, the predictions are within a factor of 3 of experiment. The predicted strength to the 1014-keV level is of the same strength as the other decays, while experimentally it is much retarded.

Lanford and Wildenthal (1973) in their compilation of calculations of allowed beta decays in the s-d shell refer to another many-particle shell-model calculation, that of Wildenthal and McGrory (1973). In this calculation the model space is again restricted. However, they allow one more particle to be in either the $2s_{1/2}$ or $1d_{3/2}$ subshell than do DeVoigt et al. Again the surface delta interaction is used. The predicted beta branches of Wildenthal and McGrory appear in Table 9. As would be expected the values are not much different from those obtained by DeVoigt et al. However, there is slightly better agreement

for the non-retarded decays (but slightly worse for the retarded decay). Wildenthal and McGrory have also predicted the decay of ^{27}Mg, obtaining values that are an order of magnitude lower than experiment (see Endt and van der Leun) for the branches to both the 1014- and 843-keV levels, indicating that the trouble predicting beta transitions for $A = 27$ is not just limited to the ^{27}Si decay to the 1014-keV level.

Thus the many-particle shell model does better than the weak-coupling model (as might be expected since more valence nucleons are considered), but both models cannot predict accurately (within a factor of 100) the rate of the retarded transition to the 1014-keV level.

E. Potassium-37 Decay

1. Previous History

Beta decay for $A = 37$ has become important because of the experiments of Davis et al (1968) who are attempting to measure the flux of solar neutrinos by the ^{37}Cl$(r,e^-)^{37}$Ar reaction. Since the neutrinos may have high energy ($E_{max} \sim 14$ MeV), many states in ^{37}Ar take part in the reaction, the needed matrix elements having caused much experimental and theoretical work to be performed to unravel the $A = 37$ system.

An abbreviated energy level diagram is shown in Figure 18 for ^{37}Ar-^{37}K. Above the 3605-keV level, there are many levels of unknown spin and parity. At 4.99 MeV is the $T = 3/2$ state whose spin and parity are known by analogy with the ground state of ^{37}Cl. Of the states with known spin and parity, there are five states to which allowed decays are expected. The mirror decay to the ground state is by

far the strongest. Kavanagh (1964 and 1968) and collaborators have shown the existence of the branch to the 2796-keV level. Moss et al (1971) have detected the branch to the 3605-keV level. However, no group has reported the branch to the 1410-keV level or to the lowest T = 3/2 level. Although the branch to the 4.99 MeV level is expected to be very weak because of the small amount of energy available for its decay, the branch to the 1410-keV has more energy available than the already seen non-mirror decays.

The half-life is taken from the compilation of Endt and van der Leun (1973) who give the weighted average of rather old measurements (the last being that of Kavanagh 1964) as $t_{1/2} = 1.23 \pm 0.02$ sec. Because of an apparent mistake in the literature (which will be more fully described in the section on experimental results), the gamma ray branching was taken from Endt and van der Leun for all levels except the strongly fed 2796-keV level.

2. Experimental Results

The decay of ^{37}K was studied in two steps, first looking at the decay relative to a non-mirror transition, the transition to the 2796-keV level, and then looking at the strength of that transition relative to annihilation radiation. As no (p,n) reaction on a stable target produces ^{37}K, the $^{40}Ca(p,\alpha)$ reaction was used. At the bombarding energies used (about 10 MeV), the $^{40}Ca(p,n)^{40}Sc$ is energetically forbidden.

A thin disc (about 0.02 cm thick) of natural calcium was used as a target. To reduce oxidation and nitration, a thin layer of gold covered the disc. A non-stopping target was used to maximize the

$^{40}Ca(p,\alpha)^{37}K$ yield relative to the yield of (p,n) reactions on the other Ca isotopes present in the target.

For the relative measurements two runs were made, the first having 2.5 cm of lead separating the detector from the lucite hutch, and the second having 2.0 cm. For the absolute measurements, four different thicknesses of lead attenuator were used, 0.7 cm, 1.3 cm, 2.1 cm, and 2.5 cm.

3. Experimental Results

Since natural calcium was used as the target, many radioactive products besides ^{37}K were produced as can be seen in Figure 19, a spectrum of delayed gamma rays following 11 MeV proton bombardment of Ca. In Table 10 the various photopeaks are identified. Although the (p,n) reactions on Ca are strong, because of the long-lived products it is easy to separate ^{37}K decays from the decay of the Sc isotopes. The decay of the Sc isotopes do not present a serious background problem as the gamma rays are lower in energy than the gamma rays of interest following ^{37}K decay.

Three photopeaks having the half-life of ^{37}K were observed, 1611 keV, 2796 keV, and 3605 keV. The last two result from known decays of ^{37}K, but the gamma ray at 1611 keV has not been previously reported. If the value for the strength of the 2796-keV gamma ray relative to annihilation radiation is taken from either the work of Kavanagh or from the present work (see below), and if it is assumed that the 1611-keV results from a beta decay to the 7/2-level at 1611 keV, a log ft value of about 6.5 is obtained for this unique first-forbidden transition. However, in a recent survey, Raman and Gove (1973) have

shown that all known unique first-forbidden beta transitions have log ft's greater than 8.5. Also, according to the compilation of Endt and van der Leun, neither the 2796-keV nor the 3605-keV level decays through the 1611-keV level. As can be seen from Table 11, which contains the relative beta strengths to the various states in ^{37}Ar, the 1611-keV level if populated by only 1.6% of the decays of the 2796-keV level would explain the gamma rays seen. Taras et al (1972) put an upper limit of 2% on the decays of the 2796-keV through the 1611-keV level, but assert that there exists a $2 \pm 1\%$ branch to the 7/2+ level at 2217 keV. This latter branch according to the present results (at the 90% confidence level) is less than 0.4%. If one looks at the mirror nucleus of ^{37}Ar, ^{37}K, for some guidance, then according to the work of Goosman and Kavanagh (1967b) and Goosman (1967a), the 5/2+ level decays $(1.4 \pm 0.3)\%$ of the time through the 7/2- level. No statement concerning the possible branch through the 7/2+ level is made. From the present work and from the work of Goosman and Kavanagh, it seems that Taras et al may be mistaken about the branch to the 7/2+ level at 2217 keV, and the branch they reported is actually to the 7/2- level at 1611 keV. Thus the gamma ray at 1611 keV results not from the direct feeding of the 1611-keV level by a beta branch, but rather from a small gamma branch from the strongly fed 2796-keV level. This argument could be made even tighter by the direct observation of the 2796-keV to 1611-keV transition but, unfortunately, this energy range is obscured by the decays of the various Sc isotopes, particularly the intense gamma ray from ^{44}Sc at 1157 keV.

The other observed gamma ray associated with the ^{37}K decay, from the deexcitation of the 3605-keV level, almost certainly originates

from a beta branch feeding that level. Moss et al reported that this beta branch had an absolute strength of $(3.4 \pm 0.6) \times 10^{-4}$ by using the data of Kavanagh and Goosman (1964) for normalization. Noting that the relative error for the branch to the 3605-keV state is smaller than the relative error of the normalization, the error associated with the branch to the 3605-keV level must refer to only the uncertainty in the measurement of Moss et al. This would imply that the branch to the 3605-keV level relative to the 2796-keV level as measured by Moss et al is $(1.7 \pm 0.3) \times 10^{-2}$. This value is larger than that found in this experiment.

The four different runs used to find the absolute strength of the branch to the 2796-keV level are in good agreement with each other, and after correcting for the various effects previously mentioned, give the strength of the branch to the 2796-keV level as $(1.45 \pm 0.16) \times 10^{-2}$. This is lower than the value of Goosman and Kavanagh, but the errors overlap. Using the values obtained in this experiment, log ft values were calculated and appear in Table 12. It can be seen that the branch to the 1410-keV level is retarded, while the observed branchings have typical allowed strength.

The parity of the 5/2 state at 3170 keV is unknown. If the parity is positive, the allowed branch is also retarded. It should be noted that from the survey of Raman and Gove, a non-unique first-forbidden transition (which would result if the parity of the level at 3170 keV is negative) can have a log ft as low as 5.9 in this Z region. Thus, it seems that even if the beta branch is observed to the 3170-keV level, the log ft value will not be able to be used to assign a parity to the state.

4. Theoretical Work

Since nuclear matrix elements were needed to estimate the cross section for the solar neutrino experiment and few experimental values were available, various groups have predicted the beta transitions for A = 37 . Each used a version of the shell model, each being more sophisticated than the treatment before.

Bahcall (1964) in the original paper on solar neutrino cross sections coupled three $1d_{3/2}$ particles to an inert 0^+ ^{40}Ca core. With only angular momentum considerations and assuming that the overlap between each $1d_{3/2}$ particle was reduced by the same value as for the ^{37}Ar decay, Bahcall predicted the beta transition from ^{37}K to three states in ^{37}Ar, J = $3/2^+$, $1/2^+$, and $5/2^+$. The values he predicted are presented in Table 13 along with the experimental values. Even though Bahcall associated the $5/2^+$ state with the 1611-keV level rather than with the 2796-keV level, the value calculated for log ft for the branch to the $5/2^+$ level does not change. Bahcall greatly overestimated the strength of the retarded branch to the 1/2+ state and underestimated the branch to the 5/2+ by an order of magnitude.

Engelbertink and Brussaard (1966) used a much less restricted space, allowing all $(2s_{1/2})(1d_{3/2})$ particles to be active around an inert ^{28}Si core. The matrix elements were obtained by reproducing the energies of the ground states and low-lying levels. Their calculated values for log ft also appear in Table 13. It can be seen that the gap between experiment and theory narrows as more active particles are considered. However, the strength of the branch to the 1410-keV level is still overestimated.

Wildenthal et al (1971) produced a many-particle shell-model calculation that allows all (2s)(1d) particles to be active outside a ^{16}O inert core. They used the two-body matrix elements of Kuo (1967) and the single-particle energies from ^{17}O. Their values for log ft are also in Table 13. This is the only calculation which predicts the strength to a second 5/2+ state. Associating the 5/2+ state with the 3605-keV level (as predicted by the model and consistent with the known spin information), the predicted log ft value agrees well with experiment. The predicted log ft for the retarded branch is approaching the lower limit of the experimental log ft , indicating an improvement over more restricted configuration spaces.

Dieperink and Brussaard (1969b) used the same configuration space as Wildenthal et al but used the Tabakin (1964) two-body matrix elements instead of those of Kuo. The Tabakin interaction is a sum of separable potentials which fit S-, P-, and D-wave phase shifts for free nucleon-nucleon scattering fairly well. These calculations, whose results are also shown in Table 13, predict strengths for the decay to the 3/2+ and (first)5/2+ states which are nearly the same as those of Wildenthal et al. However, the strength predicted for the branch to the 1/2+ state is quite different in the two models. Using the Tabakin interaction, the branch is predicted to be very retarded (log ft = 7.6) consistent with the experimental lower limit, while Wildenthal et al predict the branch to be 20 times stronger.

Also in Table 13 are the results of the calculation by Glaudemans which are mentioned as a private communication in the paper of Dieperink

and Brussaard. Glaudemans used the modified surface delta interaction and the same configuration space as Wildenthal et al and Dieperink and Brussaard. It can be seen that the results are nearly the same as for the calculation of Engelbertink and Brussaard who used a more restricted space but the same type of interaction.

The importance of the nuclear Hamiltonian is clearly illustrated in the last three columns of Table 13. The three calculations used the same configuration space, but by using different Hamiltonians they obtain very different predictions, particularly for the branch to the 1410-keV level.

F. Potassium-38 Decay

1. Previous History

The level diagram for ^{38}K-^{38}Ar is shown in Figure 20. Both the ground state and first excited state of ^{38}K are beta emitters. The half-life of the isomeric state at 131 keV is short ($t_{1/2}$ = 0.929 sec according to the compilation of Endt and van der Leun 1973). All decays of the isomeric level except the known branch to the ground state of ^{38}Ar require either isospin mixtures in the states of ^{38}Ar or have so little energy available for the decay that only electron capture is allowed. Since both these conditions make expected branching extremely small (especially considering that nuclear structure is also against these branchings), the study of the decay of the isomeric level was not attempted.

As can be seen from Figure 20, the decay of the ground state of ^{38}K has many possible allowed branches. Only two of them, the branch

to the 2168-keV level and the branch to the 3937-keV level, have been observed (Kavanagh 1968). Green and Richardson (1956) report that less than 0.6% of the ground state decays go to the 0^+ ground state of ^{38}Ar (as might be expected since this branch is a fourth-forbidden transition). Thus the 511-keV annihilation radiation can be ignored, since the total number of decays (after correcting for cascading and for efficiency) is given by the number of non-511-keV gamma rays seen.

The half-life used for the calculations of log ft is the mean of five measurements, which are not in too good mutual agreement, $t_{1/2} = 7.64 \pm 0.02$ min (Endt and van der Leun).

2. Experimental Details

Since the lifetime of the ground state of ^{38}K is so long, the rabbit system described in Section III is not needed. Instead, manual transfer of the target was used. During bombardment by an 11 MeV alpha beam, the target $BaCl_2$ on Ta backing was held in a glass tee by a Zr holder. As 511-keV radiation produced only count rate but no additional information, 3.8 cm of Pb was inserted between the Zr holder and the Ge(Li). No gamma rays were observed that could be associated with bombardment on ^{37}Cl, Zr, Ba, or Ta. The only delayed gamma rays observed were from the $^{35}Cl(\alpha,n)^{38}K$ reaction.

As high energy gamma rays were expected and since the highest energy gamma ray in ^{56}Co is about 3.5 MeV, ^{66}Ga was used to calibrate the Ge(Li) detection efficiency. Gallium-66, made from the $^{66}Zn(p,n)^{66}Ga$ reaction, has gamma rays up to 4.8 MeV and its decay scheme, although complex, is well known (Camp and Meredith 1971). In addition to

calibrating for photopeak efficiency, single and double escape peak efficiencies were also measured.

3. Experimental Results

A typical spectrum is shown in Figure 21. Since the target was bombarded in vacuum, the gamma ray at 2313 keV (due to ^{14}O decay which appeared whenever the rabbit system was used) is absent. The observed peaks are associated with the decay of the ground state of ^{38}K, the half-life of the isomeric state being very much shorter than the transit time (about 60 sec). Only two gamma rays are seen, the 2168 keV and the 3937 keV. The cascade from the 3937-keV level to the 2168-keV level is not observed, but the observed upper limit for this gamma branch is larger than from earlier work (Endt and van der Leun). This cascade was included in the calculations for the strength of the beta branch to the 3937-keV level. In Table 14 appears the strengths of the beta branches from the ground state decay of ^{38}K, along with the calculated log ft values. The upper limits for unobserved transitions is higher in this decay than others studied in this work since the efficiency for detection of the most intense branch is nearly the same as for the weaker branches. For some levels in ^{38}Ar, no branching limits are given as the gamma rays depopulating the level did not appear in the energy range surveyed in the current study.

The branch to the 2168-keV level has a typical log ft value, 4.98. The other observed transition to 3937-keV level is slightly retarded, having a log ft of 5.92. The other allowed transitions decay predominantly, if not exclusively, by electron capture and the

available phase space for the decay is small. The limits for log ft for these transitions eliminate strong transitions but do not deny typical decay strengths.

The value for the branching ratio found in this experiment for the transition to the 3937-keV level, $(1.50 \pm 0.05) \times 10^{-3}$, is less than found by Kavanagh et al $(2.0 \pm 0.3) \times 10^{-3}$.

4. Theoretical Work

Much theoretical work exists predicting the beta decay strength for the decay to the 2168-keV level in ^{38}Ar. These predictions, as well as the experimentally obtained value, are shown in Table 15. Only one prediction exists for the decay strength to the 3937-keV level.

The first model was by Engelbertink and Brussaard (1966) who used an inert core of ^{28}Si with active particles restricted to the $2s_{1/2}$ and $1d_{3/2}$ subshells. The effective Hamiltonian was chosen to reproduce the ground and low-lying states for A = 35-38. The value predicted for the decay to the 2168-keV level suggests a stronger transition by a factor of 5.

Evers and Stocker (1970) extended the configuration space to include either 0 or 2 particles in the $1f_{7/2}$ subshell. This lowers the predicted value of log ft , increasing the discrepancy between experiment and theory. Evers and Stocker then added a tensor interaction which

had no effect upon the predicted strength of the transition. It did affect the predicted decay of the isomeric level.

Dieperink and Glaudemans (1969a) and Dieperink and Brussaard (1969b) report basically the same calculation. Each used the full s-d space. In the first calculation (of two) a modified surface delta interaction was used, the parameters being obtained by a least-squares fit to the excitation energies for A = 35-39. The predicted strength for the decay to the 2168-keV level is practically the same as for the more restricted space of Engelbertink and Brussaard. The next calculation used the same configuration space but used the Tabakin (1964) interaction. This interaction fits the phase shifts for free nucleon-nucleon scattering. The prediction of log ft = 4.75 agrees well with the experimental value.

Finally, Wildenthal et al (1971) as compiled in Lanford and Wildenthal (1973) predicted values for both observed beta branches from the ground state of ^{38}K. They used the two-body matrix elements of Kuo (1967). Their predictions are very close to experimental values (2168 keV: 4.97 against 4.98 experimentally, and for 3937-keV level: 5.76 against 5.98).

G. Calcium-39 Decay

1. Previous History

The only branch previously reported in the beta decay of ^{39}Ca is the mirror transition to the ground state of ^{39}K. Calcium-39 has the largest amount of energy available for any mirror decay in the s-d shell. This implies a short half-life and many allowed transitions.

As there are so many levels in ^{39}K to which ^{39}Ca would decay, only the low-lying states are shown in Figure 22. The half-life used, (0.876 ± 0.006) sec, is the weighted average of six measurements compiled in Endt and van der Leun (1973).

2. Experimental Details

Potassium iodide salt was inserted into the rabbit and held in place by a thin Ta foil. The ^{41}K in the target presented no problems, as the (p,n) reaction produces 10^5year ^{41}Ca and the (p,α) reaction produces stable ^{38}Ar. In order to reduce the detection efficiency for annihilation radiation, 2.5 cm of lead separated the detector and the lucite hutch.

3. Experimental Results

One of the spectra of the delayed gamma rays is shown in Figure 23. Only the 511-keV photopeak can be ascribed to the beta decay of ^{39}Ca. The upper limits (at the 90% confidence level) for the strength of the beta transitions to the various states in ^{39}K are tabulated in Table 16, along with the associated log ft values.

The beta transition to the 2523-keV level is retarded, having a log ft greater than 6.4. The transition to the 4096-keV level has a log ft greater than 5. The beta transitions to the 3939, 3943, 4083, 4514, and 4521-keV levels may be allowed, as the spins lie in the proper range, but the parity for these states is not known. The branch to the 3939-keV level (if allowed) has some retardation as does the branch to the 4083-keV level (again assuming the transition is allowed). Since the upper limits of the log ft values for the other transitions

are less than 5, no nuclear structure information can be inferred.

4. Theoretical Work

There has not been much theoretical work performed on ^{39}Ca beyond the single particle model. If one restricts the configuration space so that only $2s_{1/2}$ and $1d_{3/2}$ subshell particles are active, then the only allowed transition having a finite log ft is the mirror decay. Thus a fuller configuration space is needed to predict other decays. However, since ^{39}K-^{39}Ca are only one hole from a doubly magic nucleus, ^{40}Ca, the low-lying states of ^{39}K and ^{39}Ca will have very little configuration mixing, and hence the log ft values for the non-mirror transitions will be high.

VI. DISCUSSION AND CONCLUSIONS

A. Discussion of Shell-Model Predictions

This section will present a more global view of the ability of the many-particle shell model to predict the strength of beta transitions. In Figure 24 the ratio of the theoretical ft values as obtained by Wildenthal and his collaborators (as compiled by Lanford and Wildenthal 1973) to the experimental ft values obtained in this work is presented. This ratio, which is also equal to the square of the experimental nuclear matrix element divided by the square of the theoretical matrix element, is plotted against the theoretical log ft value.

With the exception of the beta decay of ^{27}Si to the 1014-keV level in ^{27}Al, the predictions are good, in most cases within a factor of 2. However, the very retarded ^{27}Si decay to the 1014-keV level, and to a lesser extent the ^{27}Si decay to the 2734-keV level which is predicted to be ten times stronger than observed, present problems. McGrory (1970) has shown that for A = 18-22, large changes in the predicted log ft values can occur when the configuration space of the model is increased to the full s-d shell. However, whether a larger configuration will resolve the discrepancy, only a calculation using all particles active in the s-d shell will show.

As shown by the calculations for the beta decays of ^{37}K and ^{38}K, the choice of the Hamiltonian used in the calculation can greatly affect the predicted values. This is particularly true for the decay of ^{37}K to the 1410-keV level. Even though the same configuration space was used,

the predicted strengths for the decay are 1 (Dieperink and Brussaard 1969, using the Tabakin interaction); 20 (Wildenthal et al, using the Kuo interaction); 400 (Dieperink and Glaudemans 1969, using the modified surface delta interaction). For this particular branch the Tabakin interaction gives the best agreement; yet the predictions of Wildenthal et al for the other branches from the decay of ^{37}K are in excellent agreement with experiment as are their values for the decay of ^{38}K. To clarify the situation, calculations for the entire s-d shell using the various interactions must be carried out.

The modified surface delta interaction seems to produce the least accurate predictions of any of the interactions used. The agreement is poor for the ^{27}Si, ^{37}K, and ^{38}K decays. Yet this interaction is usually used in many-particle shell-model calculations presumably because of its ease of application. Our results seem to indicate that the use of one of the "realistic" interactions, such as the Elliot, Kuo, or Tabakin interactions, may lead to more accurate predictions.

B. Conclusions

This part of the thesis has described the experimental study of six beta decays in the s-d shell, ^{19}Ne, ^{23}Mg, ^{27}Si, ^{37}K, ^{38}K, and ^{39}Ca. Two previously unreported allowed transitions were found, and limits for unobserved transitions have been strengthened. In general, the many-particle shell model of Wildenthal and his collaborators does well, although there are several notable exceptions.

APPENDIX A

DIGITAL SEQUENCE TIMER

I. Introduction

The digital sequence timer allows the user to generate electric signals at digitally preset times. These times may be independent of each other or may be part of a periodic pattern, or both. As all signals are digitally derived from a basic clock, the time difference between the signals is determined only by settings on the sequence timer and not by charging or discharging components.

This appendix is a condensation and revision of material found in the Kellogg Electronics Shop (Kellogg number K 39C). Complete schematics for the unit may be found in the circuits file.

The digital sequence timer produces signals at 13 user-selected times and produces signals at a user-chosen frequency. Twelve of the thirteen signals are paired so that for each pair a square wave signal starts at the first preset time and falls at the second. Each square wave signal drives a light-emitting diode (LED) and a relay. The thirteenth signal, a pulse lasting about 11 μsec, resets the timer.

The periodic signals are available from a front-panel BNC connector. The number of such signals since the last reset is displayed in binary on the front panel by LED's. Voltage levels corresponding to the state of the LED's are available on the front panel via BNC connectors and on the rear panel via a 14 pin connector.

The unit can be started, stopped, and reset manually, automatically, or by remote signals. The unit may be singly cycled or repeatedly cycled.

II. Use of the Timer

A. Overview

There are five logical blocks in the sequence timer: the control section, the basic clock section, the reset section, the random pulse section, and the periodic pulse section. Although all five sections may not be needed, the knowledge of their operation will make using the timer much easier. Figure 25 shows the front panel of the sequence timer.

The first requirement in the use of the timer is the determination of the times at which signals are wanted. As the unit is a digital (i.e., discrete) device, the user does not have complete freedom to choose times. However, this lack of freedom is unlikely to be important in practice. The basic unit of time must be a 10^Nsec (where N=0,1,$\cdots$,7) and the selected times must be an integral multiple of this basic time unit (but less than 10,000). The user must next determine whether this set of signals should occur once or should reoccur indefinitely. If a recycling mode is desired, the length of the cycle (again an integral multiple of the basic clock unit but less than 10,000 clock units) must be determined.

If randomly timed signals are chosen, then the user can use either the voltage levels on the front panels or the relay contacts on the rear panel. If periodic signals are chosen, then the user can use the pulses generated at the end of each period or can use the voltages on the front panel which represent the number of periods since the start of the cycle.

B. Control Section

The control section consists of the three-position rotary switch located next to the power switch. In the far left position the unit will not start. In the middle position the unit will operate (after being started) until stopped or until the reset time is reached, when the unit will reset all scalers to zero and then stop. In the far right position the unit will reset all scalers when the preset time is reached, but the unit will restart. If the control switch is in the center position, the unit may be started by pressing the manual start switch or by applying +5V to the remote start BNC connector on the front panel. If the control switch is not in the far right position, the unit will stop (but not reset scalers or outputs) if the manual stop button is pressed or if +5V is applied to the remote stop BNC connector. If the control switch is in the far right position, the unit will remain running independent of the start and stop circuits.

The LED to the right of the control switch will be lit whenever the scalers are in operation.

C. Basic Clock Unit

The basic clock frequency determines the basic unit of time. All times are an integral multiple of this unit. The sequence timer is usually used with an internal 1 MHz quartz crystal clock, accurate to 10 ppm. However, an external clock (maximum frequency is 4 MHz, no minimum frequency) can be used by sending a 5V clock pulse into the External Clock BNC connector and by selecting the external clock circuit by switching the Clock toggle switch. The frequency of either the

internal or the external clock can be digitally divided by 10^N (where N=0,1,···,7) by placing the appropriate numeral in the Clock Thumbwheel switch. Thus using the 1 MHz quartz crystal internal clock, the basic clock period can be 1 μsec, 10 μsec, ··· 10 sec. Although a 1 MHz crystal is normally used, slower crystals may be substituted. The pulses generated by the basic clock circuit can be inspected by looking at the Time Out BNC connector on the front panel.

D. Reset Circuit

To the right of the Clock Section is the Reset Section. When the number of pulses in the cycle reaches the number preset on the Reset Thumbwheel Switch, all scalers and outputs are reset to zero. A pulse, lasting about 11 μsec is also generated at the Reset Out BNC connector. If the unit is in either the single cycle mode or the hold mode, the unit will stop after reset; if in the auto mode, the unit will restart. The same effect as reaching the preset reset number can be achieved by pressing the manual reset button or by applying a +5V pulse to the Remote Reset BNC connector located next to the Reset Thumbwheel switch.

E. Random Pulse Generation

The user can preset 12 independent times. These times are arranged in pairs, so that the pair is "off" until the first preset number of the pair is reached; then it is "on" until the second preset number or until the preset reset number is reached; the pair then goes "off". The preset times are selected by using the thumbwheel switches located along the top of the front panel. The top row of thumbwheel switches selects the first preset number of the pair, while the next row of

thumbwheel switches selects the second number of the pair.

Two outputs, voltage levels capable of driving most NIM modules (located on the front panel) and relay contacts capable of handling 120V AC (located on the rear panel), are available. When the pair is "off", the voltage level is near 0 V, while when the pair is "on", the voltage level is about +7 V. The output impedance from the BNC connectors is about 100Ω. Three contacts are available when using the relay contacts located on the rear panel, C (Common), NO (normally open, i.e., infinite resistance when the pair is "off"), and NC (normally closed).

F. Periodic Pulser Generation

The user can select a period such that whenever an integral number of periods has occurred since the last reset and start, a pulse will occur at the Timer Out BNC connector. This period is selected through the use of the Timer Thumbwheel switch located in the lower right hand side of the front panel. These voltage pulses can be gated by applying a signal to the Gate Input BNC, next to the Timer Thumbwheel switch. The pulses since the beginning of the cycle are counted, the result displayed in binary representation. The representation is shown via LED's and is available through BNC's on the front panel and a 14-pin connector on the rear panel. These outputs are very useful in routing signals as a function of time.

III. Example of Use

Statement of the Problem: A radioactive source with a mean life of 100 sec is to be made and its activity counted. The beam will be on target for 3/4 of a mean life. There will be 4 counting periods, each

lasting 1 mean life, with the first starting 1/2 mean life after bombardment.

It is assumed that a router is used to collect the spectra as a function of time and that 5V is sufficient to activate it. It is assumed that a beam chopping magnet is used to start and stop bombardment, the current for the magnet being switched by a relay. Finally, it is assumed that the ADC of the analyzer used has a blocking input which blocks ADC output whenever the input is grounded.

The first step is to determine the times of the wanted pulses:

0 sec	beam on
75 sec	beam off
125 sec	start counting group #1
225 sec	start counting group #2
325 sec	start counting group #3
425 sec	start counting group #4
525 sec	stop counting

These timing requirements can be set up in many ways. One way will be described in detail, while two others are briefly noted.

The chopping magnet will be controlled by a relay governed by the timing of one pair of random pulse generators; the ADC will be blocked by another relay; and the router will be set by the Periodic Pulse Unit

The length of the cycle is 525 sec. However, the times when counting begins in each group are quite inconvenient for this method. It would be far easier if the times could be represented by $2^{(m-1)} \cdot X$

where m is the group number about to be counted and X is the length of the counting period. This also cannot easily be done, but the starting times can be written as $(2^{(m-1)} + 2^p) \cdot X$, where p is a small integer constant. That is, the first group starts at 400 sec, the second group at 500 sec, and so on. Thus $X = 100$ sec, $p = 2$. The new timing becomes

275 sec	beam on
350 sec	beam off
400 sec	start counting group #1
500 sec	start counting group #2
600 sec	start counting group #3
700 sec	start counting group #4
800 sec	stop counting

The total time in a cycle is 800 sec. Since times can be selected up to 9999, the basic clock period can be selected as 0.1 sec. The internal 1 MHz quartz crystal clock can be used with a divisor of 10^5. Thus 5 is placed into the Clock Thumbwheel switch. 8000 is placed into the Reset Thumbwheel switch. If only one cycle is desired, the master control switch is placed in the single cycle position (the center position); if more than one cycle is desired, then the switch will be placed into the auto position (the far right position) when the cycles are to begin.

The beam is to be on from 2750 to 3500 basic clock units. Thus 2750 is placed into one of the Random Pulse Thumbwheels along the top row, while 3500 is placed into the thumbwheel switch below it. The magnet is then connected to its power supply by the relay contacts on the

rear panel corresponding to the Random Pulse Generator selected (#1-6). The ADC must be blocked from 0000 units to 4000 units. Thus 0000 and 4000 are placed into another pair of thumbwheels just as were the times for the chopping magnet. A cable connects the relay contacts with the ADC blocking input (assumed to have one side of the cable grounded.) Since groups are to be changed every 100 sec (or 1000 clock units), 1000 is placed into the Timer Thumbwheel switch. A cable will go from the 2^1 counting output to the first input of the router; a second cable goes from the 2^2 output to the second router input. This, of course, assumes that the router merely patches into memory.

The equipment will function as follows:

0-275 sec	no beam, ADC blocked;
275-350 sec	beam on, ADC blocked;
350-400 sec	beam off, ADC blocked;
400-500 sec	beam off, count and store in first group;
500-600 sec	no beam, count and store in second group;
600-700 sec	no beam, count and store in third group;
700-800 sec	no beam, count and store in fourth group;
800 sec	reset.

If only one cycle is desired, press manual start to begin run. The timer will stop after one cycle is completed. If many cycles are desired, put the master control switch in the auto position, and the unit will start. To stop the unit, put the master control switch in

the single cycle during the last wanted cycle. The unit will stop at the end of this cycle.

Since there are only four groups in which counting will occur, and since there are four random pulse generator pairs not used by the above scheme, these four generators can be used instead of the periodic pulse generators. The start time for each group is put into the start preset time thumbwheel switch and the stop time into the stop thumbwheel switch. Using this scheme, the counting groups need not be of equal time. However, the router must be capable of accepting pulses which determine which line is active into the ADC rather than indicating which part of memory is used. Since the periodic pulse generator is not used, there need be no wasted time inserted into the cycle.

One may circumvent this time wastage in another way by counting before bombardment. That is, the counting part of the cycle occurs in the $n+1^{st}$ period, while the bombardment occurs in the n^{th} period. In this scheme, counting (for the example cited) is done between 0 and 400 sec, while bombardment is from 400 to 525 sec (assuming no waiting time between tne end of counting and the start of bombardment). This scheme has the advantage of being able to use many counting groups (up to 256). However, for efficient use of time, many cycles should be used.

REFERENCES - PART 1

Ajzenberg-Selove, F. and Lauritsen, T. 1968, Nucl. Phys. A114, 1.

Ajzenberg-Selove, F. 1970, Nucl. Phys. A152, 1.

Ajzenberg-Selove, F. 1971, Nucl. Phys. A166, 1.

Ajzenberg-Selove, F. 1972, Nucl. Phys. A190, 1.

Ajzenberg-Selove, F. and Lauritsen, T. 1974, Nucl. Phys. A227, 1.

Alburger, D. 1974, Phys. Rev. C9, 991.

Azuelos, G., Crawford, J. E., and Kitching, J. E. 1974, Phys. Rev. C9, 1213.

Bahcall, J. 1964, Phys. Rev. 135, B137.

Bahcall, J. 1966, Nucl. Phys. 75, 10.

Behrens, H. and Buhring, W. 1971, Nucl. Phys. A162, 111.

Benson, H. G. and Flowers, B. H. 1969, Nucl. Phys. A126, 305.

Berenyi, D., Hutcheon, D. A., Start, D.F.H., and Weaver, J. J. 1971, A178, 76.

Bethe, H. A. 1930, Ann. Phys. 5, 325.

Bethe, H. A. 1932, Z. Phys. 76, 293.

Bethe, H. A. 1933, Proc. Royal Soc. (London) A150, 129.

Bhabha, H. J. 1936, Proc. Royal Soc. (London) A154, 195.

Buhring, W. 1963a, Nucl. Phys. 40, 472.

Buhring, W. 1963b, Nucl. Phys. 49, 190.

Camp. D. C. and Meredith, G. L. 1971, Nucl. Phys. A166, 349.

Davis, R. Jr., Harmer, D. S., and Hoffman, K. C. 1968, Phys. Rev. Lett. 20, 1205.

Détraz, C., Moss, C. E., and Zaidins, C. S. 1971, Phys. Lett. 34B, 128.

Détraz, C., 1972, private communication.

DeVoigt, M.J.A., Glaudemans, P.W.M., and Wildenthal, B. H. 1972, Nucl. Phys. A186, 365.

Dieperink, A.E.L. and Glaudemans, P.W.M. 1969a, Phys. Lett. 28B, 531.

Dieperink, A.E.L. and Brussaard, P.J. 1969b, Nucl. Phys. A128, 34.

Dirac, P.A.M. 1930, Proc. Cambridge Phil. Soc. 26, 361.

Donnelly, T. W., Hitlin, D., Schwartz, M., Walecka, J. D., and Wiesner, S. J. 1974, Phys. Lett. 49B, 8.

Earwaker, L. G., Jenkin, J. G., and Titterton, E. W. 1962, Nature 195, 271.

Eckart, C. 1930, Rev. Mod. Phys. 2, 305.

Elliot, J. P., Jackson, A. D., Mavromatis, H. A., Sanderson, E. A., and Singh, B. 1968, Nucl. Phys. A121, 241.

Endt, P. M. and van der Leun, C. 1973, Nucl. Phys. A214, 1.

Engelbertink, G.A.P. and Brussaard, P. J. 1966, Nucl. Phys. 76, 442.

Evers, D. and Stocker, W. 1970, Phys. Lett. 33B, 559.

Fermi, E. 1934, Z. Phys. 88, 161.

Fermi, E. 1949, Nuclear Physics, The University of Chicago Press, Chicago

Feynman, R. P. and Gell-Mann, M. 1958, Phys. Rev. 109, 193.

French, J. B., Halberg, E. C., McGrory, J. B., and Wong, S.S.M. 1966, Adv. Nucl. Phys. Vol. 3 (Barranger and Vogt, eds.)

French, W. R., LaShure, R. L., and Curran, J. L. 1969, Amer. J. Phys. 37, 11.

Gerhart, J. B., Carlson, B. C., and Sherr, R. 1954, Phys. Rev. 94, 917.

Glaudemans, P.W.M., Brussaard, P.J., and Wildenthal, B.H. 1967, Nucl. Phys. A102, 593.

Goosman, D. R. 1967a, Phys. Rev. 161, 1156.

Goosman, D. R. and Kavanagh, R. W. 1967b, Phys. Rev. 163, 1219.

Gorodetzky, S., Gallmann, A., Frick, G., Coffin, J. P., and Jundt, F. 1964, Compt. Rend. Cong. Int. Phys. Nucl. (Paris) Vol. II, p. 408.

Gorodetzky, S., Aslanides, E., Gallmann, A., and Frick, G. 1968, Nucl. Phys. A109, 417.

Goss, J. D., Riffle, F. L., Parsignault, D. R., and Harris, J. C. 1968, Nucl. Phys. A115, 113.

Gove, N. B. and Martin, M. J. 1971, Nucl. Data Tables 10, 205.

Green, D. and Richardson, J. R. 1956, Phys. Rev. 101, 776.

Gunye, M. R. 1973, Phys. Rev. C7, 216.

Heitler, W. 1954, The Quantum Theory of Radiation, 3rd ed., Oxford University Press

Jackson, J. D. 1962, Classical Electrodynamics, John Wiley & Sons, Inc.

Janecke, von J. 1960, Z. F. Naturf. 15A, 593.

Jones, G. A., Phillips, W. R., Johnson, C.M.P., and Wilkinson, D. H. 1954, Phys. Rev. 96, 547.

Kallen, G. 1967, Nucl. Phys. B1, 225.

Kavanagh, R. W. and Goosman, D. R. 1964, Phys. Lett. 12, 229.

Kavanagh, R. W., Gallmann, A., Aslanides, E., Jundt, F., and Jacobs, E. 1968, Phys. Rev. 175, 1426

Kendall, H. W. and Deutsch, M. 1956, Phys. Rev. 101, 20.

Kotani, T. and Ross, M. 1958, Prog. Theo. Phys. (Japan) 20, 643.

Kuo, T.T.S. 1967, Nucl. Phys. A103, 71.

Lanford, W. A. and Wildenthal, B. H. 1973, Phys. Rev. C7, 668

Lewis, M. B. 1971, Nucl. Data Sheets 5, 243.

Lu, C. C., Carlson, T. A., Malik, F. B., Tucker, T. C., and Nestor, C. W. Jr. 1971, Atomic Data Sheets 3, 1.

McGrory, J. B. 1970, Phys. Lett. 33B, 327.

McGrory, J. B. and Wildenthal, B. H. 1971, Phys. Lett. 34B, 373.

McGrory, J. B. 1973, Proc. Int. Conf. Nucl. Phys. (Munich) Vol. II, p. 145.

Moss, C. E., Détraz, C., and Zaidins, C. S. 1971, Nucl. Phys. A170, 111.

Mukhopadhyay, N. C. and Miller, L. D. 1973, Phys. Lett. 47B, 415.

Nelms, A. T. 1956, Nat. Bur. Std. (USA), Circ. 577.

Nelms, A. T. 1958, Nat. Bur. Std. (USA), Circ. 577 suppl.

Pancholi, S. C. and Martin, M. J. 1972, Nucl. Data Sheets 8, 165.

Paul, E. B., Evans, J. E., and Montague, J. H. 1961, Proc. Rutherford Jubilee Int. Conf. (Manchester), p. 313.

Paul, H. 1970, Nucl. Phys. A154, 160.

Pauli, W. 1958, Encyclopedia of Phys. (ed. Flugge), Vol. V/1. (Also appeared in 1933 edition).

Raman, S. and Gove, N. B. 1973, Phys. Rev. 49, 727.

Rohrlich, F. and Carlson, B. C. 1954, Phys. Rev. 93, 38.

Rose, M. E. 1936, Phys. Rev. 49, 727.

Rose, M. E. and Holmes, D. K. 1951, Phys. Rev. 83, 190.

Schülke, L. 1964, Z. Phys. 179, 331.

Slater, J. C. 1951, Phys. Rev. 81, 385.

Stech, B. and Schülke, L. 1964, Z. Phys. 179, 314.

Storey, R. G. and McNeil, K. G. 1959, Can. J. Phys. 37, 1072.

Tabakin, F. 1964, Annals Phys. 30, 51.

Talbert, W. L. and Stewart, M. G. 1960, Phys. Rev. 119, 272.

Taras, W. L., Turcotte, A., and Vaillancourt, R. 1972, Can. J. Phys. 50, 1182.

Thankappan, V. K. 1966, Phys. Rev. 141, 957.

Towner, I. S. and Hardy, J. C. 1973, Nucl. Phys. A205, 33.

Vasil'ev S. S. and Shavtvalov, L. Ya 1961, JETP (Soviet Phys.) 12, 851.

Weinberg, S. 1967, Phys. Rev. Lett. 19, 1264.

Whitehead, R. R. 1972, Nucl. Phys. A182, 290.

Wigner, E. P. 1927, Z. Phys. 43, 624.

Wildenthal, B. H., Halbert, E. C., McGrory, J. B., and Kuo, T.T.S. 1971, Phys. Rev. C4, 1266.

Wildenthal, B. H. and McGrory, J. B. 1973, Phys. Rev. C7, 714.

Wu, C. S., Ambler, E., Hayward, R. W., Hoppes, D. D., and Hudson, R. P. 1957, Phys. Rev. 105, 1413.

Zaidins, C. S. 1973, private communications.

Zucker, A. P., Buck, B., and McGrory, J. B. 1968, Phys. Rev. Lett. 21, 39.

TABLE 1

Products resulting from light-ion bombardment of ^{9}Be. All reactions which have a Q value greater than -12 MeV are listed. Neutron, proton, or deuteron bombardment of ^{9}Be produce no product which emits a delayed gamma ray. Alpha bombardment makes ^{12}B which when decaying to ^{12}C emits a 4.4 MeV gamma in 1.3% of the decays. Normally this would not be a problem. Helium-3 bombardment is the only case which produces significant amounts of delayed radiation. In all the cases in which beryllium was used in the experiments described in this thesis, a proton beam was used. By looking through the table, it can be seen that no product is produced either by the primary beam or a secondary beam which would produce interfering delayed γ-radiation.

(See page 21.)

TABLE 1

Reaction	Q(MeV)	$T_{1/2}$(Product)	Delayed γ-Ray Energy (MeV)
$^{9}Be(n,\gamma)^{10}Be$	6.81	10^{6} yr	...
$,2n)^{8}Be$	-1.67	10^{-16}sec	...
$,t)^{7}Li$	-10.44	...	...
$,\alpha)^{6}He$	-0.60	0.8 sec	...
$,\alpha n)^{5}He$	-2.53	10^{-21}sec	...
$^{9}Be(p,\gamma)^{10}B$	6.59	...	...
$,n)^{9}B$	-1.85	10^{-18}sec	...
$,d)^{8}Be$	0.56	10^{-16}sec	...
$,\tau)^{7}Li$	-11.20	...	...
$,\alpha)^{6}Li$	2.13	...	...
$,\alpha n)^{5}Li$	-3.54	10^{-21}sec	...
$^{9}Be(d,\gamma)^{11}B$	15.82	...	...
$,n)^{10}B$	4.36	...	...
$,2n)^{9}B$	-4.07	10^{-18}sec	...
$,p)^{10}Be$	4.59	10^{6}yr	...
$,t)^{8}Be$	4.59	10^{-16}sec	...
$,\tau)^{8}Li$	-11.39	0.8 sec	...
$,\alpha)^{7}Li$	7.15	...	...
$,\alpha n)^{6}Li$	-1.06	...	...
$,\alpha p)^{6}He$	-4.57	0.8 sec	...

TABLE 1 (Cont.)

Reaction	Q(MeV)	$T_{1/2}$(Product)	Delayed γ-Ray Energy (MeV)
$^{9}Be(\tau,\gamma)^{12}C$	26.28	...	...
$,n)^{11}C$	7.56	20 min	0.51
$,2n)^{10}C$	-5.52	19 sec	0.51,0.72
$,p)^{11}B$	10.33	...	...
$,d)^{10}B$	1.09	...	...
$,t)^{9}B$	-1.09	10^{-18}sec	...
$,\alpha)^{8}Be$	18.91	10^{-16}sec	...
$,\alpha n)^{7}Be$	0.02	53 days	0.48
$,\alpha p)^{7}Li$	1.66	...	...
$,^{6}Li)^{6}He$	-5.4	0.8 sec	...
$^{9}Be(\alpha,\gamma)^{13}C$	10.65	...	...
$,n)^{12}C$	5.70	...	...
$,p)^{12}B$	-6.88	.02 sec	4.44
$,d)^{11}B$	-8.03	...	...
$,\alpha n)^{8}Be$	-1.665	10^{-16}sec	...

TABLE 2

Experimental branching ratio for ^{23}Mg beta decay to the first excited state of ^{23}Na. The weighted average of these measurements is shown on the last line. This weighted average was used in subsequent calculations rather than the result found in the present experiment since the assigned error is twice as small.

(See page 43.)

TABLE 2

Authors	Intensity (%)
Storey and McNeil 1959	6.5 ± 2.5
Talbert and Stewart 1960	9.1 ± 0.5
Gorodetzky et al 1968	8.6 ± 0.3
Détraz et al 1971	6 ± 3
Alburger 1974	9.1 ± 0.4
Present Work	8.1 ± 0.4
Weighted Average	8.7 ± 0.2

TABLE 3

Experimental beta branching of ^{23}Mg relative to the beta branch to the 0.440 MeV level in ^{23}Na. The branch to the 2.391 MeV has not been previously reported.

(See page 46.)

TABLE 3

E_x(MeV)	Relative Beta Branch
2.076	$< 5.3 \times 10^{-4}$
2.391	$(8.1 \pm 1.1) \times 10^{-4}$
2.640	$< 3.8 \times 10^{-5}$
2.704	$< 1.6 \times 10^{-4}$
2.983	$< 5.9 \times 10^{-5}$
3.678	$< 1.4 \times 10^{-5}$

TABLE 4

Experimental results for the beta decay of ^{23}Mg. The weighted average of values appearing in Table 2 is combined with the results found in this experiment (listed in Table 3) to obtain the branching ratios shown.

The beta branch to the 2.391 MeV level has not been previously reported.

(See page 47).

TABLE 4

E_x(MeV)	J^π	Branching	f	log ft
0.000	$3/2^+$	0.913 ± .002	377	3.67 ± .01
0.440	$5/2^+$	0.087 ± .002	187	4.39 ± .01
2.076	$7/2^+$	$< 4.6 \times 10^{-5}$	2.7	> 5.8
2.391	$1/2^+$	$(7.0 \pm 0.9) \times 10^{-5}$	0.58	4.97 ± .06
2.640	$1/2^-$	$< 3.3 \times 10^{-6}$	0.11	> 5.6
2.704	$9/2^+$	$< 1.4 \times 10^{-5}$	0.07	> 4.7
2.983	$3/2^+$	$< 5.1 \times 10^{-6}$	0.02	> 4.6
3.678	$3/2^-$	$< 1.2 \times 10^{-6}$	0.002	> 5.2

TABLE 5

Theoretical predictions for the beta decay of ^{23}Mg and experimental log ft values. Sources for the theoretical log ft calculations are

Gunye: Gunye 1973
multi-shell Hartree-Fock

L&W: Lanford and Wildenthal 1973
many-particle shell model

(See page 49.)

TABLE 5

E_x(MeV)	J^π	exp.	Gunye	L&W
0.000	$3/2^+$	3.67 ± .01	3.92	3.68
0.440	$5/2^+$	4.39 ± .01	4.15	4.68
2.391	$1/2^+$	4.97 ± .06	..	4.69

TABLE 6

Intensity of the beta branch from ^{27}Si to the $7/2^+$ level at 2211 keV in ^{27}Al. There is much scatter in the measurements. The weighted average of these measurements is shown on the last line. The error on this weighted average is the external standard as it is about twice as large as the calculated internal error. The weighted average and its error is used in the subsequent calculations.

(See page 49.)

TABLE 6

Authors	Intensity (%)
Talbert and Stewart 1960	< 0.2
Vasil'ev and Shvtvalov 1961	10
Paul et al 1961	6 ± 3
Gorodetzky et al 1964	0.10 ± 0.02
Détraz et al 1971	0.15 ± 0.07
Berenyi et al 1971	0.18 ± 0.05
Present work	0.181 ± 0.014
Weighted average	0.156 ± .021[a)]

[a)] External standard error

TABLE 7

Experimental beta branching of ^{27}Si relative to the beta branch to the 2.211 MeV in ^{27}Al. The results of Détraz et al (1971) are presented along with present results. The discrepancy between the value for the branch to the 1.014 MeV level can be explained by the presence of the branch to the 2.734 MeV level.

Branches to the states at 0.843 and 3.001 MeV are not allowed transitions.

(See page 51.)

TABLE 7

E_x(MeV)	Détraz et al	Present work
0.843	< 75	< 22
1.014	160 ± 50	27 ± 13
2.211	≡ 1000	≡ 1000
2.734	< 60	86 ± 7
2.982	165 ± 25	144 ± 8
3.001	< 15	< 8

TABLE 8

Experimental results for the beta decay of ^{27}Si. The weighted average of the values appearing in Table 6 is combined with the results found in this experiment (listed in Table 7) to obtain the branching ratios shown.

The beta branch to the 2.734 MeV state has not been previously reported.

(See page 52.)

TABLE 8

E_x(MeV)	J^π	Branching	f	log ft
0.000	$5/2^+$	.9981 ± .0021	984	3.61 ± .01
0.844	$1/2^+$	$< 3.4 \times 10^{-5}$	316	> 7.6
1.014	$3/2^+$	$(4.2 \pm 2.0) \times 10^{-5}$	242	7.4 ± .2
2.211	$7/2^+$	$(1.56 \pm .21) \times 10^{-3}$	20.8	4.75 ± .06
2.734	$3/2^+$	$(1.34 \pm .21) \times 10^{-4}$	3.9	5.08 ± .07
2.981	$3/2^+$	$(2.25 \pm .31) \times 10^{-4}$	1.3	4.40 ± .06
3.004	$9/2^+$	$< 1.4 \times 10^{-5}$	1.2	> 5.5

TABLE 9

Theoretical predictions for the beta decay of ^{27}Si. Also present are log ft values experimentally determined. Sources for the theoretical log ft calculations are

BHSW: (Berenyi, Hutcheon, Start, and Weaver 1971)
weak coupling model

DGW: (DeVoigt, Glaudemans, and Wildenthal 1972)
many-particle shell model

L&W (Lanford and Wildenthal 1973)
many-particle shell model

The model used by Berenyi et al does not predict a second $3/2^+$ level.

(See page 53.)

TABLE 9

E_x(MeV)	J^π	exp.	BHSW	DGW	L&W
0.000	$5/2^+$	3.61 ± .01	3.68	3.53	3.53
1.014	$3/2^+$	7.4 ± .2	5.60	5.24	5.01
2.211	$7/2^+$	4.75 ± .06	5.57	5.12	5.04
2.734	$5/2^+$	5.08 ± .07	6.05	5.19	5.08
2.981	$3/2^+$	4.40 ± .06	..	4.72	4.72

TABLE 10

Delayed gamma rays observed following proton bombardment of calcium. Most of the gamma rays result from (p,n) reactions on calcium isotopes. Oxygen-14 results from the proton bombardment of nitrogen in the shuttle or on the surface of the gold-covered calcium. The gamma ray peaks of interest result from the $^{40}Ca(p,\alpha)^{37}K$ reaction.

(See page 57.)

TABLE 10

E (keV)	decay	source
511	$m_e c^2$	...
983	^{48}Sc	$^{48}Ca(p,n)$
1040	^{48}Sc	$^{48}Ca(p,n)$
1157	^{44}Sc	$^{44}Ca(p,n)$
1227	^{42}Sc	$^{42}Ca(p,n)$
1291	^{14}O(D.E.)	$^{14}N(p,n)$
1312	^{48}Sc	$^{48}Ca(p,n)$
1499	^{44}Sc	$^{44}Ca(p,n)$
1524	^{42}Sc	$^{42}Ca(p,n)$
1774	^{37}K(D.E.)	$^{40}Ca(p,\alpha)$
1802	^{14}O(S.E.)	$^{14}N(p,n)$
2285	^{37}K(S.E.)	$^{40}Ca(p,\alpha)$
2313	^{14}O	$^{14}N(p,n)$
2583	^{37}K(D.E.)	$^{40}Ca(p,\alpha)$
2796	^{37}K	$^{40}Ca(p,\alpha)$
3094	^{37}K(S.E.)	$^{40}Ca(p,\alpha)$
3605	^{37}K	$^{40}Ca(p,\alpha)$

D.E. double escape peak

S.E. single escape peak

TABLE 11

Experimental beta branching of ^{37}K relative to the beta branch to the 2.796 MeV level in ^{37}Ar. The branch entered for the 1.611 MeV level probably results from a gamma cascade from the 2.796 MeV level rather than from a direct beta branch. See the text for more details concerning the branch to the 1.611 MeV level.

(See page 58.)

TABLE 11

E_x(MeV)	Relative Beta Branch (%)
1.410	< 0.8
1.611	$\leq$ 1.6 ± .3 probably γ branch
2.217	< 0.4
2.490	< 0.5
2.796	100.
3.170	< 0.2
3.186	< 0.7
3.272	< 0.4
3.517	< 0.6
3.526	< 0.4
3.605	0.97 ± .13
3.939	< 0.1
3.981	< 0.1
4.45	< 0.4
4.58	< 0.4
4.64	< 0.3
5.09	< 0.3

TABLE 12

Experimental results for the beta decay of ^{37}K. The listed branch to the 1.611 MeV level assumes feeding of this level directly from beta decay, although as explained in the text (p. 59) it is more likely the feeding results from a gamma transition from the 2.796 MeV level.

No new branch was found.

TABLE 12

E(MeV)	J^{π}	Branching	f	log ft
0.000	$3/2^{+}$	0.9985 ± 0.0002	3582	3.66 ± .01
1.410	$1/2^{+}$	$< 1.5 \times 10^{-4}$	821	> 6.8
1.611	$7/2^{-}$	$\leq 2.3 \times 10^{-4}$	638	$\geq$ 6.5
2.217	$7/2^{+}$	$< 6 \times 10^{-4}$	273	> 5.7
2.490	$3/2^{-}$	$< 8 \times 10^{-4}$	176	> 5.4
2.796	$5/2^{+}$	$(1.45 \pm 0.16) \times 10^{-2}$	102	3.94 ± .05
3.170	5/2	$< 3 \times 10^{-5}$	48	> 6.3
3.186	$9/2^{-}$	$< 1 \times 10^{-4}$	46	> 5.7
3.272	$(3/2^{-})$	$< 6 \times 10^{-4}$	39	> 4.9
3.517	$3/2^{-}$	$< 1 \times 10^{-4}$	21	> 5.4
3.526	$7/2^{-}$	$< 9 \times 10^{-5}$	20	> 5.4
3.605	$(3/2,5/2)^{+}$	$(1.4 \pm 0.2) \times 10^{-4}$	16	5.16 ± 0.06
3.939		$< 1.5 \times 10^{-5}$	5.9	> 5.7
3.981		$< 1.5 \times 10^{-5}$	5.1	> 5.6
4.448	$(1/2,3/2)^{-}$	$< 6 \times 10^{-5}$	.8	> 4.2
4.579		$< 6 \times 10^{-5}$	.41	> 3.9
4.638		$< 5 \times 10^{-5}$	.32	> 3.8
5.090	$(1/2,3/2)^{-}$	$< 5 \times 10^{-5}$	.09	> 3.3

TABLE 13

Theoretical predictions for beta decay of ^{37}K. Also present are log ft values experimentally found in this work. Sources for the theoretical log ft calculations are

Bah: (Bahcall 1964) $1d_{3/2}$ space

E&B (Engelbertink and Brussaard 1966)

$2s_{1/2}$ and $1d_{3/2}$ space

L&W: (Lanford and Wildenthal 1973)

$1d_{5/2}$, $1d_{3/2}$, and $2s_{1/2}$

Gla: (Glaudemans, reported in Dieperink and Brussaard 1969b)

$1d_{5/2}$, $1d_{3/2}$, and $2s_{1/2}$

D&B: (Dieperink and Brussaard 1969b)

$1d_{5/2}$, $1d_{3/2}$, and $2s_{1/2}$

(See page 60.)

TABLE 13

E_x(MeV)	J^π	exp	Bah	E&B	L&W	Gla	D&B
0.000	$3/2^+$	3.66 ±.01	3.72	3.63	3.53	3.62	3.55
1.410	$1/2^+$	> 6.8	5.06	5.21	6.32	5.17	7.61
2.796	$5/2^+$	3.94 ± .05	4.90	4.34	3.41	4.14	3.49
3.605	$(3/2,5/2)^+$	5.16 ± .06			5.29[a]		

[a]This assumes that 3.605 MeV level is second $5/2^+$ state, which is predicted to be at 3.04 MeV. The second $3/2^+$ state is predicted to be at 4.63 MeV and have a log ft of 4.64.

TABLE 14

Experimental results for the beta decay of ^{38}K. No information was obtained concerning the branches to the levels at 0.0, 4.71, and 5.73 MeV as the branch to the first level emits no gamma ray, while the branches to the other two states emit gamma rays which did not fall into the energy range observed. However, because of the spin and parity of these three levels, no significant beta decay strength is expected.

No new branch was found.

(See page 64.)

TABLE 14

E(MeV)	J^{π}	Branching	f	log ft
0.000	0^+	...		
2.168	2^+	0.999 ± 0.001	206	4.98 ± 0.01
3.377	0^+	$< 2 \times 10^{-3}$	16.5	> 6.5
3.810	3^-	$<1.5 \times 10^{-3}$	4.2	> 6.1
3.937	2^+	$(1.41 \pm 0.05) \times 10^{-3}$	2.6	5.92 ± .02
4.480	4^-	$<1.5 \times 10^{-3}$	.23	> 4.8
4.565	2^+	$<1.5 \times 10^{-3}$	.17	> 4.7
4.585	5^-	$<1.5 \times 10^{-3}$	.17	> 4.7
4.710	0^+	...		
4.877	3^-	$< 3 \times 10^{-3}$	.083	> 5.1
5.084	$(1\text{-}3)^-$	$<2.5 \times 10^{-2}$	.054	> 3.0
5.157	2^+	$< 2 \times 10^{-4}$	.045	> 4.9
5.349	$(3,4)^+$	$<2.5 \times 10^{-4}$	.025	> 4.6
5.513	3^-	$<2.5 \times 10^{-4}$	.013	> 4.4
5.552	$(1,2)^+$	$<2.5 \times 10^{-4}$	.010	> 4.2
5.595	1^-	$< 9 \times 10^{-4}$	.008	> 3.6
5.658	5^-	$< 3 \times 10^{-3}$	.006	> 2.9
5.734	1^-	...		
5.825	3^-	$< 4 \times 10^{-4}$	.0007	> 2.9
5.857	$(2,3)^-$	$< 9 \times 10^{-4}$	.0003	> 2.2

TABLE 15

Theoretical predictions for beta decay of ^{38}K to the first excited state of ^{38}Ar at 2.17 MeV ($J^{\pi} = 2^{+}$). The first line contains the value found experimentally. Sources for the theoretical log ft calculations are

E&B: Engelbertink and Brussæard 1966

E&S: Evers and Stocker 1970

D&G: Dieperink and Glaudemans 1969a

D&B: Dieperink and Brussaard 1969

L&W: Lanford and Wildenthal 1973

The interaction used in each calculation is shown, the modified surface delta interaction (MSDI), an interaction involving a tensor term (tensor), and a realistic interaction obtained by Kuo (Kuo). See text for additional details. The configuration for these shell-model calculations is also shown.

(See page 65.)

TABLE 15

Authors	Space	Interaction	log ft
Present work--experimental			$4.98 \pm .01$
E&B (1966)	$s_{1/2}, d_{3/2}$	MSDI	4.32
E&S (1970)	$s_{1/2}, d_{3/2}, f_{7/2}$	MSDI	4.05
		Tensor	4.05
D&G (1969)	$s_{1/2}, d_{3/2}, d_{5/2}$	MSDI	4.75
D&B (1969)		Tensor	4.34
L&W (1973)	$s_{1/2}, d_{3/2}, d_{5/2}$	Kuo	4.97

TABLE 16

Experimental results for the beta decay of ^{39}Ca. No new transitions were found.

(See page 66.)

TABLE 16

E(MeV)	J^{π}	Branching	f	log ft
0.000	$3/2^{+}$	1.00	4869	3.63 ± .01
2.523	$1/2^{+}$	$< 1 \times 10^{-4}$	298	> 6.4
2.814	$7/2^{-}$	$< 1 \times 10^{-4}$	189	> 6.2
3.019	$3/2^{-}$	$< 6 \times 10^{-5}$	133	> 6.3
3.598	$(7/2,9/2)^{-}$	$< 4 \times 10^{-5}$	40.3	> 5.9
3.883	$(3/2,5/2)^{-}$	$< 3 \times 10^{-5}$	21.0	> 5.8
3.939	(1/2-5/2)	$< 4 \times 10^{-5}$	17.9	> 5.6
3.943	(5/2-11/2)	$< 2 \times 10^{-4}$	17.7	> 4.9
4.083	3/2	$< 3 \times 10^{-5}$	12.0	> 5.4
4.096	$1/2^{+}$	$< 1 \times 10^{-4}$	11.5	> 5.0
4.126	$(3/2-9/2)^{-}$	$< 1 \times 10^{-4}$	10.6	> 5.0
4.476		$< 4 \times 10^{-5}$	3.3	> 4.8
4.514	(1/2-7/2)	$< 2 \times 10^{-5}$	3.0	> 5.1
4.520	(5/2-11/2)	$< 5 \times 10^{-5}$	2.7	> 4.7

FIGURE 1

Histogram showing distribution of beta decay strengths for allowed transitions for $A \leq 44$. The peak at log ft = 3.6 corresponds to Fermi transitions having nuclear matrix elements near unity. The existence of another peak, at log ft = 5.0 , suggests that nuclear matrix elements between non-mirror states are approximately equal. It should be noted that for log ft greater than 7.0, few transitions are known in this mass region, and only one transition (the famous decay of ^{14}C) has a log ft greater or equal to 9.0 .

(See page 14.)

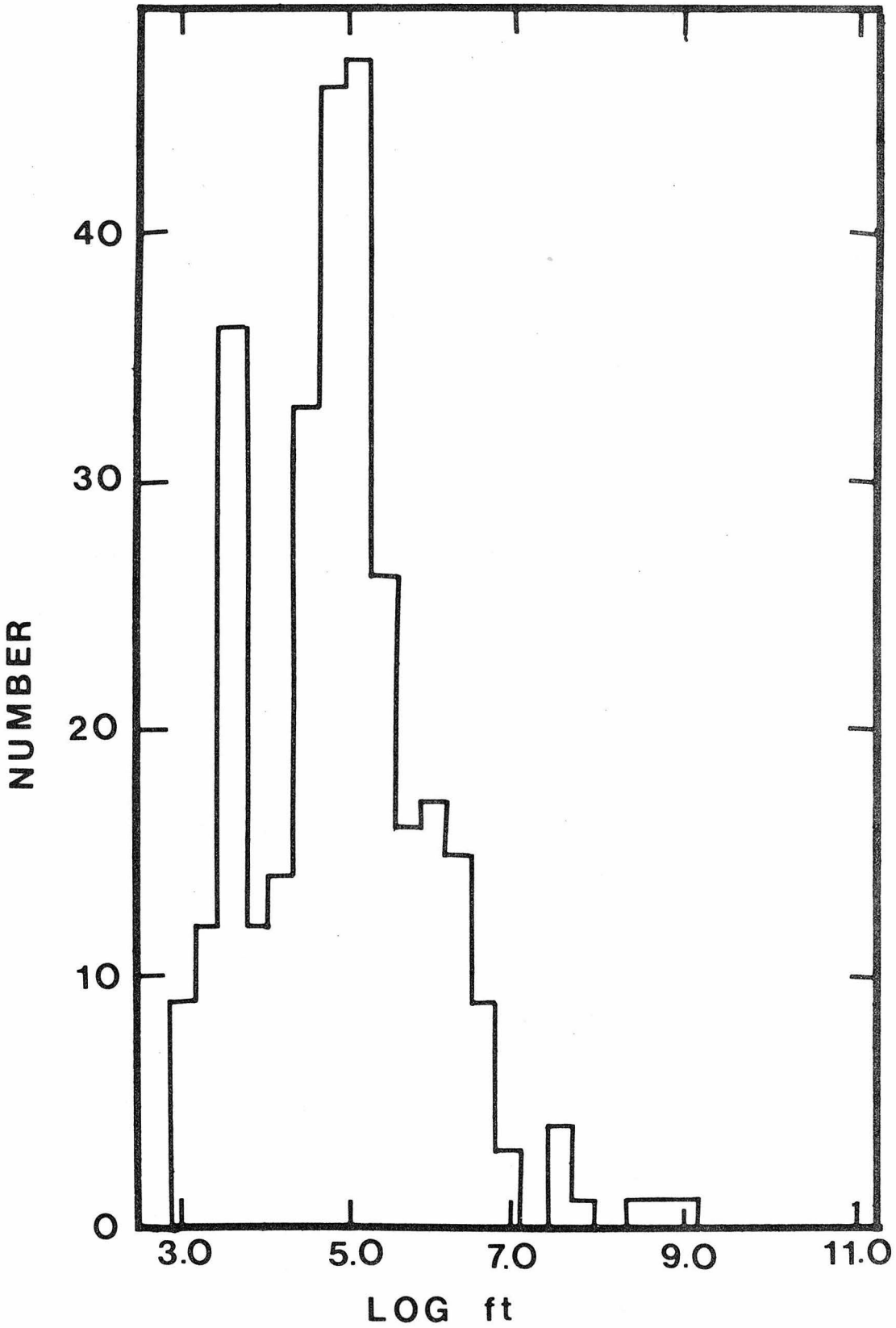
NUMBER
0
10
20
30
40
3.0
5.0
7.0
9.0
11.0
LOG ft

FIGURE 2

Block diagram of rabbit system. The beam hutch (shown in detail in Figure 3) is located in the target room of the CIT-ONR Tandem accelerator, while the detector hutch (shown in detail in Figure 4) is located 17 meters away in the shielded control room. The rabbit travelled the 17 meters through a plastic tubing. The roughing pump is a rotary model, built around 1930. The propellant gas is either air or argon. Argon was used whenever delayed radiation produced by bombardment of air interfered with the observation of weak delayed gamma rays under study. The values were controlled by an electronic sequence timer which powered mercury-wetted relays.

(See page 19.)

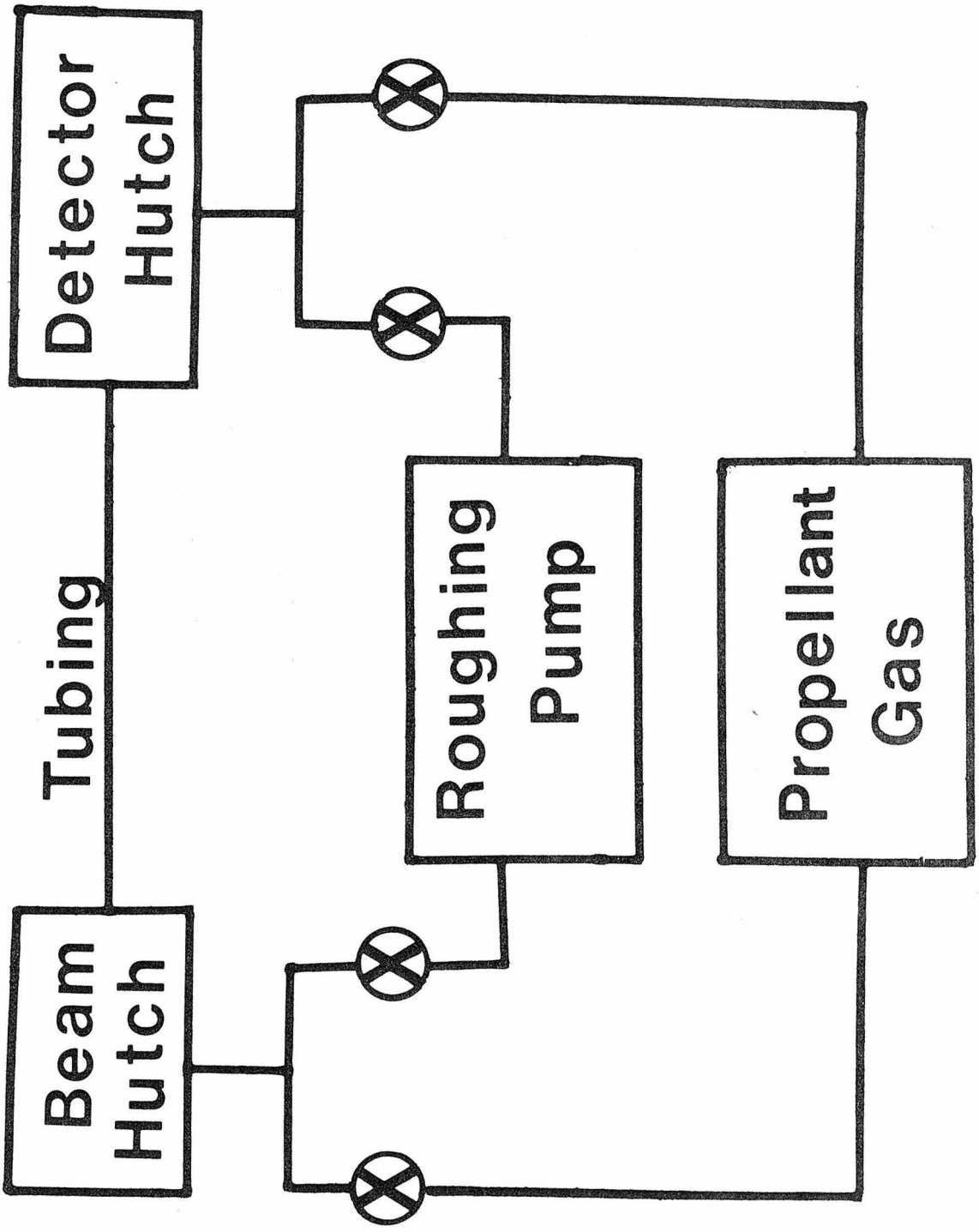
Detector Hutch
Tubing
Beam Hutch
Roughing Pump
Propellant Gas

FIGURE 3

Rabbit system at end of accelerator beam line. The beam enters from the right, having been partially collimated by tantalum discs, passes through an aluminum tube which further collimates the beam. At the end of the aluminum tube, a thin aluminum foil maintains the pressure differential between the beam tube and the rabbit system. The nylon holder serves to electrically isolate the hutch from the beam line, so that crude beam integration can be performed. The rabbit enters from the left and stops by compressing the O-rings at the end of the rabbit hutch. The hutch is made from heat treated stainless steel, so that repeated impacts will not fatigue the material. The hutch holder seals onto the nylon holder and the rabbit tubing, providing a cavity through which the propelling gas is passed.

(See page 19).

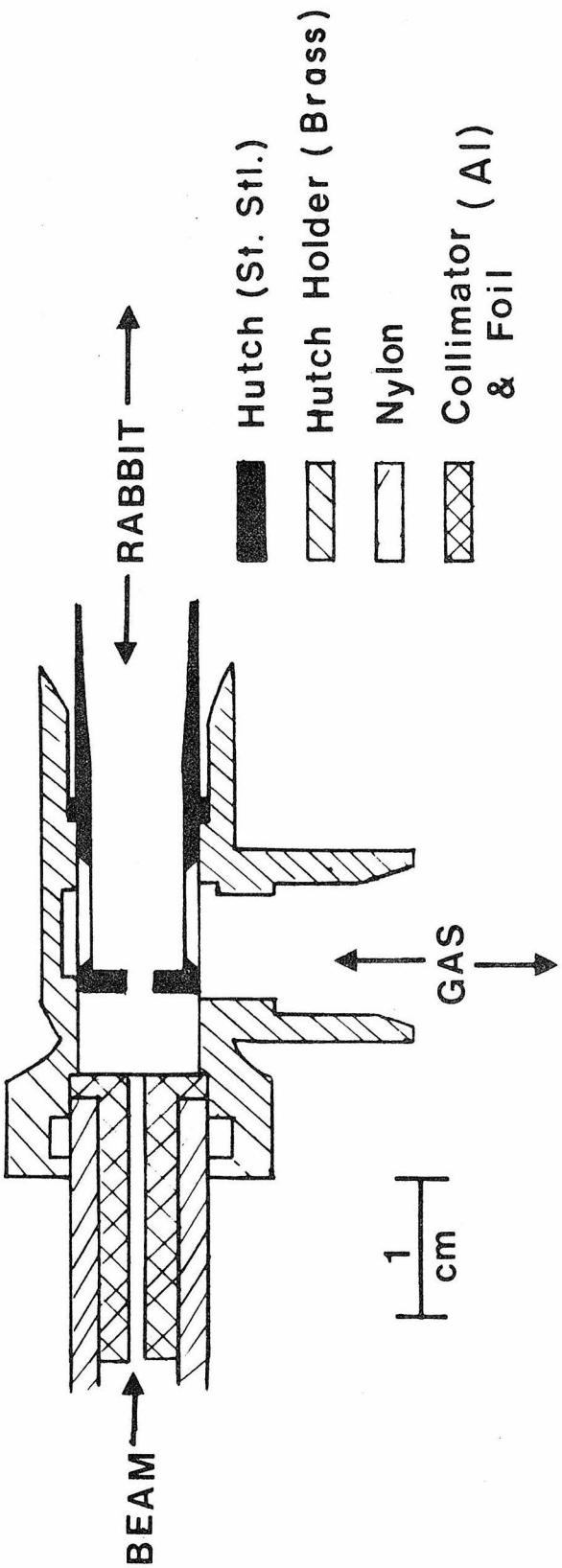
RABBIT
Hutch (St. Stl.)
Hutch Holder (Brass)
Nylon
Collimator & Foil (Al)
GAS
1 cm
BEAM

FIGURE 4

Rabbit system and detector system located in accelerator control room. The rabbit enters the lucite hutch from the viewer's position. Air or argon is pumped out of the hutch from behind the figure. The hutch is of such a size that 5 MeV positrons will stop witnin the lucite, and not in the lead absorber near the Ge(Li). The lead absorber is used to attenuate the annihilation radiation more strongly than the higher energy gamma rays of interest. No lead absorber to 5 cm of lead absorber were used in the experiments. Additional lead shielding was placed around the detector to reduce room background. One of two Ge(Li) detectors, 50 cc or 73 cc, was placed as close as possible to the hutch.

(See page 20.)

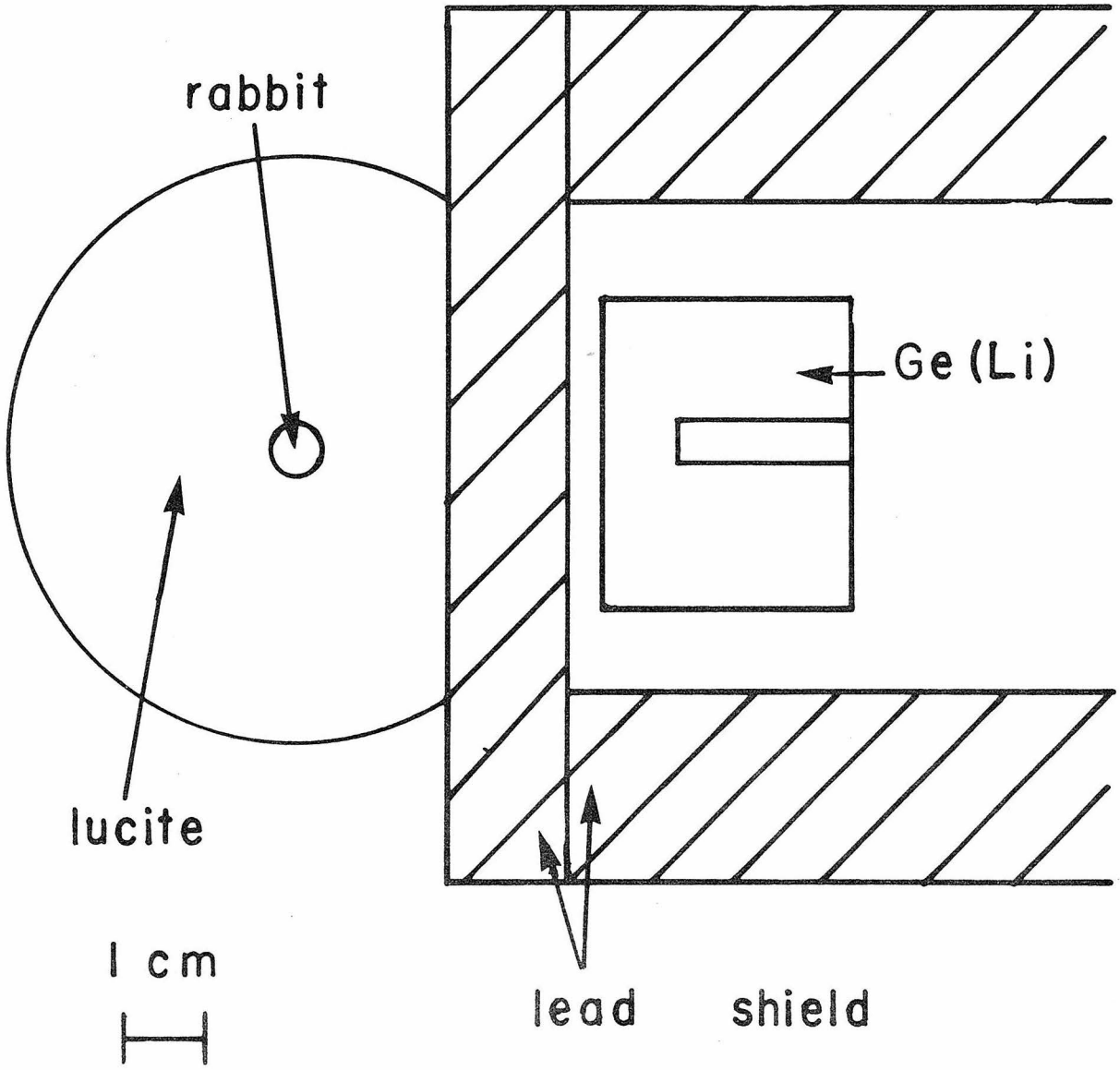
rabbit
Ge (Li)
lucite
1 cm
lead
shield

FIGURE 5

The rabbit. For most of the decays studied, the target material was a salt in powder form. The salt was held inside a beryllium shell by a thin tantalum foil and a nylon tail. Additional tantalum was placed behind the powder to stop the beam. For the study of the decay of ^{37}K, a metallic disc of calcium replaced the salt and the first tantalum foil. In the study of the decay of ^{27}Si, an aluminum cylinder replaced the rabbit shown in the figure. Finally for the study of the ^{38}K decay, the target, $BaCl_2$ evaporated on a tantalum backing, was hand transferred as the half-life was sufficiently long for manual transfer.

(See page 21.)

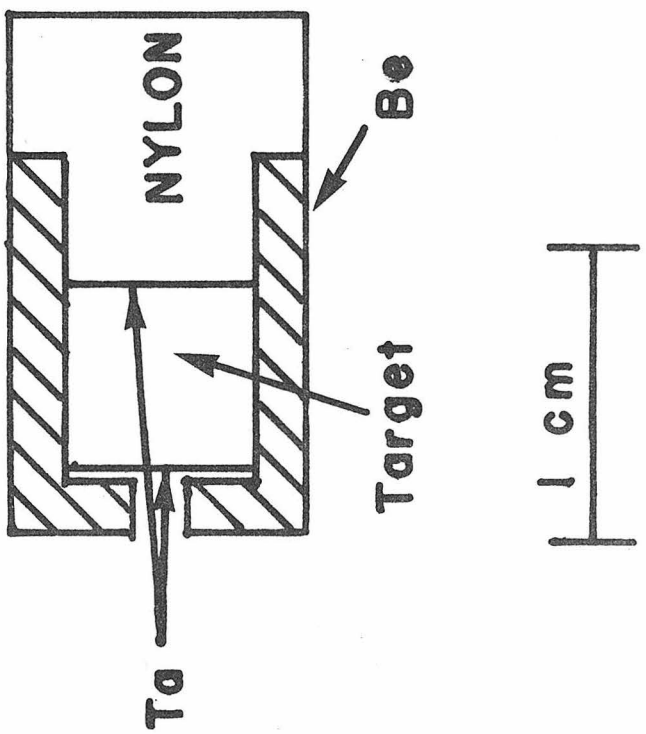
NYLON
Be
Target
Ta
1 cm

FIGURE 6

Relative gamma-ray detection efficiency of the 73 cc Ge(Li) detector for the geometry in Figure 4. Three curves are shown, the highest for no lead separating the hutch and the detector, the middle having 2.5 cm of lead separating the hutch and the detector, and the lowest curve having 5.1 cm of lead. The three curves have the same normalization, the scale along the vertical axis being in arbitrary units.

Two effects are seen: the effect of lead absorbing gamma rays, particularly those of lower energy, and increased source-to-detector distance. It can be seen that through the addition of lead absorber, the relative photopeak detection efficiency can be changed. When no lead is used, .51 MeV gamma rays are 4 times as likely to be observed as 2.0 MeV gamma rays. With 5.1 cm of lead separating the hutch and the detector, the .51 MeV gammas are detected only 1/40 as often as 2.0 MeV gamma rays.

The curves for the other Ge(Li) used, a 50 cc detector would be similar, but would have a slightly steeper slope for the higher energy gamma rays.

(See page 22.)

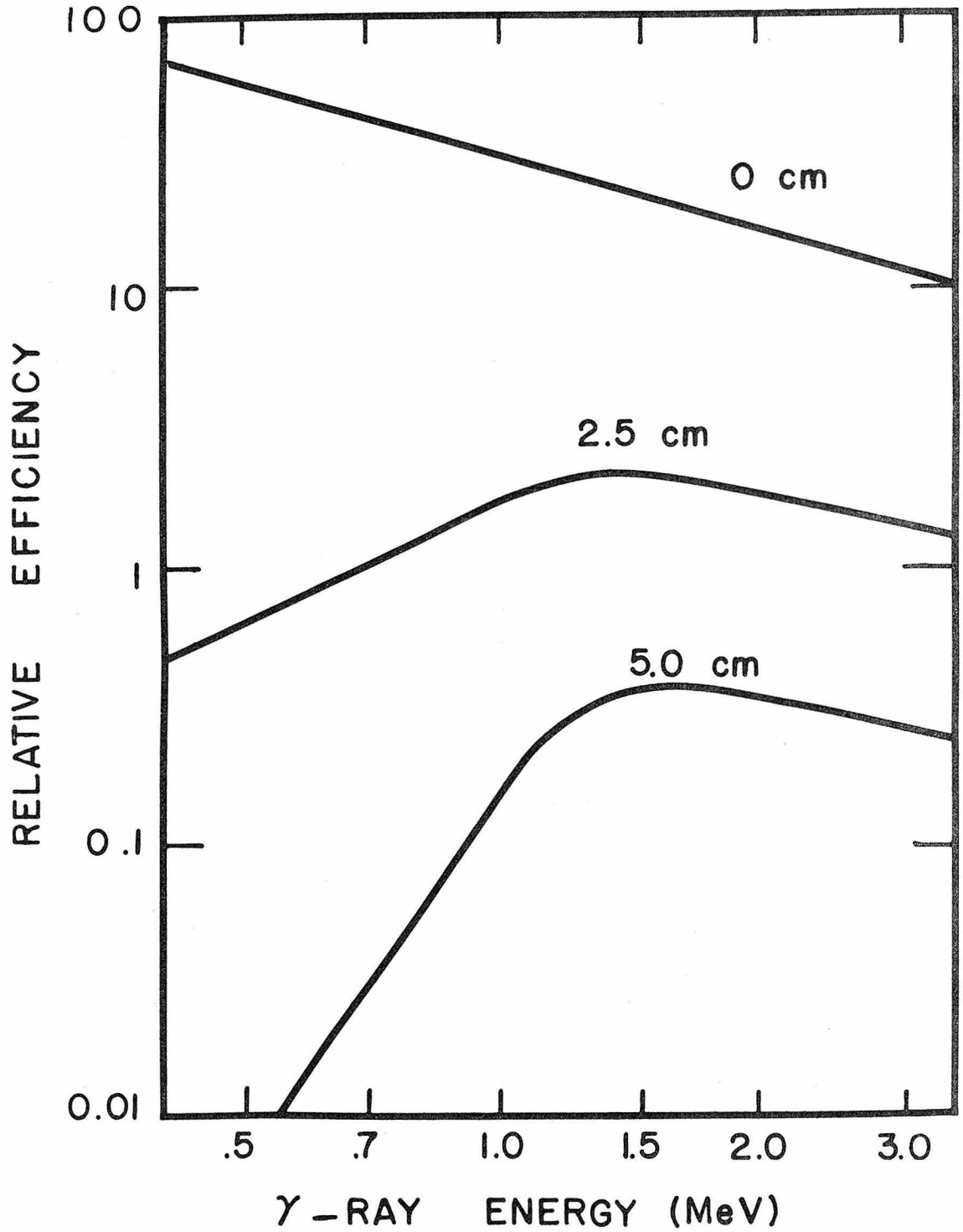
100
10
1
0.1
0.01
RELATIVE EFFICIENCY
0 cm
2.5 cm
5.0 cm
.5
.7
1.0
1.5
2.0
3.0
γ-RAY ENERGY (MeV)

FIGURE 7

Block diagram of electronics used in beta-decay studies. The high voltage power supply provided bias for the Ge(Li) detector (normally about 2400 V). The 60 Hz (line frequency) pulser provided a convenient method to monitor dead time and to observe any gain shifts. The preamplifiers are integral parts of the Ge(Li) detectors and used low-noise FET inputs. The shaping amplifier was a Tennelec TC-200. Other newer amplifiers were tried but did not give significantly better resolution. Three different multichannel analyzers, the RIDL 34-27, the Nuclear Data ND 160, and the Nuclear Data 4420, were used. The sequence timers, either analog or digital, were used to control the rabbit system and the multichannel analyzer. Also the sequence timer controlled the timing of beam bombardment.

(See page 24.)

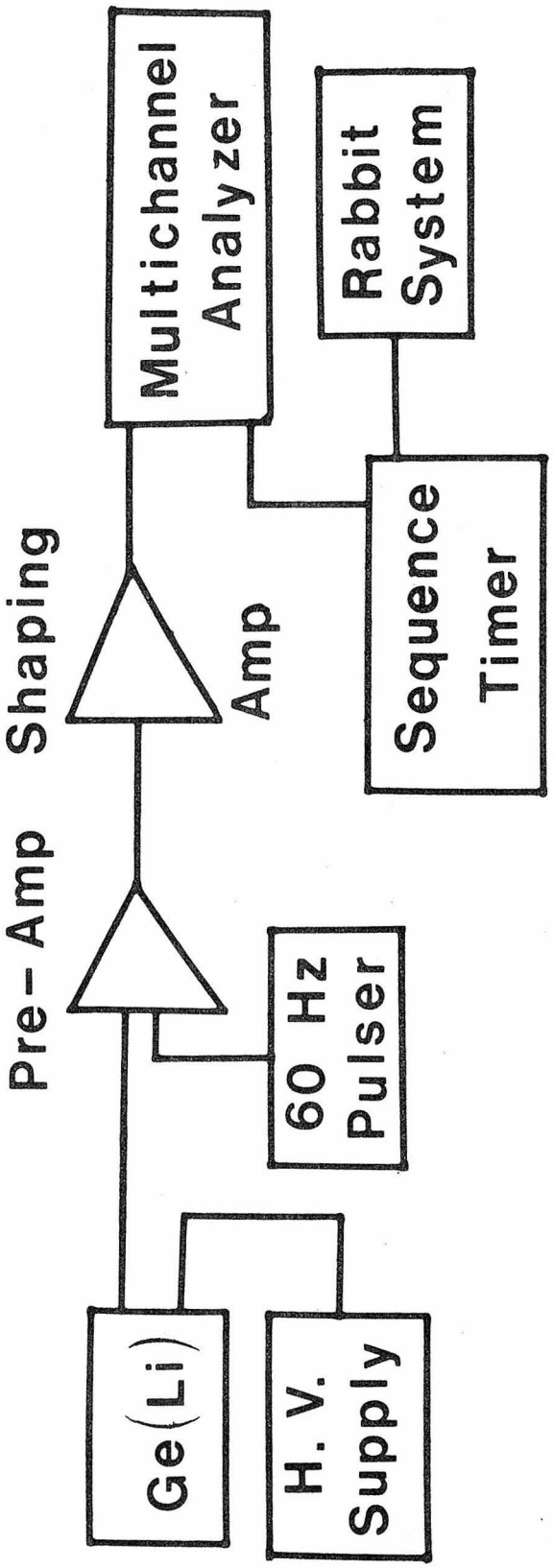
Multichannel Analyzer
Rabbit System
Shaping Amp
Sequence Timer
Pre-Amp
60 Hz Pulser
Ge(Li)
H. V. Supply

FIGURE 8

Number of gamma rays per MeV per positron resulting from annihilation in flight. The upper curve is for positrons annihilating in tantalum, while the lower curve is for positrons annihilating in lucite. Using lucite as the stopping medium reduces the amount of gamma radiation produced by positrons annihilating in flight, particularly at higher gamma ray energies.

(See page 34.)

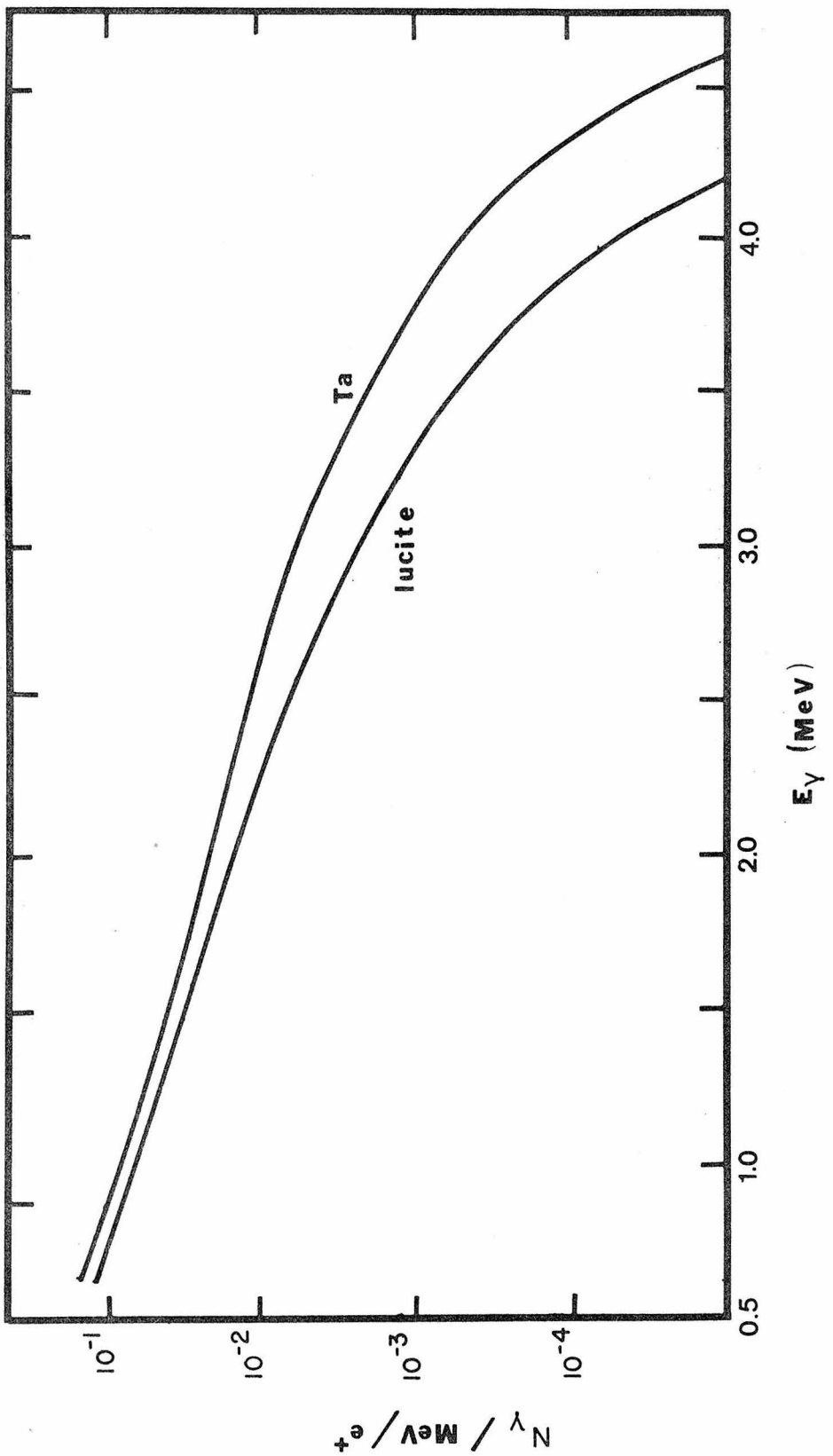
Ta
lucite
10^{-1}
10^{-2}
10^{-3}
10^{-4}
N_γ / MeV / e^+
0.5
1.0
2.0
3.0
4.0
E_γ (MeV)

FIGURE 9

Percentage of missed annihilation radiation due to annihilation in flight as a function of positron endpoint energy. The curve shown is for positrons annihilating in lucite and is based on the theory described in the text (p. 34.) The cross represents the percentage lost for positrons annihilating in tantalum.

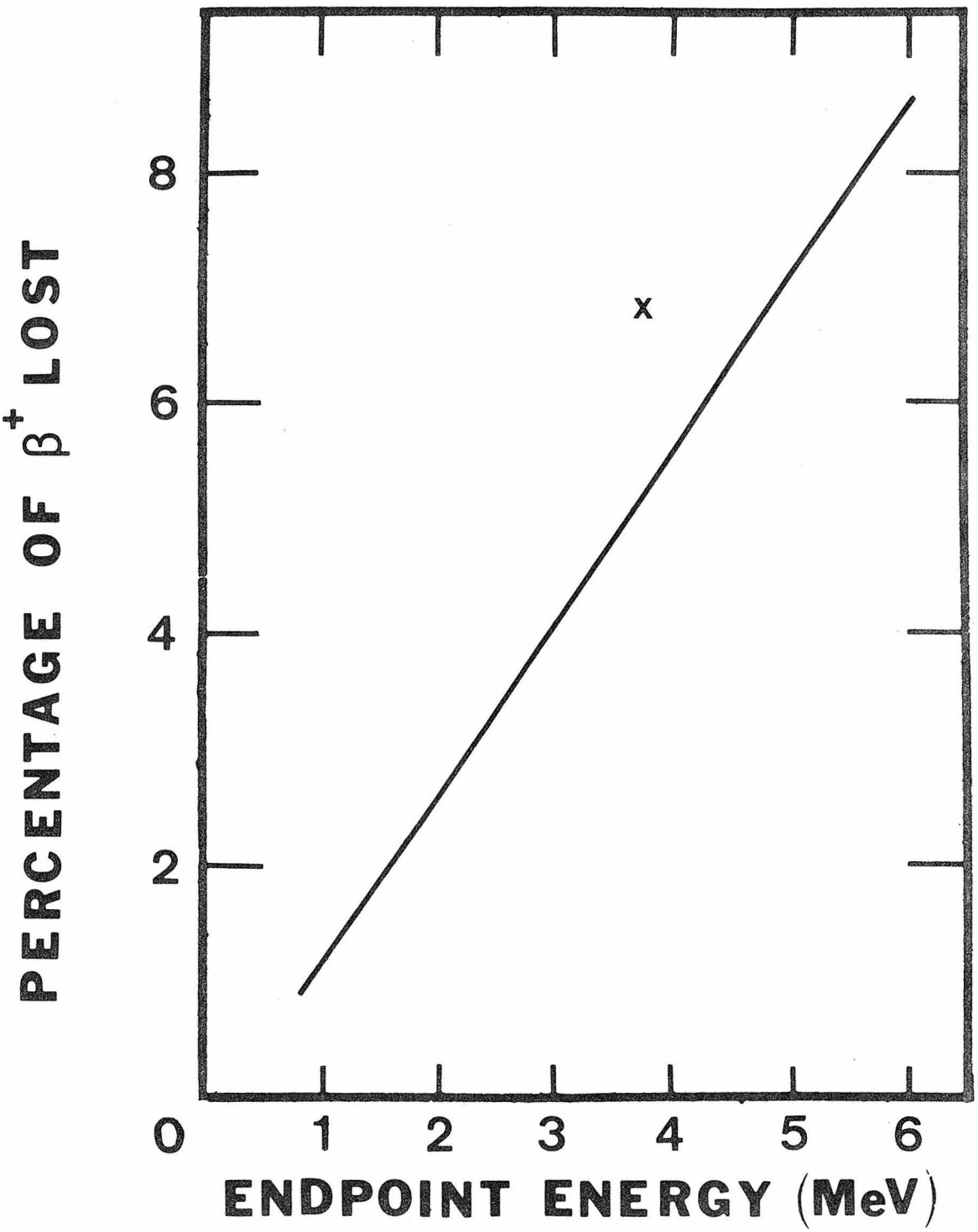
PERCENTAGE OF β+ LOST
0
2
4
6
8
1
2
3
4
5
6
ENDPOINT ENERGY (MeV)
x

FIGURE 10

Energy level diagram for ^{19}F and ^{19}Ne. All levels in ^{19}F for which beta decay is energetically possible are shown. Only two of these levels, however, can be involved in allowed beta transitions, the ground state and the state at 1.554 MeV. The branch to the ground state of ^{19}F is well known, but the branch to the 1.554 MeV has not been seen. This branch was the object of the search.

(See page 38.)

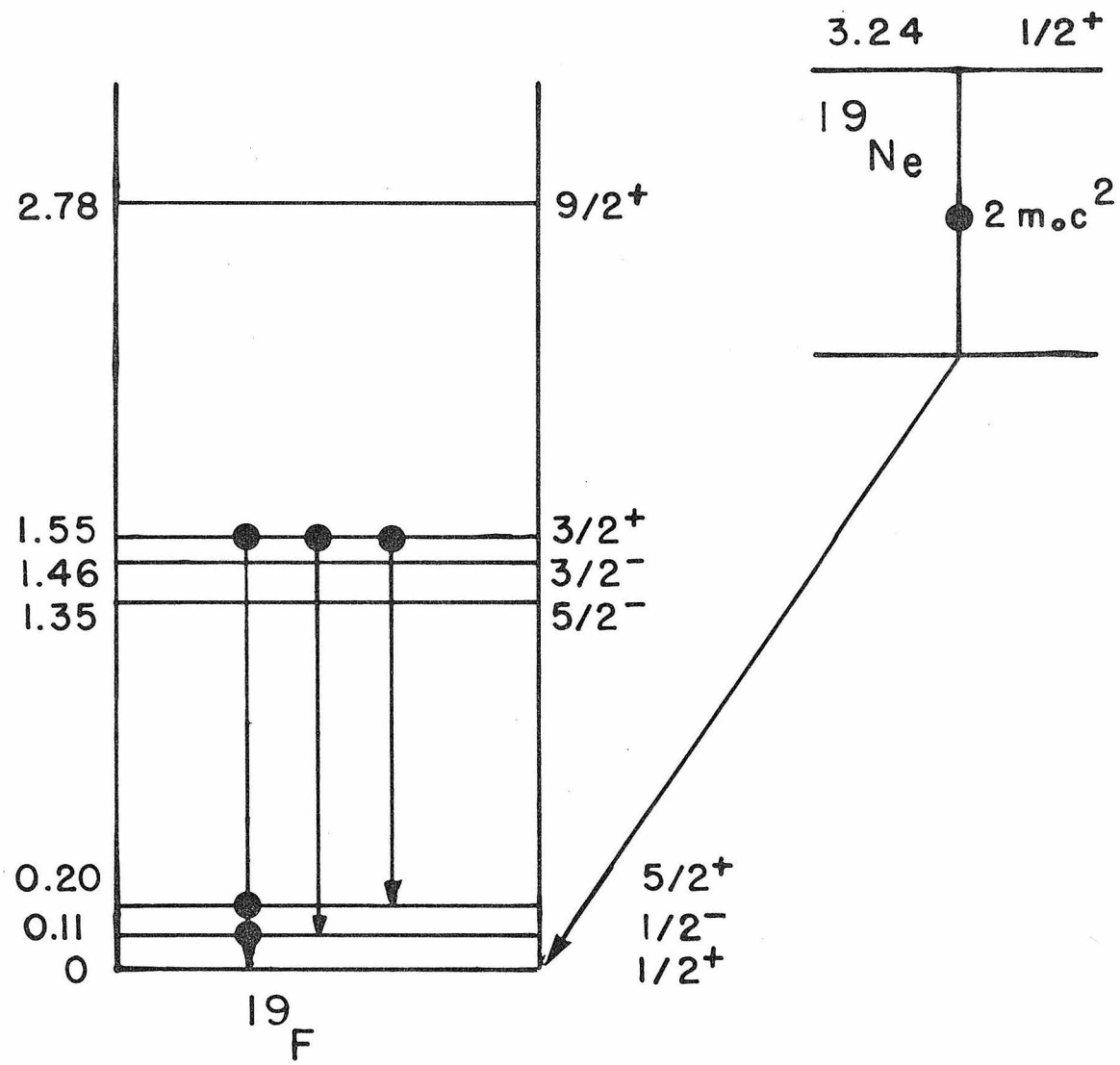
3.24
1/2+
19 Ne
2 m₀c²
2.78
9/2+
1.55
3/2+
1.46
3/2−
1.35
5/2−
0.20
5/2+
0.11
1/2−
0
1/2+
19 F

FIGURE 11

Delayed gamma ray spectrum following proton bombardment of PbF_2. Only the 511-keV gamma ray has the half-life corresponding to ^{19}Ne decay. The other gamma rays result from (p,n) reactions on ^{14}N (trapped in the PbF_2 powder), Pb, and stainless steel (the rabbit hutch in the target room). The gamma ray corresponding to the decay of the 1554-keV level would be at 1357 keV.

(See page 40.)

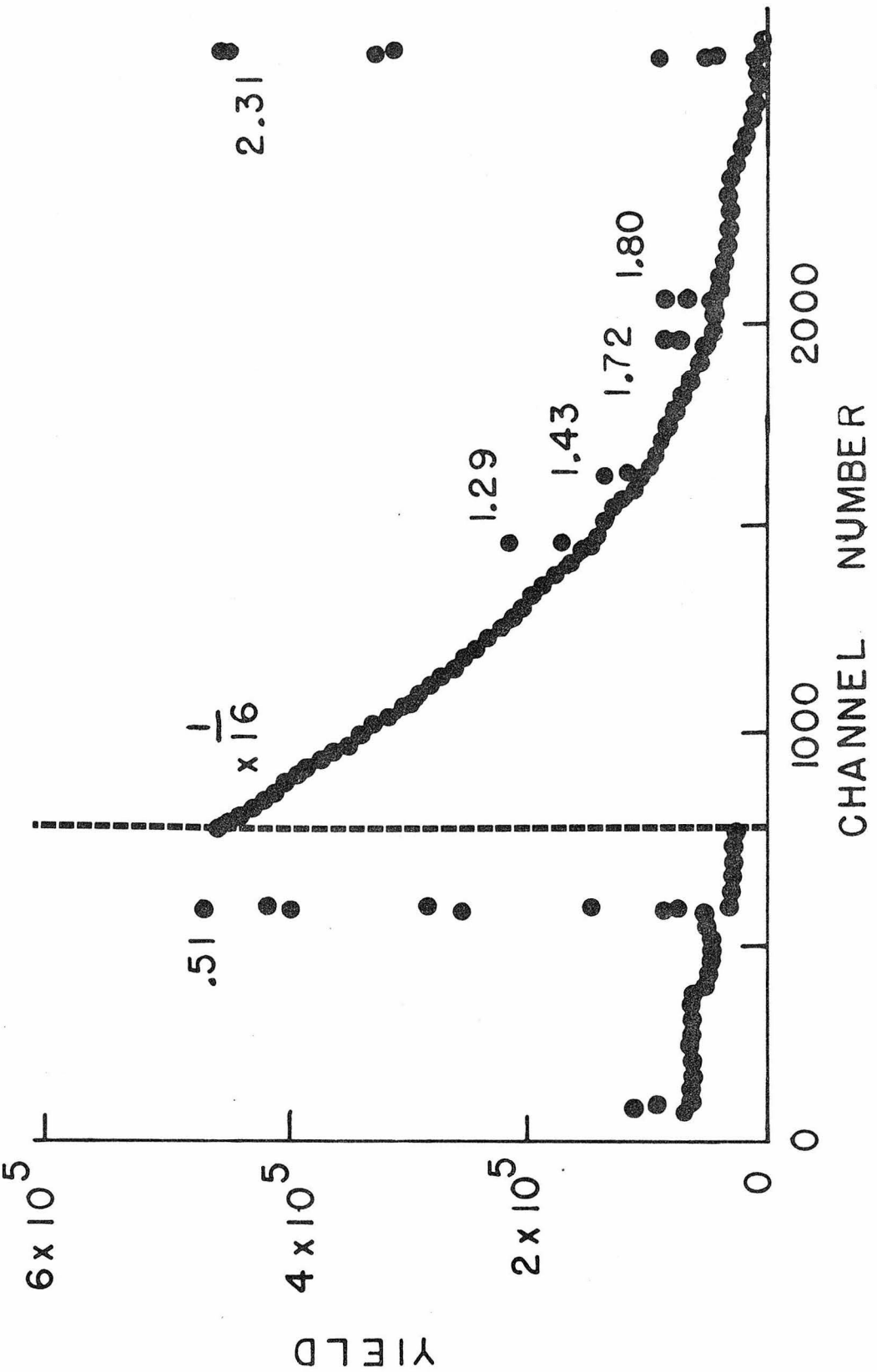
YIELD
6 x 10^5
4 x 10^5
2 x 10^5
0
0
1000
2000
CHANNEL NUMBER
1/16 x
.51
1.29
1.43
1.72
1.80
2.31

FIGURE 12

Expanded view of Figure 11 around the region where the expected 1357-keV gamma ray from the decay of ^{19}Ne should appear. The peak at the left is the second escape peak of the 2313-keV gamma ray produced in ^{14}O decay, while the peak at the right is the 1434-keV photopeak from the decay of $^{52}Mn^{*}$. No indication of a peak is seen at the channel corresponding to 1357 keV.

(See page 41.)

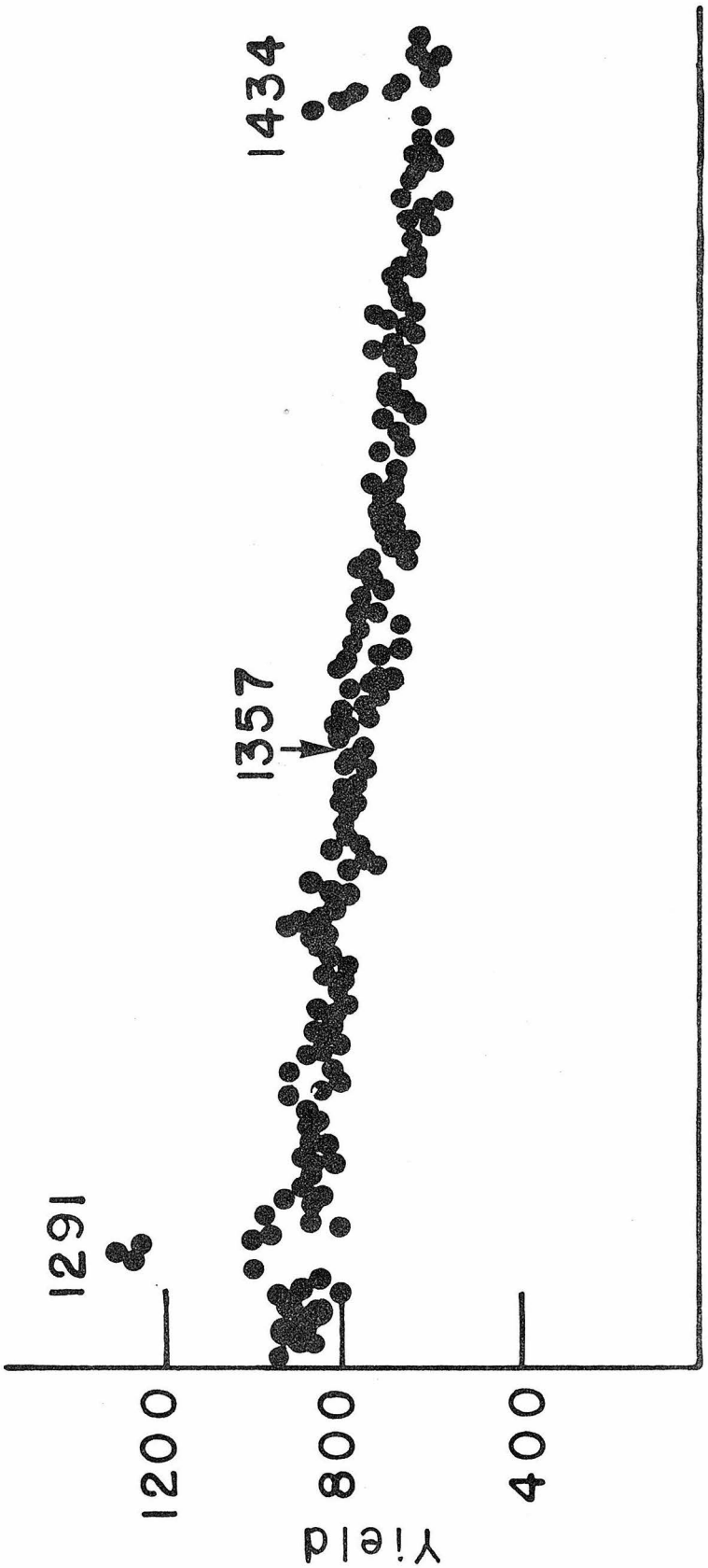
1291
1357
1434
1200
800
400
Yield
γ-Ray Energy (keV)

FIGURE 13

Energy level diagram for ^{23}Na and ^{23}Mg. All levels below 3 MeV are shown. The branch to the 2391-keV level has not been previously reported.

(See page 43.)

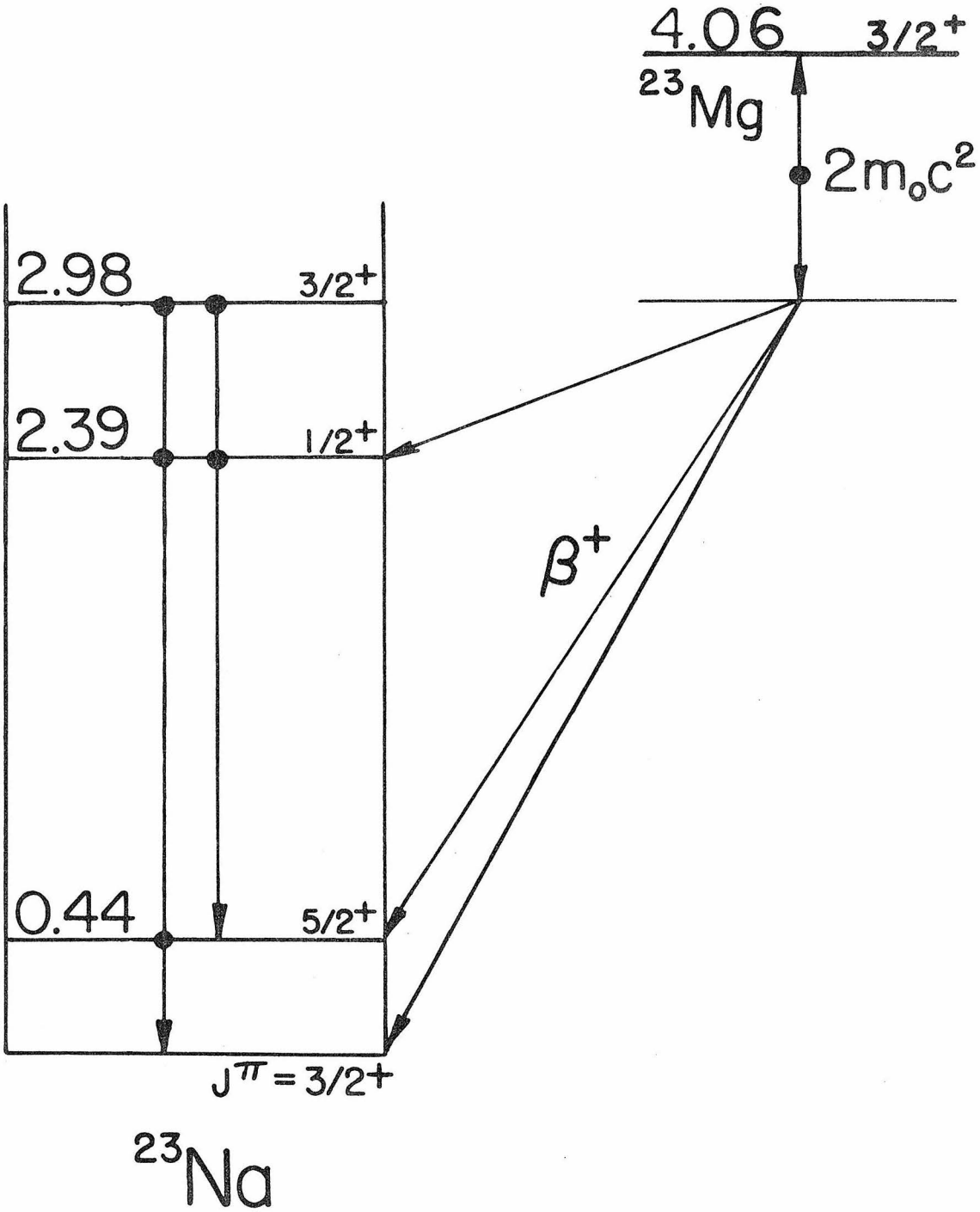
4.06
3/2+
23Mg
2mₒc²
2.98
3/2+
2.39
1/2+
β+
0.44
5/2+
J^π = 3/2+
23Na

FIGURE 14

Gamma ray spectrum following ^{23}Mg decay with NaF as the target material and 2.5 cm of lead separating the lucite hutch and the Ge(Li) detector. The 0.44 MeV is clearly seen in the hollow between the 0.51 MeV photopeak and the Compton edge. Also seen is the ground state decay and cascade decay through the 0.44 MeV state of the 2391-keV level. The beta branch to the 2391-keV has not been previously reported.

(See page 45.)

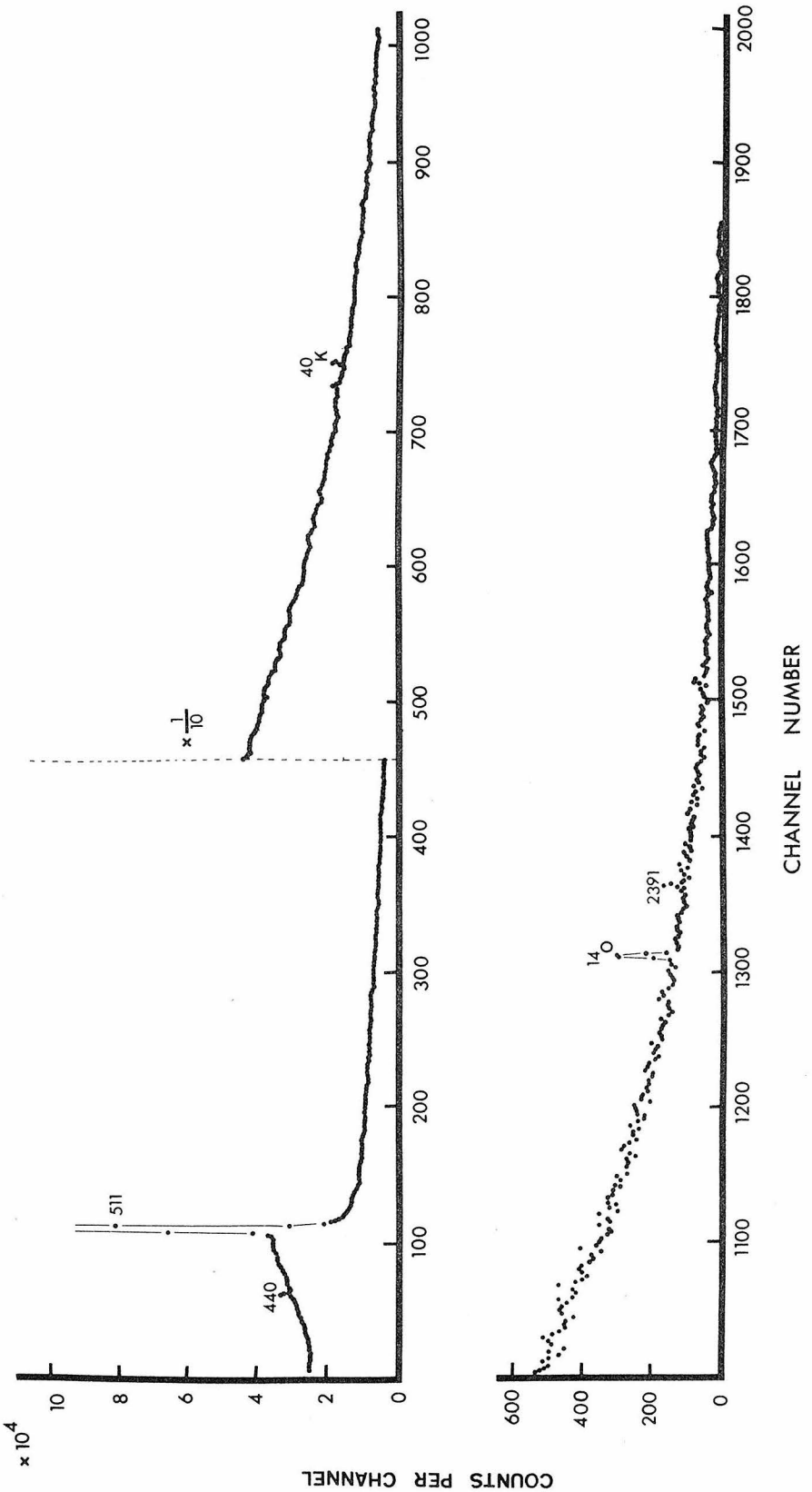
COUNTS PER CHANNEL
CHANNEL NUMBER
× 10^4
511
440
× 1/10
40 K
14 O
2391

FIGURE 15

Gamma ray spectrum following ^{23}Mg decay with Na_2WO_4 as the target material and no lead between the lucite hutch and the Ge(Li) detector. Gamma rays at 0.44 and 0.51 MeV are seen. This is the first spectrum of four time groups that were taken. The backscatter peak is large since a lead brick was placed behind the lucite hutch to reduce background annihilation radiation.

(See page 46.)

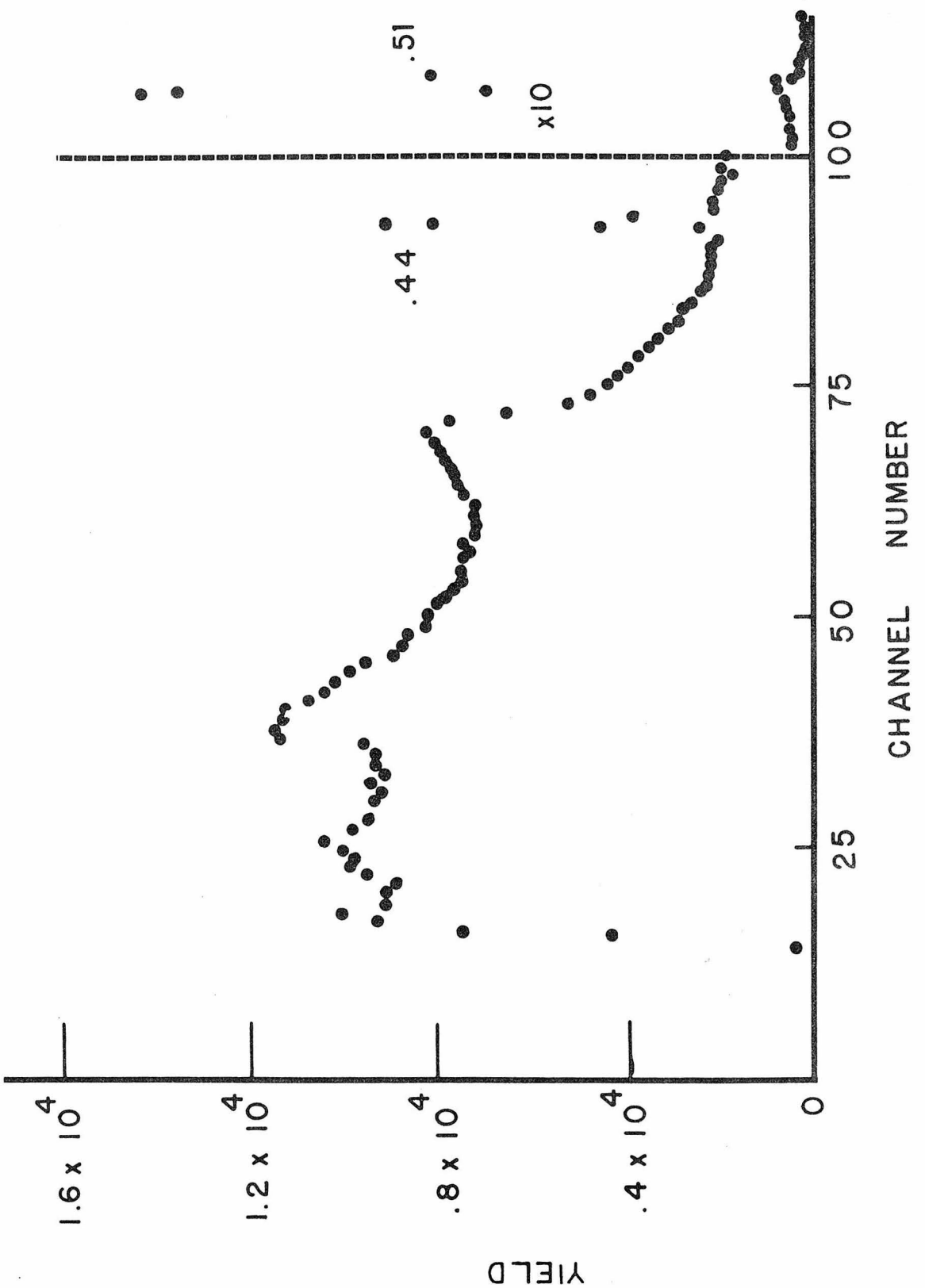
YIELD
1.6 x 10^4
1.2 x 10^4
.8 x 10^4
.4 x 10^4
0
25
50
75
100
CHANNEL NUMBER
.44
.51
x10

FIGURE 16

Energy level diagram for ^{27}Si and ^{27}Al. The levels below 3 MeV are shown. The branch to the 2734-keV level has not been previously reported.

(See page 49.)

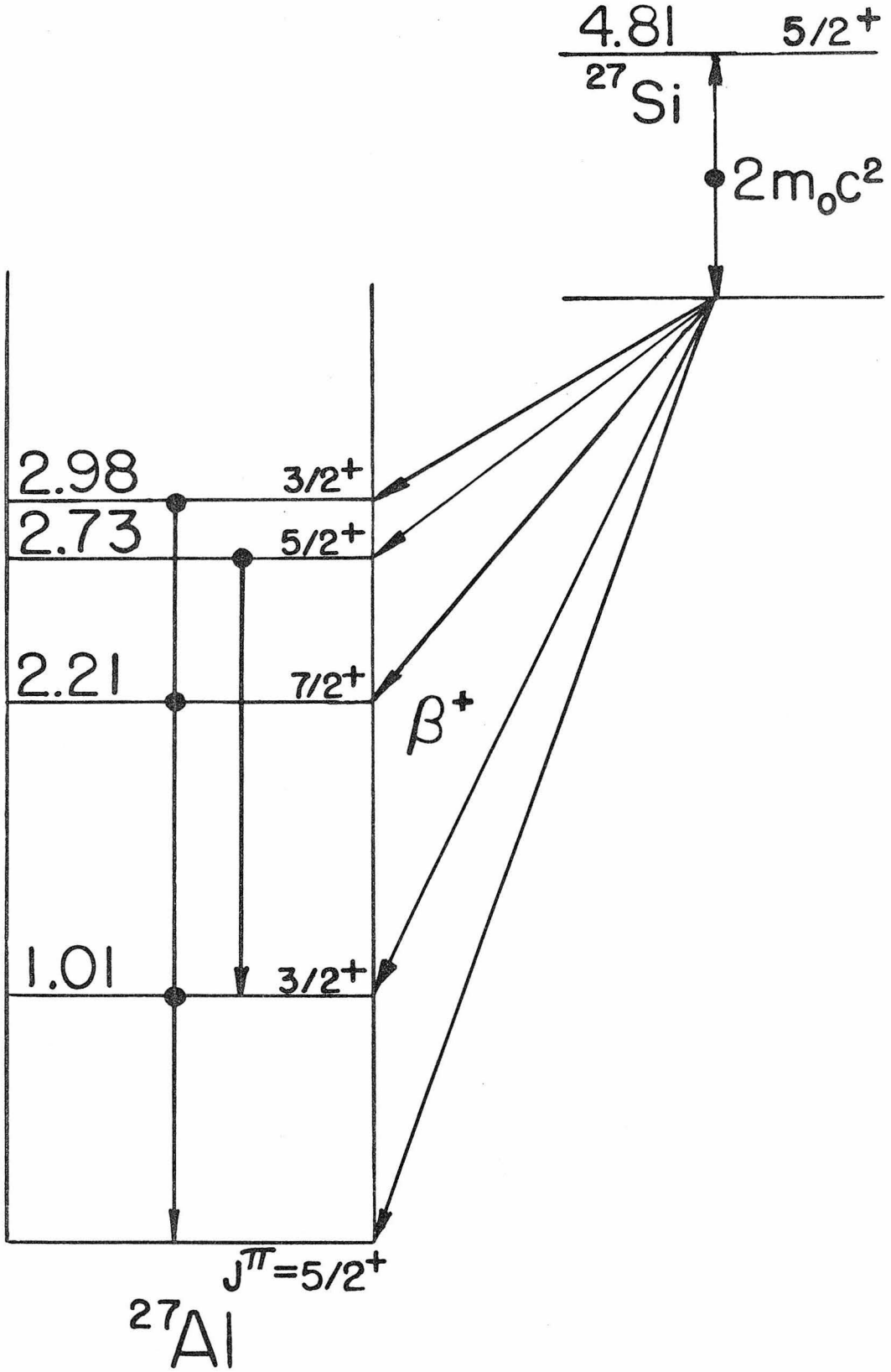
4.81
5/2+
27Si
2moc2
2.98
3/2+
2.73
5/2+
2.21
7/2+
β+
1.01
3/2+
Jπ=5/2+
27Al

FIGURE 17

Gamma ray spectrum following ^{27}Si decay with 3.3 cm of lead separating the Ge(Li) and the lucite hutch. Gamma rays depopulating states at 1014, 2211, 2734, and 2981 keV are seen. Both the ground state decay and cascade decay through the 1014-keV level for the 2734-keV level are seen. The beta branch to the 2734-keV level has not been previously reported.

(See page 51.)

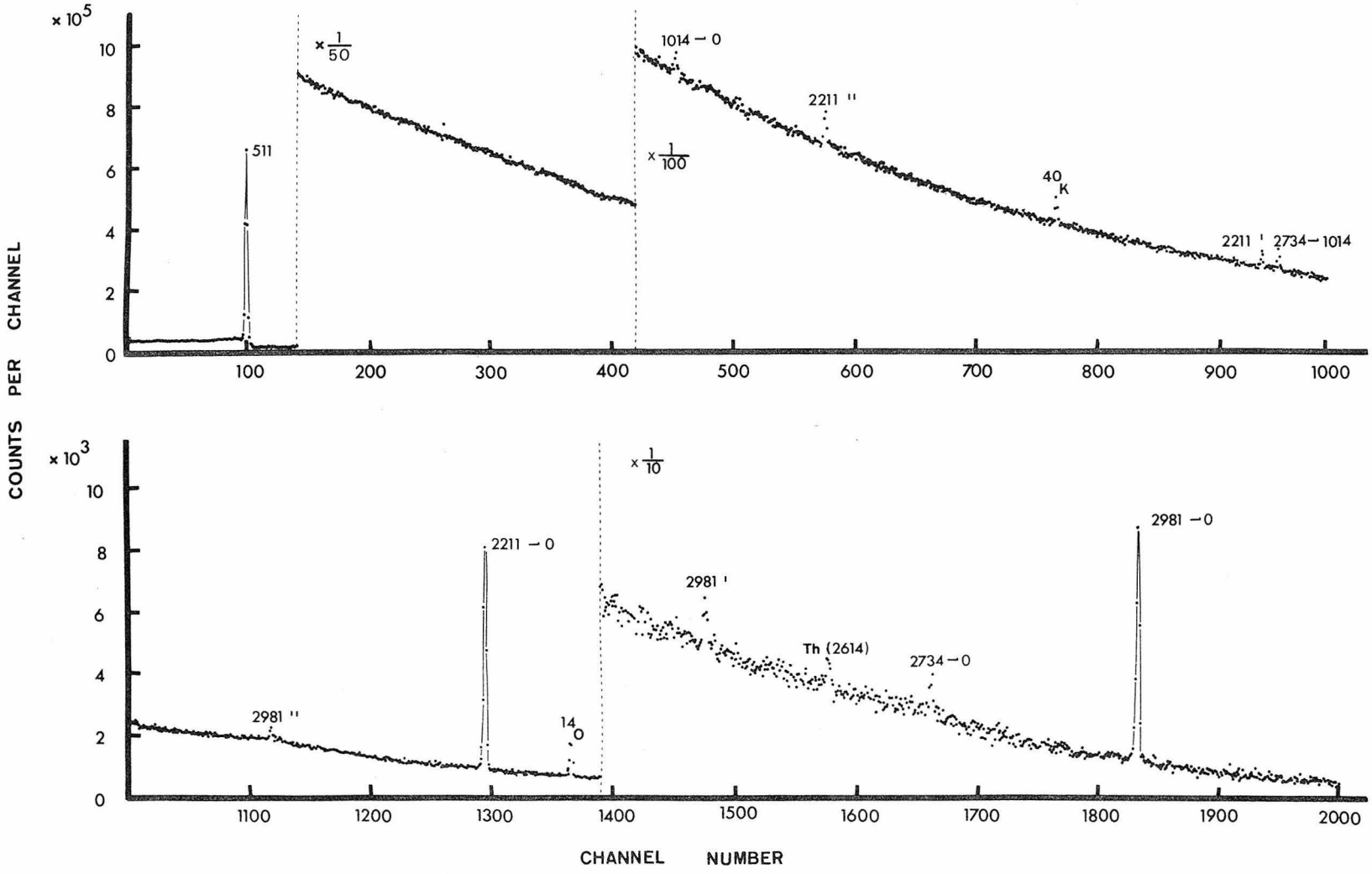
× 10^5
10
8
6
4
2
0
× 1/50
× 1/100
511
1014 — 0
2211 ''
40 K
2211 '
2734 — 1014
100
200
300
400
500
600
700
800
900
1000
× 10^3
10
8
6
4
2
0
× 1/10
2211 — 0
2981 '
2981 — 0
Th (2614)
2734 — 0
2981 ''
14 O
1100
1200
1300
1400
1500
1600
1700
1800
1900
2000
COUNTS PER CHANNEL
CHANNEL NUMBER

FIGURE 18

Energy level diagram for ^{37}Ar and ^{37}K. The only levels shown are those below 2.80 MeV and those levels which could partake in allowed beta transitions. The three beta branches shown are known from previous work. No branch has been reported to the $1/2^+$ state at 1.41 MeV. This branch was the main object of the study of ^{37}K beta decay.

(See page 55.)

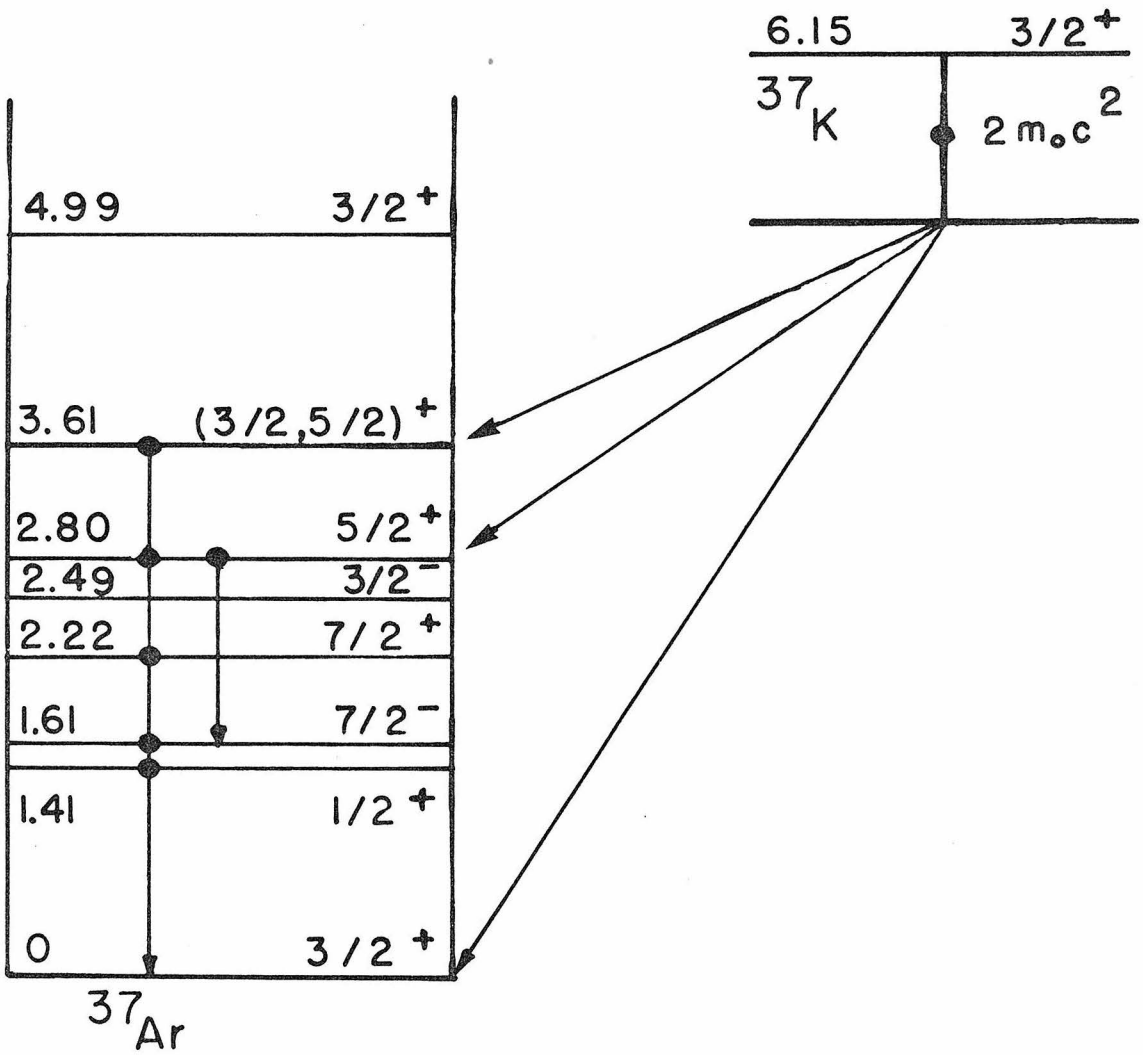
6.15
3/2+
37K
2 m0c2
4.99
3/2+
3.61
(3/2,5/2)+
2.80
5/2+
2.49
3/2−
2.22
7/2+
1.61
7/2−
1.41
1/2+
0
3/2+
37Ar

FIGURE 19

Delayed gamma spectrum following 10 MeV proton bombardment of Ca. The sources of the gamma rays seen in this figure are given in Table 10. The gamma rays of interest in the beta decay of ^{37}K are the 2796 keV and 3605 keV. A gamma ray is expected at 1410 keV, corresponding to the allowed decay to that state. Not seen in the figure, because of the scale chosen, is the 1611-keV gamma ray. The source of this gamma ray (which depopulates the 1611-keV state in ^{37}Ar) is believed to be a previously unreported gamma branch of the 2796-keV level rather than a beta branch from ^{37}K.

(See page 57.)

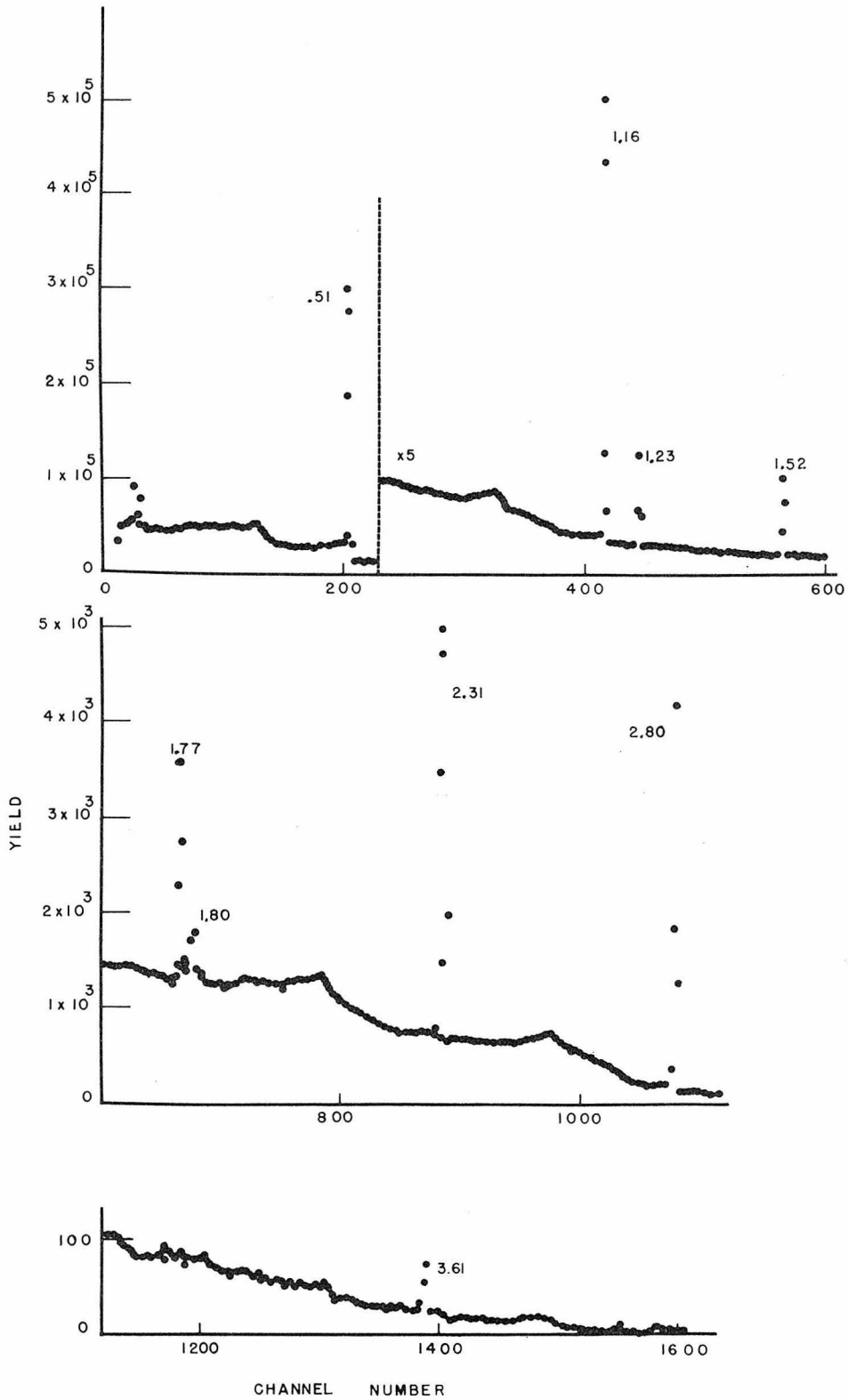
5 x 10^5
4 x 10^5
3 x 10^5
2 x 10^5
1 x 10^5
0
.51
1.16
x5
1.23
1.52
0
200
400
600
5 x 10^3
4 x 10^3
3 x 10^3
2 x 10^3
1 x 10^3
0
1.77
1.80
2.31
2.80
800
1000
YIELD
100
0
3.61
1200
1400
1600
CHANNEL NUMBER

FIGURE 20

Energy level diagram for ^{38}Ar and ^{38}K. The only levels shown are those below 3.94 MeV and those levels which could partake in allowed beta transitions from ^{38}K. Other levels have been omitted for clarity. The two beta branches shown are known from previous work. The object of this work was to find the remaining allowed branches.

(See page 62.)

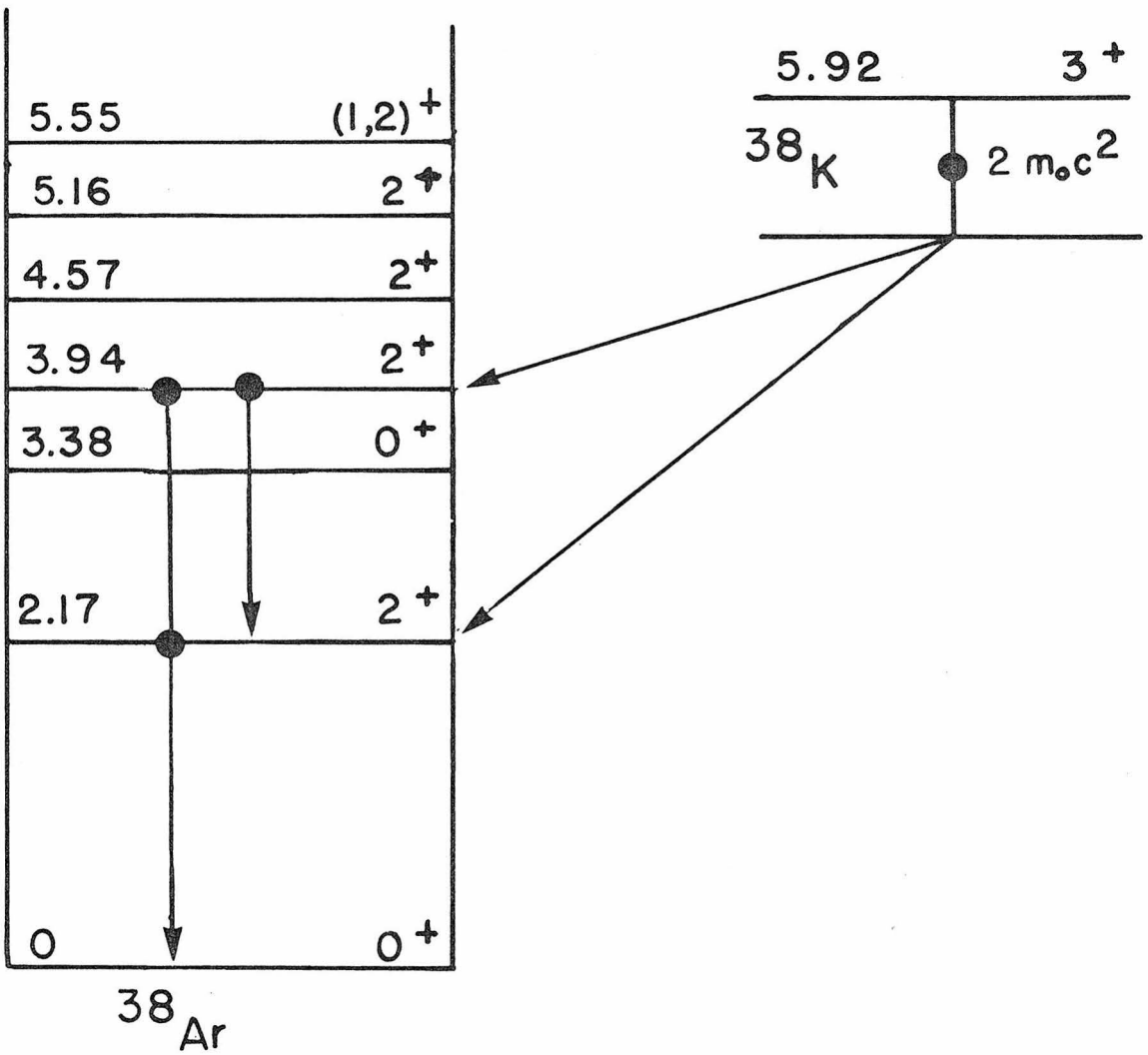
5.92
3+
38K
2 m0c2
5.55
(1,2)+
5.16
2+
4.57
2+
3.94
2+
3.38
0+
2.17
2+
0
0+
38Ar

FIGURE 21

Gamma ray spectrum following the decay of ^{38}K. This figure displays only those gamma rays following the ground state decay, as the lifetime of the isomeric state of ^{38}K is short compared to the manual transfer time taken to bring the target to the Ge(Li) detector. The two photopeaks at 2167 and 3937 keV have been previously reported. No new beta branches were inferred from these data.

(See page 64.)

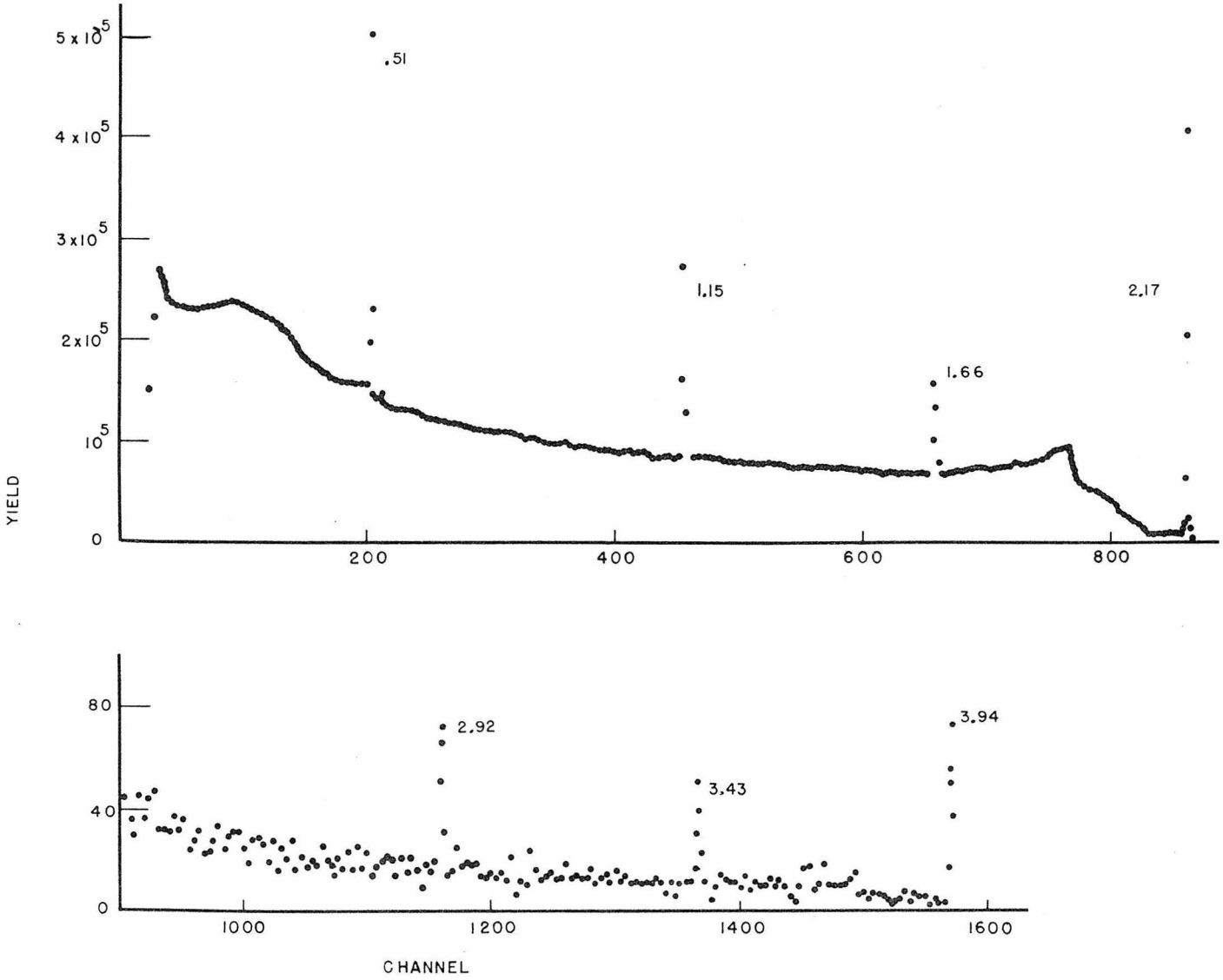
5 x 10^5
4 x 10^5
3 x 10^5
2 x 10^5
10^5
0
YIELD
.51
1.15
1.66
2.17
200
400
600
800
80
40
0
2.92
3.43
3.94
1000
1200
1400
1600
CHANNEL

FIGURE 22

Energy level diagram for ^{39}Ca and ^{39}K. All levels below 4.10 MeV are shown, although not labelled. The only levels which are labelled are those which can partake in allowed beta transitions in the decay of ^{39}Ca. The only branch known is the mirror transition to the ground state of ^{39}K.

No new branch was found in this work.

(See page 67.)

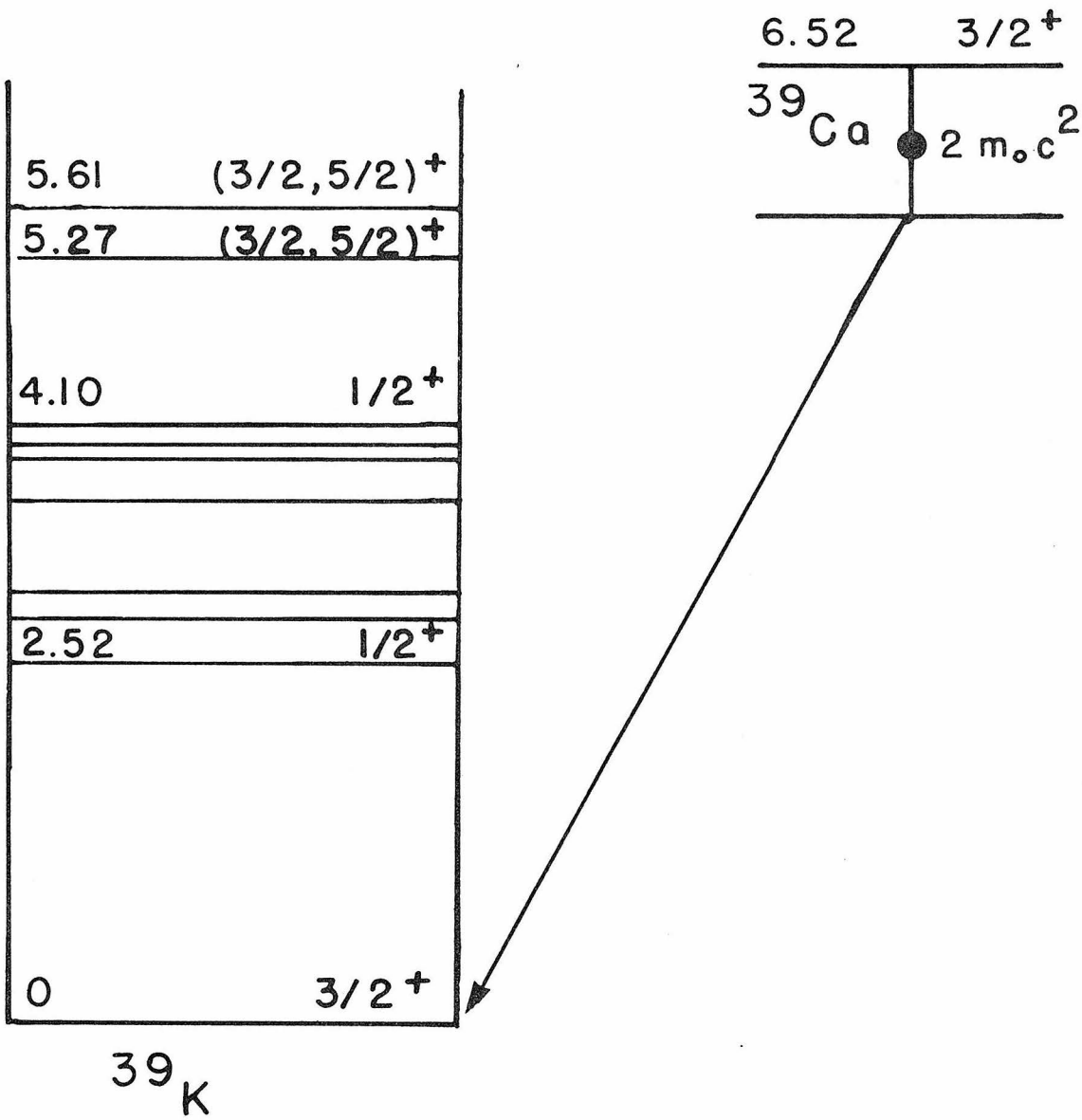
6.52 3/2+
39Ca
2 m0c2
5.61 (3/2,5/2)+
5.27 (3/2,5/2)+
4.10 1/2+
2.52 1/2+
0 3/2+
39K

FIGURE 23

Gamma ray spectrum following ^{39}Ca decay. Only the annihilation peak can be ascribed to ^{39}Ca decay. The other peaks are from background radiation and contaminant-produced radiation. Little strength is expected for the non-mirror decays because of the hole in the doubly magic ^{40}Ca core structure of ^{39}Ca.

(See page 67.)

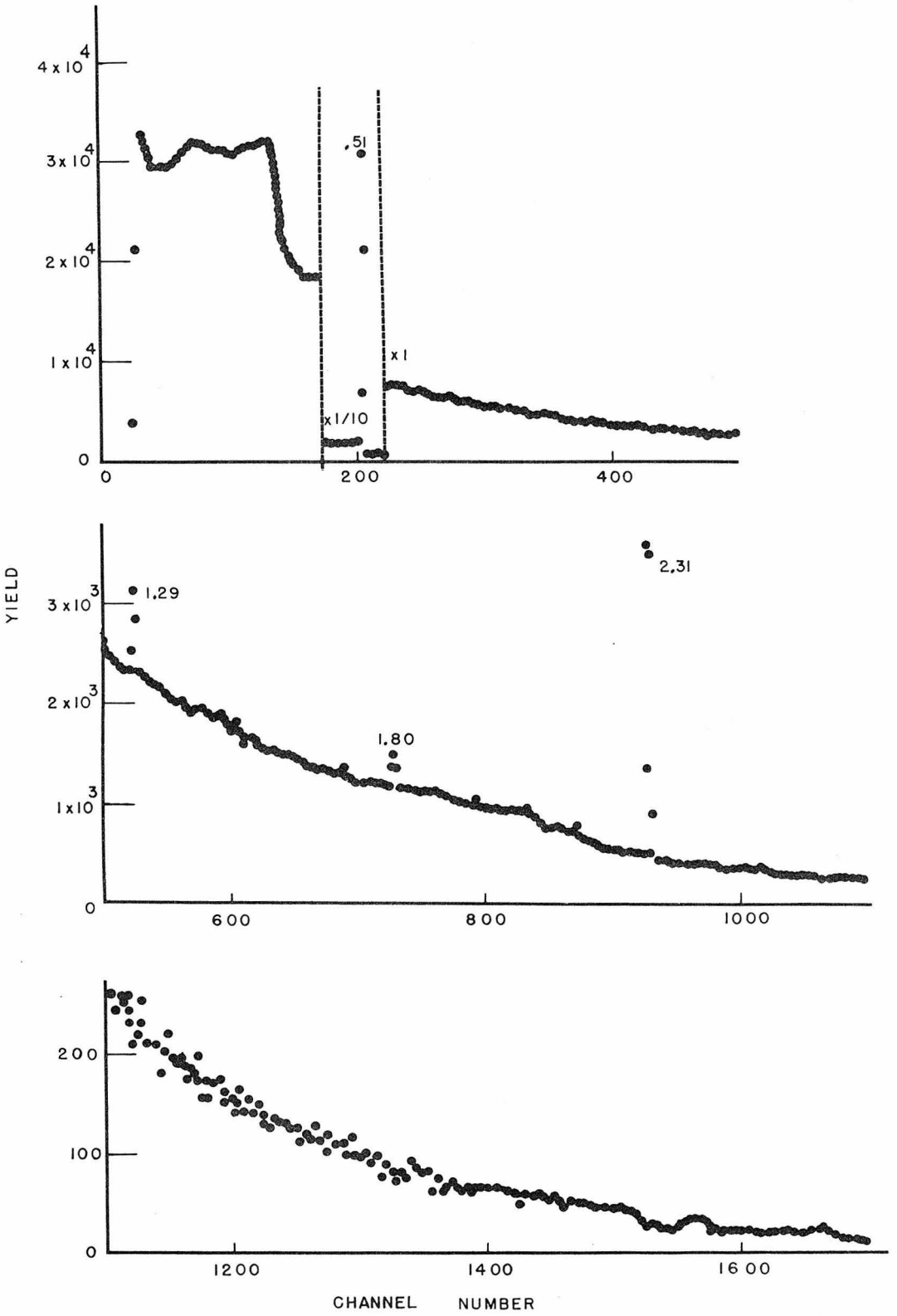
4 x 10^4
3 x 10^4
2 x 10^4
1 x 10^4
0
0
200
400
.51
x1
x1/10
YIELD
3 x 10^3
2 x 10^3
1 x 10^3
0
600
800
1000
1.29
1.80
2.31
200
100
0
1200
1400
1600
CHANNEL NUMBER

FIGURE 24

Comparison between experimental and theoretical values for log ft for the decays studied. The theoretical values are taken from the compilation of Lanford and Wildenthal (1973) and the experimental values from Tables 4, 8, 12, and 14. Values for ^{19}Ne and ^{39}Ca are not shown since they involve only mirror decays. Each decay is shown by a separate symbol as defined in the upper left corner. The abscissa, ft_{exp}/ft_{th}, is proportional to $|M_{th}|^2 / |M_{exp}|^2$ where M is the nuclear matrix element.

Except for a few decays the theoretical values agree quite well with experiment. The exceptions are the ^{27}Si decay to the 1.01 MeV state in ^{27}Al (the transition being 250 times weaker than predicted) and the ^{37}K decay to the 1.41 MeV level in ^{37}Ar (the transition being at least 3 times weaker than predicted) and the ^{37}K decay to the 1.41 MeV level in ^{37}Ar (the transition being at least 3 times weaker than predicted.) The transition to the 2.796 MeV level in ^{37}Ar from the ^{37}K is predicted to be 3 times stronger than experimentally seen, this representing the worst remaining case.

(See page 69.)

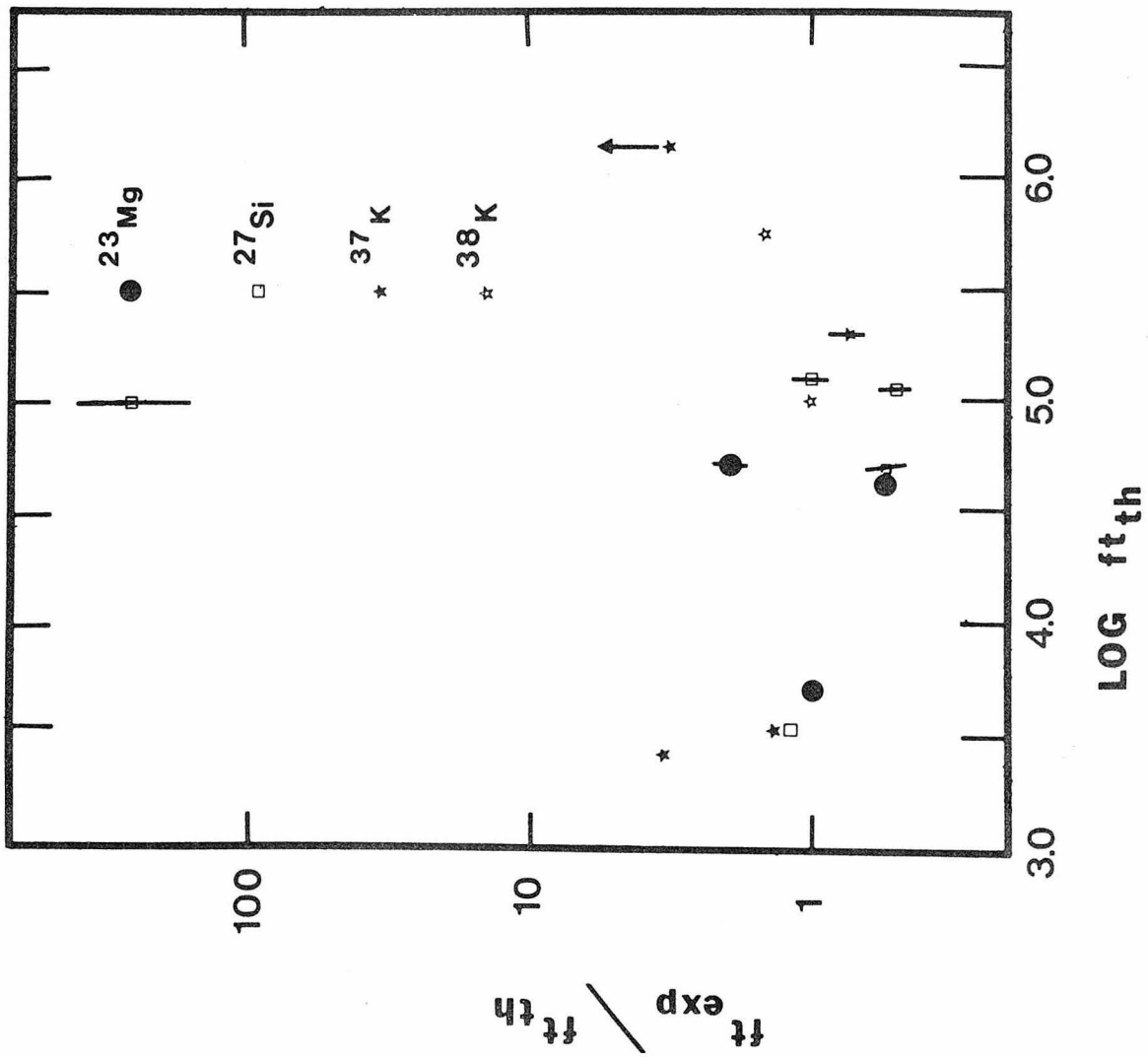
^{23}Mg
^{27}Si
^{37}K
^{38}K
100
10
1
3.0
4.0
5.0
6.0
LOG ft_{th}
ft_{exp} / ft_{th}

FIGURE 25

The front panel of the digital sequence timer. The timer is described in Appendix A.

(See page 72.)

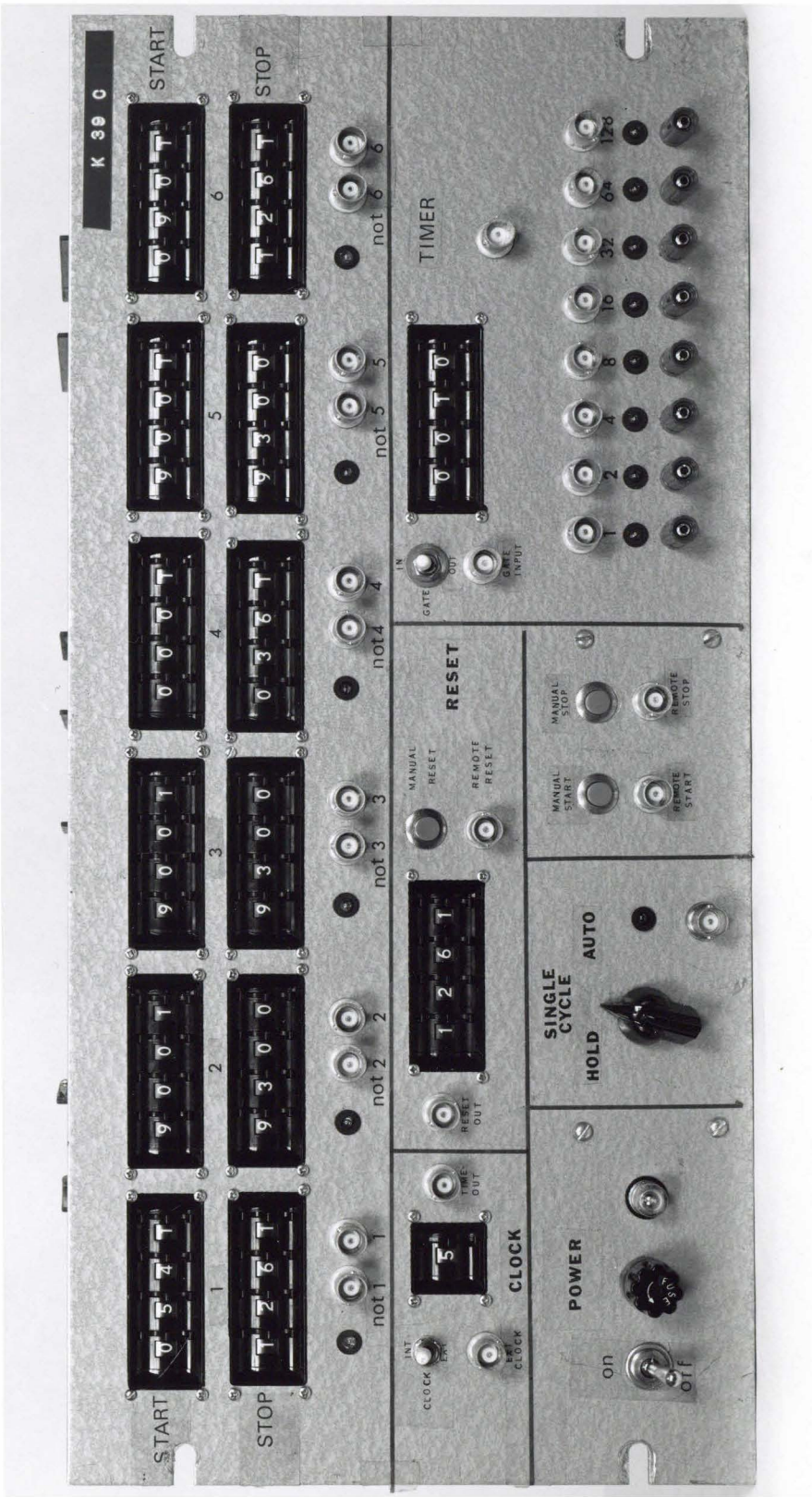
K 30 C
START
STOP
START
STOP
TIMER
RESET
CLOCK
POWER
SINGLE CYCLE
HOLD
AUTO
on
off
not 1
not 2
not 3
not 4
not 5
not 6
MANUAL RESET
REMOTE RESET
MANUAL START
REMOTE START
MANUAL STOP
REMOTE STOP
GATE
GATE INPUT
TIME OUT
RESET OUT
CLOCK
EXT CLOCK
1
2
4
8
16
32
64
128

PART II

COMPARISON OF EXPERIMENTAL REACTION CROSS SECTIONS WITH THE HAUSER-FESHBACH MODEL

I. INTRODUCTION

Not only are concepts in physics probed and checked by experimental measurements, but also the data from such measurements often prove useful to problems in other fields. The determination of nuclear reaction cross sections is an example of such measurements. The cross section data provide part of the necessary input information for calculations of stellar evolution and nucleosynthesis. Similarly, the rates of energy production from thermonuclear reactions, together with the associated radiation damage effects, rely upon such information.

Measurements at the Kellogg Radiation Laboratory have provided many of the cross sections needed for nucleosynthesis calculations, especially those concerned with hydrogen, helium, and (recently) carbon burning. Also recently a program has been started to measure cross sections which may be important in energy production using "exotic" thermonuclear reactions (i.e., reactions other than d+d or d+t).

However, the demand for cross section data is growing faster than the rate at which experimentalists can produce the needed numbers. In many cases, cross sections are wanted that cannot be readily measured in the laboratory using available techniques. For example, astrophysicists have long asked for cross sections at energies so low that it would take years, or in some cases millennia, to perform the measurement. Also, information is now required for cross sections on nuclei which decay in seconds or less. Nuclear engineers want information concerning damage and gas production rates by neutron-induced reactions occurring during fission and fusion processes, yet such information is

difficult to obtain because of the limited number of neutron beam facilities. Thus a theoretical method must be constructed to predict cross sections accurately.

This part of the thesis will describe such a theory: the statistical model of nuclear reactions. Although the model was first discussed 40 years ago by Bethe, it is only recently with the introduction of computers having large memory units and fast computational units that cross sections can be accurately and quickly predicted. Section II will describe the statistical model and examine the various concepts underlying the theory. At the end of this section, a computer coding for this model is described. Section III describes the experimental measurement of several reaction cross sections, the results of which are discussed in Section IV and compared to the predictions of the statistical model in Section V. Finally, Section VI summarizes the state of the statistical model of nuclear reactions and suggests further applications of its use.

II. THEORETICAL CONSIDERATIONS

A. Introduction

This section will present the basic theory of the statistical model of nuclear reactions and examine the various components, such as level-density parameterization and transmission coefficient calculations, which are needed if the theory is to produce numbers. At the end of this section the computer code used to perform the statistical model calculations is given.

An excellent discussion of nuclear reactions and the theories which attempt to explain them may be found in the book by Hodgson (1971), Nuclear Reactions and Nuclear Structure. The model that will be described here is often known as the Hauser-Feshbach (1952) model after the authors who first introduced angular momentum constraints into the calculation. Wolfenstein (1951) anticipated the work of Hauser and Feshbach, and occasionally the model is referred to as the Wolfenstein-Hauser-Feshbach model.

When a projectile interacts with a nucleus, either it scatters elastically or reacts. Following absorption, the projectile may quickly (in the time it takes to transverse the nucleus, $\sim 10^{-21}$ sec) interact with one or more nucleons, and these particles, as a group or individually, may leave the nucleus. However, the projectile may interact with the nucleus as a whole (with the many nucleons quickly sharing the incoming projectile's energy) and a long-lived (10^{-18} sec) state may form. This so-called compound-nucleus state then decays into one of many possible channels. The two processes, direct and compound,

are obviously extreme cases. Often, however, a nuclear reaction can be considered as proceeding by one mechanism or the other.

Direct reactions depend strongly on the nature of the initial and final wavefunctions. These may vary considerably from nucleus to nucleus because of shell effects and nuclear deformations. At low energies compound nuclear reactions are also unpredictable because of the presence of resonances whose properties vary in energy and from nucleus to nucleus. However, at moderate energies the resonances overlap and a statistical analysis can be applied to the nuclear properties. Experimental evidence shows that compound-nucleus formation usually predominates at low and moderate energies (up to $\sim$15 MeV for nucleon-induced reactions), and direct reactions are more important at high energies. However, the possibility of significant direct reaction contributions at low energies must be considered in many cases.

B. Statistical Model of Nuclear Reactions

1. Elementary Approach

In its most elementary form, the statistical model involves three assumptions:

1. That all matrices describing the reactions are unitary. This follows from the conservation of flux. It is also assumed that direct reactions play a negligible role in the reaction.
2. That time-reversal invariance holds. Only for the weak interaction does evidence exist which contradicts this assumption, but weak interactions play no role in the theory.

3. That within the energy averaging interval there exist enough states of the proper spin and parity that a statistical treatment will be valid.

The third assumption is the most tenuous; however, it forms the basis of the theory. Such a statistical approach to the decay of the compound nucleus state is analogous to Bohr's (1936) hypothesis that the compound nucleus decays independently of its formation (amnesia assumption). In later parts of this section, modifications of the third assumption will lead to slightly different results from those derived immediately below.

In the treatment of Friedman and Weisskopf (1955), the scattering cross section $\sigma_{\alpha\beta}$ from entrance channel α to exit channel β is expressed in terms of the U (or collision) matrix as

$$\sigma_{\alpha\beta} = \frac{\pi \lambda\!\!\!^{-2}_{\alpha}}{(2I_{\alpha_1}+1)(2I_{\alpha_2}+1)} \sum_{J^\pi} (2J+1) \left|\delta_{\alpha\beta} - U_{\alpha\beta}\right|^2 \qquad (1)$$

where $\lambda\!\!\!^{-}_{\alpha}$ is the reduced wavelength ($\hbar$ divided by the center of mass momentum of the incident projectile), J^π is the spin and parity of the compound nucleus state, and I_{α_i} is the spin of particle i in the entrance channel. The presence of resonances will cause strong fluctuations in the cross section as the energy is varied. Thus the collision matrix is represented as the sum of an average part $\overline{U}$ which does not vary with energy over the energy average interval and a fluctuating part $\tilde{U}$ which may vary appreciably with energy but which is assumed to average to zero over the averaging interval; thus

$$U_{\alpha\beta} = \overline{U}_{\alpha\beta} + \tilde{U}_{\alpha\beta} \tag{2}$$

with

$$\overline{U}_{\alpha\beta} = \langle U_{\alpha\beta} \rangle = \text{constant} \tag{3}$$

and

$$\langle \tilde{U}_{\alpha\beta} \rangle = 0 \tag{4}$$

After averaging over the energy interval, equation 1 becomes

$$\sigma_{\alpha\beta}^{J^\pi} = \frac{\pi \lambda_\alpha^2 (2J+1)}{(2I_{\alpha_1}+1)(2I_{\alpha_2}+1)} \{ |\delta_{\alpha\beta} - \overline{U}_{\alpha\beta}|^2 + \langle |\tilde{U}_{\alpha\beta}|^2 \rangle \} \tag{5}$$

The first term, $|\delta_{\alpha\beta} - \overline{U}_{\alpha\beta}|^2$, corresponds to direct reactions and is usually neglected in this theory. If the direct reaction component is known, however, it can be added to the compound nuclear component corresponding to the second term $\langle |\tilde{U}_{\alpha\beta}|^2 \rangle$. There is no interference term since the fluctuating part $\tilde{U}_{\alpha\beta}$ of the collision matrix is assumed to average to zero.

By hypothesis, the compound-nucleus decay is independent of the mode of formation, which implies that the cross section for the reaction can be written as a product of two factors,

$$\sigma_{\alpha\beta} = \sum_{J^\pi} \sigma_\alpha^{CN}(J^\pi) \cdot P_\beta(J^\pi) \tag{6}$$

where $\sigma_\alpha^{CN}(J^\pi)$ is the cross section for producing the compound nucleus having spin J and parity π and where $P_\beta(J^\pi)$ is the probability that the compound nucleus will decay into channel β. The summation over spin and parity is necessary since the compound nucleus must obey

the conservation laws of angular momentum and of reflection (as well as energy). The cross section for forming the compound nucleus (noting that $\Sigma_\beta P_\beta(J^\pi) = 1$ for each J^π) is just

$$\sigma_\alpha^{CN} = \sum_\beta \sigma_{\alpha\beta} = \frac{\lambda_\alpha^2 (2J+1)}{(2I_{\alpha_1}+1)(2I_{\alpha_2}+1)} \sum_\beta \langle |\tilde{U}_{\alpha\beta}|^2 \rangle \tag{7}$$

By using the unitarity assumption,

$$\langle \sum_\beta U_{\alpha\beta} U_{\alpha\beta}^* \rangle = 1 = \langle \sum_\alpha (\bar{U}_{\alpha\beta} + \tilde{U}_{\alpha\beta})(\bar{U}_{\alpha\beta}^* + \tilde{U}_{\alpha\beta}^*) \rangle \tag{8}$$

and noting that equation 4 implies that the sum over $\tilde{U}_{\alpha\beta}$ is zero, the cross section for compound nucleus formation can be written as

$$\sigma_\alpha^{CN} = \frac{\pi \lambda^2 \sum_{J^\pi} (2J+1)(1 - \sum_\beta |\bar{U}_{\alpha\beta}|^2)}{(2I_{\alpha_1}+1)(2I_{\alpha_2}+1)} \tag{9}$$

It should be noted that the direct reaction matrix element $(U_{\alpha\beta})$ predicts the cross section for the formation of the compound nucleus. The transmission coefficient T

$$T_\alpha = 1 - \sum_\beta |\bar{U}_{\alpha\beta}|^2 \tag{10}$$

expresses the loss of flux. Thus the formation cross section for the compound nucleus can be written as

$$\sigma_\alpha^{CN} = \frac{\pi \lambda^2 \sum_{J^\pi} (2J+1)\, T_\alpha}{(2I_{\alpha_1}+1)(2I_{\alpha_2}+1)} \tag{11}$$

To find the probability P_β that the compound nucleus will decay into channel β, time reversal symmetry is invoked for each spin and

parity,

$$\sigma_{\alpha\beta}^{(J^\pi)} = \sigma_{\hat{\alpha}\hat{\beta}}^{(J^\pi)} \tag{12}$$

where the circumflex over the letter implies the time-reversed state. Rewriting equation 12, we obtain

$$T_\alpha P_\beta = T_{\hat{\beta}} P_{\hat{\alpha}} \tag{13}$$

But this is true for all channels so

$$\frac{P_{\hat{\alpha}}}{T_\alpha} = \frac{P_\beta}{T_{\hat{\beta}}} = \text{constant} \equiv \lambda \tag{14}$$

But

$$\sum_{\hat{\alpha}} P_{\hat{\alpha}} = 1 = \lambda \sum_{\alpha} T_\alpha \tag{15}$$

implying

$$P_\beta = \lambda T_{\hat{\beta}} = T_{\hat{\beta}} / \Sigma_\gamma T_\gamma \tag{16}$$

where the sum over γ is a sum of all channels to which the compound nucleus may decay. Combining equations 11 and 16, the cross section for the reaction $\alpha \to \beta$ is

$$\sigma_{\alpha\beta} = \frac{\pi \lambda_\alpha^2}{(2I_{\alpha_1}+1)(2I_{\alpha_2}+1)} \sum_J \pi (2J+1) \frac{T_\alpha T_{\hat{\beta}}}{\Sigma_\gamma T_\gamma} \tag{17}$$

The circumflex over β is usually not explicitly included although it is indeed the transmission coefficients for the time-reversed channel that are needed.

Thus to calculate the reaction cross section (neglecting direct reaction contributions or including them separately) one must first

calculate the transmission coefficients and do the proper sums. As can be seen from equation 10, the transmission coefficients are obtained from the direct collision matrix elements for elastic scattering. It should be remembered that the elastic scattering process consists of the direct process ($\overline{U}$) and the compound ($\tilde{U}$). Thus when transmission coefficients are obtained, the effect of compound elastic scattering must be calculated if the true value for T_ℓ is to be obtained.

C. Improvements to the Elementary Theory

1. Initial Comments

As noted above, the most tenuous assumption in the statistical model is the assumption that the compound nucleus forgets how it was formed. If the number of states in the compound nucleus is not sufficient then nuclear properties may play a dominant role. This can be clearly seen if the above derivation is carried out using explicit states in the compound nucleus as was first done by Bethe (1937). Depending upon the formalism used, energy averages over the states in the compound nucleus are taken, but the form of the scattering matrix is very reminiscent of summations over Breit-Wigner (1936) forms,

$$S^{J^\pi} \sim \pi \left(\frac{\Gamma_\alpha^{J^\pi}}{E - E_\gamma + i\Gamma^{J^\pi}/2} \right) \tag{18}$$

where $\Gamma_\alpha^{J^\pi}$ is the partial width of the compound state γ having spin and parity J^π for decay into channel α, E_γ is the energy of state γ, and Γ^{J^π} is the sum of $\Gamma_\alpha^{J\pi}$. If equation 18 is now averaged over

an energy interval, the cross section becomes

$$\sigma_{\alpha\beta} = \frac{\pi\lambda\!\!\!^{-2}_{\alpha}}{(2I_{\alpha_1}+1)(2I_{\alpha_2}+1)} \sum_{J^\pi} (2J+1) \frac{2\pi}{D_{J^\pi}} < \frac{\Gamma_\alpha \Gamma_\beta}{\Gamma} >_{J^\pi} \qquad (19)$$

where D_{J^π} is the mean spacing between states in the compound nucleus having spin and parity J^π and the energy average is done for each J^π. In order to obtain an equation similar to equation 17, one assumes that

$$< \frac{\Gamma_\alpha \Gamma_\beta}{\Gamma} > = \frac{<\Gamma_\alpha> <\Gamma_\beta>}{<\Gamma>} \qquad (20)$$

and notes that for small values of Γ/D, most models give (Moldauer 1967, 1968 and 1969)

$$T = 2\pi \frac{\Gamma}{D} \qquad (21)$$

Using equations 18, 19, 20, and 21, one obtains equation 17, the expression normally used to calculate compound nuclear cross sections when averaging over many resonances (or compound nuclear states).

In most applications, the correlations between widths are neglected (i.e., equation 20 is assumed to be valid) and the relationship (equation 21) between T and Γ/D is assumed to hold for all values of Γ/D. If a justification is attempted, an appeal is made that there are enough levels so that the properties of any particular level are averaged out and that any second-order terms in the determination of T are unimportant. Any shortcomings in the theoretical predictions can usually be attributed to the presence of a significant direct-reaction component or the uncertainty in the parameters of the

calculation.

2. Work of Moldauer

The statistical model of nuclear reactions has received careful scrutiny in recent years by Moldauer, who in 1964 published a detailed consideration of the model.

Instead of assuming equality in equation 20, Moldauer introduced $W_{\alpha\beta}$, the width fluctuation correction,

$$W_{\alpha\beta} = \langle \frac{\Gamma_\alpha \Gamma_\beta}{\Gamma} \rangle / \frac{\langle \Gamma_\alpha \rangle \langle \Gamma_\beta \rangle}{\langle \Gamma \rangle} \tag{22}$$

This correction can be calculated once a distribution for the widths of the levels in the compound nucleus is determined. Since for most reactions the excitation energy of the compound nucleus is quite high (greater than 10 MeV), the levels in the compound nucleus may be imagined to be superpositions of very complicated configurations. The amplitude γ of a level is thus the sum of a large number of random variables, both positive and negative. Thus using the theory of errors, the distribution of γ is a Gaussian distribution,

$$P(\gamma)\, d\gamma = \frac{1}{\sqrt{2\pi}} \frac{1}{\sqrt{\langle \gamma^2 \rangle}} \exp\left(- \frac{\gamma^2}{2\langle \gamma^2 \rangle}\right) d\gamma \tag{23}$$

The amplitudes are related to widths by

$$\Gamma = 2P\gamma^2 \tag{24}$$

where P is the penetrability. Defining $x = \Gamma/\langle \Gamma \rangle$ equation 23 becomes a Porter-Thomas (1956) distribution,

$$P(x)\,dx = \frac{x/2}{(\frac{x}{2} - 1)!} \tag{25}$$

It should be noted that Rohr and Frieland (1967) have shown that the Porter-Thomas distribution describes the low energy neutron resonances for ^{52}Mn quite well. As the total width Γ is the sum of the partial widths, its distribution is that of the sum of the squares of n quantities (n being the number of partial widths), the factorial distribution for $(n/2)x$,

$$P_n(x)dx = \frac{1}{(\frac{x}{2} - 1)!}\ (\tfrac{1}{2} nx)^{\frac{n}{2}-1}\ e^{-\frac{n}{2}x}\ \tfrac{n}{2}\,dx \tag{26}$$

Substituting this result into equation 22, the width fluctuation correction becomes

$$W_{\alpha\beta} = (1 + 2\delta_{\alpha\beta}) \int_0^\infty (1 + \frac{2x\ T_\alpha}{\Sigma T_c})^{-1}\ (1 + \frac{2x\ T_\beta}{\Sigma T_c})^{-1}$$

$$* \prod_i (1 + \frac{2x\ T_i}{\Sigma T_c})^{-1/2}\ dx \tag{27}$$

Equation 27 assumes that $T = 2\pi\Gamma/D$ for all values of Γ/D . The integral of equation 27 can be evaluated analytically only for $j \leq 2$. If $\alpha \neq \beta$ then $W_{\alpha\beta}$ is always less than unity. As noted by Satchler (1963) since the total cross section must remain the same, $W_{\alpha\alpha}$ is greater than unity. As the number of available channels increases $W_{\alpha\beta}$ becomes independent of the entrance and exit channels and approaches unity.

Moldauer has also considered the relationship between the transmission coefficient and Γ/D (equation 21). He concludes (1967, 1968 and 1969) that

$$T = 1 - \exp(2\pi\Gamma/D) \qquad (28)$$

However, Shaw et al (1969) (considering $^{27}Al(p,\alpha)^{24}Mg$) show that if the standard expression for the cross section is used (equation 17), the agreement is better than if transmission coefficients of the form of equation 28 are used, even though Γ/D is large. As Shaw et al point out, Γ may not be related to any physically observable quantity. Hence at high energies, the question may not be whether Γ/D is small enough for the theory to successfully predict cross sections, but rather if the contributions from direct processes which are ignored in the treatment are significant.

A final note of caution should be added concerning the corrections ($W_{\alpha\beta}$ and T dependence on Γ/D) introduced by Moldauer. Any cross section calculated using the statistical theory of nuclear reactions is very dependent upon the parameters used to determine the transmission coefficients. These coefficients are derived from elastic-scattering experiments after the compound-nuclear contribution has been subtracted. If one uses the Moldauer corrections, then to be consistent one should include those corrections when the transmission coefficients are determined. This is rarely done.

3. Work of Weidenmuller

Engelbrecht and Weidenmuller (1973) have shown that using general properties of the S-matrix such as analyticity and unitarity, equation

17 (the defining equation for the statistical model) can be consistently derived from a pole expansion of the S-matrix only when all the transmission coefficients are small. But as noted above, equation 17 or its modification by Moldauer continues to be used. Tepel, Hoffmann, and Weidenmuller (1974) attempt to justify such use by computing cross sections numerically from a random-matrix model which ignores any direct reaction contributions. It should be stressed that their approach is a Monte-Carlo calculation and not an analytic derivation. They find that the Bohr assumption of independence of the decay of the compound nucleus is borne out for the inelastic channels, while a width fluctuation correction W_α must be applied for the elastic channel. They find that the width fluctuation correction depends only on the one channel,

$$W_\alpha = 2/(1 + T_\alpha^{1/2}) \tag{29}$$

The transmission coefficients are slightly modified,

$$T_{\alpha,J} \rightarrow \mathcal{T}_{\alpha,J} = T_{\alpha,J}[1 + T_{\alpha J} W_J / \Sigma_c T_{cJ}] \tag{30}$$

but they note that the form of the predicted cross section is similar to the classical expression

$$\sigma_{\alpha\beta} = \frac{\pi \lambda_\alpha^2 \sum_{J\pi}(2J+1)}{(2I_{\alpha_1}+1)(2I_{\alpha_2}+1)} \frac{\mathcal{T}_\alpha \mathcal{T}_\beta}{\Sigma \mathcal{T}_c} (1 + \delta_{\alpha\beta} W_\alpha) \tag{31}$$

In the limit of many competing channels, the modification to the transmission coefficients goes to zero and the classical expression is obtained. Tepel, Hoffmann, and Weidenmuller note that their formalism fits their numerical "experimental" data better than the

formalism of Moldauer. There has been too little time since publication for experiments to check whether the formalism of Tepel et al is more effective. However, it is much simpler to use than the modifications of Moldauer and may prove successful.

D. Level-Density Parameterization

1. Initial Comments

For any given reaction it is usually possible to populate many different states in the residual nuclei. Unfortunately, only a small number of these are of known energy, spin, and parity. Somehow the remaining levels have to be included in the calculation. For low-energy bombardment the dependence on such a parameterization is usually small since the residual states have known properties. However, at higher incident energies the need to invoke some general formalism to represent the level distribution can result in considerable uncertainty in the cross section calculation.

2. Spin Dependence

Not only is the number of levels per MeV needed, but also the distribution as a function of spin and parity must be known. Following the treatment of Bethe (1936,1937), the spin J of a level (as also its z component M) is conceived as being composed of the initial angular momenta j_i (z component m_i) of the constituent particles of which n are excited. It is further assumed that for each j_i, m_i may have any value between $-j_i$ and j_i with equal probability and that the density of states can be factored into two terms,

$$\rho(E^*,M) = P(M)\,\rho(E^*) \tag{32}$$

where $P(M)$ depends only weakly (if at all) on the excitation energy E^*. Since the number of states having a net spin J is the difference between those states where $M = J$ and those where $M = J+1$, then the density of states becomes

$$\rho(E^*,J) = \rho(E^*)\,[P(M=J) - P(M=J+1)] \tag{33}$$

or

$$\rho(E^*,J) = \left.\frac{d\rho}{dM}\right|_{M=J+1} \rho(E^*) \tag{34}$$

since it is expected that $P(M)$ varies slowly with M. To evaluate the derivative, the functional dependence of $P(M)$ must be known. It is assumed that $P(M)$ has a normal distribution (which is plausible when many of the individual constituent nucleons are excited),

$$P(M) = \frac{1}{(2\pi\sigma^2)^{1/2}} \exp(-M^2/2\sigma^2) \tag{35}$$

The variance σ^2 (known as the spin cutoff parameter) can be calculated from the value of $\langle m_i \rangle^2$ if some model for the nuclear structure (such as the shell model) is assumed,

$$\sigma^2 = n\ \langle m_i \rangle^2 \tag{36}$$

Jensen and Luttinger (1952) have shown that $\langle m_i \rangle^2$ is proportional to $A^{2/3}$ by considering the succession of states in the shell model. The number of excited nucleons (n) is usually obtained by considering the

nucleus as a Fermi gas (see subsection 3), where n becomes proportional to $(E^*)^{1/2} A$. The constant of proportionality depends upon which paper is consulted. Although the parameters in the level density formula, $\rho(E^*)$, are determined by experiments which normally do not determine the spin dependence, inconsistencies can result if σ^2 and the level density parameters are inferred from separate investigations. By substituting equation 35 into equation 34, one obtains

$$\rho(E^*,J) = \frac{(2J+1)}{(8\pi)^{1/2}\ \sigma^3}\ \exp[-\frac{(J+1)^2}{2\sigma^2}]\ \rho(E^*) \qquad (37)$$

Although equation 37 is expected to hold at high excitation energies where many configurations enter into each level, significant deviations can occur at low excitation energies. Firstly, the spins and parities of low-lying levels will be largely determined by the shells near the valence nucleons. Particularly, the numbers of even and odd parity states are usually unequal. Secondly, rotational bands will be built on the lowest-lying states. Neither effect is included in equation 37.

3. Energy Dependence

Most treatments of level density follow the work of Bethe (1936, 1937). The treatment given below assumes certain standard relations from statistical mechanics; for their derivation and justification, see a text on statistical mechanics such as ter Haar (1954).

A grand canonical ensemble is used to represent the nucleons inside the nucleus,

$$n(\alpha,\beta,\theta) = \sum_N \sum_Z \sum_k \gamma_k \exp(\alpha Z + \beta N - \theta k) \tag{38}$$

where γ_k is the multiplicity of the nuclear energy level E_k ; Z is the proton number; N the neutron number; α , β , and θ are Lagrange multipliers. θ will, of course, turn out to be $1/kT$ where k is the Boltzmann factor and T the nuclear "temperature". Replacing the sums by integrals and introducing the level density $\rho(E,Z,N)$, $n(\alpha,\beta,\theta)$ can be written as

$$n(\alpha,\beta,\theta) = \int dZ \int dN \int dE\ \rho(E,Z,N) \exp(\alpha Z + \beta N - \theta E) \tag{39}$$

Since the integrand is assumed to be sharply peaked, the method of steepest descents can be used to approximate n ,

$$n(\alpha,\beta,\theta) \cong \rho(E,Z,N) \exp(\alpha Z + \beta N - \theta E)\left[-\frac{\pi^3}{8} \frac{\partial Z}{\partial \alpha} \frac{\partial N}{\partial \beta} \frac{\partial E}{\partial \theta}\right]^{1/2} \tag{40}$$

Moreover, the entropy S is related to the grand partition function n by

$$S/k = \ell n\ n(\alpha,\beta,\theta) - \alpha Z - \beta N + \theta E \tag{41}$$

Thus the density of states can be written as

$$\rho(E,Z,N) = e^{S/k}\left[-\frac{\pi^3}{8} \frac{\partial Z}{\partial \alpha} \frac{\partial N}{\partial \beta} \frac{\partial E}{\partial \theta}\right]^{-1/2} \tag{42}$$

The level density can thus be found if some model for the nucleus is assumed by calculating the entropy S and the needed derivatives. Ter Haar gives three examples: the non-interacting particle model, the independent particle model, and the fluid drop model. Only

the first case will be included here, as the non-interacting particle model is the model normally used for calculating nuclear level densities. For a detailed derivation of this case, see the appendices in Gilbert and Cameron (1965a).

The nucleus is considered as a highly degenerate Fermi gas of two components, protons and neutrons. The number of "proton" (or "neutron") levels in this gas is

$$Z \sim \alpha(kT)^{3/2} = \alpha\theta^{-3/2} \tag{43}$$

The relationship between the excitation energy, U , and the nuclear temperature is

$$U = E - \Delta = a(kT)^2 \tag{44}$$

where Δ represents, in some sense, the zero point energy and not necessarily the ground state energy.

Thus using the relationship among energy, temperature, and entropy,

$$S/k = \int \frac{dE}{d\theta}\,\theta\,d\theta = \int \frac{dE}{dkT}\,\frac{dkT}{kT} \tag{45}$$

the entropy becomes

$$S/k = 2(aU)^{1/2} \tag{46}$$

Using equations 42, 43, 44 and 46, the density of states is thus proportional to

$$\rho(E) \propto U^{-5/4}\,\exp[2(aU)^{1/2}] \tag{47}$$

If the proper normalization is included and the density of spins from equation 37 is inserted, then the most commonly used expression for the

density of states as a function of energy, spin, and parity is obtained,

$$\rho(E,J) = \frac{2J+1}{24\sqrt{2}\,\sigma^3\, a^{1/4}} \quad \frac{\exp[2(aU)^{1/2} - J(J+1)/(2\sigma^2)]}{U^{5/4}} \qquad (48)$$

Different models will give different energy dependences. However, practically all efforts to determine empirically the nuclear-level density have used equation 48.

Currently three parameterizations for the parameters a, E_o, and σ^2 are in vogue: Gilbert and Cameron (1965a), Facchini and Saetta-Menichella (1968), and Dilg, Schantl, Vonach, and Uhl (1973). The early parameterization of Newton (1956) has fallen out of use, as it was based on very early experimental data. The parameterization of Vonach and Hille (1969) has been superseded by the more recent work of Dilg et al for $A \geq 40$.

All the workers find that for the best fits to experimental data the effective excitation energy U (as defined in equation 44) does not correspond to the actual excitation energy but must be shifted. Each parameterization uses data from s-wave neutron resonances and, in some cases, low energy proton resonances. (None of the parameterizations attempts to fit experimentally known levels, even though information for some nuclei seems complete to energies greater than the resonance information used.) After obtaining fits to as many nuclei as possible, the parameters were smoothed and were themselves fitted by a simple expression. The work of the three most-cited parameterizations will be discussed next.

4. Gilbert and Cameron (1965a)

Gilbert, Chen, and Cameron (1965b) found that for excitation energies up to about 10 MeV for light nuclei ($Z \leq 30$) the level density

$$\rho(E) = \frac{1}{T} \exp[(E - E_0)/T] \tag{49}$$

fitted the data well, where E_0 and T are parameters independent of energy. Since T does not depend upon the excitation energy, this level density is known as the constant-temperature formula. From the data in Huizenga and Katsanos (1967) for nuclei in the iron region, the constant temperature formula does indeed do well for low excitation energy. Thus Gilbert and Cameron use equation 49 for low excitation energies and equation 48 at high excitation energies. The matching energy E_x is chosen so that two level densities merge smoothly into each other. The shift of the effective excitation energy is taken to be due to pairing effects. Gilbert and Cameron use the pairing corrections of Cameron and Elkin (1965) and define Δ as

$$\Delta = PZ(Z) + PN(N) \tag{50}$$

where the pairing energies P were determined by fitting the ground state masses with a liquid drop formula and requiring $PZ(\text{odd } Z) = PN(\text{odd } N) = 0$. The parameter σ^2 is taken from Jensen and Luttinger (1952)

$$\sigma^2 = 0.0888\ akT\ A^{2/3} \tag{51}$$

Using equation 48, the values of Δ_0 and σ^2 as given in equations 50 and 51, and experimental data near the neutron separation energy, the level-density parameter a is determined. Then by requiring a smooth

transition into equation 48, the parameters E_o , T , and E_x were determined. They find that

$$a = (0.142 + W)\ A \quad MeV^{-1} \tag{52}$$

$$E_x = 2.5 + 150/A + PZ(Z) + PN(N) \quad MeV \tag{53}$$

$$T = (a/X)^{1/2} - 1.5/X \quad MeV \tag{54}$$

$$E_o = E_x - T\ \ell n(TY) \quad MeV \tag{55}$$

where W is a small correction due to shell effects, $X = 2.5 + 150/A = E_x - PZ(Z) - PN(N)$, and Y is from equation 48 evaluated at E_x . It should be noted that a different set of expressions for the parameters is given if the nucleus is deformed. Neglecting the shell corrections and only considering undeformed nuclei, the spin cutoff parameter becomes

$$\sigma^2 = 0.0126\ kT\ A^{5/3} \tag{56}$$

5. Facchini and Saetta-Menichella (1968)

Facchini and Saetta-Menichella use only the Fermi gas formula of equation 48. They adopt the shift (Δ) in excitation energy proposed by Gilbert and Cameron (equation 49) but use a different value for the spin cutoff parameter. Citing the work of Lang (1966), they use

$$\sigma^2 = 0.143a\ kT\ \ A^{2/3} \tag{57}$$

Having fitted the experimental data, Facchini and Saetta-Menichella find

$$a = 0.133A \quad MeV^{-1} \tag{58}$$

and hence

$$\sigma^2 = 0.0290 \text{ kT } A^{5/3} \tag{59}$$

6. Back-Shifted Fermi Gas Formula

As noted above, an effective excitation energy must be used in the calculation of level densities. Gilbert and Cameron (and others using their shift functions) obtain their shift functions from knowledge of the ground state masses. However, as pointed out by Gadioli and Zetta (1968), the ground state has no such importance; rather the shift functions should be determined by the observed level densities. Thus one obtains shift functions which are shifted downward (or "back-shifted") from previous parameterizations.

Dilg et al (1973) use equation 48, the conventional Fermi gas formula, but treat both a and Δ as free parameters. Dilg et al follow the work of Lang and LeCouteur (1954) who define the effective excitation energy in terms of the nuclear temperature as

$$U = a(kT)^2 + kT \tag{60}$$

instead of the expression shown in equation 44. In practice this difference has little effect in the calculated-level densities but does slightly change the value of the parameters. Dilg et al use a spin cutoff parameter based upon the moment of inertia rather than on the shell model,

$$\sigma^2 = kT\ I/\hbar^2 = 0.0150\ A^{5/3}\ (kT) \tag{61}$$

This value lies between the values of Gilbert and Cameron and of Facchini and Saetta-Menichella. After fitting available experimental data (s-wave neutron resonances and level counting at low energy), Dilg et al obtain for the smooth behavior of their parameters for $40 \leq A \leq 63$,

$$a = 2.40 + 0.067\,A \ \text{MeV}^{-1} \tag{62}$$

$$\Delta = -130/A + P \ \text{MeV} \tag{63}$$

where P is the pairing correction, taken from Kümmel et al (1966)

$$\begin{aligned} P(\text{even-even}) &= 2q\,A^{-1/2} \\ P(\text{even-odd}) &= q\,A^{-1/2} \\ P(\text{odd-odd}) &= p\,A^{-1} \end{aligned} \qquad \begin{aligned} q &= 12.8 \ \text{MeV} \\ p &= 29.4 \ \text{MeV} \end{aligned} \tag{64}$$

7. Comparison with Experiment

There are very few experimental data concerning level densities other than level counting at low energies, proton resonances, and neutron resonances. However, recently much work has been performed for nuclei around $A = 60$. The level densities have been determined from fluctuation widths in the cross sections (Katsanos et al 1970, Kopsch and Cierjacks 1972, and Huizenga et al 1969); high resolution elastic scattering (Lindstrom et al 1971, and Browne et al 1970); and compound nucleus cross sections (Lu et al 1972a). These measurements all tend to support the back-shifted Fermi gas formula. The actual values for the parameters a and Δ differ slightly, but the calculated level densities closely approximate the experimentally derived

level densities. Also Lu et al (1972b) have found that the spin cutoff parameter is nearly the value used by Dilg et al,

$$\sigma^2 = (0.014 \pm 0.001)\ A^{5/3}\ (kT) \qquad (65)$$

E. Calculation of Transmission Coefficients

1. Introduction

The transmission coefficients, T_ℓ , could if sufficient data existed be obtained from elastic scattering data as described in Section B. However, this would have to be done for each energy desired and is impossible when transmission coefficients are for unstable nuclei.

An alternative is to use a potential which can generate the transmission coefficients through the solution of the Schrödinger equation. Several problems arise from this approach. The Schrödinger equation for a projectile on a target is a many-body problem and the potential between nucleons is not entirely understood. Instead of using this many-body approach, a potential of few variables (and in most cases only one variable) is used to generate the transmission coefficients. Normally these potentials have parameters which are adjusted to optimize the agreement between theory and experiment.

Such a potential may be based upon the shell model which is generally able to account for positions of bound states in nuclei. However, as shown by Bethe (1935) such a potential cannot account for non-elastic cross sections. Serber (1947), in analogy with scattering and absorption of light through a cloudy crystal ball, proposed a model

which used a complex potential to generate a complex index of refraction. This and succeeding models which use complex potentials have been known as optical models. Fernbach et al (1949) use the theory to explain scattering and absorption of 90 MeV neutrons.

Many attempts have been made to justify the optical model. Feshbach (1958) has provided an account which is too long to include here. Starting with a potential between nucleons (but neglecting antisymmetrization) Feshbach demonstrated that the nucleon-nucleus potential has a complex, energy-dependent, and non-local character. Although the potential can be calculated given the nucleon-nucleon potential and the energy levels of the target nucleus, such a calculation is extremely lengthy and difficult.

Greenlees et al (1968, 1970a, and 1970b) take a more pragmatic approach which seems to be able to account for the experimental data. They propose that the optical potential should be of the form

$$V(\vec{r}) = \int \rho(\vec{r}') \; v(|\vec{r}-\vec{r}'|) \; d\vec{r}' \qquad (66)$$

where $\rho(r)$ is the distribution of nucleons in the nucleus and $v(|r-r'|)$ is the nucleon-nucleon potential. This classical expression is just the first term of the quantum-mechanically derived formulas of Feshbach. Kidawaiand Rook (1971) have shown that equation 66 neglects higher-order processes in the interaction, the indistinguishability of the nucleons, and the correlations of multiple scattering. However, they show that these deletions have a negligible effect on the predicted cross section.

Although the optical model has proven very useful, it has some inherent limitations. The model ignores most of the detailed features of nuclear structure. The nucleus is treated as a blob of nuclear matter giving rise to a potential of a certain radius and diffuseness (compare equation 66). Thus the model is able to give the gross structure of the scattering and features dependent upon single-particle states but cannot give properties which arise from more complicated configurations. In particular, the "quasi-elastic" scattering from the ground state of a rotational nucleus to a member of the ground state band is not predicted by the model.

2. Forms of the Optical Potential

Historically, the optical potential is expressed as a square well because of the ease of solving the Schrödinger equation for this form of the potential. The transmission coefficients can be expressed as analytical functions of the depth $(V_o + i\, W_o)$ and the width R_o (Vogt 1968)

$$T_\ell = \frac{4\pi P_\ell \; \mathrm{Im}(S_\ell)}{[1 - S_\ell \mathrm{Re}(f_\ell) + P_\ell \; \mathrm{Im}(f_\ell)]^2 + [P_\ell \mathrm{Re}(f_\ell) + S_\ell \; \mathrm{Im}(f_\ell)]^2} \qquad (67)$$

Here P_ℓ is the usual penetration factor,

$$P_\ell = kR/[F^2(kR) + G^2(kR)] \qquad (68)$$

where F_ℓ and G_ℓ are the regular and irregular Coulomb wavefunctions respectively, R is the radius outside of which the nuclear potential no longer has any appreciable effect, and k is the wave number at

infinity of the approaching projectile in the center of mass. The S_ℓ are the usual shift functions of nuclear reaction theory,

$$S_\ell = -b_\ell + \left\{\frac{rF_\ell\, dF_\ell/dr + rG_\ell(dG_\ell/dr)}{F_\ell^2 + G_\ell^2}\right\}_{r=R} \tag{69}$$

where b_ℓ are boundary-condition numbers determined by resonance properties of the well.

It was found, however, that the sharp edge of the square well gave too much "reflection". Michaud, Sherk, and Vogt (1970b) proposed an equivalent square well which at low bombarding energies produces the same transmission coefficients as potentials with more diffuse shapes but retains the ease of calculation of the square well. The depth and width of the potential are slightly changed and a reflection factor, f, increases the transmission coefficient. When the transmission coefficients are much smaller than unity, they are given by

$$T_\ell = 4\pi\, P_\ell\, \mathrm{Im}\, s_\ell\, f \tag{70}$$

where the penetration factor and the strength function s_ℓ

$$s_\ell = [\pi r(d\psi/dr)/\psi]_{r=R} - \pi\, b_\ell]^{-1} \tag{71}$$

are evaluated with the new depth and width. However, as the bombarding energy increases equation 70 increasingly over-estimates the transmission coefficients.

Most of the recent work has used the Woods-Saxon potential (Woods and Saxon 1954),

$$V(r) = \frac{V_o}{1 + \exp[(r-r_o)/a]} \tag{72}$$

where V_o is the depth of the potential, r_o is the width, and a is the diffuseness. This shape is generally used for both the real and imaginary parts of the potential, although the value of the parameters may be different. Some authors (especially for nucleon scattering) add a surface-peaked absorption term. This term usually takes the form of a derivative Woods-Saxon,

$$V_s = 4a\, V_o \frac{e^{(r-r_o)/a}}{[1+e^{(r-r_o)/a}]^2} \tag{73}$$

There is some evidence that the depth of the real potential depends upon energy, charge (aside from the normal Coulomb interaction), and isospin. The energy dependence is thought to arise from a dependence upon the kinetic energy of the nucleons inside the nucleus. Thomas and Burge (1969) have shown that the potential depths which describe proton scattering vary by more than 30% for energies from 10 MeV to 60 MeV. The dependence on charge arises because the potential is now energy dependent. This term has a slightly different radial dependence than the Woods-Saxon form assumed for the main potential, but since this term is small, it is customary to replace it by an equivalent form which has the Woods-Saxon radial dependence. The isospin dependence can be seen from equation 66. If the protons and neutrons have nearly the same distribution inside the nucleus, and the nucleon-nucleon isospin potential has the same radial dependence as the non-isospin potential, then a term proportional to $(N - Z)/A$ occurs.

If the projectile and the target are charged, then the Coulomb potential must be added to the real term. Although the exact charge distribution of the nucleus should be used, Woods and Saxon (1954) and Glassgold and Kellogg (1957) have found the transmission coefficients to be relatively insensitive to the nuclear charge distribution that is assumed. Thus the potential from a uniformly charged sphere is usually used,

$$V_c = \begin{cases} ZZ' e^2/r & r \geq R \\ (ZZ' e^2/2R)(3 - r^2/R^2) & r \leq R \end{cases} \qquad (74)$$

With the potentials described so far, the optical model is unable to predict polarizations. The form for the spin-orbit part of the potential is taken from atomic physics not only for its familiarity but also because it can formally be shown to be appropriate (Fernbach et al 1955, and McDonald and Hull 1966). Although nuclear spin dependent terms might exist, Rahman-Khan (1966) has shown that no evidence exists to warrant their inclusion.

Thus the transmission coefficients are obtained by solving

$$-\frac{1}{r^2}\frac{d}{dr}\left(r^2 \frac{d\psi}{dr}\right) + \frac{2m}{\hbar^2}\left[E - \frac{\hbar^2 \ell(\ell+1)}{2m\, r^2} + V(r)\right] = 0 \qquad (75)$$

with

$$\begin{aligned} V(r) = V_c(r) &- [V_v - V_E\, Z/A - V_s(N-Z)/A]\, f(r) \\ &- i\, W_v\, g(r) - iW_s\, h(r) \\ &+ (V_{so} + iW_{so})\, (\hbar^2/m^2c^4)\, j(r) \end{aligned} \qquad (76)$$

where

$V_c(r)$: the repulsive central Coulomb potential given by equation 74;

V_v : energy dependent real part of the central potential, $V_v = V_o + dV_o \cdot E$;

V_E : correction to V_v due to charged particles experiencing energy dependent potential;

V_S : correction to V_v because of the presence of isospin dependent potentials;

W_v : energy dependent imaginary part of the central potential having Woods-Saxon radial dependence: $W_v = W_o + dW_o \cdot E$;

W_s : energy dependent imaginary part of the central potential peaking at the nuclear surface, $W_s = W_{sur} + dW_s \cdot E$;

V_{so} : real part of the spin-orbit potential;

W_{so} : imaginary part of the spin-orbit potential;

$f(r)$ and $g(r)$: Woods-Saxon shape of equation 71;

$h(r)$: derivative of Woods-Saxon, $(-4a)\, dg(r)/dr$;

$j(r)$: Thomas potential shape, $(df(r)/dr)/r$.

Sheldon (1963) has shown that if the spin-orbit potential is neglected, the transmission coefficients T_ℓ are weighted averages of the spin dependent transmission coefficients $T_{\ell j}$, where $\vec{j} = \vec{\ell} + \vec{s}$.

Finally, especially for heavy-ion reactions where the projectile can have a large fraction of the total mass, the so-called universal potentials are used. These will be described in the section concerning transmission coefficients for heavy-ion reactions (Section 3e).

3. Parameter Searches

a. Ambiguities

Even if the elastic scattering cross sections were known exactly it is not in general possible to find a unique potential (Bargmann 1949a and 1949b, and Gel'fand and Levitan 1951a and 1951b). Many authors (see Cage et al 1973, for a recent discussion) have studied the causes and consequences of ambiguities arising from inexact knowledge of scattering cross sections. Both discrete and continuous ambiguities arise because the incident particles are strongly absorbed, and hence only a few partial waves having impact parameters near the nuclear surface contribute to the elastic scattering.

The best known continuous ambiguity is the $V_0 r_0^n$ ambiguity, where n is a constant normally about 2. Forest (1965) has investigated this ambiguity for square well potentials. Another continuous ambiguity, the $W_0 a$ ambiguity, has been investigated by Hentschel and Heinreich (1970) and has been shown to be associated with nuclear deformation. Finally,

$$V(R_x) = V_0(1 + \exp(R_x - R_0)/a_r)^{-1} = \text{constant} \qquad (77)$$

results from the fact that scattering occurs in a region around R_x and hence the potential is determined only around that region.

An interesting ambiguity is the discrete ambiguity associated with the real potential. As the real potential is increased the agreement between theory and experiment becomes alternately better and worse. Austern (1961) has explained this behavior by using the WKB approximation and showing that the number of half wavelengths increases

by unity as one goes from one good fit to the next.

Very little information exists on the true shape of the nuclear potential. Hence there is an ambiguity as to what shape the nuclear potential (especially the imaginary part) should take.

b. Proton Potentials

A wealth of information exists on proton elastic scattering. Hence there have been many systematic attempts to obtain parameters which yield fits to many reactions (Perey 1963, Buck 1963, Rosen et al 1965, and Becchetti and Greenlees 1969a). Using the potential described in equation 76, the values for the parameters achieved in these searches are shown in Table I. The search by Becchetti and Greenlees being the most recent, incorporates the most data, 46 data sets of differential elastic scattering measurements, polarization measurements, and reaction cross section measurements. They also provide a table showing how the fit improves (degrades) as various terms are added or assumptions are made. They note that the most apparent discrepancy is in the prediction of reaction cross sections for nuclei having masses less than 90. However, these are the cross sections of interest here when the statistical model of nuclear reactions is used. Perey and Perey (1972) note that most of the data used in the analysis of Becchetti and Greenlees come from measurements with incident proton energies between 30 and 40 MeV. They suggest that the analysis by Perey gives an alternative set of parameters for incident energies less than 20 MeV.

Another parameter set should be mentioned. Michaud and Fowler (1970a) in their discussion concerning the calculation of cross sections for astrophysical applications suggest V_v = 50 MeV, W_v = 4 MeV, $R_V = R_W = 1.25A\,(\text{target})^{1/3}$f, and $a_v = a_W$ = 0.75 f. This set does not result from a systematic fit to experimental cross sections but does seem to do well.

In Figure 1 are shown the transmission coefficients for ^{23}Na + p with $\ell = 0,1,2,3,4$ for E_{cm} = 0.1 MeV to 6 MeV. The transmission coefficients were calculated by the computer program described in Section 3f. The effect of the Coulomb and centrifugal barriers is seen.

c. Neutron Potentials

A large amount of experimental data also exists for neutron induced reactions. Perey and Buck (1962) and Schulz and Wiebicke (1966) have obtained non-local potentials. However, since it is much easier to solve the differential Schrödinger equation than an integro-differential equation (which results from the use of non-local potentials), these potentials have not been widely used.

Wilmore and Hodgson (1964) (with a revision by Hodgson 1967) have obtained a local potential which is equivalent to the non-local potential of Perey and Buck. The parameters of this local potential appear in Table II along with the parameters of Rosen et al (1965) and Becchetti and Greenlees (1969a). Engelbrecht and Feidelberg (1967), Gorlov et al (1967), and Aver'yanov and Purtseladze (1967) provide systematic fits using a Gaussian shape for the imaginary potential. Perey and Perey note the potential of Becchetti and Greenlees was

derived without fully calculating the compound elastic contribution to the elastic scattering cross section. Therefore they recommend for low energies that the potential of Wilmore and Hodgson be used.

Michaud and Fowler (1970a) suggest that the same potential they used for proton scattering (page 202) be used for neutron scattering, although as can be seen from Table II, there are slight differences between the neutron and proton potentials derived by other authors.

In Figure 2 are shown the transmission coefficients for $^{23}Mg + n$ with $\ell=0,1,2,3$ for E_{cm} = 0.01 to 10 MeV. The transmission coefficient for $\ell = 0$ is near unity even for very low incident energies. This is due to the absence of both the Coulomb and centrifugal barriers. The other ℓ values are lower because of the presence of the centrifugal barrier.

d. Light-Ion Potentials

Light ions in this context will be projectiles with $2 \leq A \leq 4$. Relative to nucleon scattering, little effort has been expended in achieving systematic potentials for these ions. Each of these projectiles is strongly absorbed which suggests that the interaction is confined to the surface region of the nucleus. Because of this localization, the ambiguities described in Section 3a are extremely serious.

The deuteron has special problems for optical model analysis because it is so loosely bound. The early analysis of Perey and Perey (1963) is applicable below 25 MeV but should be used with caution below 12 MeV (Perey and Perey 1972) since both the real and imaginary

potentials tend to increase rapidly. The parameters of this potential, which has been used extensively to calculate stripping reactions, are

$$V_v = 81.0 - 0.22E + 2.0\ Z/A^{1/3}\ \text{MeV}$$
$$W_s = 14.4 + 0.24E\ \text{MeV}$$
$$R_v = 1.15\ A^{1/3}\ \text{fm} \qquad R_w = 1.34\ A^{1/3}\ \text{fm}$$
$$a_v = 0.81\ \text{fm} \qquad a_w = 0.68\ \text{fm} \tag{78}$$

The study of systematic parameter variation for ^{3}H and ^{3}He scattering is still in a primitive state. Although some analyses have been performed over a limited energy or mass range, only the unpublished results of Becchetti and Greenlees (1969b) have included a large set of data. The parameters of the ^{3}H potential were deduced to be

$$V_v = 136.4 - 0.17E + 55\ (N-Z)/A\ \text{MeV}$$
$$W_v = 41.3 - 0.33E + 63\ (N-Z)/A\ \text{MeV}$$
$$R_v = 1.2\ A^{1/3}\ \text{fm} \qquad R_w = 1.4\ A^{1/3}\ \text{fm}$$
$$a_v = 0.72\ \text{fm} \qquad a_w = 0.86\ \text{fm} \tag{79}$$

while the parameters of the ^{3}He potential were found to be

$$V_v = 165 - 0.17E - 7(N-Z)/A\ \text{MeV}$$
$$W_v = 46 - 0.33E - 110(N-Z)/A\ \text{MeV} \tag{80}$$

with the radius and diffuseness parameters as for ^{3}H. The Coulomb potential is that of a uniformly charged sphere of radius R_v. It should be noted that these fits are not unique. As for reactions induced by

deuterons, reactions induced by ^{3}H or ^{3}He usually proceed through direct reactions rather than by forming a compound nucleus.

No systematic search for potential parameters for alpha scattering has yet been performed. This is most likely due to the existence of parameter ambiguities and because of the absence of low energy data for many nuclei. Michaud and Fowler (1970a) in their discussion of the applicability of the optical model to calculations of astrophysically relevant cross sections suggest

$$\begin{aligned} V_v &= 60 \text{ MeV} & R &= 1.25\ A^{1/3} + 1.09 \text{ fm} \\ W_v &= 10 \text{ MeV} & a &= 0.50 \text{ fm} \end{aligned} \tag{81}$$

Igo (1959a and 1959b) has shown that most of the interaction occurs on the tail of the potential and on the basis of a limited data sample suggests the tail should have the form

$$\begin{aligned} V(r) &= -1100 \exp -(r - 1.17A^{1/3})/0.574 \text{ MeV} \\ W(r) &= -45.7 \exp -(r - 1.40A^{1/3})/0.578 \text{ MeV} \end{aligned} \tag{82}$$

This is equivalent to a Woods-Saxon potential (for $R = 1.17A^{1/3} + r_o$) if

$$\begin{aligned} &\ell n(V_v) - 1.74\ r_o = 7.00 \\ &\ell n(W_v) - 1.74\ r_o = 3.82 \\ &R_v = 1.17A^{1/3} + r_o \text{ fm} \\ &R_W = 1.40A^{1/3} + r_o \text{ fm} \end{aligned} \tag{83}$$

for V_v and W_v in MeV, and r_o in fm .

In fact, Igo uses Woods-Saxon potentials to fit reaction cross sections. These potentials can be fitted by the formulas

$$\begin{aligned} V_v &= 50 \text{ MeV} \\ W_v &= 4.21 + 0.103A - 0.33(N-Z)/A \text{ MeV} \\ R &= 1.17\, A^{1/3} + 1.77 \text{ fm} \\ a &= 0.576 \text{ fm} \end{aligned} \tag{84}$$

McFadden and Satchler (1966) report good fits for elastic scattering on numerous nuclei for 24.7 MeV alpha particles. However, they observed no systematic trends and suggest that

$$\begin{aligned} V_v &= 185 \text{ MeV} \\ W_v &= 25 \text{ MeV} \\ R &= 1.4\, A^{1/3} \text{ fm} \\ a &= 0.52 \text{ fm} \end{aligned} \tag{85}$$

would be appropriate values to start a search program for V_v between 150 and 200 MeV. There is some evidence (Put and Paans 1974) that for very nigh energy ($E \geq 100$ MeV) the real potential has an energy dependence which is about a third as strong as for the nucleon real potentials. Figure 3 shows the transmission coefficients for $^{20}Ne + \alpha$ for $\ell = 0,1,2$ and 3 for $E_{cm} = 1$ to 10 MeV. The Coulomb barrier is very significant even though the atomic number of neon is relatively low.

e. Heavy-Ion Potentials

No global potential has been obtained for heavy-ion reactions. This is not surprising as the target and the projectile often have nearly the same mass and the Woods-Saxon potential might not seem to apply.

However, elastic scattering data can be successfully fitted through the use of a Woods-Saxon potential (see, for example, Gobbi 1971, or Reilley et al 1973).

In the absence of a general potential which describes a variety of heavy-ion reactions with small systematic parameter variations, it is often necessary to interpolate or extrapolate from known cases. The compilations of Perey and Perey (1972 and 1974) will prove helpful.

Another approach is to use a universal real potential based upon folding the nucleon-nucleon potential over the densities of the interacting particles. Such an approach has been considered by many authors (Broglia and Winther 1972, Meyers 1974, and Brink and Rowley 1974) and usually results in a good description of heavy-ion scattering with reasonable parameters. This method has the advantage of fewer parameters as no imaginary component is developed.

f. Gamma Rays

Effective gamma-ray transmission coefficients are invariantly calculated by using the single-particle estimates of Weisskopf (1951) and introducing a normalization constant. Thus for El transitions,

$$T^{(El)}_{J^\pi} = N_0(2\pi/D)\,\Gamma(El)$$
$$= 5.592\, N_0\, A^{2/3} \int_0^{E^*} E^3\, \rho(E,(J^\pi)')\, dE \qquad (86)$$

where N_0 is the normalization constant, E^* is the excitation energy of the nucleus, $(J^\pi)'$ are those spins and parity which are allowed to take part in El transitions from a level having spin and parity J^π.

Magnetic and other electric multipolarities can be similarly calculated, although usually only the lowest multipolarities are used. Bollinger and Thomas (1970) noted that better agreement with experiment can be obtained if the exponent in equation 86 is changed from 3 to 5. This is thought to reflect the Lorentzian-shaped giant dipole resonance (when still on the low energy tail) which causes the transmission coefficient to exhibit an energy dependence stronger than the Weisskopf estimate.

Woosley et al (1975) have made a study of gamma ray transmission coefficients. They consider only E1 and M1 contributions and define

$$T^{J^\pi} = T^{J^\pi}_{E1} + T^{J^\pi}_{M1} \tag{87}$$

where $T^{J^\pi}_{E1}$ is the E1 contribution,

$$T^{J}_{E1}(E^*) = 3.48 \times 10^{-6} * SMR \times GR$$

$$* \left\{ \sum_{J'^{\pi'}} \int \frac{(E^* - E)^4 \, p(E,J'^{\pi'}) \, dE}{[(E^* - E)^2 - ER^2]^2 + GR^2(E^* - E)^2} \right.$$

$$\left. + \sum_{\substack{\text{discrete} \\ \text{states}}} \frac{(E^* - E_{disc})^4}{[(E^* - E)^2 - ER^2]^2 + GR^2(E^* - E)^2} \right\} \tag{88}$$

and $T^{J^\pi}_{M1}$ is the M1 contribution,

$$T^{J^\pi}_{M1}(E^*) = 3.89 \times 10^{-7} / D_o$$

$$* \left\{ \sum_{J'^{\pi'}} \int (E^* - E)^3 \, p(E,J'^{\pi'}) dE + \sum_{\substack{\text{discrete} \\ \text{states}}} (E^* - E_{disc})^3 \right\} \tag{89}$$

where SMR is the fraction of the E1 sum rule (=0.22), GR is the giant-dipole width (0.6 for either N or Z magic; 0.8 if N or Z is within 2 units of magic, but neither magic; 1.2 if the nucleus is deformed; and 1.0 otherwise), ER is the giant resonance peak energy ($35\ A^{-1/6}$), and D_0 is the M1 hindrance factor (20). The density of states is the back-shifted Fermi gas formula (see Section II.B) with parameters determined in a similar manner to Dilg et al (1973), except that the nuclear temperature is defined as

$$E^* - \Delta = U = a(kT)^2 \qquad (90)$$

By this method, they were able to predict within a factor of 2 (n,γ), (p,γ), and (α,γ) cross sections.

F. HAUSER*2: Computer Code to Calculate Nuclear Cross Sections Using the Statistical Model

Although many computer codes exist which calculate cross sections using the statistical model of nuclear reactions based upon the statistical model ["Helene" (Penny 1965), "Statis" (Stokstad 1972), "Cindy" (Sheldon and Rogers 1973)], a new computer program was written to increase computation speed and include those features of interest in the experiments described later in this thesis.

The code, designated HAUSER*2 (the 2 referring to the second version), is based on the optical-model code of Fox (1973) and on the statistical-model code of Stokstad (1972), "Statis". The program was written for the CDC 7600 computer, but with minor modifications it can be run on an IBM 360/370 computer.

The advantage of the present code is its ability to compute transmission coefficients and then interpolate between these values when necessary. The lengthy process of computing the transmission coefficients at each required energy and the memory consuming process of storing multidimensional arrays of the coefficients for later use are thereby avoided.

The transmission coefficients are calculated by integrating the Schrödinger equation using Cowell's method (Cowell and Crommelin 1910, and Fox and Goodwin 1949). The integration extends to a radius beyond which the nuclear potential has no further effect on the wave function. This distance is usually less than the classical distance of closest approach but is adjustable within the program. The transmission coefficients are then derived from the phase shift of the wave function (for $T_\ell \geq 0.0001$) or by integrating the absolute square of the wave function weighted by the imaginary part of the potential (for $T_\ell \leq 0.0001$). The integration procedure is necessary for small T_ℓ's as the phase shifts become very small and one subtracts two nearly equal numbers to obtain T_ℓ . The code does not compute either transmission coefficients which depend upon the channel spin (i.e., spin orbit terms in the potential are neglected), or gamma ray channel T_ℓ's. The transmission coefficients have been compared with those calculated by "Helene" for $^{35}Cl + \alpha$, $^{38}Ar + p$, and $^{38}K + n$ for energies between 0.1 and 10 MeV. The two programs yield values in agreement to better than one percent.

The cross sections are calculated according to equation 17. The angular momentum coupling and parity are correctly included for

particles of any spin. The maximum allowed angular momentum in the compound nucleus is 32 and the maximum orbital angular momentum in any reaction channel is also 32. Both of these limits can be changed by changing the dimensions of appropriate arrays. However, no attempt is made to set an upper limit to the angular momentum that the compound nucleus can support (the Yrast limit). For reactions involving light ions, this absence is unimportant.

This program, unlike "Statis", allows the use of the level density of Gilbert and Cameron (1965a) as well as the back-shifted formulas of Dilg et al (1973). It also has the provision to approximately account for the effect of unbound states if the user supplies an effective gamma ray transmission coefficient.

HAUSER*2 has been compared with "Helene" for the $^{35}Cl + \alpha$ reaction for E_{cm} = 5.5 to 10 MeV. The results for each pair of products agree to better than 3%, the difference probably being due to the interpolation (rather than calculation) of transmission coefficients by HAUSER*2.

III. EXPERIMENTAL PROCEDURE

A. Introduction

This project started as part of an effort by the Kellogg Radiation Laboratory to determine with what accuracy the statistical model of nuclear reactions could predict the total reaction cross sections for a wide range of reactions. (See Howard et al 1974, and Rios et al 1974 for a description of the other work.) The reactions studied in this part of the project were $^{23}Na(p,n)^{23}Mg$, $^{35}Cl(\alpha,n)^{38}K$, $^{59}Co(\alpha,n)^{62}Cu$, $^{63}Cu(p,n)^{63}Zn$, $^{63}Cu(\alpha, n)^{66}Ga$, and $^{65}Cu(\alpha,n)^{68}Ga$.

Whereas the other work at Kellogg used a NaI two-crystal spectrometer to observe annihilation radiation, a high resolution Ge(Li) detector was used in the present experiments to observe other delayed gamma radiation which could be uniquely connected with a decay (and hence to a cross section). Also to test the model further, a wider range of target masses was bombarded than in the other studies.

B. Experimental Procedure

1. General Procedure

Reactions were chosen which produce radioactive parents with a half-life less than a day so that the activation technique could be used. The targets were bombarded by either protons or alpha particles from the Tandem Van de Graaff accelerator. After bombardment the delayed gamma rays were observed. Repeated runs at the same energy were made to gather adequate statistics.

As shown by Bashkin et al (1959), the yield of an activation experiment having n cycles of bombardment ($0 \leq t < t_1$) of counting

($t_2 \leq t < t_3$), and of waiting ($t_3 \leq t < t_4$) can be written as

$$Y = N_o N_1 \text{ eff } \sigma F(\lambda, t_1, t_2, t_3, t_4, n) B \tag{91}$$

where Y is the yield of the observed events, N_o is the number of target nuclei per cm^2, N_1 is the number of incident particles, eff is the detection efficiency, σ is the cross section for producing the events, λ is the decay constant of the source, B is the beam shape factor (which corrects for systematically varying beam intensity from $t = 0$ to t_1), and F is the decay function

$$F = \frac{(e^{\lambda t_1} - 1)}{\lambda t_1} \frac{(e^{\lambda t_2} - e^{\lambda t_3})}{(1 - e^{-\lambda t_4})} \left[1 - \frac{1 - e^{-n\lambda t_4}}{n(e^{\lambda t_4} - 1)}\right] \tag{92}$$

For all the experiments, the beam was on target much longer than the time needed to switch the beam on and off target (a magnetic chopping system being used) and when on the target, the beam current was constant within 10%. Thus the beam shape factor is unity for these experiments.

The energy of the incoming beam was determined by a precision 90^o magnet located about 15 m upstream from the target. This magnet was calibrated by Mak and Mann (1973) by observing known thresholds and resonances, and measuring the NMR frequencies for each of the known energies. The magnet "constant" k in the expression

$$E = kf^2q^2(m_p/m) / (1 - E/2m) \tag{93}$$

where q is the charge of the ion, m is the mass of the ion (in energy units), and m_p is the mass of the proton, was determined as a function of energy. These values for k were fitted with a cubic equation.

Repeated measurements showed that, if reasonable care is used to avoid hysteresis effects, the calibration is probably accurate to better than 0.1% in energy.

Since the maximum terminal voltage on the Van de Graaff is about 6.5 MV, the maximum proton energy is limited to about 13 MeV in the laboratory system. Using lithium exchange, negatively charged helium can be injected into the accelerator and 19-MeV alpha beams can be obtained. The current on target ranged from about 5 nA to 300 nA. Care was taken not to melt the target materials and to keep the dead time of the electronics to an acceptable level (less than 15%).

2. Gamma-Ray Detection

Cross sections were inferred from the intensity of delayed gamma radiation produced by the product of the reaction. Although NaI spectrometers have higher detection efficiency and do not suffer as severely from radiation damage caused by neutron bombardment, Ge(Li) detectors were used almost exclusively because of their much superior energy resolution. Thus for most of the products observed, a unique gamma ray could be used to infer the amount of the reaction product.

Ge(Li) detectors are now standard laboratory equipment and their properties will not be discussed here. (For a review, see French et al 1969). For the $^{35}Cl(\alpha,n)^{38}K$ measurements, a 50 cm^3 (nominal volume) Ge(Li) detector was used (serial #503). This detector has a resolution for the 1.332 MeV gamma ray from ^{60}Co decay of about 3 keV and a peak-to-Compton ratio for that energy of 25:1. For the other measurements a larger detector (having a nominal volume of 73 cm^3, serial #909) was used.

This detector has a resolution of about 2 keV and a peak-to-Compton ratio of 35:1. Both detectors were purchased from Princeton Gamma-Tech and were of coaxial design with one end open. The better detector was not used for the $^{35}Cl(\alpha,n)^{38}K$ measurements since these measurements were performed in the target room (because of the short half-life of $^{38}K^*$), thus subjecting the detector to neutron irradiation.

NaI detectors have long been used in nuclear laboratories, and their properties will not be discussed. (For a review, see Heath 1964.) A 5-cm diameter by 5-cm thick NaI detector (serial #CM990) with an RCA8575 photomultiplier tube was used for some of the $^{35}Cl(\alpha,n)^{38}K$ runs so that adequate yield could be obtained. The resolution, 10% for 511 keV annihilation radiation, although poor, was sufficient for the experiment.

a. Detection Efficiency

The intensity of gamma radiation was determined in all cases by the area in the photopeak of the gamma ray. The photopeak detection efficiency was determined experimentally by placing radioactive sources inside the target holders. (For a fuller discussion concerning calibration of gamma spectrometers for detection efficiency, see Legrand 1973.) Relative efficiency was determined from the well known decay of ^{56}Co and ^{66}Ga (Camp and Meredith 1971). The absolute detection efficiency was determined from the 1274-keV gamma ray of ^{22}Na. ^{56}Co and ^{66}Ga were made at Kellogg by the reactions $^{56}Fe(p,n)^{56}Co$ and $^{63}Cu(\alpha,n)^{66}Ga$ respectively. The ^{22}Na source, also made at Kellogg by placing a drop of $^{22}NaCl$-water solution on a metallic disk and then evaporating the water away, was calibrated by comparing the intensity of the 1274-keV gamma ray to that

of a source of known strength made by Amersham-Searle. The detection efficiency for the 73 cm^3 Ge(Li) detector in the geometry of the off-line experiments is shown in Figure 4. Also shown in this figure is the efficiency for the 50 cm^3 detector in the same geometry. It can be seen that the larger detector has a larger absolute efficiency and a smaller slope. The points were fitted with the equation

$$e = A[E(MeV)]^P \tag{94}$$

where e is the detection efficiency, and A and P are constants. This form differs from that of Freeman and Jenkin (1966) and Tokcan and Cothern (1968), but experience in this laboratory has shown that for large volume Ge(Li) detectors, equation 94 gives excellent fits to measured values with agreement to better than 5% for the energy range 0.2 to 4.8 MeV.

Since the NaI detector was used for only the $^{35}Cl(\alpha,n)^{38}K$ measurements where a Ge(Li) detector was also used, its detection efficiency was not measured. Rather the relative cross sections obtained with this detector were normalized against the absolute data taken with the Ge(Li) detector.

b. Corrections to Detection Efficiency

The most important correction is due to the summing in the detector of two (or more) gamma rays. Because of the close geometry, this correction can amount to 10%. The number of observed gamma rays, $y(1)$, is

$$y(1) = N(1)\, e(1)\, [1 - T(2)\, P(1/2)] \tag{95}$$

where $N(1)$ is the number of gamma rays of type 1 emitted, $e(1)$ is the efficiency for detection of gamma rays of energy 1 in the photopeak peak (equation 94), $T(2)$ is the efficiency for detection of gamma rays of energy 2 (whether in the photopeak or not), and $P(1/2)$ is the probability that gamma ray 2 appears given that gamma ray 1 has. Although it is difficult to calculate photopeak efficiencies for Ge(Li) detectors (because of the uncertainty of the internal detector geometry and the multitude of processes resulting in the full energy or photopeak), it is relatively simple to calculate the total detection efficiency,

$$T(E) = \int \{1 - \exp[\mu(E)t]\}\, d\Omega \qquad (96)$$

where t is the path length for the gamma radiation in the crystal for a given direction and $\mu(E)$ is the attenuation coefficient. The integral covers all directions subtended by the detector. The code used to calculate $T(E)$ includes corrections for the dead layer of Ge on the front face and the presence of an inactive core region. The attenuation coefficients are taken from Storm et al (1958) who interpolated from the values given in Grodstein (1957). The accuracy of the calculation was checked by comparing the calculated number with the experimentally found summing correction for ^{22}Na,

$$SC(1274) = PS(1274 + 511)\ PS(1274) / PF(511) \qquad (97)$$

where SC is the summing correction, PS is the photopeak intensity, and PF is the photofraction. The photofraction, the number of counts in the photopeak divided by the total number of counts in the

spectrum, was determined by using ^{68}Ga which is a positron source with negliglble high-energy gamma radiation.

Two other corrections are necessary if the gamma ray observed is annihilation radiation: annihilation in flight and the effect of a distributed source. Annihilation in flight refers to the production of non-511 keV gamma radiation when the positrons annihilate when moving as contrasted to the two 511-keV gamma rays which are produced when the positron annihilates at rest. For a discussion of this effect, see Part I of this thesis, Gerhart et al (1954), or Heitler (1954). This effect can approach 10% for high energy positrons annihilating in high Z material.

The other correction, the distributed source correction, was determined by the use of a ^{22}Na source (whose positrons are stopped within the source) variously placed in a matrix of positions. From the efficiencies measured in the matrix, the necessary correction can be calculated. This correction is in the opposite direction to the correction due to annihilation in flight.

3. Off-Line Geometry

Off-line counting is preferable to detecting the delayed radiation inside the target room, as the amount of unwanted radiation (either beam-related or natural) is usually much less. Thus whenever the yield was sufficient, the off-line geometry was used.

The geometry used for the off-line measurements is shown in Figure 5. The target was bombarded in a glass tee and then was manually transferred into the teflon holder. Concrete walls and dirt

nearly filled the 15 m separating the point of bombardment and the point of detection. The target could be transferred in about 35 sec.

4. Electronics

The electronics used in these experiments are standard. A block diagram is shown in Figure 6. A gamma-ray detector produced a pulse which was amplified by a preamplifier and then by an amplifier. The voltage signal was then fed into a multi-channel analyzer. In order to correct for the dead time of the system, a 60 Hz (line frequency) pulser was introduced at the preamplifier.

Two different MCA's were used, the Nuclear Data ND 160 (with updated ND 2200 ADC's) having 4096 channels of memory and the Nuclear Data ND4420 computer system having 8096 channels of memory. Since the computer system arrived as these experiments were in progress, little attempt was made to expand the software to detect the delayed radiation in more than two time groups. However, using the Kellogg-built router (Kellogg number 212A), the ND160 allows up to 128 counting groups, although only 16 groups were normally used to allow 256 channels of analysis for each group.

Timing is quite important in these measurements as the inference of cross section from yield depends critically upon the timings used. The digital sequence timer (Kellogg number 39C), described in the first part of this thesis (particularly in Appendix A) supplied time signals accurate to one part in 10000, selectable using four-digit thumbwheel switches.

C. Experimental Details

1. Introduction

The various experimental details for each reaction will now be given. These details will include the energy range studied, the nature of the target, and the geometry used. Particular emphasis will be placed on those aspects of the decay scheme of the reaction product which allow the value of the cross section to be inferred from yield measurements.

All Q values come from the 1971 Mass Tables of Wapstra and Gove. The values for energy loss come from the tables of Northcliffe and Schilling (1973).

2. $^{23}Na(p,n)^{23}Mg$

Besides the interest in $^{23}Na(p,n)^{23}Mg$ as a test of the statistical model of nuclear reactions, the measurement allows the cross section of the inverse cross section of $^{23}Mg(n,p_0)^{23}Na$ to be inferred. This latter reaction is important in determining the neutron-enrichment parameter (the excess of neutrons relative to protons, either bound or free, divided by the number of nucleons) in stellar evolution calculations (Arnett and Truran 1969). This parameter becomes very important in the late states of stellar evolution as it determines the abundance of many nuclei.

As the $^{23}Mg(n,p)^{23}Na$ reaction is astrophysically important only for small neutron energies, the $^{23}Na(p,n)$ reaction was measured in much finer steps near threshold than at higher energies. Two targets were used, 167 $\mu g/cm^2$ and 1060 $\mu g/cm^2$ of NaCl on Ta backing. From

Northcliffe and Schilling (1973) the energy loss of a 6-MeV proton passing through 1000 $\mu g/cm^2$ of NaCl is 52 keV. The thickness of the targets was measured by a Sloan quartz-crystal monitor whose accuracy has been shown (by measurements described later in this thesis and by other use at Kellogg) to be better than 10%.

In Table III are listed the Q values for the reactions on Na which are possible using a 11.5 MeV proton beam, the highest energy beam used in this measurement. Also included is the half-life of the products as well as the associated delayed activity. Also in Table III is similar information for proton bombardment of Cl. It can be seen from Table III that for low-energy proton bombardment of NaCl, only the $^{23}Na(p,n)^{23}Mg$ reaction produces a positron emitter. However, at higher energies other positron emitters are produced.

Besides the positrons emitted in the decay of ^{23}Mg, a 440-keV gamma ray is emitted in $(8.7 \pm 0.2)\%$ of the decays (Storey and McNeil 1959, Talbert and Stewart 1960, Gorodetzky et al 1968, Detraz et al 1971, Alburger 1974, and Mann and Kavanagh 1975). The half-life of ^{23}Mg is 11.36 ± 0.04 s, (the weighted average of Goss et al 1968, Alburger 1974, and Azuelos et al 1974). This average is smaller than older values for the half life.

The timing of the various operations is shown in Table IV. It will be noted that the interval between the end of bombardment and the start of counting is many half-lives. This long delay results from using the off-line geometry to measure the decay. The yield of neutrons is large enough even near threshold to prevent using a Ge(Li) detector for an on-line experiment. Unfortunately, near threshold the

yield is not yet large enough to obtain adequate statistics for the 440-keV gamma ray, but the 511-keV peak, being twenty-fold more intense and contaminant free, can be used to deduce the cross section. A decay curve corresponding to ^{23}Mg decay plus a background was fitted to the yield of the 511-keV radiation using the 16 groups of acquired data. No evidence was found for a short-lived activity other than ^{23}Mg. At higher energies, the yield was sufficient to obtain accurate yields of the 440-keV line, which was therefore used to obtain the cross section, independent of possible contaminant positron activity.

3. $^{35}Cl(\alpha,n)^{38}K$

The $^{35}Cl(\alpha,n)^{38}K$ reaction is an interesting test of the statistical model since the first excited state of ^{38}K is a beta-emitting isomeric state. Thus two reactions starting from the same initial state and going to different sets of states in the same nucleus can be measured. It can be determined whether the model, which ignores nuclear structure, can predict accurately the reaction cross section involving two different types of levels when using the same potential.

The half-life of the ground state of ^{38}K is (7.636 ± 0.018)m as determined by Replace (1970), Vasil'ev et al (1967), Ebrey and Gray (1965), Bormann et al (1965), and Cline and Chagnon (1957). It should be noted that although the measurements are not in good agreement, the error in the half-life is not a major factor in the determination of the cross sections. Greater than 99% of the decays of the ^{38}K ground state go to the first excited state of ^{38}Ar at 2.168 MeV (Kavanagh 1968, and the first part of this thesis.)

The half-life of the isomeric state is considerably shorter, (929 ± 3) ms (the adopted value from Endt and van der Leun (1973), from the measurements of Hardy and Alburger (1972), and Clark et al (1972).) This adopted value is lower than the less precise earlier measurements. The isomeric state decays only to the ground state of ^{38}K by a super-allowed transition.

Because of the shortness of the half-life of the isomeric state, there was not sufficient time to transport the target to the off-line geometry. Thus the geometry shown in Figure 7 was used. Since the annihilation radiation was the only signal for the decay of the isomeric state, the chamber was made of Be to reduce annihilation in flight and bremsstrahlung. Alpha bombardment of Be produces no interfering radiation. The NaI detector was used for most of the measurements because of its superior efficiency; however, the 50 cm^3 Ge(Li) detector was used to check the results and was used for the runs where an absolute measurement of the cross section was performed. Because of the superior resolution of the Ge(Li) detector, it is easier to calibrate absolute detection efficiency and to determine peak areas.

A 120 $\mu g/cm^2 BaCl_2$ target on Au backing was used for the relative measurements (target thickness was 40 keV for 6 MeV alphas). For the absolute measurements a 147 $\mu g/cm^2$ BaCl target on Au backing was used. Since $BaCl_2$ is slightly hygroscopic, special care was taken in weighing the target. After evaporation but before the admission of air into the bell jar used for the evaporation, the frequency of the Sloan thickness monitor (with a clean new quartz wafer) indicated 147 $\mu g/cm^2$. After

admission of air, the thickness as indicated by the monitor increased by 7%. The hydrated target was then weighed by the tare method with a microbalance. After allowing for the 7% increase in weight, the "dry" $BaCl_2$ weighed (147 ± 10) g/cm^2, in agreement with the Sloan monitor result.

The Q values and the delayed-gamma activities of the products of $^{35}Cl + \alpha$ and of the Ba(α,n) reactions are shown in Table V. Since the Coulomb barrier is so high for charged-particle emission from the intermediate nucleus formed by $Ba + \alpha$, only the neutron channel is expected to contribute, and that channel quite weakly because of the barrier for the incoming alphas. As can be seen from Table V, only the isomeric level of ^{38}K has a half-life less than a minute among all the products of $BaCl_2 + \alpha$. The decay of the ground state of ^{38}K is uniquely signaled by the presence of the 2.17-MeV gamma ray.

The yield of both the isomeric and ground state decays can be obtained by using many cycles, each of which is short. By using two short counting periods (as shown in Table IV), the yield of the isomeric level is linearly related to the difference of the annihilation radiation, while the yield of the ground state is proportional to the sum of the observed 2.17-MeV gamma ray. Usually 150 cycles were needed to obtain adequate statistics to determine accurately the difference between the annihilation radiation in the two counting periods.

4. $^{59}Co(\alpha,n)^{62}Cu$

Much work has been performed recently around the A = 60 region in determining level density parameters. Thus in this region where

there is scant information concerning the energies, spins, and parities of low-lying states (necessary information for calculating cross sections using the statistical model), the $^{59}Co(\alpha,n)^{62}Cu$ reaction should be calculable with good precision.

The Q values and the delayed-gamma activities for products of Co + α are shown in Table VI. Only ^{62}Cu has a short half-life. Jongsma et al (1969) have reported the half-life to be (9.73± 0.02) min. Unfortunately, as Van Patter et al (1970) have shown, $\geq$ 99.5% of the ^{62}Cu decays are to the ground state of ^{62}Ni. Thus one must observe the annihilation radiation which occurs in 98% of the decays (the remaining 2% of the decays proceeding through electron capture). To verify that the observed annihilation radiation came from ^{62}Cu and not some other positron emitter, two counting groups were used, as shown in Table IV. The use of off-line geometry, possible because of the length of the ^{62}Cu half-life, considerably reduced annihilation radiation not associated with the decay of ^{62}Cu.

Six targets of 146 $\mu g/cm^2$ Co on W backing, corresponding to an energy loss of 43 keV for 10-MeV alphas, were used. The thicknesses of the targets were found to be the same within ±2% by observing the prompt gamma rays from $^{59}Co(\alpha,p\gamma)^{62}Ni$. For the absolute measurement a seventh target was prepared, 40 $\mu g/cm^2$ as determined by weighing, using the tare method. Its thickness relative to the other targets was also determined by observing prompt gamma rays. Cobalt is a very difficult material to evaporate cleanly because cobalt alloys with the boat used in the evaporation. Thus part of the boat can be evaporated onto the

target (especially when the boat breaks because of the strain caused by the alloying). At the time the target for absolute determination of the cross section was made, cobalt was evaporated onto an Al foil. This foil was then scanned through use of a 61-cm double-focusing magnetic spectrometer by elastically scattering alpha particles from the foil. A heavy-element contamination of 1% by weight was found, presumably from the W boat used in the evaporation. This slight amount of heavy elements had no bearing on the experiment.

Because no fine structure was expected in the reaction cross section, coarse energy steps (500 keV from threshold to 13 MeV, 1 MeV from 13 to 19 MeV) were taken. At the higher energies the $^{59}Co(\alpha,2n)^{61}Cu$ competes strongly with the $^{59}Co(\alpha,n)^{62}Cu$ reaction. Even though the Coulomb barrier is high for W , delayed gamma radiation from (α,n) reactions on the backing material were observed. These, however, were not of sufficient intensity to pose any problem in the measurements.

5. $^{63}Cu(\alpha,n)^{66}Ga$ and $^{65}Cu(\alpha,n)^{68}Ga$

The (α,n) reactions on Cu are interesting since the only changes in the potentials involve the neutron number and atomic weight. Thus one can judge the importance of the mass term in the potentials.

Table VII presents the Q values and the delayed gamma activities for products of Cu + α . The production of ^{66}Ga is signaled by the delayed emission of many gamma rays. In fact, since the relative intensities of the many gamma rays are so well known (Phelps et al 1970; Camp and Meredith 1971), ^{66}Ga is often used to determine relative

detection efficiencies for Ge(Li) detectors. The absolute intensity of the gamma radiation can be determined from Camp and Langer (1963) who measured the strength of the ground-state beta branch. Although no error was given for this strength, a limit of 1.6% of the value can be determined from the error in the log ft given by them for the transition. Combining the data of Phelps et al and Camp and Langer, the 1039-keV gamma ray occurs in (37.4 ± 1.0)% of the decays of ^{66}Ga. The half-life of ^{66}Ga has been measured by Chrisler et al (1972) to be (9.49 ± 0.02) hr.

From the ratio of the number of gamma rays to annihilation radiation (Horen 1959 and Carter et al 1968) and the positron-to-electron-capture ratio (Gove and Martin 1971), the number of 1077-keV gamma rays emitted per decay of ^{68}Ga is (3.13 ± 0.27)%. The half-life has been determined by various groups (see Smith and Williams 1971, and Rao 1968), but the values are only in fair agreement. The value, $t_{1/2}(^{68}Ga)$ = (68.0 ± 0.2) min, used for these measurements is an average of the data, the error being the internal error of the values reported.

^{66}Ga and ^{68}Ga have different decay schemes but similar half-lives thus allowing natural copper to be used as the target. Measurements were made with evaporated targets on W backings (400 and 580 μg/cm^2 as determined by a quartz-crystal monitor) and oxygen-free high-conductivity (OFHC) copper foils (1640 μg/cm^2 as determined by weighing). For reference, a 10 MeV alpha beam loses about 300 keV in 1000 μg/cm^2 Cu.

The off-line geometry was used. The timing for each bombardment was different but was carefully noted. In general, for low energies

($E \leq 12$ MeV), the bombardment lasted an hour, and as the energy (and yield) increased, the length of the bombardments was decreased. At least two counting periods were taken within the first hour after bombardment. Approximately 12 to 18 hours after bombardment, the delayed activity was remeasured. There was no indication of gamma rays associated with decays other than ^{66}Ga, ^{68}Ga, room background, and products of (α,n) reactions on the backing.

6. $^{63}Cu(p,n)^{63}Zn$

This reaction is of interest as one can compare its cross section to that of alpha bombardment of ^{63}Cu. The Q values and delayed gamma activities for the products of Cu + p are shown in Table VIII. Because of the long half-life of ^{65}Zn(244 d), the yield of the 1.115 MeV γ-ray is small. Thus the $^{65}Cu(p,n)^{65}Zn$ cross section was not measured even though natural Cu targets (those from the Cu + α measurements) were used.

The decay of ^{64}Zn has been well studied (Kiuru and Holmberg 1970, Bocnert 1969, and de Frenne et al 1967). The weighted average of these measurements after correcting for electron capture (Gove and Martin 1971) shows that the 688-keV gamma ray appears in $(8.44 \pm 0.15)\%$ of the ^{63}Zn decays while the 963-keV gamma ray appears in $(6.63 \pm 0.17)\%$. The half-life, (38.4 ± 0.1) min, comes from the average of values appearing in Collé et al (1974).

The reaction was studied in coarse steps (about 500 keV at low energies, 1 MeV for high energies) from threshold to 12 MeV in order to obtain the general shape and magnitude of the cross section. As with

Cu + α , the timing was not fixed, being longer when the yield was low. For all energies two successive counting periods were used, each lasting a half-life.

IV. EXPERIMENTAL RESULTS

A. Introduction

This section deals with the spectra obtained and the cross sections determined for the six reactions measured. Also included are results from previous investigators.

B. $^{23}Na(p,n)^{23}Mg$

A typical spectrum is shown in Figure 8. The half-life for the annihilation radiation was obtained for each bombarding energy and agreed with the known half-life of ^{23}Mg. As a further check the ratio of the 440-keV gamma ray to the annihilation radiation was obtained for each energy and it too was found to be a constant.

The cross section as a function of energy is shown in Figure 9 with an insert showing an expanded view of the cross section around the neutron threshold. The values of the cross sections are also given in Table IX.

An interesting feature of the excitation function is the resonance-like behavior just above threshold. This is not an effect of $^{23}Na(p,n_1)^{23}Mg$ as the threshold for that reaction is significantly higher in energy. Endt and van der Leun (1973) in their compilation list no low-spin level in ^{24}Mg at the appropriate energy (only states with $J \geq 6$ are listed). Low spin is suggested because of the strength of the resonance so near the threshold of ^{23}Mg $(J = 3/2) + n$. Other structure is also present; even though at the (p,n) threshold, the

compound nucleus excitation is 16.5 MeV and the level density is predicted to be high (220 states/MeV from the parameters of Gilbert and Cameron 1965a) which should wash away most nuclear structure effects. After this "bumpy" region is passed, the cross section flattens out to remain constant at about 100 mb from about 1 MeV above threshold to the highest energy measured (E_{cm} = 10.2 MeV).

The cross section for $^{23}Na(p,n)^{23}Mg$ has only been measured once before (Blaser et al 1951). Rough agreement for energies near threshold can be obtained if their energy scale is shifted by 150 keV. However, for energies greater than 6 MeV, the present results are higher.

C. $^{35}Cl(\alpha,n)^{38}K$

Typical spectra are shown in Figures 10 and 11. Figure 10 shows the delayed gamma radiation following bombardment of $BaCl_2$ with 8 MeV alphas, taken with a NaI detector, while Figure 11 shows the results for the same bombarding energy when a Ge(Li) detector is used. The improvement in resolution when using a Ge(Li) detector is striking. The large peaks between the 0.51 and 2.17-MeV photopeaks are the single- and double-escape peaks of the 2.17-MeV gamma ray.

The cross section for the $^{35}Cl(\alpha,n)^{38}K$ (ground state) reaction is shown in Figure 12. This figure shows the part of the (α,n) cross section which populates either the ground state of ^{38}K or levels in ^{38}K which then gamma decay directly or indirectly to the ground state. The cross section for $^{35}Cl(\alpha,n)^{38}K$ (isomeric state) is also shown in Figure 12. The total $^{35}Cl(\alpha,n)^{38}K$ reaction cross section (regardless of which level is populated) is shown in Figure 13, i.e., the sum of the cross

sections presented in Figure 12, since even at the highest bombarding energies used in this experiment all states populated in ^{38}K are particle bound. The cross sections are also tabulated in Table X.

The $^{35}Cl(\alpha,n)^{38}K$ (ground state) cross section has also been measured by Howard et al (1974). The agreement is very good.

D. $^{59}Co(\alpha,n)^{62}Cu$

The spectrum of the delayed gamma radiation for the first counting interval for 14-MeV alpha bombardment of Co is shown in Figure 14. Besides the peak at 511 keV the only other peaks in the spectrum are the Pb X-rays (at low energy) and the weak gamma rays (0.88 and 1.17 MeV) associated with the ^{62}Cu decay. Because the 0.88 and 1.17 MeV gamma rays were so weak, the cross section was inferred from the difference of the annihilation yield in two successive counting intervals. The difference, rather than the sum, was used to reduce the effect of any long-lived contaminant. The half-life for each bombarding energy was calculated and found to agree with the accepted value for the half-life of ^{62}Cu.

The reaction cross section for $^{59}Co(\alpha,n)^{62}Cu$ is shown in Figure 15 and tabulated in Table XI. Only that part of the cross section which populated states that decay to the ground state of ^{62}Cu is included. The threshold for sequential particle emission (5.9 MeV for p , 5.4 MeV for α , and 8.9 MeV for n) are shown at the appropriate energies in Figure 15. Because of the large Coulomb barrier, a state unbound to charged-particle emission may yet gamma decay preferentially.

Also shown in Figure 15 is the work of previous investigators (Stelson and McGowan 1964, D'Auria et al 1968, and Zhukova et al 1973). The agreement among the various groups is good, except for a few isolated points. The turning over of the cross section at the highest energies is due to the $(\alpha,2n)$ reaction taking strength from the (α,n) channels.

E. $^{63}Cu(\alpha,n)^{66}Ga$ and $^{65}Cu(\alpha,n)^{68}Ga$

One of the spectra of the delayed gamma radiation following the 14.5-MeV alpha bombardment of Cu is shown in Figure 16. Gamma rays from ^{66}Ga and ^{68}Ga are seen. The gamma ray at 1039 keV was used to infer the ^{66}Ga cross section, the line at 833 keV providing a check that the yield was due to ^{66}Ga and not from some other decay. The threshold for $^{65}Cu(\alpha,3n)^{66}Ga$ is above the energy range of these measurements and hence does not confuse the assignment of the production of ^{66}Ga. The 1078-keV gamma ray was used to infer the production of ^{68}Ga.

The cross sections for $^{63}Cu(\alpha,n)^{66}Ga$ are shown in Figure 17 and tabulated in Table XII. Again only that part of the cross section which populates states in the residual nucleus which gamma decay are included. The thresholds for competing three-body reactions are shown in Figure 17 at the appropriate energies (3.3 MeV for $n\alpha$, 5.1 MeV for np, and 9.1 MeV for $2n$).

The cross sections for $^{65}Cu(\alpha,n)^{68}Ga$ are shown in Figure 18 and tabulated in Table XIII. As previously, the three-body part of the cross section which proceeds through the residual nucleus of interest

(in this case, ^{68}Ga) is not included. The thresholds for such three-body reactions are shown in Figure 18 at the appropriate energies (4.1 MeV for $n\alpha$, 6.5 MeV for np , and 8.3 MeV for $2n$).

Previous work on (α,n) reaction cross sections on Cu are shown on the appropriate figures (Stelson and McGowan 1964, Porile and Morrison 1959, Bryant et al 1963, and Hille et al 1972). The agreement is good except for the old data of Porile and Morrison.

F. $^{63}Cu(p,n)^{63}Zn$

One of the spectra of the delayed gamma radiation following the 8-MeV proton bombardment of Cu is shown in Figure 19. The gamma rays at 670 and 962 keV result from the decay of ^{63}Zn. Since the annihilation radiation remained proportional to the two gamma-ray lines, all three lines were used to infer the relative cross section for $^{63}Cu(p,n)^{63}Zn$. The lines at 670 and 962 keV were used to find the normalization constant.

The cross sections for the $^{63}Cu(p,n)^{63}Zn$ reaction are tabulated in Table XIV and displayed in Figure 20. Also shown in Figure 20 are the recent data of Collé et al (1974), who also give a review of the extensive work that has been performed on this reaction. As can be seen, the agreement between the data sets is good.

The highest bombarding energy used in this measurement was not sufficient to reach particle-unbound states in ^{63}Zn, and thus the cross sections obtained are the totals for the $^{63}Zn + n$ channels.

V. COMPARISON WITH HAUSER-FESHBACH CALCULATIONS

A. Introduction

The predictions of the statistical model of nuclear reactions depend on Q values, the properties (energy, spin, and parity) of the various states of each nucleus involved, and the potentials used to generate the transmission coefficients. Not all of these quantities can be determined from the measurements reported here. In fact, these measurements will only be able to determine how well the theory (with previously established parameters) can do. Fortunately, the Q values involved are well known (see the 1971 Mass Tables of Wapstra and Gove). Also, many level properties can be inferred from earlier nuclear-structure experiments and from level-density calculations and models.

The potentials are the most uncertain input. For the nuclei where potentials have been deduced from elastic scattering, the energies involved (particularly for the alpha-nucleus potentials) are much higher than those used here. More often, no elastic-scattering data exist, so the optical potential cannot be inferred. Thus one is forced to use "global" potentials which are a compromise between the number of parameters used and the goodness of fit.

For the calculations reported here, three sets of potentials were used for each reaction pair. For the neutron-nucleus potentials, the global potentials were from Becchetti and Greenless (1969a), Wilmore and Hodgson (1964), as revised by Hodgson (1967), and Michaud and Fowler (1970a). For the proton-nucleus potentials, the potentials of Becchetti and Greenlees, Perey (1963), and Michaud and Fowler were used. For the alpha-nucleus potentials, the potentials of Michaud and Fowler, Igo (1959a and 1959b) and McFadden and Satchler (1966) were used.

Since the parameters of Wilmore and Hodgson were derived from the non-local potential of Perey and Perey (1963), these parameters were paired with the proton parameters of Perey. Nine different potential sets for each reaction (3 nucleon x 3 alpha) were used rather than 27 (3 neutron x 3 proton x 3 alpha) so as not to use extensive computer time.

B. $^{23}Na(p,n)^{23}Mg$

Since much is known about the states populated in $^{23}Na + p$, the $^{23}Na(p,n)^{23}Mg$ might seem an excellent test of the statistical model. However, the target nucleus is deformed and there are relatively few particles in the compound system. Thus the predictions may not be as valid as the extensive knowledge of level information might otherwise imply.

A ladder diagram showing the products of $^{23}Na + p$ is shown in Figure 21. Levels up to 11 MeV in ^{20}Ne (Ajzenberg-Selove 1972) were used in the calculations, while 12 levels were used for ^{23}Na (up to 4.8 MeV excitation energy) and 11 levels for ^{23}Mg (up to 4.4 MeV). More levels were not included as the compilation of Endt and van Leun (1973) does not have spin information for states just higher than the cutoff energies used.

For proton bombardment on Na all channels are important; so all nine sets of potentials were used. The predictions (divided by the experimental cross sections) are shown in Figure 22 for the potentials of Michaud and Fowler and for the alpha potential of Igo with the nucleon potentials of Perey and of Wilmore and Hodgson. When the alpha potential of McFadden and Satchler is used, very little difference is seen (less

than 5%) from the results using the alpha potential of Michaud and Fowler. The results of potential sets not shown in Figure 22 lie in between the two shown.

Even though the level and Q value information is well known for the various channels, as can be seen from Figure 22, none of the potential sets leads to a good fit to the data. The predictions are generally however, within a factor of 2 of the measured values, which may be considered good agreement, since the potentials were derived for more massive nuclei.

The parameters in the level density formula are not the cause of the disagreement as they play no role below E_{cm} = 7 MeV and only a very minor role (< 10%) at the highest bombarding energy used. Rather a possible explanation for the overestimates may be found in the presence of direct reactions. Hellstrom et al (1970) and Vasil'ev et al (1968) have, by looking at the inelastic scattering of protons on Na at 8 to 12 MeV and at 6.5 MeV, respectively, shown that a large amount of the inelastic cross section proceeds through direct reactions. The presence of this direct component "robs" from the (p,n) channels since (p,n) is less likely to be involved in a direct reaction process that the ground state band members populated in (p,p'). Following this line of argument, the statistical model should overpredict (p,α) and (p,n) channels and underpredict the (p,p') channels. From the data of Hellstrom et al and Mann et al (1975) for the proton channels, the present data for the neutron channels, and Warsh et al (1963) for the alpha channels, this appears to be the case.

C. $^{35}Cl(\alpha,n)^{38}K$

The level information for the channels populated by the $^{35}Cl + \alpha$ reaction is nearly as complete as for the $^{23}Na + p$ reaction. Moreover, more particles are involved in the compound nucleus (making resonance structure such as is present in the ^{24}Mg compound system unlikely here) and the incident particle is an alpha particle rather than a nucleon (making direct reactions less likely).

The level information (from the compilation of Endt and van der Leun 1973) for the reaction products is shown in Figure 23. Five levels were explicitly included in ^{38}K (up to 2.41 MeV), 10 in ^{38}Ar (to 4.81 MeV) and 7 levels in ^{35}Cl (to 3.26 MeV). More levels were not included because of the absence of spin information. Above the last included level, the level density parameterization of Gilbert and Cameron (1965a) was used.

Again, all the channels are important in the calculation, so nine sets of potentials were used. In Figure 24 appear results of four of the potential sets divided by the experimental results. Both the theory and experiment are for all neutron channels (i.e., the yield to the ground and isomeric states having been added). The results calculated using the alpha potential of McFadden and Satchler are very similar to those of Michaud and Fowler and the results using the nucleon potentials of Becchetti and Greenlees are very similar to those using the potentials of Perey and of Wilmore and Hodgson.

As can be seen from Figure 24, the potentials of Michaud and Fowler fit the data extremely well. The dip at high energies occurs when the neutron level-density parameterization becomes significant and

suggests that the predicted density of states may be too low. The calculations using the other potentials predict too much (α,n) cross section, but the agreement is not bad (about 50% high on average).

Figure 25 shows the prediction of the calculation using the potentials of Michaud and Fowler for the ground state and isomeric state of ^{38}K (divided by the observed values). Because spin information is only known up to the state at 2.41 MeV, the predicted cross sections must stop at E_{cm} = 8.5 MeV so that states with unknown spin (but known gamma branching) will not contribute. Below E_{cm} = 8.5 MeV, excited states in ^{38}K decay only to the isomer. As can be seen, the predictions fit the ground-state and isomeric-state reactions with excellent agreement. It should be noted that the potential of McFadden and Satchler provides similar results.

D. $^{59}Co(\alpha,n)^{62}$

The level information for the channels involved in this reaction is much poorer than for either the ^{23}Na + p or for the ^{35}Cl + α reaction. Not only is less known about the excited states of the nuclei involved in this reaction, but also the center-of-mass energies reached are much higher. However, because of the large Coulomb barrier for charged particles, most of the flux from the compound system is in the neutron channel (approximately 85% using the level density of Dilg et al 1973). Thus changes in the level-density parameters will cause small changes in the predicted (α,n) cross sections but cause large changes in the (α,α') and (α,p) channels. For example, doubling the number of levels in the neutron channel will change the predicted (α,n) cross

section by less than 10%, but will change the (α,α') and (α,p) cross sections by nearly a factor of 2.

Because most of the flux is in the neutron channel, only the potential which determines the total reaction cross section is important. Changes in the other potentials do not greatly affect the (α,n) cross section. Changes in the alpha potential do vary the predicted (α,n) cross sections as these vary the cross section for formation of the compound nucleus on which the (α,n) reaction depends linearly.

The ladder diagram for the products of $^{59}Co + \alpha$ is shown in Figure 26. The discrete level information is from Coop et al (1970) and Vervier (1968) for ^{59}Co (8 levels), from Verheul (1967a) and van Patter et al (1970) for ^{62}Ni (6 levels) and from Daehnick et al (1973) for ^{62}Cu (14 levels). Even though many levels are explicitly included in the calculation, the level information is sparse above 2.5-MeV excitation energy. Above the last included level, the level density of Dilg et al was used. The parameters for ^{62}Cu were obtained from their default parameters, equations 62 and 63.

A feature not present in the low energy measurements of the $^{23}Na(p,n)^{23}Mg$ and $^{35}Cl(\alpha,n)^{38}K$ cross sections is the presence of particle unbound levels. If these levels are excited in the reaction, they may not decay to the ground state of ^{62}Cu and the high-energy part of the calculated excitation function will be increased. Figure 27 presents the predicted cross section as a function of the degree of unboundness. The need to incorporate this competition is evident from the experimental data shown in Figure 15 which decrease at high energy.

In Figure 28 are shown the results of the calculations (divided by the experimental cross sections) for the nucleon potentials of

Becchetti and Greenlees and the 3 sets of alpha potentials. As is noted above, the use of different nucleon potentials does not significantly change the results. The alpha potential of McFadden and Satchler agrees with the experimental data better than do the other two alpha potentials. If one compares the theoretical calculations to the $^{59}Co(\alpha,p)^{62}Ni$ cross sections as measured by Lassen and Sidorov (1960), the potential of McFadden and Satchler again does well. This conclusion must be tempered by noting that this cross section is very dependent upon the parameters taken for the various level densities. The potential of Igo does almost as well for both $^{59}Co(\alpha,n)$ and (α,p).

D'Auria et al (1968) have measured $^{59}Co(\alpha,n)$, (α,p), and (α,α'). Their values disagree with other workers. However, because of the strong dependence on level-density parameters, their cross sections can be obtained if the level-density parameters are allowed to vary enough.

E. $^{63}Cu(\alpha,n)^{66}$

Because of the highly negative Q value for the (α,n) reaction on ^{63}Cu as compared with the (α,α) and (α,p) reactions, the (α,n) cross section is not as large a percentage of the total reaction cross section as for the (α,n) reactions on ^{59}Co or ^{65}Cu. However, at several MeV above threshold, the Coulomb barrier still retards charged-particle emission enough so that the Hauser-Feshbach model predicts that neutron channels should take 2/3 of the total reaction cross section.

Again, level information is scarce. The discrete level information is taken from Smith et al (1968) for ^{63}Cu (9 levels), from Hudson and Glover (1972) for ^{66}Zn, and from Najam et al (1971) for ^{66}Ga. Again,

the level-density parameters of Dilg et al were used when the known level information ran out. A ladder diagram showing the levels is presented in Figure 29.

In Figure 30 are shown the predictions of the statistical model divided by the experimental values. The effect of particle unbound levels was treated in the same manner as for $^{59}Co(\alpha,n)^{62}Cu$. Two curves are shown, the lower from the alpha potential of Michaud and Fowler, the upper from the alpha potential of Igo. The choice of the nucleon potential made very little difference. As in previous examples, the potential of McFadden and Satchler was between the other two alpha potentials. All potentials give comparable predictions for this cross section.

The $^{63}Cu(\alpha,p)^{66}Zn$ data of Lassen and Sidorov can be used as a further test of the model. Again, good agreement is obtained with each set of potentials.

F. $^{65}Cu(\alpha,n)^{68}Ga$

The Q value for this reaction is 2 MeV lower than for the $^{63}Cu(\alpha,n)^{66}Ga$ reaction. Thus the reaction $^{65}Cu(\alpha,n)$ should have a larger cross section than for the (α,n) reaction on ^{63}Cu. Experimentally and theoretically this is the case.

The level information (shown in Figure 31) comes from Smith et al for ^{65}Cu, from Glover and Hudson (1972) for ^{68}Zn, and from Rao (1968) for ^{68}Ga. The level density parameters are from Dilg et al.

Figure 32 shows the predicted values for the $^{65}Cu(\alpha,n)^{68}Ga$ reaction divided by the measured values. The higher curve uses the alpha potential of Igo, while the lower curve uses the potential of Michaud-Fowler,

the results from the McFadden-Satchler potential falling in between. The choice of the nucleon potentials does not make much difference. The potential of Igo fits the data much better than do the other two potentials. This may be due to the isospin and mass dependence Igo uses for the imaginary-potential depth. Neither Michaud and Fowler nor McFadden and Satchler include such a term. The dependence of the imaginary-potential depth on mass and isospin seems well established for nucleon potentials (compare the potentials in Tables I and II) and such a term may be needed in the alpha potential as well.

The $^{65}Cu(\alpha,p)^{68}Zn$ cross sections of Lassen and Sidorov (1960) are much lower than the values predicted by the theory. This most likely results from an incorrect parameter in the neutron level density parameterization. Changing these parameters would have little effect on the (α,n) cross section but the predicted (α,p) could be lowered significantly.

G. $^{63}Cu(p,n)^{63}Zn$

This reaction is a good test of the statistical theory because information exists not only for the (p,n) reaction but also for the (p,p') and (p,α) reactions. Also, since the $|Q|$ value for the (p,n) reaction is fairly high, the other channels are likely to have a sizable cross section.

The largest uncertainty in the comparison between theory and experiment for this system is the almost total lack of knowledge of the level structure in ^{63}Zn. The levels of ^{63}Cu are known from the work of Smith et al (1968) and levels in ^{60}Ni are known from the work of Ronsin

et al (1973). However, only the first two states of ^{63}Zn have definite spin and parity assignments (Verheul 1967b). One is forced to rely heavily upon the level-density parameters which, as for all the work around the A = 60 region presented in this thesis, is from Dilg et al (1973). A ladder diagram for the $^{63}Cu + p$ system is shown in Figure 33.

Figure 34 shows the results of the statistical theory for different values of the "level-density parameter", parameter a of equation 47, for ^{63}Zn. It can be seen that this parameter strongly affects the predicted cross section. If the value for a is taken from the default equation of Dilg et al (equation 62), then the (p,n) cross section is underpredicted as can be seen by comparing Figures 20 and 34. Although the potentials used to generate the transmission coefficients might be incorrect and thus cause the difference between theory and experiment, this is unlikely because the total reaction cross section for $^{63}Cu + p$ is predicted correctly and the (p,p) and (p,α) reactions are overpredicted. This suggests that the more likely cause for the disagreement lies with the level density information. This is fairly well known for ^{60}Ni and ^{63}Cu, but as noted above the information is almost totally absent for ^{63}Zn. Therefore, the a parameter for ^{63}Zn was increased by 25%, so that theory and experiment would agree for the (p,n) cross sections for $E_{cm} \sim 10$ MeV.

In Figure 35 the theoretical predictions divided by the measured values are presented for (p,n), (p,p'), and (p,α) reactions on ^{63}Cu. The experimental values for ^{63}Cu(p,p') and ^{63}Cu(p,α) are from Benveniste et al (1961). It can be seen that the various potentials do quite well. The small discrepancies between theory and experiment can be made to

vanish by very small changes in the level density parameters.

It should be noted that although the $^{63}Cu(p,\alpha)^{60}Ni$ reaction cross section is well predicted if all alpha groups are included in the calculation, if one compares the data of Kumabe et al (1963) for the cross sections for individual alpha groups, then as the bombarding energy increases, the theoretical values are too low. This discrepancy can be attributed to the increasing presence of direct reactions, since Kumabe et al have showed that at 11 MeV the (p,α_0) cross section proceeds 50% of the time via direct reactions, the (p,α_1) cross section 30%, and the $(p,\alpha_2+\alpha_3)$ 15%. These estimates are obtained from the asymmetry of the measured angular distribution around 90^o.

Because of the presence of direct reactions and the uncertainty of the level-density parameters, little comment can be made concerning which potentials fit the data best. However, all potentials seem to be able to predict cross sections within 50% when using a "level-density parameter" for the neutron channels slightly higher than given by the default equation of Dilg et al. It should be remembered that this agreement is for each of the reaction pairs.

VI. CONCLUSIONS

All the remarks in this section must be tempered in view of the small number of reactions studied, i.e., although these reactions are presumably typical of the mass regions of the various targets, only a limited sample is used. Also only a small number of potentials were studied. The potentials studied are the potentials that have usually been used by various groups, but they by no means exhaust all significant possibilities.

As seen, especially in the case of $^{63}Cu + p$, an accurate knowledge of level information is required. Discrete level information is preferred, but a level-density parameterization is quite adequate if only cross sections averaged over many hundreds of keV are desired. Unfortunately, except for a few nuclei (most alpha-cluster nuclei with low mass numbers), the knowledge of the energies, spins, and parities of discrete states ends at a quite low excitation energy. Level-density parameterizations are plagued by the uncertainty as to which formula (or formulas) should be used and what values the parameters should take. This is particularly true for masses below $A = 40$ where the standard assumption of equal numbers of even and odd parity states breaks down even for energies above 8 MeV. Also, for many nuclei the level density has not been measured at any energy, so global prescriptions (such as equations 52-59 and 63-64) must be used. As can be seen in the case of $^{63}Cu + p$, such a global description can lead to a very inaccurate prediction.

The choice of the best potential to use in a statistical-model calculation is difficult. Obviously, wherever possible the potentials derived from elastic scattering for that projectile and target in the observed energy range should be used. Since such potentials are rarely available, one must often rely on a global potential. Using the limited data base presented, the nucleon potentials of Becchetti and Greenlees (1969a) and the alpha potential of McFadden and Satchler (1966) most often seem to predict accurately the observed cross sections. The proton potential of Perey (1963) and the neutron potential of Wilmore and Hodgson (1964) as revised by Hodgson (1967) also seem to fit the data well in most cases.

It should be noted that using any of the potentials and any of the established sets of level-density parameterizations, the predicted cross sections are almost always within a factor of two of the measured values. This is true even when direct-reaction mechanisms are involved or when the level-density parameterization is (seemingly) incorrect. Thus one can be fairly sure that the predicted cross sections for an arbitrary reaction (for nuclei not too far from the region of known parameters) should yield values which reasonably approximate the true values. The charged-particle cross-section compilations of McGowan and Milner (1973) and of the Nuclear Data Group will prove useful in providing test cases in the mass region of interest if a set of potentials is to be examined.

A word of caution must be inserted about low-energy cross sections. Not only is the model on much less firm footing (as resonances

do not necessarily overlap and the resonance properties do not average), but gamma-ray transmission coefficients and fluctuation corrections must be included. For the cases studied here, these were unimportant (except, maybe, at the lowest energies measured). However, for low-energy bombardment, particularly when the neutron channels have not yet opened, the fluctuation corrections can vary the predicted cross section by twofold, and the gamma-ray channel may be by far the most important channel.

However, with these provisions, it can be seen that the statistical model of nuclear reactions can provide a useful guide to cross sections which cannot be measured in the laboratory (for example, the hundreds of cross sections needed for nucleosynthesis calculations (Clayton and Woosley 1973) or which are difficult to measure (for example, (n,α) reactions on materials to be used for reactor walls). With moderate computational time and cost, fairly accurate information can be obtained.

REFERENCES (Part 2)

Ajzenberg-Selove, F. 1972, Nucl. Phys. A190, 1.

Alburger, D. 1974, Phys. Rev. C9, 991.

Arnett, W. D. and Truran, T. W. 1969, Astrophys. J. 157, 339.

Austern, N. 1961, Ann. Phys. 15, 299.

Aver'yanov, I. K. and Purtseladze, Z. Z. 1967, Yad. Fiz. (SSSR) 6, 293 or Sov. J. Nucl. Phys. 6, 212.

Azuelos, G., Crawford, J. E., and Kitching, J. E. 1974, Phys. Rev. C9, 1213.

Bargmann, V. 1949a, Phys. Rev. 75, 301;
1949b, Rev. Mod. Phys. 21, 488.

Bashkin, S., Kavanagh, R. W., and Parker, P. D. 1959, Phys. Rev. Lett. 3, 518.

Becchetti, F. D. Jr. and Greenlees, G. W. 1969a, Phys. Rev. 182, 1190.

Becchetti, F. D. Jr. and Greenlees, G. W. 1969b, Annual Report of the J. H. Williams Laboratory of Nucl. Physics, University of Minn.

Benveniste, J., Booth, R., and Mitchell, A. 1961, Phys. Rev. 123, 1818.

Bethe, H. A. 1935, Phys. Rev. 47, 747;
1936, Phys. Rev. 50, 332;
1937, Rev. Mod. Phys. 9, 69.

Blaser, J. P., Boehm, F., Marmier, P., and Scherrer, P. 1951, Helv. Phys. Acta 24, 465.

Bocnert, I. 1969, Z. Phys. 223, 473.

Bonr, N. 1936, Nature 137, 344.

Bollinger, L. M. and Thomas, G. E. 1970, Phys. Rev. C2, 1951.

Bormann, M. E., Fretwurst, E., Schehka, P., Wiege, G., Büttner, H., Linder, A., and Meldner, H. 1965, Nucl. Phys. 63, 438.

Breit, G. and Wigner, E. P. 1935, Phys. Rev. 48, 918 (L).

Brink, D. M. and Rowley, N. 1974, Nucl. Phys. A219, 79.

Broglia, R. A. and Winther, A. 1972, Phys. Rep. 4C, 153.

Browne, J. C., Newson, H. W., Bilpunch, E. G., and Mitchell, G. E. 1970, Nucl. Phys. A153, 481.

Bryant, E. A., Cochran, D.R.F., and Knight, J. D. 1963, Phys. Rev. 130, 1512.

Buck, B. 1963, Phys. Rev. 130, 712.

Cage, M. E., Cole, A. J., and Pyle, G. J. 1973, Nucl. Phys. A201, 418.

Cameron, A.G.W. and Elkin, R. M. 1965, Can. J. Phys. 43, 1288.

Camp, D. C. and Langer, L. M. 1963, Phys. Rev. 129, 1782.

Camp, D. C. and Meredith, G. L. 1971, Nucl. Phys. A166, 349.

Carter, H. K., Hamilton, J. H., Ramayya, A. V., and Pinajaiin, J. J. 1968, Phys. Rev. 174, 1329.

Chrisler, D. F., Eldridge, H. B., Kunselman, R., and Zaidins, C. S. 1972, Phys. Rev. C5, 419.

Clark, G. J., Draper, J. E., Freeman, J. M., Ryder, J. S., Burcham, W. E., and Squier, G.T.A 1972, AERE (Harwell) Nucl. Phys. Div. Prog. Report, March 23.

Clayton, D. D. and Woosley, S. G. 1973, Proceedings of Int. Conf. Nucl. Phys. (Munich). Vol. 2, p. 717.

Cline, J. E. and Chagnon, P. R. 1957, Phys. Rev. 108, 1495.

Collé, R., Kishore, R., and Cumming, J. B. 1974, Phys. Rev. C9, 1819.

Coop, K. L., Graham, I. G., and Titterton, E. W. 1970, Nucl. Phys. A150, 346.

Cowell, P. H. and Crommelin, A.C.D. 1910, Appendix to Greenwich Observatories for 1909, Edinburgh.

Daehnick, W. W., Park, Y. S., Dittmer, D. L. 1973, Phys. Rev. C8, 1394.

D'Auria, J. M., Fluss, M. J., Kowalski, L., and Miller, J. M. 1968, Phys. Rev. 168, 1224.

deFrenne, D., Dorikens, M., Dorikens-Vanpraet, L., and Demuynik, J. 1967, Nucl. Phys. 103, 203.

Détraz, C., Moss, C. E., and Zaidins, C. S. 1971, Phys. Lett. 34B, 128.

Dilg, W., Schantl, W., Vonach, H., and Uhl, M. 1973, Nucl. Phys. A217, 269.

Ebrey, T. G. and Gray, P. R. 1965, Nucl. Phys. 61, 479.

Endt, P. M. and van der Leun, C. 1973, Nucl. Phys. A214, 1.

Engelbrecht, C. A. and Fiedelberg, H. 1967, Ann. Phys. 42, 262.

Engelbrecht, C. A. and Weidenmüller, H. A. 1974, Phys. Rev. C8, 859.

Facchini, U., and Saetta-Menichella, E. 1968, Energia Nucleare 15, 54.

Fernbach, S., Serber, R., and Taylor, T. B. 1949, Phys. Rev. 75, 1352.

Fernbach, S., Heckrothe, W., and Lepore, J. V. 1955, Phys. Rev. 97, 1059.

Feshbach, H. 1958, Ann. Phys. 5, 357.

Forest, A. E. 1965, Thesis, Oxford (unpublished): quoted by P. E. Hodgson in Adv. Phys. 15 (1966) 329.

Fox, G. 1973, private communication.

Fox, L., and Goodwin, E. T. 1949, Proc. Cambridge Phil. Soc. 45, 373.

Freeman, J. M. and Jenkin, J. G. 1966, Nucl. Inst. and Meth. 43, 269.

French, W. R., LaShure, R. L., and Curran, J. L. 1969, Amer. J. Phys. 37, 11.

Friedman, F. L. and Weisskopf, V. F. 1955, "The Compound Nucleus" in Niels Bohr and the Development of Physics (W. Pauli, ed.)

Gadioli, E. and Zetta, L. 1968, Phys. Rev. 167, 1016.

Gel'fand, I. M. and Levitan, B. M. 1951a, Doklady Akad. Nauk SSSR 77, 557.

Gel'fand, I. M. and Levitan, B. M. 1951b, Isv. Akad. Nauk. SSSR 15, 309.

Gerhart, J. B., Carlson, B. C., and Sherr, R. 1954, Phys. Rev. 94, 917.

Gilbert, A. and Cameron, A.G.W. 1965a, Can. J. Phys. 43, 1446.

Gilbert, A., Chen, F. S., and Cameron, A.G.W. 1965b, Can. J. Phys. 43, 1248.

Glassgold, A. E. and Kellogg, P. J. 1957, Phys. Rev. 107, 1372.

Gobbi, A. 1971, Conference on Heavy Ion Scattering (Argonne), p. 63.

Gorlov, G. V., Lebedeva, N. S., and Morozov, V. M. 1967, Yad. Fiz. SSSR 5, 910, or Sov. J. Nucl. Phys. 5, 663.

Gorodetzky, S., Aslanides, E., Gallmann, A., and Frick, G. 1968, Nucl. Phys. A109, 417.

Goss, J. D., Riffle, F. L., Parsignault, D. R., and Harris, J. C. 1968 Nucl. Phys. A115, 113.

Gove, H. B. and Martin, M. J. 1971, Nucl. Data Tables 10, 205.

Greenlees, G. W., Pyle, G. J., and Yang, Y. C. 1968, Phys. Rev. 171, 1115.

Greenlees, G. W., Makofske, W., and Pyle, G. J. 1970a, Phys. Rev. C1, 1145.

Greenlees, G. W., Knizdo, V., Karban, O., Lowe, J., and Makofske, W. 1970b, Phys. Rev. C2, 1063.

Grodstein, G. 1957, Nat. Bur. Std. (U.S.A.) Circ. #583.

Hardy, J. C. and Alburger, D. E. 1972, Phys. Lett. 42B, 341.

Heath, R. L. 1964, Scintillation Spectrometry: Gamma Ray Spectrum Catalogue, 2nd ed. Phillips Petroleum Co. Report IDO-16880 (unpublished).

Heitler, W. 1954, The Quantum Theory of Radiation, 3rd ed., Clarendon Press.

Hellstrom, J., Dallimore, P. J., and Davidson, W. F. 1970, Nucl. Phys. A144, 654.

Hentschel, E. and Heinreich, E. G. 1970, Nucl. Phys. A144, 92.

Hille, M., Hille, P., Uhl, M., and Weisz, W. 1972, Nucl. Phys. A198, 625.

Hodgson, P. E. 1967, Ann. Rev. Nucl. Sci. 17, 1.
1971, Nuclear Reactions and Nuclear Structure, Clarendon Press.

Horen, D. J. 1959, Phys. Rev. 113, 572.

Howard, A. J., Jensen, H. B., Rios, M., Fowler, W. A., and Zimmerman, B. A. 1974, Astrophys. J. 188, 131.

Hudson, F. R. and Glover, R. N. 1972, Nucl. Phys. A189, 264.

Huizenga, J. R. and Katsanos, A. A. 1967, Nucl. Phys. A98, 64

Huizenga, J. R., Vonach, H. K., Katsanos, A. A., Gorski, A. J., and Stephen, C. J. 1969, Phys. Rev. 182, 119.

Igo, G. 1959a, Phys. Rev. 115, 1665.
1959b, Phys. Rev. Lett. 3, 308.

Jensen, J.H.D. and Luttinger, J. M. 1952, Phys. Rev. 86, 907.

Jongsma, H. W., Bengtssom, B., Dufler, G. H., and Verheul, H., 1969 Physica 42, 303.

Katsanos, A. A., Shaw, R. W., Vandebusch, R. , and Chamberlain, D. 1970, Phys. Rev. C1, 594.

Kavanagh, R. W., Gallmann, A., Aslanides, E., Jundt, F., and Jacobs, E. 1968, Phys. Rev. 175, 1426.

Kidawai, H. and Rook, J. R. 1971, Nucl. Phys. A169, 417.

Kiuru, A. and Holmberg, P. 1970, Z. Phys. 233, 146.

Kopsch, D. and Cierjacks, S. 1972, Statistical Properties of Nuclei (ed., J. B. Garg), Plenum Press.

Kumabe, I., Ognata, H., Komatuzaki, T., Inoue, N., Tomita, S., Yamada, Y., Yamaki, T., and Matsumoto, S. 1963, Nucl. Phys. 46, 454.

Kümmel, H., Mattauch, J.H.E., Thiele, W., and Wapstra, A. H. 1966, Nucl. Phys. 81, 129.

Lang, D. W. 1966, Nucl. Phys. 77, 545.

Lang, J.M.B. and LeCouteur, K. J. 1954, Proc. Phys. Soc. A67, 585.

Lassen, N. O. and Sidorov, V. A. 1960, Nucl. Phys. 19, 579.

Lederer, C. M., Hollander, J. M., and Perlman, I. 1967, Table of Isotopes, 6th ed., John Wiley and Sons, Inc.

Legrand, J. 1973, Nucl. Inst. and Meth. 112, 229.

Lindstrom, D. P., Newson, H. W., Bilpunch, E. G., and Mitchell, G. E. 1971, Nucl. Phys. A168, 37.

Lu, C. C., Vaz, L. C., and Huizenga, J. R. 1972a, Nucl. Phys. A190, 289.

Lu, C. C., Vaz, L. C., and Huizenga, J. R. 1972b, Nucl. Phys. A197, 321.

Mak, H. B. and Mann, F. M. 1973, private communication.

Mann, F. M. and Kavanagh, R. W. 1974, private communications, and submitted for publication.

Mann, F. M., Kneff, D. W., and Switkowski, Z. E. 1975, private communication.

McDonald, F. A. and Hull, M. H., Jr. 1966, Phys. Rev. 143, 838.

McFadden, L. and Satchler, G. R. 1966, Nucl. Phys. 84, 177.

McGowan, F. K. and Milner, W. T. 1973, Atomic and Nuclear Data Reprints, Vol. 2, Charged Particle Reaction List, 1948-1971, Academic Press. (For more recent information, see "reaction lists" appearing in Nuclear Data Tables and in Atomic and Nuclear Data Tables).

Meyers, W. 1974, Proceedings of the Int. Conf. on Reactions on Complex Nuclei (Nashville, Tenn.), to be published.

Michaud, G. and Fowler, W. A. 1970a, Phys. Rev. C2, 2041.

Michaud, G., Scherk, L., and Vogt, E. 1970b, Phys. Rev. C1, 864.

Moldauer, P. A. 1964, Phys. Rev. 135, B642.
1967, Phys. Rev. 157, 907.
1968, Phys. Rev. 171, 1164.
1969, Phys. Rev. 177, 1844.

Najam, M. R., Davidson, W. F., Zuk, W. M., Carlson, L. E., and Awal, M. A. 1971, Nucl. Phys. 173, 577.

Newton, T. D. 1956, Can. J. Phys. 34, 804.

Northcliffe, L. C. and Schilling, R. F. 1973, Nucl. Data Tables 7, 233.

Penny, S. K. 1965, ORNL-TM-2590 (unpublished) Oak Ridge National Laboratory.

Perey, C. M. and Perey, F. G. 1963, Phys. Rev. 132, 755.

Perey, C. M. and Perey, F. G. 1972, Nucl. Data Tables 10, 539.

Perey, C. M. and Perey, F. G. 1974, Atom. and Nucl. Data Tables 13, 293.

Perey, F. G. and Buck, B. 1962, Nucl. Phys. 32, 353.

Perey, F. G. 1963, Phys. Rev. 131, 745.

Phelps, M. E., Sarantities, D. G., and Winn, W. G. 1970, Nucl. Phys. A149, 647.

Porter, C. E. and Thomas, R. G. 1956, Phys. Rev. 104, 483.

Porile, N. J. and Morrison, D. L. 1959, Phys. Rev. 116, 1193.

Put, L. W. and Paans, A.M.J. 1974, Phys. Lett. 49B, 266.

Rahman-Khan, M. Z. 1966, Nucl. Phys. 76, 475.

Rao, M. N. 1968, Nucl. Data Tables 2, B2-6-93.

Reilley, W., Wieland, R., Gobbi, A., Sachs, M. W., and Bromley, D. A. 1973, Nuovo Cim. 13A, 897.

Replace, J. L. 1970, Radiochim. Acta 14, 46.

Rios, M., Anderson, B., and Schweitzer, J. 1974, private communication and to be published.

Rohr, G. and Frieland, E. 1967, Nucl. Phys. 104, 1.

Ronsin, H., Beuzit, P., Delaunay, J., Ballini, R., Fodor, I., and Fouar, J. P. 1973, Nucl. Phys. A207, 577.

Rosen, L., Beery, J. G., Goldhaber, A. S., and Auerbach, E. H. 1965, Ann. Phys. 34, 96.

Satchler, G. R. 1963, "The Distorted Wave Theory of Direct Nuclear Reactions" in Direct Interactions and Nuclear Reaction Mechanisms, Gordon and Breach.

Schulz, H. and Wiebicke, H. 1966, Phys. Lett. 21, 190.

Serber, R. 1947, Phys. Rev. 72, 1008.

Shaw, R. W. Jr., Katsanos, A. A., Vandenbusch, R. 1969, Phys. Rev. 184, 1089.

Sheldon, E. 1963, Rev. Mod. Phys. 35, 795.

Sheldon, E. and Rogers, V. C. 1973, Computer Phys. 6, 99.

Smith, D. L., Young, H. J., and Enge, H. A. 1968, Nucl. Phys. A116, 545.

Smith, D. and Williams, A. 1971, Int. J. Appl. Rad. Isotopes 22, 615.

Stelson, P. H. and McGowan, F. K. 1964, Phys. Rev. 133, B911.

Stokstad, R. G. 1972, Yale Internal Report #72 (unpublished).

Storey, R. G. and McNeil, K. G. 1959, Can. J. Phys. 37, 1072.

Storm, E., Gilbert, E., and Israel, H. 1958, Los Alamos Sci. Lab. Report LA-2237 (unpublished).

Talbert, W. L. and Stewart, M. G. 1960, Phys. Rev. 119, 272.

Tepel, J. W., Hoffmann, H. M., and Weidenmuller, H. A. 1974, Phys. Lett. 49B, 1.

ter Haar, D. 1954, Elements of Statistical Mechanics, North-Holland Publ. Co.

Thomas, G. L. and Burge, E. J. 1969, Nucl. Phys. A128, 545.

Tokcan, G. and Cothern, C. R. 1968, Nucl. Inst. Meth. 64, 219.

van Patter, D. M., Neuffer, D., Scott, H. L., Moazed, C., and H Hinrichsen, P. F. 1970, Nucl. Phys. A146, 427.

Vasil'ev, S. S., George, E. T., and Shavtvalov, L. Ya. 1967, Izv. Akad. Nauk 31, 284, or Bull. Akad. Nauk 31, 264.

Vasil'ev, S. S., Mikhaleva, T. N., and Chuprunoe, D. L. 1968, Izv. Akad. Nauk 32, 587, or Bull. Akad. Nauk 32, 539.

Verheul, H. 1967a, Nucl. Data Tables 2, B2-3-1.
1967b, Nucl. Data Tables 2, B2-3-31.

Vervier, J. 1968, Nucl. Data Tables 2, B2-5-41.

Vogt, E. W. 1968, Adv. in Nucl. Phys. 1, 261.

Vonach, H. and Hille, M. 1969, Nucl. Phys. A127, 289.

Wapstra, A. H. and Gove, N. B. 1971, Nucl. Data Tables 9, 267.

Warsh, K. L., Temmer, G. M., and Blieden, H. R. 1963, Nucl. Phys. 46, 45.

Weisskopf, V. F. 1951, Phys. Rev. 83, 1073.

Wilmore, D. and Hodgson, P. E. 1964, Nucl. Phys. 55, 673.

Wolfenstein, L. 1951, Phys. Rev. 82, 690.

Woosley, S. G., Holmes, J. A., Fowler, W. A., and Zimmerman, B. A. 1975, private communication.

Woods, R. D. and Saxon, D. S. 1954, Phys. Rev. 95, 577.

Zhukova, O. A., Kanashevich, V. I., Laptev, S. V., and Chursin, G. P. 1973, Yad. Fiz. SSSR 16, 242, or Sov. J. Nucl. Phys. 16, 134.

TABLE I

Parameters of the Woods-Saxon potential for proton-induced reactions. The significance of the parameters is discussed in the text (see page 198, particularly equation 76). All potential depths are in MeV and all radii in Fermis. The symbol E denotes bombarding energy and is in MeV. The Coulomb term, $V_c(r)$, is taken to be that of a uniformly charged sphere of radius R_V (equation 79). The parameters are taken from the work of

Perey (1963) (The values for W_S and V_{SO} are for E less than 17 MeV. For E greater than 17 MeV, the values are $W_S = 3A^{**}(1/3)$ and $V_{SO} = 8.5$);

Buck (1963);

Rosen et al (1965);

Becchetti and Greenlees (1969a) (The values for V_V, W_V, and W_S are either zero or the values given, whichever is larger. W_S has another term, +12(N-Z), which should be added to the term shown. The diffuseness a_W also has a similar additional term, +0.7(N-Z)/A).

None of the potentials has an imaginary spin-orbit term.

TABLE I

Parameter	Perey	Buck	Rosen	Becchetti
V_v	53.3-0.55E	52.6-0.28E	53.8-0.33E	54.0-0.32E
V_E	0.4	0.0	0.0	0.4
V_S	27	0.0	0.0	24
W_v	0.0	0.0	0.0	0.22E-1.7
W_s	13.5	10.6	7.5	11.8-0.25E
V_{so}	7.5	8.0	5.5	6.2
$R_V/A^{1/3}$	1.25	1.25	1.25	1.17
$R_W/A^{1/3}$	1.25	1.25	1.25	1.32
$R_{so}/A^{1/3}$	1.25	1.25	1.25	1.01
a_V	0.65	0.65	0.65	0.75
a_W	0.47	0.47	0.7	0.51*
a_{so}	0.65	0.65	0.65	0.75

TABLE II

Parameters of the Woods-Saxon potential for neutron-induced reactions. The significance of the parameters is discussed in the text (see page 198, particularly equation 76). All potential depths are in MeV and all radii are in Fermis. The parameters are taken from the work of

Wilmore and Hodgson (1964), which is the local potential equivalent to the non-local potential of Perey and Buck (1962);

Rosen et al (1965);

Becchetti and Greenlees (1969a).

None of the potentials has an imaginary spin-orbit term.

TABLE II

Parameter	Wilmore and Hodgson	Rosen et al	Becchetti and Greenless
V_V	$47.01-0.267E-0.0018E^2$	49.3-0.33E	56.3-0.32E
V_E	0.0	0.0	0.0
V_S	0.0	0.0	-24
W_V	0.0	0.0	0.22E-1.56
W_S	9.52-0.053E	5.75	13-0.25E-12(N-Z)/A
V_{SO}	0.0	5.5	6.2
$R_V/A^{1/3}$	1.322-0.00076A(1-0.005A)	1.25	1.17
$R_S/A^{1/3}$	1.266-0.00037A(1-0.005A)	1.25	1.26
$R_{SO}/A^{1/3}$	...	1.25	1.1
a_V	0.66	0.65	0.75
a_S	0.48	0.7	0.58
a_{SO}	...	0.65	0.75

TABLE III

Q values and activities for products of p + NaCl. The reaction of interest is $^{23}Na(p,n)^{23}Mg$ with a Q value of -4.84 MeV. As seen from the table, this is the only reaction which has a Q value above -6.75 MeV which emits annihilation radiation. The half-life information and activity information (energies of delayed gamma radiation) is from Lederer et al (1967). The Q values are deduced from the 1971 Mass Tables of Wapstra and Gove.

(See page 221.)

TABLE III

Reaction	Q Value	Half-Life	Activity
$^{23}Na(p,\gamma)^{24}Mg$	11.69	...	...
$,n)^{23}Mg$	-4.84	11 s	.51,.44
$,d)^{22}Na$	-10.19	2.6 y	.51,1.27
$,^{3}He)^{21}Ne$	-11.44	...	...
$,\alpha)^{20}Ne$	2.38	...	...
$,2p)^{22}Ne$	-8.79	...	...
$,\alpha p)^{19}F$	-10.47	...	...
$,2\alpha)^{16}O$	-2.35	...	...
$^{35}Cl(p,\gamma)^{36}Ar$	8.51	...	...
$,n)^{35}Ar$	-6.75	1.8 s	.51,1.22
$,d)^{34}Cl$	-10.41	1.6 s	.51
$,d)^{34}Cl^{*}$	-10.56	32 m	.51,2.13
$,^{3}He)^{33}S$	-10.07	...	...
$,\alpha)^{32}S$	1.86	...	...
$,2p)^{34}S$	-6.37	...	...
$,\alpha p)^{31}P$	-7.00	...	...
$,2\alpha)^{28}Si$	-4.99	...	...
$^{37}Cl(p,\gamma)^{38}Ar$	10.24	...	...
$,n)^{37}Ar$	-1.60	35 d	...

TABLE III (Contd)

Reaction	Q Value	Half-Life	Activity
$^{37}Cl(p,d)^{36}Cl$	-8.09	10^5 y	...
$,t)^{35}Cl$	-10.41	...	...
$,^3He)^{35}S$	-10.56	88 d	...
$,\alpha)^{34}S$	3.03	...	...
$,2n)^{36}Ar$	-10.39	...	...
$,2p)^{36}S$	-8.40	...	...
$,\alpha n)^{33}S$	-8.39	...	...
$,\alpha p)^{33}P$	-7.85	25 d	...
$,2\alpha)^{30}Si$	-4.89	...	...

TABLE IV

Timing chart for the reactions studied. The timings used for bombardment, waiting, and counting are shown for $^{23}Na(p,n)^{23}Mg$ and $^{35}Cl(\alpha,n)^{38}K$. The timings used for alpha bombardment of Cu and Co and for proton bombardment of Cu are not shown as they varied as the energy of the beam (and yield of the reaction) increased.

The timings for the $^{23}Na(p,n)$ and $^{35}Cl(\alpha,n)$ reactions were controlled by a digital sequence timer having a time precision of 0.1 s for $^{23}Na + p$ and 0.001 s for $^{35}Cl + \alpha$. The timings for the other reactions were manually controlled. The imprecision in the manual control is small compared to the uncertainty in the half-lives of the products.

(See page 221.)

TABLE IV

Activity	$^{23}Na(p,n)^{23}Mg$	$^{35}Cl(\alpha,n)^{38}K$
Bombardment	12.0 sec	1.365 sec
Wait	60.0 sec	0.200 sec
Count	20.0 sec (4 groups)	1.365 sec (2 groups)
$t_{1/2}$	11.4 sec	7.64 m (g.s.)
		0.929 s (i.s.)

TABLE V

Q values and activities for products of $\alpha + BaCl_2$ which have Q values above -11.0 MeV. The reactions of interest are $^{35}Cl(\alpha,n)^{38}K$ and $^{35}Cl(\alpha,n)^{38}K^*$ whose Q values are -5.88 and -6.01 MeV, respectively.

As can be seen from the table, there exists no short-lived annihilation-radiation emitter except for $^{38}K^*$. Also the 2.17-MeV gamma ray provides a unique signal for the production of ^{38}K(g.s.).

The half-life and activity information (energies in MeV of delayed gamma radiation) is from Lederer et al (1967). The Q values are from the 1971 Mass Tables of Wapstra and Gove.

(See page 224.)

TABLE V

Reaction	Q Value	Half-Life	Activity
$^{35}Cl(\alpha,\gamma)^{39}K$	7.21	...	...
$,n)^{38}K$	-5.87	7.7 m	.51,2.17
$,n)^{38}K^*$	-6.00	.95 s	.51
$,p)^{38}Ar$	0.84	...	...
$,d)^{37}Ar$	-8.77	35 d	...
$,2p)^{37}Cl$	-9.40	...	...
$,\alpha p)^{34}S$	-6.37	...	...
$,2\alpha)^{31}P$	-7.00	...	...
$^{37}Cl(\alpha,\gamma)^{41}K$	6.21	...	...
$,n)^{40}K$	-3.88	10^9 y	1.46
$,p)^{40}Ar$	-1.59	...	...
$,d)^{39}Ar$	-9.24	269 y	...
$,t)^{38}Ar$	-9.57	...	...
$,\alpha n)^{36}Cl$	-10.32	10^5 y	...
$,\alpha p)^{36}S$	-8.40	...	...
$,2\alpha)^{33}P$	-7.85	25 d	...
$^{130}Ba(\alpha,n)^{133}Ca$	-10.31	6 h	.51
$^{132}Ba(\alpha,n)^{135}Ce$	-9.40	17 h	.51,.3
$^{134}Ba(\alpha,n)^{137}Ce$	-8.18	9 h	...
$(\alpha,n)^{137}Ce^*$	-8.35	34 h	.25
$^{135}Ba(\alpha,n)^{138}Ce$	-5.91	...	...

TABLE V (Contd)

Reaction	Q Value	Half-Life	Activity
$^{136}Ba(\alpha,n)^{139}Ce$	-7.63	140 d	.17
$^{137}Ba(\alpha,n)^{140}Ce$	-5.54	...	...
$^{138}Ba(\alpha,n)^{141}Ce$	-8.64	53 d	.15

TABLE VI

Q values and activities for products of α + Co. The reaction of interest is $^{59}Co(\alpha,n)^{62}Cu$. Below the threshold for $^{59}Co(\alpha,\alpha n)^{58}Co$, only the $^{59}Co(\alpha,n)^{62}Cu$ reaction produces annihilation radiation. Above this energy, decays which have annihilation radiation also have an associated gamma ray.

The half-life and activity information (energies in MeV of delayed gamma radiation) is from Lederer et al (1967). The Q values are from the 1971 Mass Tables of Wapstra and Gove.

(See page 225.)

TABLE VI

Reaction	Q Value	Half-Life	Activity
$^{59}Co(\alpha,\gamma)^{63}Cu$	5.78	...	...
$,n)^{62}Cu$	-5.08	9.8 m	.51
$,p)^{62}Ni$	- .35	...	...
$,d)^{61}Ni$	-8.72	...	...
$,t)^{60}Ni$	-10.29	...	...
$,^{3}He)^{60}Co$	-13.09	5.7 y	1.17,1.33
$,^{3}He)^{60}Co^{*}$	-13.15	11 m	.06
$,2n)^{61}Cu$	-13.97	3.3 h	.51,.28,.66
$,2p)^{61}Co$	-11.46	99 m	.07
$,\alpha n)^{58}Co$	-10.46	71 d	.51,.81
$,\alpha n)^{58}Co^{*}$	-10.50	9 h	.03
$,\alpha p)^{58}Fe$	-7.38	...	...
$,2\alpha)^{55}Mn$	-6.95	...	...

TABLE VII

Q values and activities for products of α + Cu. The reactions of interest are $^{63}Cu(\alpha,n)^{66}Ga$ and $^{65}Cu(\alpha,n)^{68}Ga$ which have Q values of -7.52 and -5.84 MeV. The production of ^{68}Ga and ^{66}Ga is signalled by the emission of delayed gamma rays. The $^{65}Cu(\alpha,^{3}He)^{66}Cu$ produces one of the delayed gamma rays produced by $^{63}Cu(\alpha,n)^{66}Ga$. However, the half-life of ^{66}Cu is much shorter than ^{66}Ga and only a moderate wait makes the contribution from ^{66}Cu insignificant compared to ^{66}Ga.

The half-life and activity information (energies in MeV of the delayed gamma radiation) is from Lederer et al (1967). The Q values are from the 1971 Mass Tables of Wapstra and Gove.

(See page 226.)

TABLE VII

Reaction	Q Value	Half-Life	Activity
$^{63}Cu(\alpha,\gamma)^{67}Ga$	3.70	78 h	.29,.18,.09
$,n)^{66}Ga$	-7.52	9.4 h	.51,2.74,1.04
$,p)^{66}Zn$	-1.57	...	...
$,d)^{65}Zn$	-10.38	245 d	1.12,.51
$,t)^{64}Zn$	-12.11	...	...
$,^{3}He)^{64}Cu$	-12.66	13 h	.51
$,2n)^{65}Ga$	-16.64	15 m	.51,.12
$,2p)^{65}Cu$	-10.57	...	...
$,\alpha n)^{62}Cu$	-10.86	10 m	.51
$,\alpha p)^{62}Ni$	-6.12	...	...
$,2\alpha)^{59}Co$	-5.78	...	...
$^{65}Cu(\alpha,\gamma)^{69}Ga$	4.49	...	...
$,n)^{68}Ga$	-5.83	68 m	.51,1.078
$,p(^{68}Zn$	-2.14	...	...
$,d)^{67}Zn$	-10.11	...	...
$,t)^{66}Zn$	-10.91	...	...
$,^{3}He)^{66}Cu$	-13.52	5.1 m	1.04
$,2n)^{67}Ga$	-14.12	78 h	.09,.18,.29
$,2p)^{67}Cu$	-12.13	59 h	.19,.09
$,\alpha n)^{64}Cu$	-9.91	13 h	.51
$,p\alpha)^{64}Ni$	-7.45	...	...
$,2\alpha)^{61}Co$	-6.76	99 m	.07

TABLE VIII

Q values and activities for products of p + Cu which have Q values above -11 MeV. The reaction of interest is $^{63}Cu(p,n)^{63}Zn$ which has a Q value of -4.15 MeV. The production of ^{63}Zn is signalled by the emission of two delayed gamma rays, 0.67 and 0.96 MeV.

The half-life and activity information (energies in MeV of the delayed gamma radiation) is from Lederer et al (1967). The Q values are from the 1971 Mass Tables of Wapstra and Gove.

(See page 228.)

TABLE VIII

Reaction	Q Value	Half-Life	Activity
$^{63}Cu(p,\gamma)^{64}Zn$	7.71	...	...
$,n)^{63}Zn$	-4.15	38 m	.51,.67,.96
$,d)^{62}Cu$	-8.62	10 m	.51
$,t)^{61}Cu$	-11.26	3.3 h	.51,.28,.66
$,^{3}He)^{61}Ni$	-9.01	...	...
$,\alpha)^{60}Ni$	3.75	...	...
$,2p)^{62}Ni$	-6.12	...	...
$,\alpha n)^{59}Ni$	-7.63	10^5 y	...
$,\alpha p)^{59}Co$	-5.78	...	...
$,2\alpha)^{56}Fe$	-3.97	...	...
$^{65}Cu(p,\gamma)^{66}Zn$	8.90	...	...
$,n)^{65}Zn$	-2.13	245 d	.51, 1.12
$,d)^{64}Cu$	-7.69	13 h	.51
$,t)^{63}Cu$	-9.34	...	...
$,^{3}He)^{63}Ni$	-9.39	92 y	...
$,\alpha)^{62}Ni$	4.35	...	...
$,2n)^{64}Zn$	-10.12	...	...
$,2p^{64}Ni$	-7.45	...	...
$,\alpha n)^{61}Ni$	-6.25	...	...
$,\alpha p)^{61}Co$	-6.76	99 m	.07
$,2\alpha)^{58}Fe$	-3.29	...	...

TABLE IX

Cross section for $^{23}Na(p,n)^{23}Mg$. The normalization uncertainty is 8.5%. The energies given are in the center of mass system and are the energies at the center of the target. Below E_{cm} = 5.38 MeV, a 10 keV thick target (at $E_{cm} \sim 5$ MeV) was used; above 5.38 MeV a target four times as thick was used.

The Q value of the reaction is (-4839.0 $\pm$ 2.2) keV.

(See page 230.)

TABLE IX

E_{cm}(MeV)	σ(mb)	E_{cm}(MeV)	σ(mb)
4.845	1.8 ± 0.6	5.439	44.2 ± 0.9
4.864	2.3 ± 0.4	5.486	65.8 ± 1.1
4.884	2.9 ± 0.4	5.534	63.1 ± 1.2
4.903	6.2 ± 0.7	5.582	70.3 ± 1.4
4.922	13.4 ± 0.8	5.630	73.7 ± 1.5
4.941	20.7 ± 1.0	5.678	66.1 ± 1.4
4.960	15.0 ± 0.9	5.726	63.9 ± 1.5
4.979	13.9 ± 0.8	5.774	66.1 ± 1.5
4.999	14.9 ± 1.3	5.822	83.3 ± 1.8
5.018	14.8 ± 1.3	5.870	66.9 ± 1.7
5.037	15.5 ± 0.8	5.918	52.3 ± 1.5
5.056	9.8 ± 0.8	5.966	57.3 ± 1.7
5.075	11.7 ± 0.9	6.014	70.7 ± 1.8
5.094	13.0 ± 0.9	6.061	77.9 ± 1.7
5.114	15.3 ± 1.0	6.109	73.1 ± 1.6
5.133	14.9 ± 1.0	6.157	67.3 ± 1.6
5.152	17.7 ± 1.2	6.205	78.0 ± 1.8
5.171	16.1 ± 1.5	6.253	97.0 ± 1.8
5.190	23.3 ± 1.1	6.301	92.1 ± 1.8
5.209	28.2 ± 1.1	6.349	91.9 ± 1.8
5.229	29.2 ± 1.2	6.397	99.1 ± 1.8
5.248	33.9 ± 1.3	6.445	88.2 ± 1.7
5.266	35.3 ± 1.3	6.493	85.2 ± 1.2
5.285	39.7 ± 1.7	6.541	91.2 ± 1.3
5.304	41.4 ± 1.6	6.589	95.5 ± 1.4
5.324	50.4 ± 1.7	6.636	105.8 ± 1.4
5.343	36.1 ± 1.5	6.684	103.4 ± 1.4
5.362	28.6 ± 1.3	6.732	92.8 ± 1.4
5.391	30.5 ± 0.7	6.780	90.4 ± 1.3

TABLE IX (Contd)

E_{cm}(MeV)	σ(mb)	E_{cm}(MeV)	σ(mb)
6.831	86.5 ± 1.3	8.033	102.8 ± 1.3
6.879	84.0 ± 1.4	8.129	118.0 ± 1.5
6.927	84.9 ± 1.2	8.224	92.3 ± 1.4
6.975	91.9 ± 1.3	8.320	109.0 ± 1.5
7.071	109.5 ± 1.5	8.417	103.9 ± 1.4
7.166	94.0 ± 1.4	8.514	119.3 ± 1.6
7.263	93.1 ± 1.8	8.610	123.3 ± 1.8
7.360	97.8 ± 1.3	8.849	100.9 ± 1.4
7.456	71.7 ± 1.2	9.089	122.0 ± 1.4
7.552	83.3 ± 1.3	9.329	125.3 ± 1.5
7.647	105.6 ± 1.7	9.809	107.0 ± 1.6
7.743	99.9 ± 1.4	10.289	110.8 ± 1.4
7.839	93.8 ± 1.2	10.527	108.0 ± 2.0
7.935	94.1 ± 1.2		

TABLE X

Total reaction cross section for $^{35}Cl(\alpha,n)^{38}K$. All cross sections are in mb. The energies given are in the center of mass and are the energies at the center of the target. σ(g.s.) is the cross section for producing states which eventually decay to the ^{38}K ground state. Similarly σ(i.s.) is the cross section for those states which eventually decay to the isomeric level at 131 keV. σ(total) is the total cross section for formation of ^{38}K and is just the sum of σ(g.s.) and σ(i.s.).

The Q value for $^{35}Cl(\alpha,n)^{38}K$(g.s.) is (-5868 ± 8) keV, while the Q value for $^{35}Cl(\alpha,n)^{38}K$(i.s.) is (-5999 ± 8) keV.

The normalization uncertainty is 15%.

(See page 232.)

TABLE X

E_{cm}(MeV)	σ(g.s)	σ(i.s.)	σ(total)
5.905	2.3 ± 0.2	...	2.3 ± 0.2
5.995	4.2 ± 0.3	...	4.2 ± 0.3
6.085	6.4 ± 0.3	0.7 ± 0.2	7.1 ± 0.4
6.174	7.3 ± 0.4	0.8 ± 0.3	8.1 ± 0.5
6.265	9.4 ± 0.4	1.2 ± 0.3	10.6 ± 0.5
6.355	13.4 ± 0.5	3.8 ± 0.4	17.2 ± 0.7
6.444	17.5 ± 0.6	6.4 ± 0.5	23.9 ± 0.8
6.534	16.9 ± 0.6	8.3 ± 0.5	25.2 ± 0.8
6.624	16.3 ± 0.6	6.3 ± 0.5	22.6 ± 0.8
6.714	19.0 ± 0.6	7.1 ± 0.6	26.1 ± 0.8
6.803	22.4 ± 0.7	6.3 ± 0.7	28.7 ± 1.0
6.894	24.9 ± 0.7	8.1 ± 0.8	33.0 ± 1.1
6.984	21.1 ± 0.6	7.7 ± 0.7	28.8 ± 0.9
7.074	28.3 ± 0.8	11.7 ± 0.9	44.0 ± 1.2
7.163	26.6 ± 0.8	6.4 ± 1.1	33.0 ± 1.3
7.253	26.9 ± 0.8	7.6 ± 0.8	34.5 ± 1.2
7.343	25.9 ± 0.8	7.4 ± 0.8	33.3 ± 1.1
7.433	26.0 ± 0.6	13.3 ± 0.8	39.3 ± 1.1
7.522	26.5 ± 0.8	11.3 ± 0.9	37.8 ± 1.2
7.613	29.0 ± 0.8	11.8 ± 1.0	40.8 ± 1.3
7.703	24.0 ± 0.8	11.1 ± 0.9	35.3 ± 1.2
7.792	23.0 ± 0.7	14.5 ± 0.9	34.5 ± 1.2
7.882	26.1 ± 0.8	13.8 ± 0.9	39.9 ± 1.2
7.972	28.2 ± 0.8	15.2 ± 1.0	43.4 ± 1.3
8.062	26.8 ± 0.8	12.0 ± 1.0	38.8 ± 1.3
8.152	27.7 ± 0.8	14.6 ± 1.0	42.3 ± 1.3
8.242	25.3 ± 0.8	15.4 ± 1.0	40.7 ± 1.3
8.332	27.7 ± 0.8	16.1 ± 1.1	43.8 ± 1.4
8.421	26.5 ± 0.8	16.6 ± 1.1	43.1 ± 1.3
8.511	28.3 ± 0.9	13.2 ± 1.1	41.5 ± 1.4

TABLE X (Contd)

E_{cm}(MeV)	σ(g.s.)	σ(i.s.)	σ(total)
8.601	28.7 ± 0.9	16.0 ± 1.1	44.7 ± 1.4
8.692	32.2 ± 1.1	16.3 ± 1.2	48.5 ± 1.6
8.781	31.6 ± 1.1	17.6 ± 1.2	49.2 ± 1.7
8.871	31.5 ± 1.1	16.8 ± 1.2	48.3 ± 1.6
8.961	29.4 ± 1.0	17.4 ± 1.2	46.8 ± 1.6
9.051	28.2 ± 1.0	14.7 ± 1.2	42.9 ± 1.6
9.140	30.5 ± 1.2	14.9 ± 1.4	45.4 ± 1.8
9.321	32.9 ± 1.1	16.8 ± 1.4	49.7 ± 1.8
9.411	35.7 ± 1.1	18.5 ± 1.8	54.2 ± 2.1
9.500	41.8 ± 1.2	18.4 ± 1.7	60.2 ± 2.1
9.590	49.4 ± 1.5	21.4 ± 1.8	70.8 ± 2.3
9.680	49.0 ± 1.4	22.0 ± 1.8	71.0 ± 2.3
9.770	52.3 ± 1.5	22.7 ± 1.9	75.0 ± 2.4
9.860	50.8 ± 1.5	22.6 ± 1.8	73.4 ± 2.4
9.950	57.5 ± 1.6	19.2 ± 1.9	76.7 ± 2.5
10.040	56.6 ± 1.8	21.4 ± 2.0	78.0 ± 2.6
10.129	63.2 ± 1.8	23.5 ± 2.1	86.7 ± 3.9
10.220	60.3 ± 1.8	19.9 ± 2.3	80.2 ± 3.2
10.310	62.2 ± 1.8	24.1 ± 2.5	86.3 ± 3.1
10.399	62.4 ± 1.8	25.1 ± 2.6	87.5 ± 3.2
10.489	68.1 ± 2.0	26.6 ± 3.1	94.7 ± 3.7
10.580	66.6 ± 2.0	24.3 ± 2.9	90.9 ± 3.6
10.670	64.9 ± 2.0	37.9 ± 3.0	102.8 ± 3.6
10.759	73.8 ± 2.3	31.3 ± 3.4	105.1 ± 4.1

TABLE XI

Total reaction cross sections for $^{59}Co(\alpha,n)^{62}Cu$. The energies given are in the center of mass and have been corrected for cross section effects by assuming that the Coulomb potential is the main cause of the variation with energy.

The normalization uncertainty for these cross sections is 10%. The Q value for the reaction is -5077 ± 5 keV. The cross sections given are only for the two-body reaction and do not include any three-body channels that may have passed through ^{62}Cu. The Q value for $(\alpha,2n)$ is -14.0 MeV, for (α,np) it is -11.0 MeV, and for $(\alpha,\alpha n)$ is -10.5 MeV. Only the $(\alpha,2n)$ reaction has any appreciable cross section because of the Coulomb barrier for charged particle emission.

(See page 232.)

TABLE XI

E_{cm}	σ(mb)
5.140	0.028 ± 0.002
5.492	0.099 ± 0.003
5.974	1.05 ± 0.01
6.475	4.25 ± 0.04
6.976	14.0 ± 0.2
7.478	34.3 ± 0.4
7.977	75.9 ± 0.8
8.480	131 ± 1
8.979	213 ± 2
9.476	282 ± 3
9.980	379 ± 4
10.481	441 ± 5
10.701	488 ± 5
10.751	507 ± 5
11.482	591 ± 6
11.983	596 ± 6
12.483	690 ± 7
12.983	744 ± 8
13.485	781 ± 8
13.985	775 ± 9
14.987	756 ± 8
15.995	719 ± 8
16.986	630 ± 7
17.988	561 ± 7
18.487	496 ± 6
18.987	435 ± 5

TABLE XII

Total reaction cross sections for $^{63}Cu(\alpha,n)^{66}Ga$. The effective energies given are in the center of mass and have been corrected for cross section effects by assuming that the Coulomb barrier is the main cause of the variation with energy.

The normalization uncertainty is 10%. The Q value for the reaction is -7515 ± 6 keV. The cross sections given are only for the two-body reaction and do not include any three-body channels that may have passed through ^{66}Ga. The Q values are: for $(\alpha,2n)$ -16.8 MeV, for (α,np) -12.2 MeV, and for $(\alpha,\alpha n)$ -10.9 MeV. Only the $(\alpha,2n)$ reaction has any appreciable cross section because of the Coulomb barrier for charged particle emission.

(See page 233.)

TABLE XII

E_{cm}(MeV)	σ(mb)
7.910	10.9 ± 0.1
8.386	37.6 ± 0.4
8.836	85.0 ± 1.0
9.798	183 ± 2
10.742	323 ± 4
11.686	441 ± 5
12.649	488 ± 6
13.591	593 ± 7
14.533	652 ± 8
16.417	672 ± 9
17.358	595 ± 6

TABLE XIII

Total reaction cross sections for $^{65}Cu(\alpha,n)^{68}Ga$. The energies given are in the center of mass and have been corrected for cross section effects by assuming that the Coulomb barrier is the main cause of the variation with energy.

The normalization uncertainty is 10%. The Q value for the reaction is -5827 ± 6 keV. The cross sections given are only for the two-body reaction and do not include any three-body channels that may have passed through ^{68}Ga. The Q values are: for $(\alpha,2n)$ -14.1 MeV, for (α,np) -12.3 MeV, and for (α, n) -9.9 MeV. Only the $(\alpha,2n)$ reaction has any appreciable cross section because of the Coulomb barrier for charged particle emission.

(See page 233.)

TABLE XIII

E_{cm}(MeV)	σ(mb)
6.032	0.08 ± 0.04
6.978	5.8 ± 0.3
7.924	41.7 ± 1.5
8.397	77.7 ± 2.7
8.870	147 ± 3
9.816	280 ± 5
10.762	555 ± 6
11.708	644 ± 7
12.672	670 ± 9
13.616	790 ± 11
14.560	878 ± 11
16.447	865 ± 11
17.391	752 ± 11

TABLE XIV

Total reaction cross section for $^{63}Cu(p,n)^{63}Zn$. The energies are in the center of mass system and are for the center of the target.

The normalization uncertainty for these cross sections is 10%. The Q value for the reaction is -4148.0 ± 2.8 keV. For the energies measured, all states in ^{63}Zn populated by the reaction are bound.

(See page 234.)

TABLE XIV

E_{cm}(MeV)	σ(mb)
4.168	10.5 ± 0.1
4.217	14.0 ± 0.2
4.485	53.3 ± 0.6
4.986	117 ± 1
5.487	182 ± 2
5.988	193 ± 2
7.011	285 ± 3
7.990	325 ± 4
8.991	407 ± 6
9.992	451 ± 9
11.991	448 ± 15

Figure 1

Transmission coefficients for $^{23}Na + p$ for $\ell = 0,1,2,3$ and 4 for $E_{cm} = 0.1$ to 10 MeV. The proton potential of Becchetti and Greenlees (1969a) was used to generate the coefficients. Other potentials will show similar behavior, the main difference being in absolute magnitude.

The effect of the Coulomb and centrifugal barriers is clearly seen. At high enough energies all transmission coefficients approach unity.

(See page 202.)

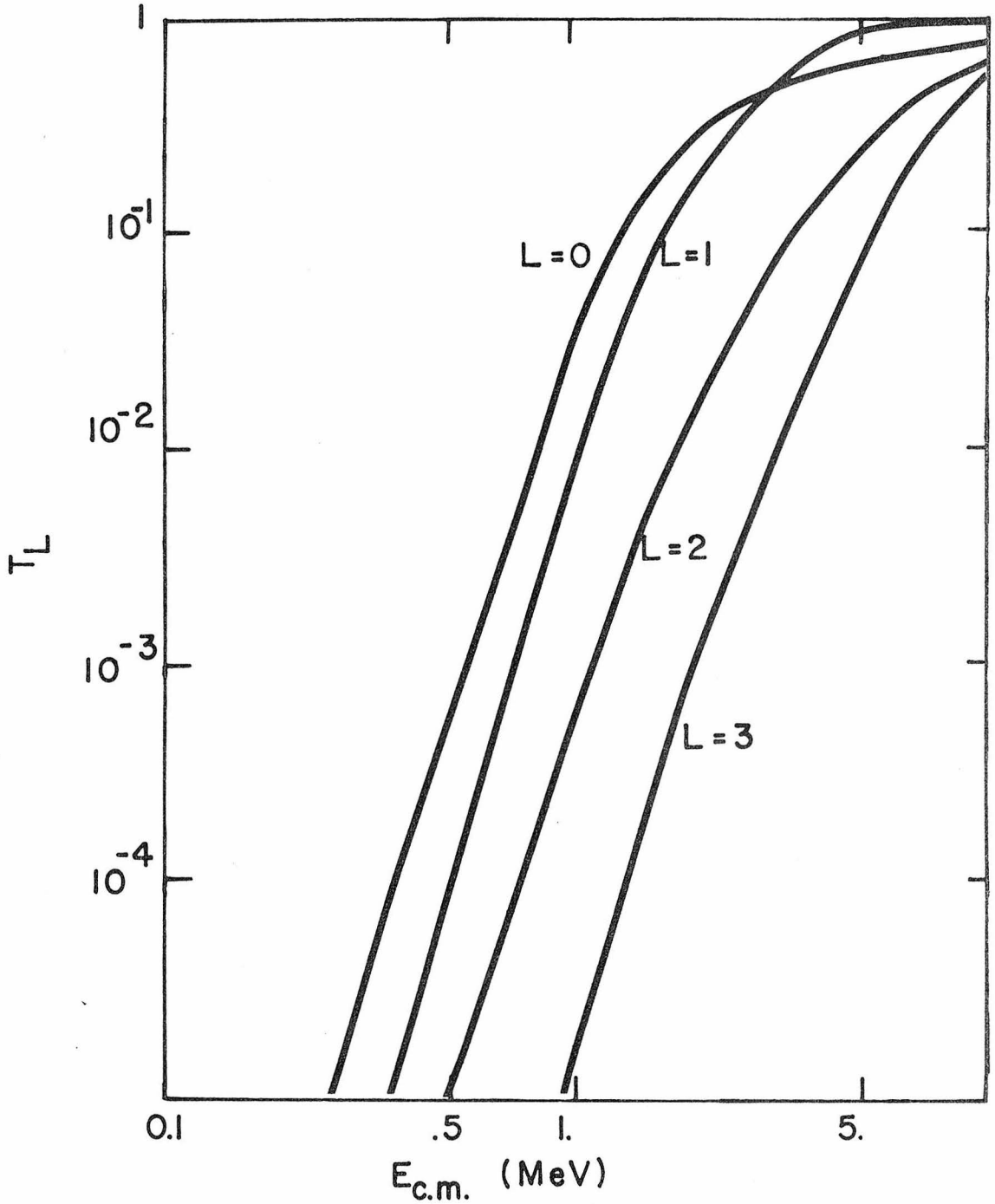
1
10^{-1}
10^{-2}
10^{-3}
10^{-4}
T_L
L=0
L=1
L=2
L=3
0.1
.5
1.
5.
$E_{c.m.}$ (MeV)

Figure 2

Transmission coefficients for $^{23}Mg + n$ for $\ell = 0,1,2$, and 3 for $E_{cm} = 0.01$ to 10 MeV. The neutron potential of Becchetti and Greenlees (1969a) was used to generate the coefficients. Other potentials will show similar behavior.

The lack of a Coulomb barrier is evidenced by the large values of the T_ℓ's at low energy. This is particularly true for $\ell = 0$, where $T_{\ell=0}$ is near unity even for very low energies. Other ℓ values are smaller due to the presence of the centrifugal barrier.

(See page 203.)

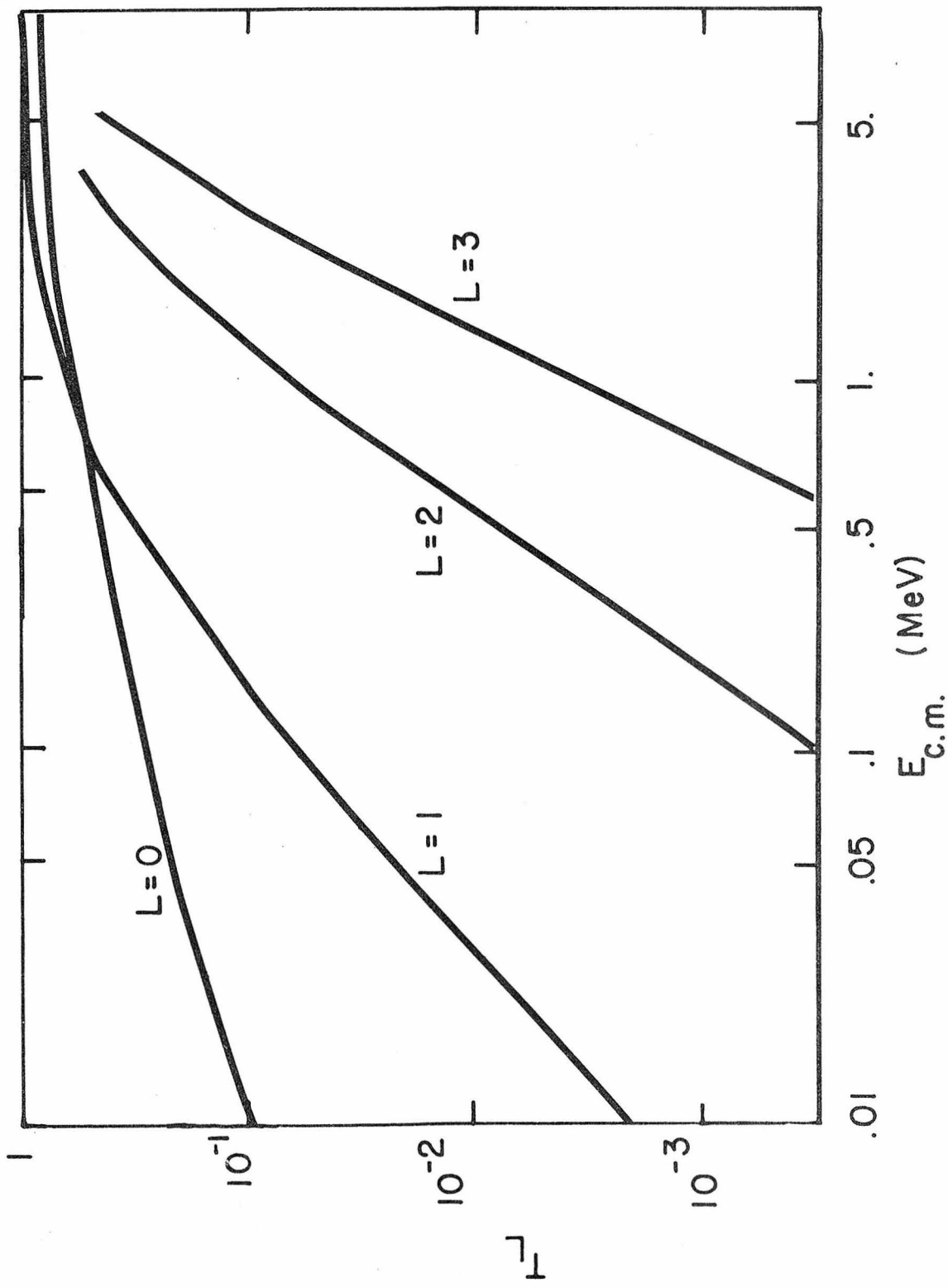
1
10^{-1}
10^{-2}
10^{-3}
T
.01
.05
.1
.5
1.
5.
$E_{c.m.}$ (MeV)
L=0
L=1
L=2
L=3

Figure 3

Transmission coefficients for $^{20}Ne + \alpha$ for $\ell = 0,1,2,$ and 3 for $E_{cm} = 1$ to 10 MeV. The alpha potential of Michaud and Fowler (1970a) was used to generate the coefficients. Other potentials will show similar behavior.

The Coulomb barrier is very significant even though the atomic number of neon is very low. For nuclei with higher Z (and hence a higher Coulomb barrier) the increase of T_ℓ with energy is even more dramatic. The centrifugal barrier, although of less significance, still plays an important role.

(See page 206.)

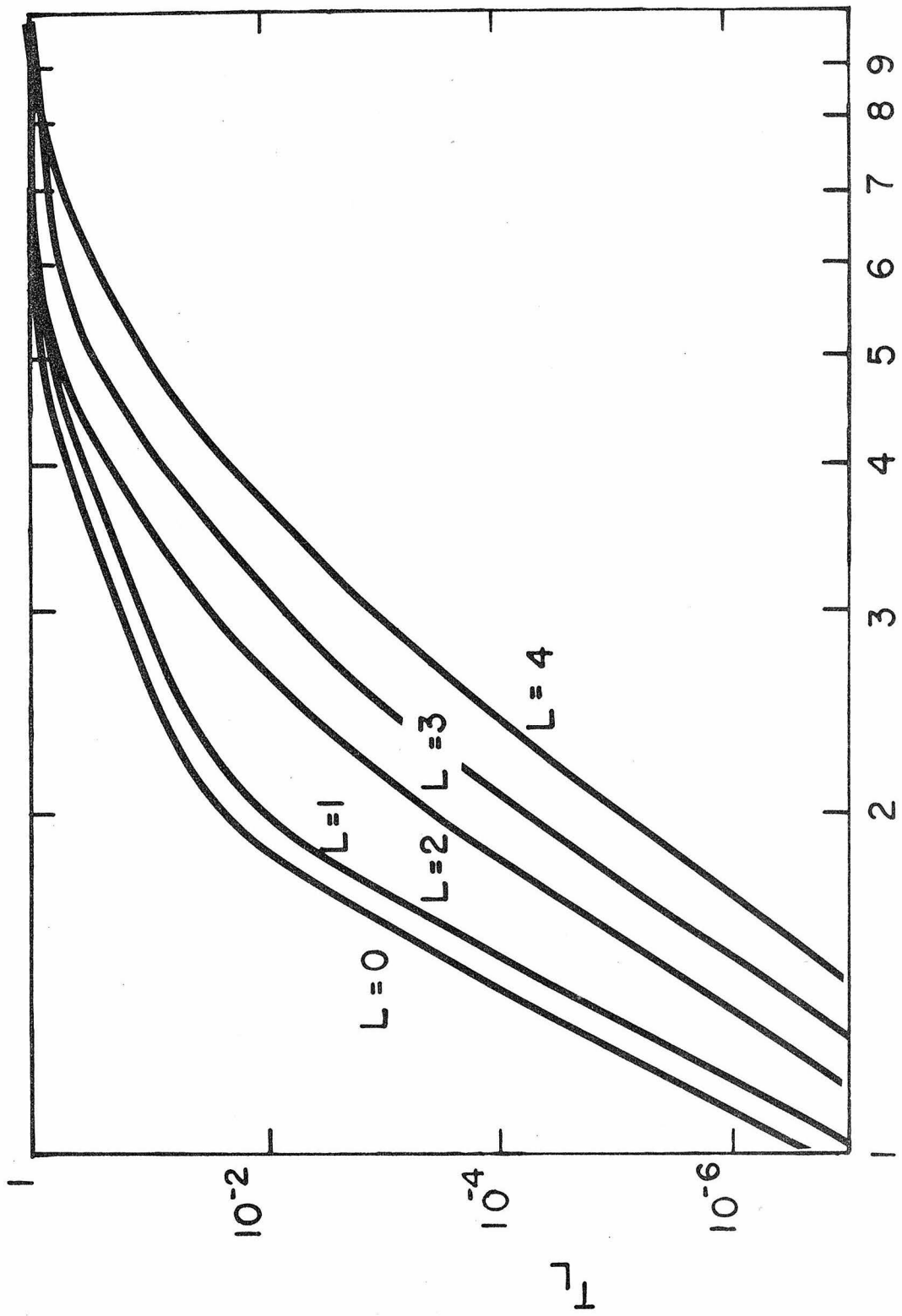
1
10^{-2}
10^{-4}
10^{-6}
T
1
2
3
4
5
6
7
8
9
$E_{c.m.}$ (MeV)
L=0
L=1
L=2
L=3
L=4

Figure 4

Absolute detection efficiency for off-line geometry (Figure 5) when using the 73 cm^3 or 50 cm^3 Ge(Li) detector. Although the smaller Ge(Li) was not used in this geometry, the comparison is useful, as only the normalization changes (to a good approximation) when the 50 cm^3 is used in the on-line geometry (Figure 7).

The larger detector has a larger absolute detection efficiency, of course, and the variation of efficiency with energy is less than for the smaller detector.

The lines shown are the result of a least squares fit to the decays of ^{56}Co, ^{22}Na, and ThB. See text (page 216) for additional details.

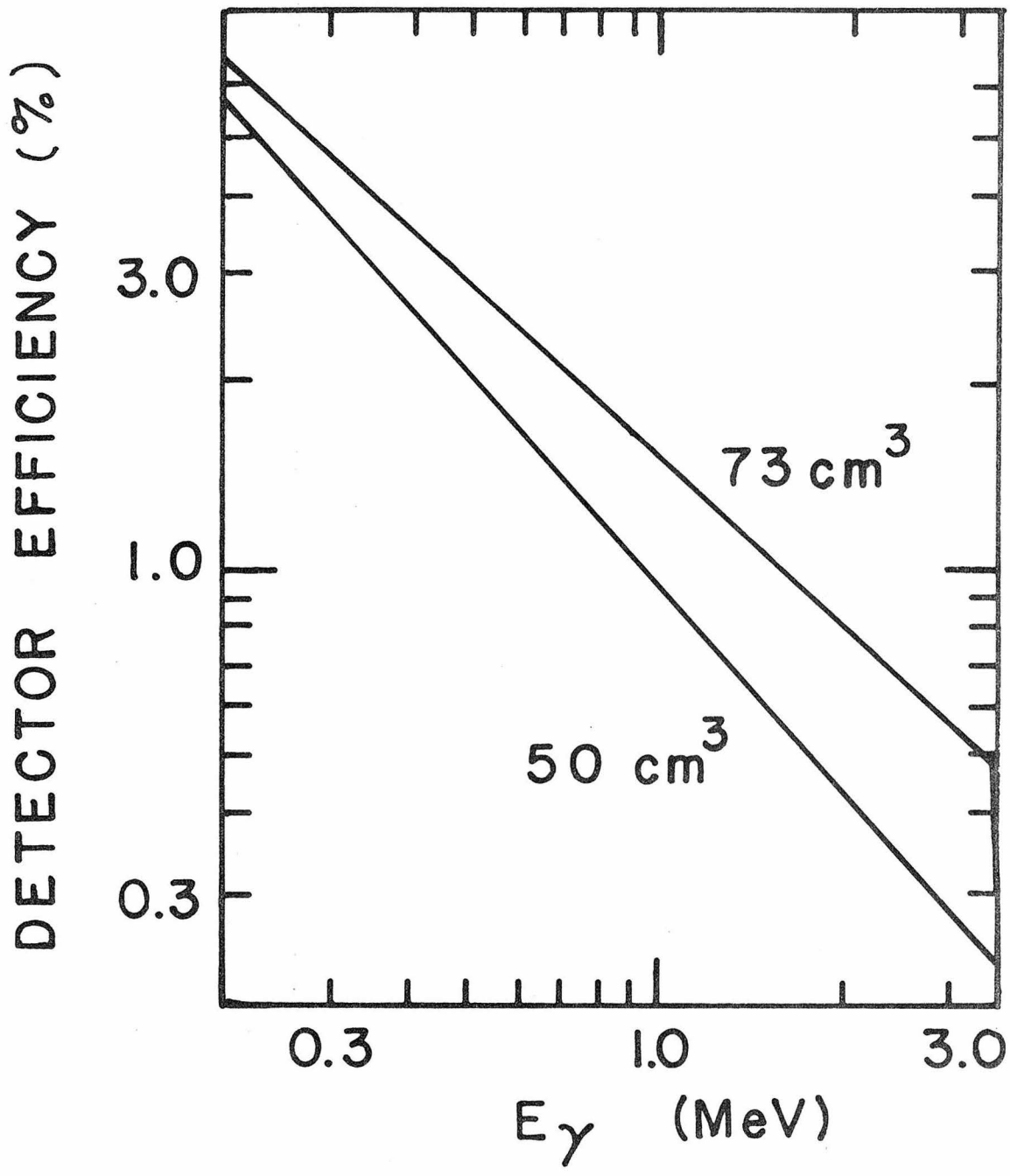
DETECTOR EFFICIENCY (%)
3.0
1.0
0.3
73 cm3
50 cm3
0.3
1.0
3.0
Eγ (MeV)

Figure 5

Off-line geometry. The activated target was inserted into the teflon holder.

Lead shielding was placed around the detector to reduce room background to a negligible level. An X-ray filter was placed between the detector and the teflon holder to absorb low energy gamma radiation and to stop any beta particles emerging from the holder from entering the detector.

(See page 218.)

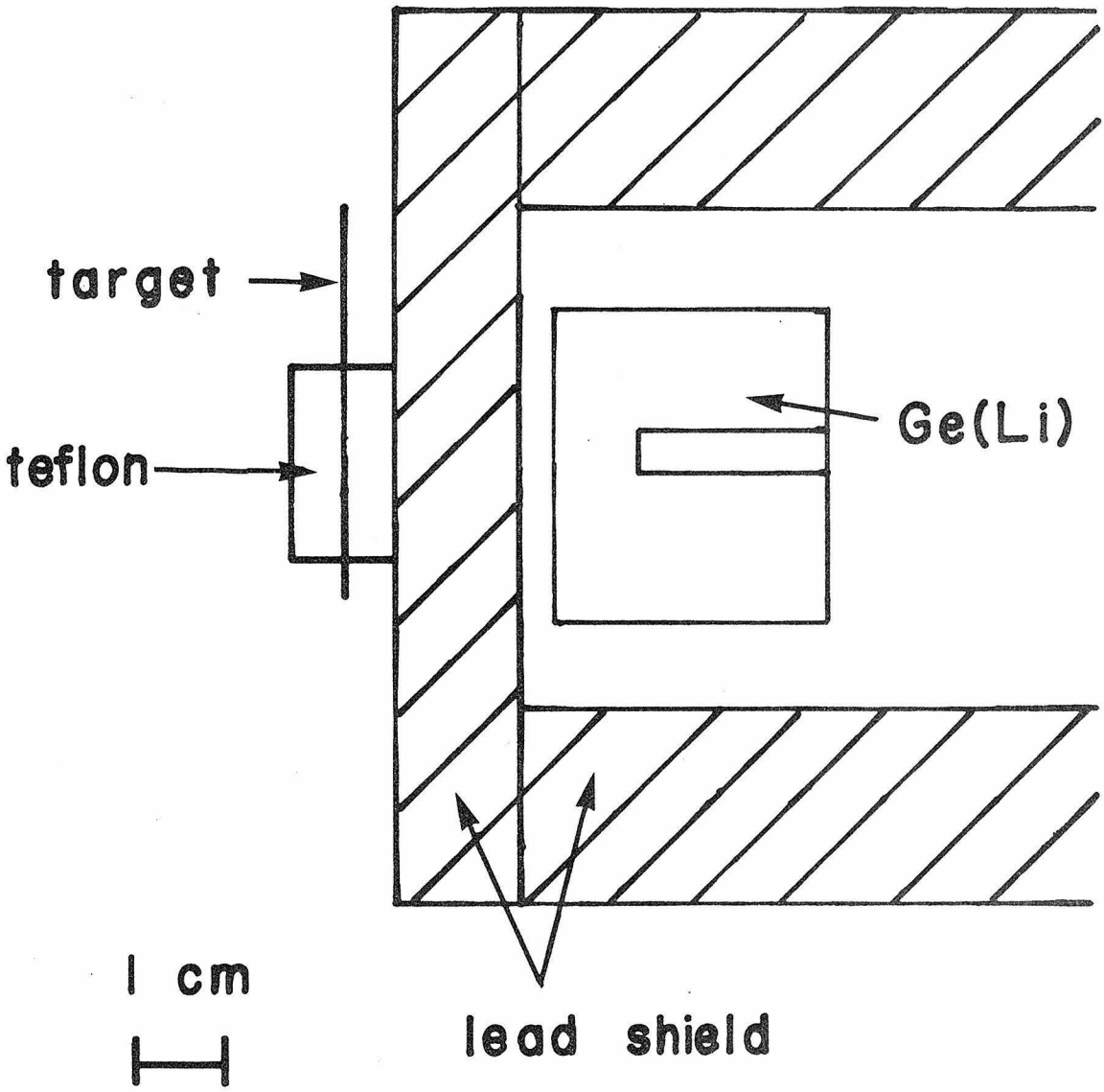
target
teflon
Ge(Li)
1 cm
lead shield

Figure 6

Block diagram for the electronics. The electronics used are quite standard. The amplified charge pulse produced by the detector is analyzed by either a Nuclear Data ND 160 or ND 4420 Multichannel Analyzer. A 60 Hz pulser is introduced at the preamplifier in order to determine the dead-time of the electronics and any gain drifts.

The digital sequence timer was used in those experiments for which the half-life of the product was short ($^{23}Na(p,n)^{23}Mg$ and $^{35}Cl(\alpha,n)^{38}K$). For the other reactions, the timing was manually controlled.

(See page 219.)

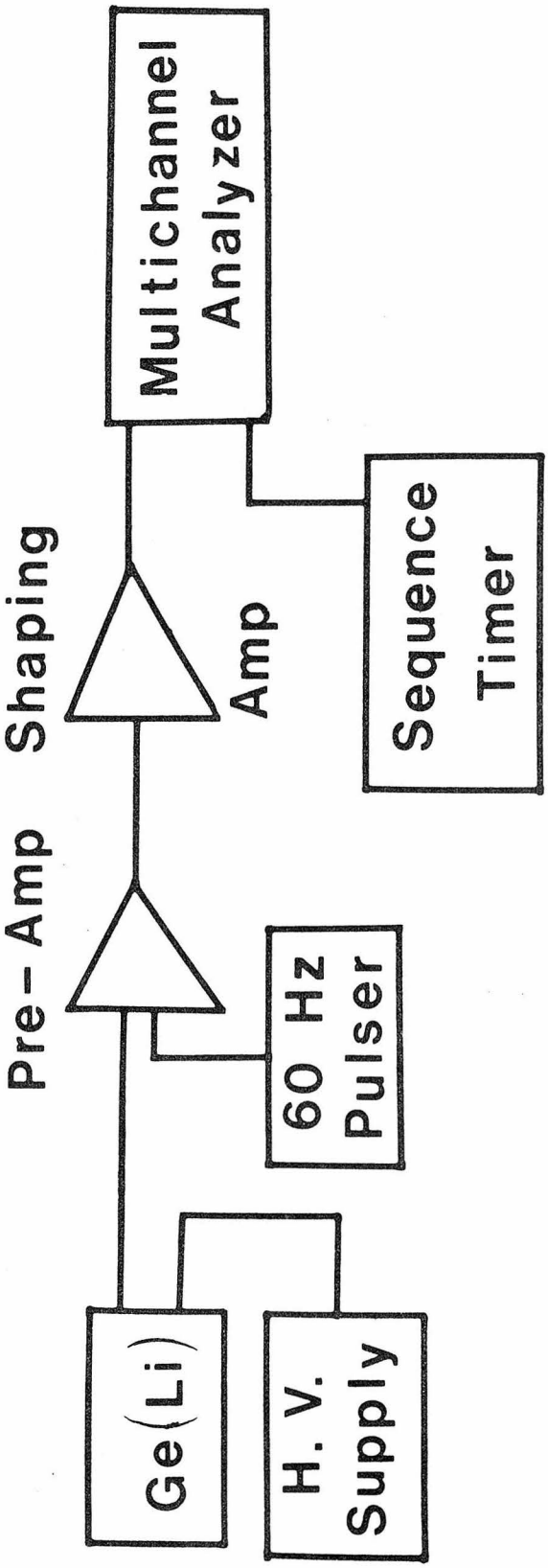
Multichannel Analyzer
Sequence Timer
Shaping Amp
Pre-Amp
60 Hz Pulser
Ge(Li)
H. V. Supply

Figure 7

On-line geometry. This geometry was only used in the measurement of the $^{35}Cl(\alpha,n)^{38}K$ cross section. The chamber is made of Be in order to reduce annihilation in flight and bremsstrahlung. Alpha bombardment of Be produces no interfering delayed radiation.

Both a 50 cm^3 Ge(Li) and a 5 cm x 5 cm NaI detector were used at different times during the measurement. The Ge(Li) offered superior resolution, but the NaI had better detection efficiency.

(See page 223.)

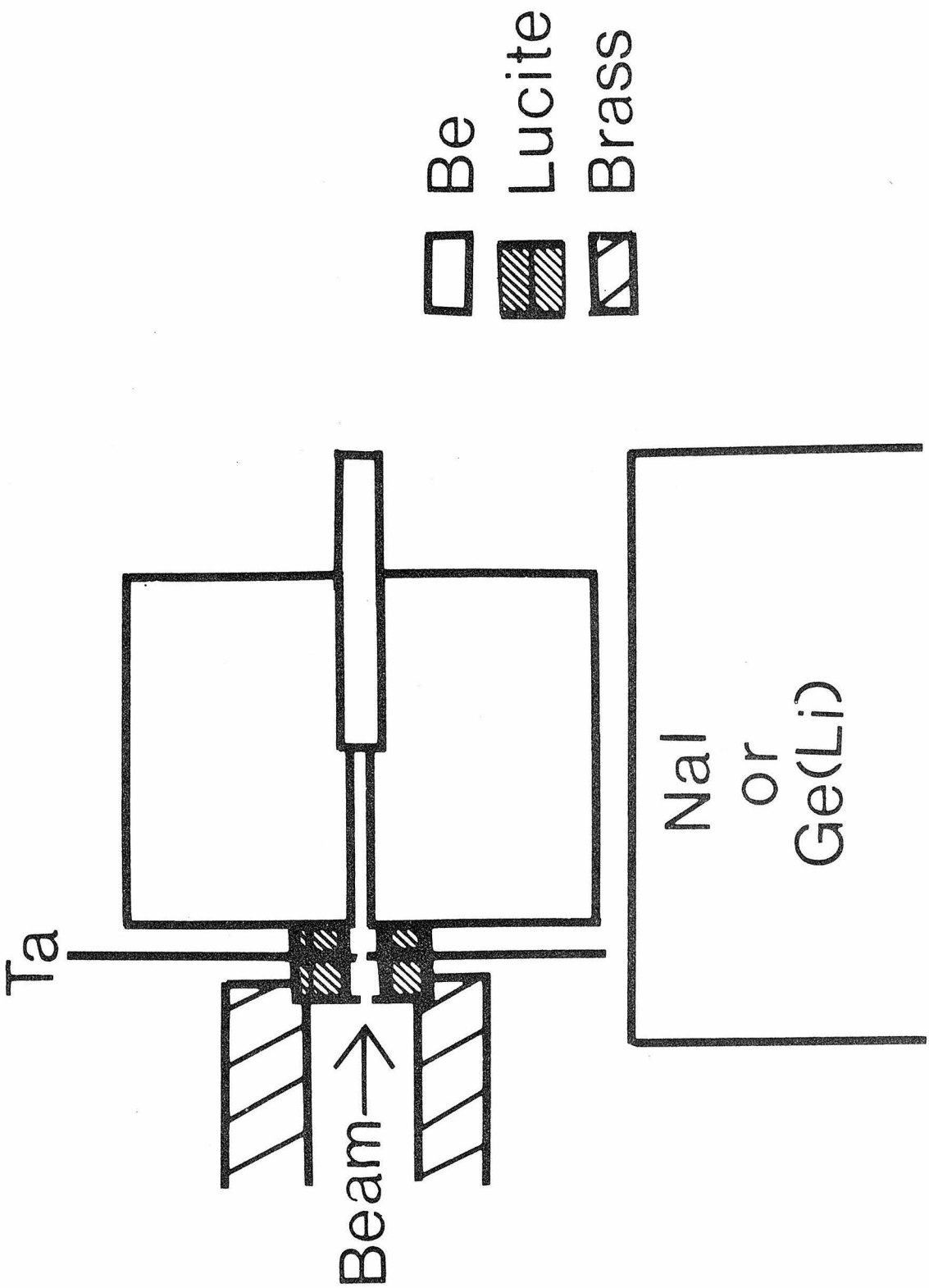
Be
Lucite
Brass
Ta
Beam
NaI
or
Ge(Li)

Figure 8

Typical delayed gamma spectrum following proton bombardment of NaCl. The spectrum shown is for $E_{cm} \sim 8.0$ MeV. Even though many half-lives have occurred between the end of bombardment and the start of the counting of this spectrum, only 511- and 440-keV radiation is present.

The cross section for the $^{23}Na(p,n)^{23}Mg$ reaction was inferred by use of both gamma rays when possible. The spectra were taken in 4 sequential time groups. The yield of the 511-keV gamma rays was fitted by a curve corresponding to the decay of ^{23}Mg and a long-lived component. In none of the runs was there any indication of a short-lived component other than ^{23}Mg. At low bombarding energies the yield of 440-keV radiation was insufficient to produce accurate cross sections from use of this gamma ray.

(See page 230.)

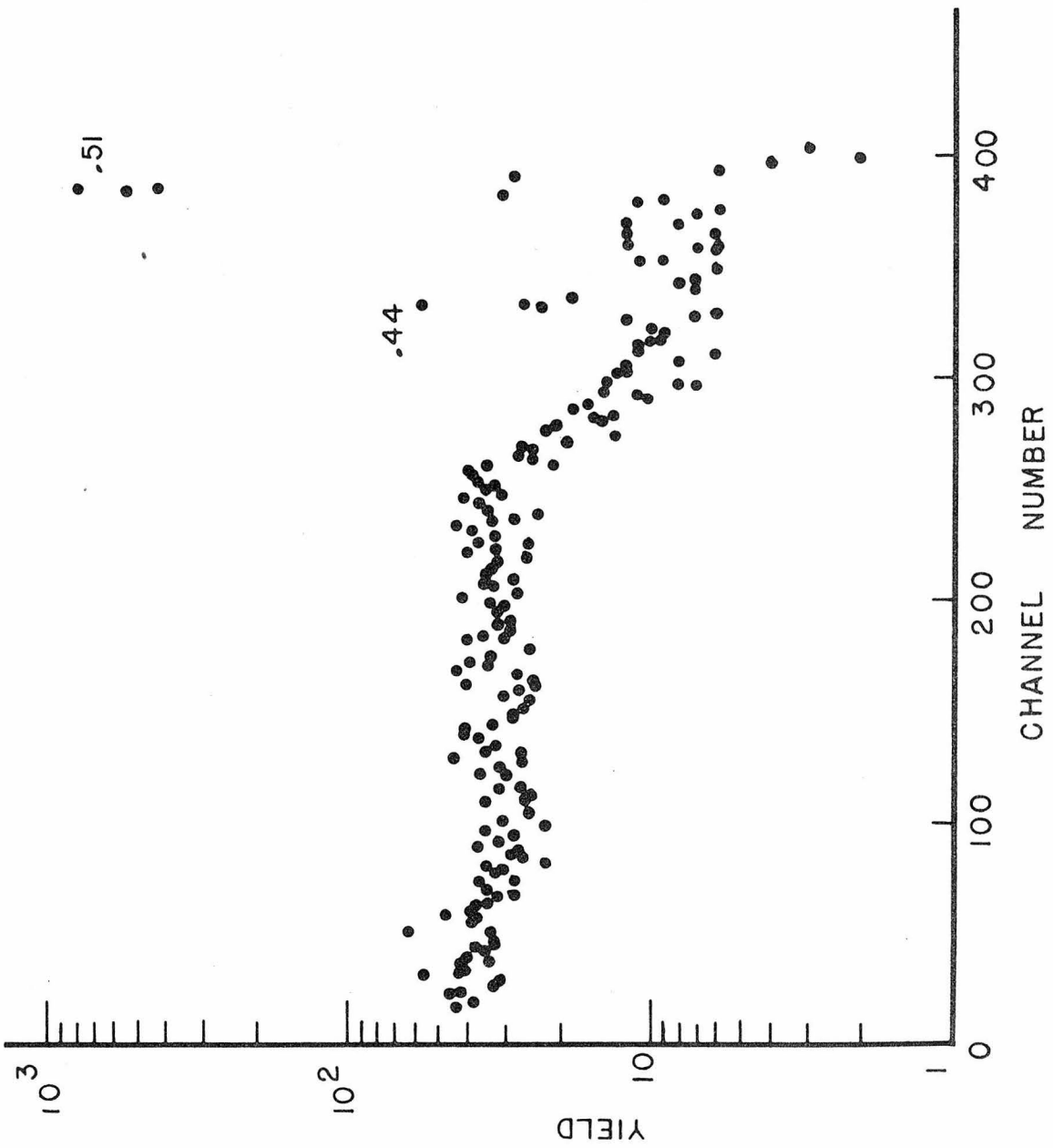
.51
.44
YIELD
10^3
10^2
10
1
0
100
200
300
400
CHANNEL NUMBER

Figure 9

Reaction cross section for $^{23}Na(p,n)^{23}Mg$ from E_{cm} = 4.85 to 10.53 MeV. The Q of this reaction is -4.84 MeV. The insert shows an expanded view of the cross section near threshold. The cross sections are listed in Table IX.

Several resonance-like structures are seen. The large peak just above threshold is not due to the opening of the (p,n_1) channel, as this occurs several hundred keV higher. Once the bumpy region is passed, the cross section is relatively flat to the highest energy measured.

Only Blaser et al (1951) have measured this cross section before. Rough agreement is obtained for energies near threshold if their energy scale is shifted by 150 keV. For energies greater than 6 MeV, the present results are higher.

(See page 230.)

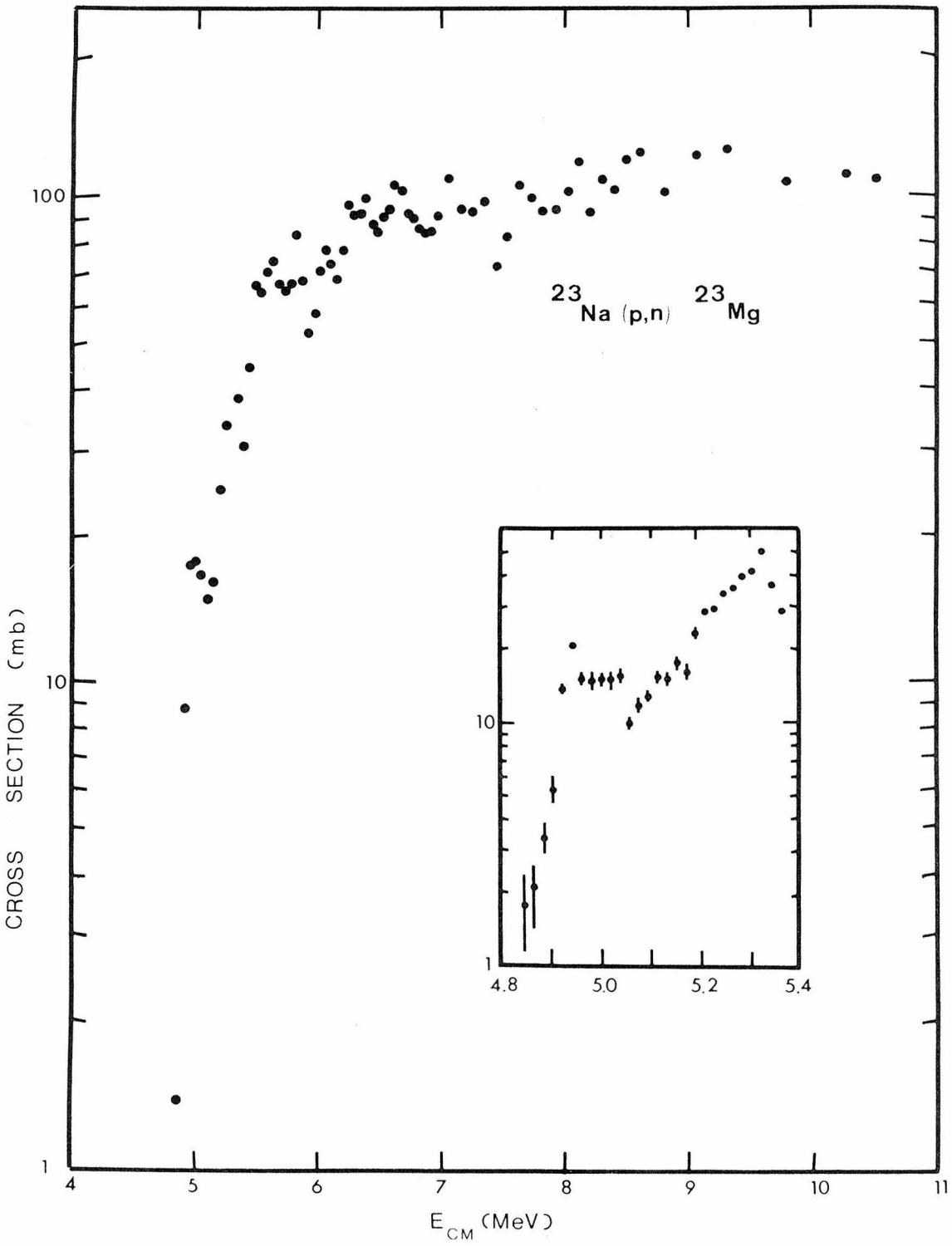
100
10
1
CROSS SECTION (mb)
^{23}Na (p,n) ^{23}Mg
10
1
4.8
5.0
5.2
5.4
4
5
6
7
8
9
10
11
E_{CM} (MeV)

Figure 10

Typical delayed gamma spectrum following alpha bombardment of $BaCl_2$. The spectrum shown is for $E_{cm} \sim 8.0$ MeV and was taken with a 5 cm x 5 cm NaI detector. The gamma rays present are from the decay of ^{38}K (0.51 Mev, 0.95, 1.46, and 2.17 MeV) and room background. The peaks at 0.95 and 1.46 MeV are the single- and double-escape peaks of the 2.17 MeV gamma ray.

Two spectra were taken for each bombarding energy. The cross section for the $^{35}Cl(\alpha,n)^{38}K(g.s.)$ reaction was determined by summing the yields of the 2.17 MeV gamma rays in the two spectra. The yield for the $^{35}Cl(\alpha,n)^{38}K(i.s.)$ was determined by subtracting the yield of the 511-keV peak in the second group from the yield in the first group. Since the counting periods were short compared to the half-life of the ground state of ^{38}K, the difference in the 511-keV radiation is proportional to the number of decays of the isomeric level, which has a short half-life.

(See page 231.)

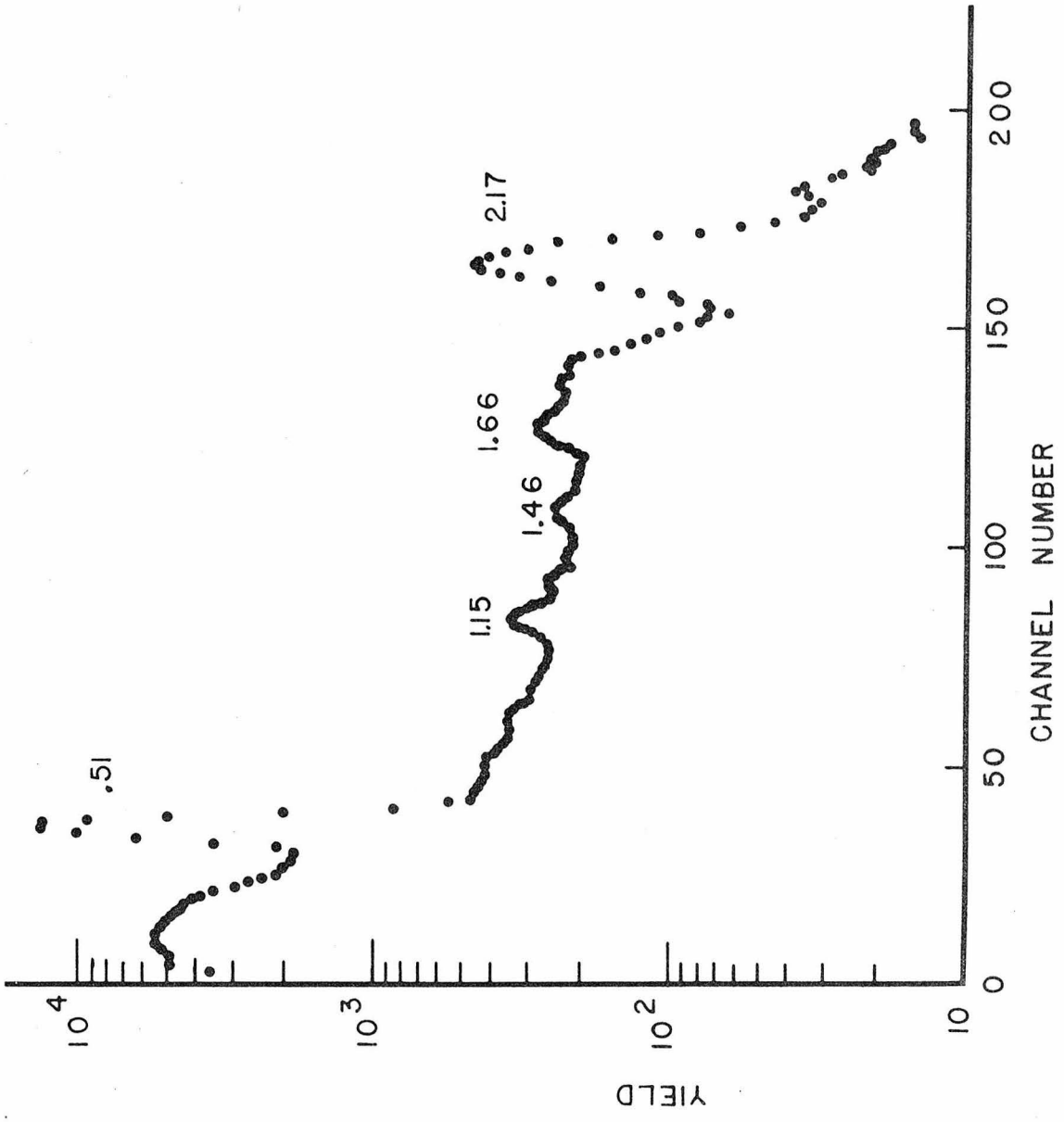
YIELD
10^4
10^3
10^2
10
0
50
100
150
200
CHANNEL NUMBER
.51
1.15
1.46
1.66
2.17

Figure 11

Typical delayed gamma ray spectrum following alpha bombardment of $BaCl_2$. The spectrum shown is for $E_{cm} \sim 8.0$ MeV and was taken with a 50 cm^3 Ge(Li) detector.

By comparing Figures 10 and 11, the superior resolution of the Ge(Li) detector is quite evident. The same gamma rays appear in both spectra, and the analysis was the same.

(See page 231.)

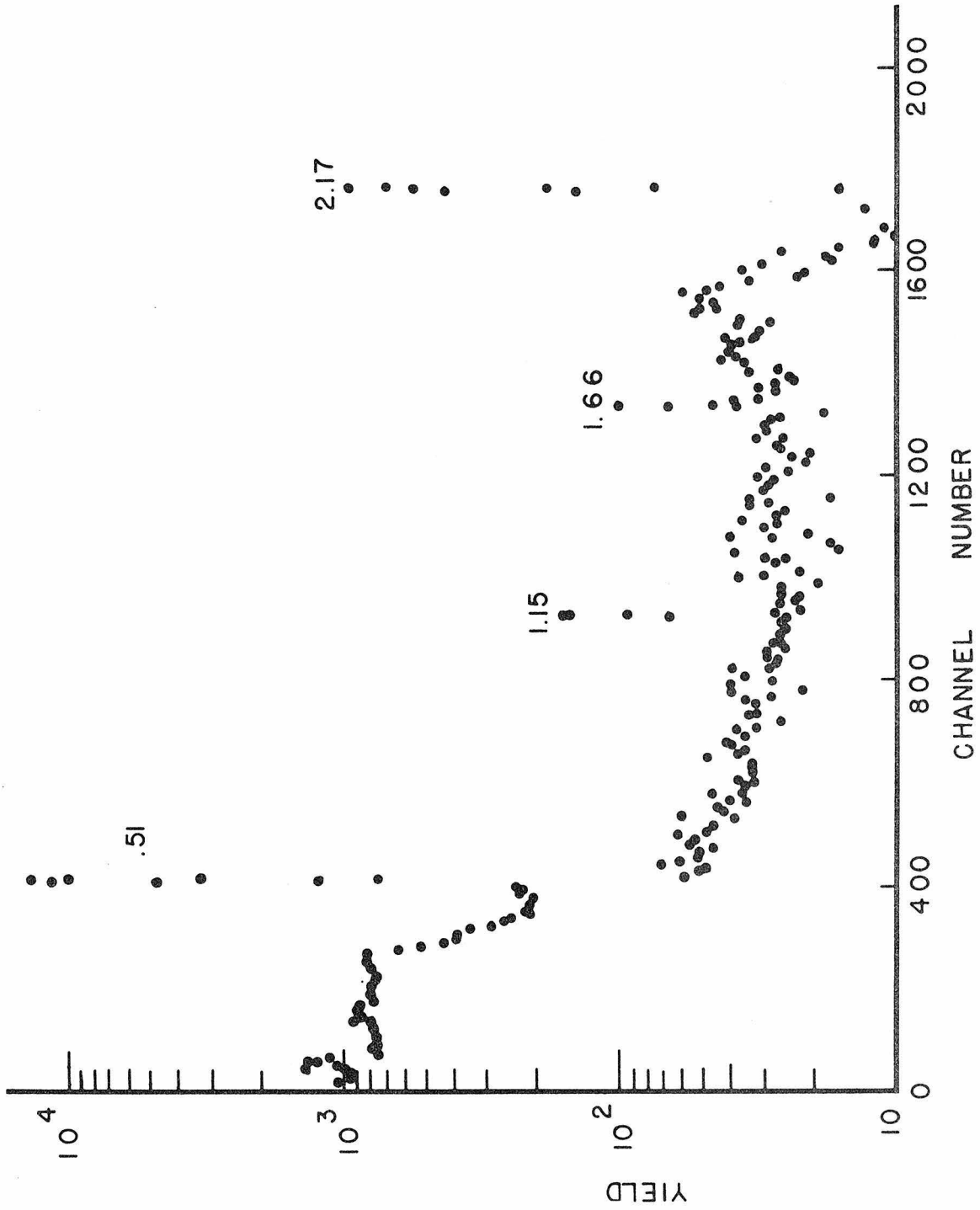
.51
1.15
1.66
2.17
YIELD
10^4
10^3
10^2
10
0
400
800
1200
1600
2000
CHANNEL NUMBER

Figure 12

Cross section for $^{35}Cl(\alpha,n)^{38}K(g.s.)$ and $^{35}Cl(\alpha,n)^{38}K$ (i.s.) for E_{cm} = 5.91 to 10.76 MeV. The Q value for the ground state reaction is -5.88 MeV.

The cross section to $^{38}K(g.s.)$ denotes the part of the $^{35}Cl(\alpha,n)$ cross section which populates either the ground state of ^{38}K or levels in ^{38}K which then gamma decay directly or indirectly to the ground state. Similarly the cross section to ^{38}K(isomeric state) denotes the part of the $^{35}Cl(\alpha,n)$ cross section which populates the beta-decay isomeric state of ^{38}K at 0.13 MeV or to levels in ^{38}K which gamma decay to the isomeric level.

The early flatness and subsequent rise of the $^{35}Cl(\alpha,n)^{38}K(g.s.)$ cross section is due to the early absence of states which decay to the ground state and subsequent population of many states which do gamma decay to the ground state of ^{38}K.

The values of the cross sections are presented in Table X. The cross section for $^{35}Cl(\alpha,n)^{38}K(g.s.)$ has been measured once before by Howard et al (1974). The agreement between the two sets of data is good.

(See page 231.)

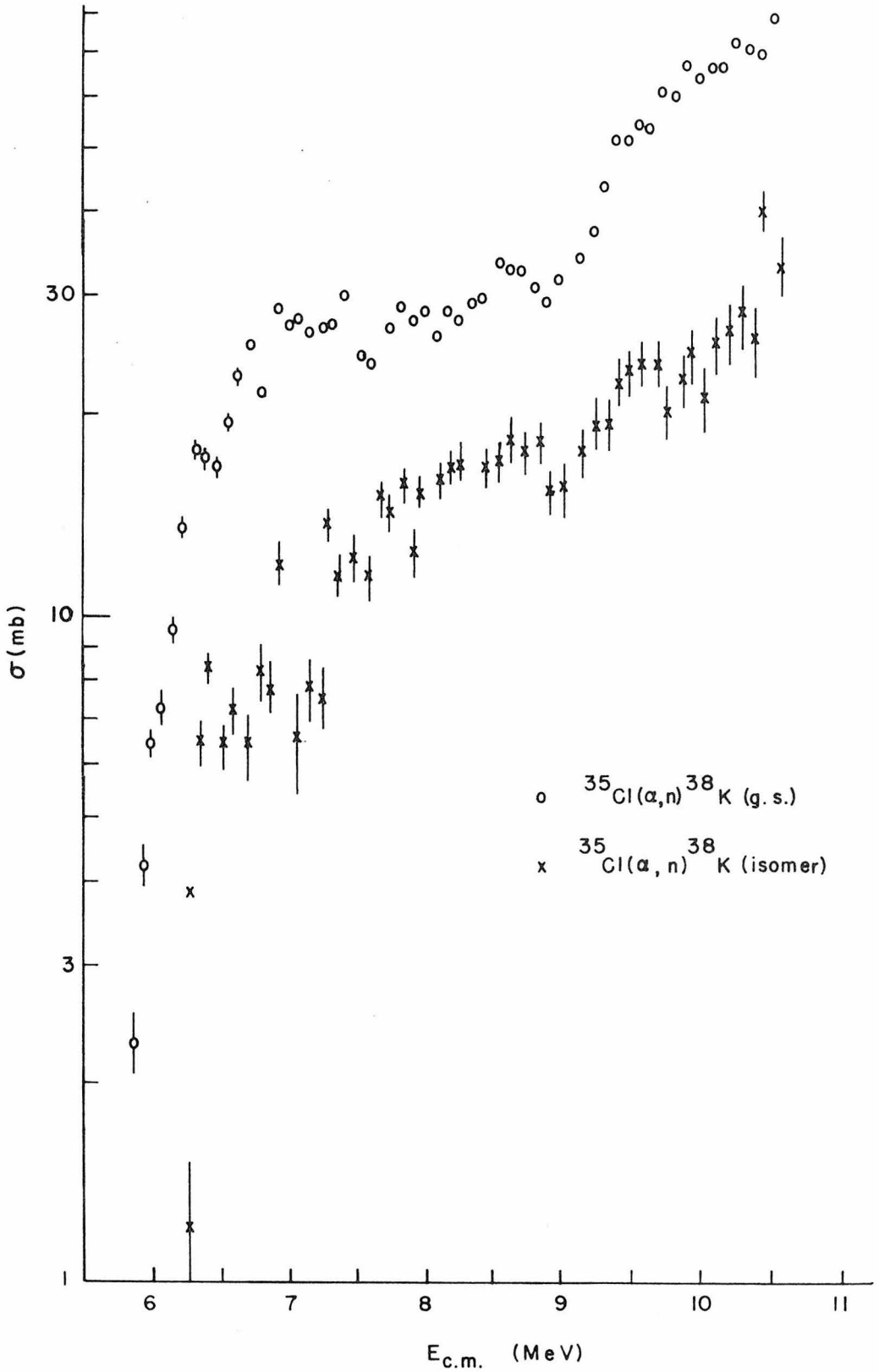
30
10
3
1
σ (mb)
o 35Cl(α,n)38K (g.s.)
x 35Cl(α,n)38K (isomer)
6
7
8
9
10
11
Ec.m. (MeV)

Figure 13

Cross section for $^{35}Cl(\alpha,n)^{38}K$ for E_{cm} = 5.91 to 10.76 MeV. The Q value for the reaction is -5.88 MeV.

This cross section is just the sum of the cross sections presented in Figure 12. The values of the cross section are presented in Table X.

(See page 231.)

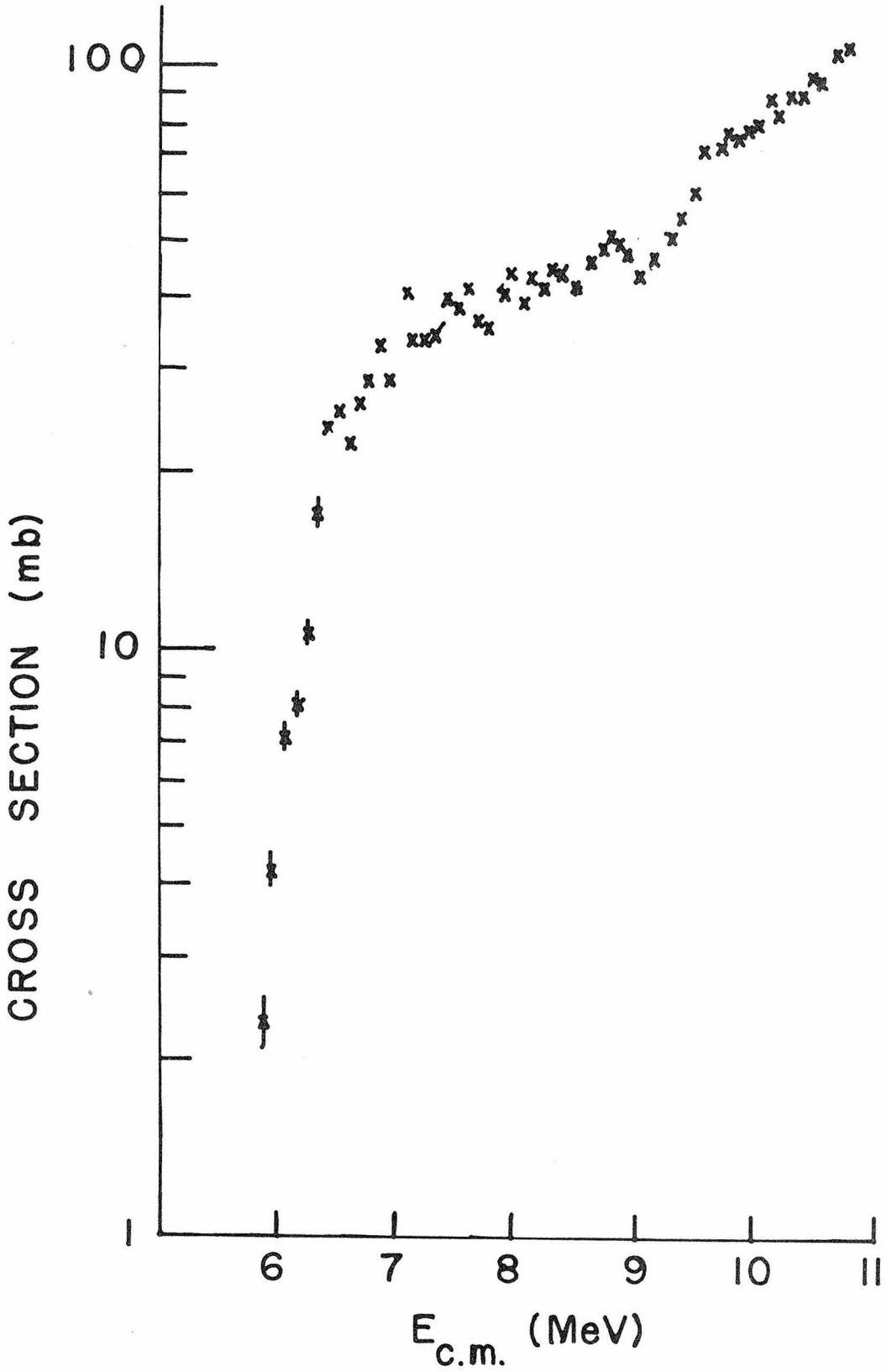
100
10
1
CROSS SECTION (mb)
6
7
8
9
10
11
$E_{c.m.}$ (MeV)

Figure 14

Typical delayed gamma spectrum following alpha bombardment of Co. The spectrum shown is for $E_{cm} \sim 14$ MeV. The largest gamma ray present is the annihilation radiation from ^{62}Cu decay. Also weakly present are the two gamma rays which sometimes accompany the decay of ^{62}Cu (0.88 and 1.17 MeV). Also present at very low energies are Pb X-rays.

The cross section for $^{59}Co(\alpha,n)^{62}Cu$ was inferred by taking the difference in yield of the annihilation radiation in two sequential groups. The difference of yields was used to reduce the effect of any long-lived contaminant.

(See page 232.)

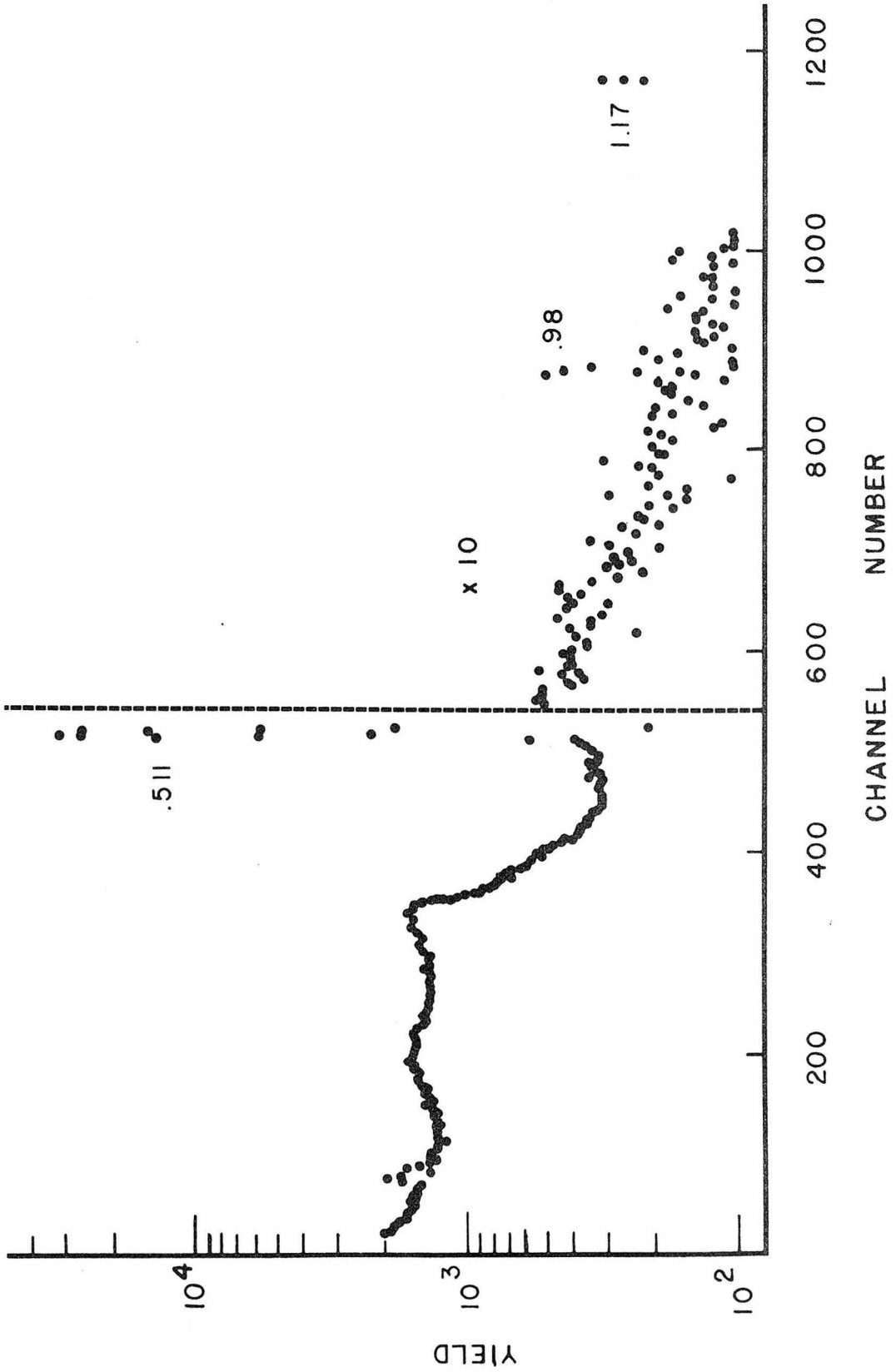
YIELD
10^4
10^3
10^2
.511
x 10
.98
1.17
200
400
600
800
1000
1200
CHANNEL NUMBER

Figure 15

Cross section for $^{59}Co(\alpha,n)^{62}Cu$ for E_{cm} = 5.14 to 19.0 MeV. The Q value for this reaction is -5.07 MeV. The cross sections are also listed in Table XI.

Also shown are the Q values for sequential particle emission, which takes strength from the ^{62}Cu + n channels.

The work of previous investigators (Stelson and McGowan 1964, D'Auria et al 1968, and Zhukova et al 1973) is also presented. The agreement is good.

(See page 232.)

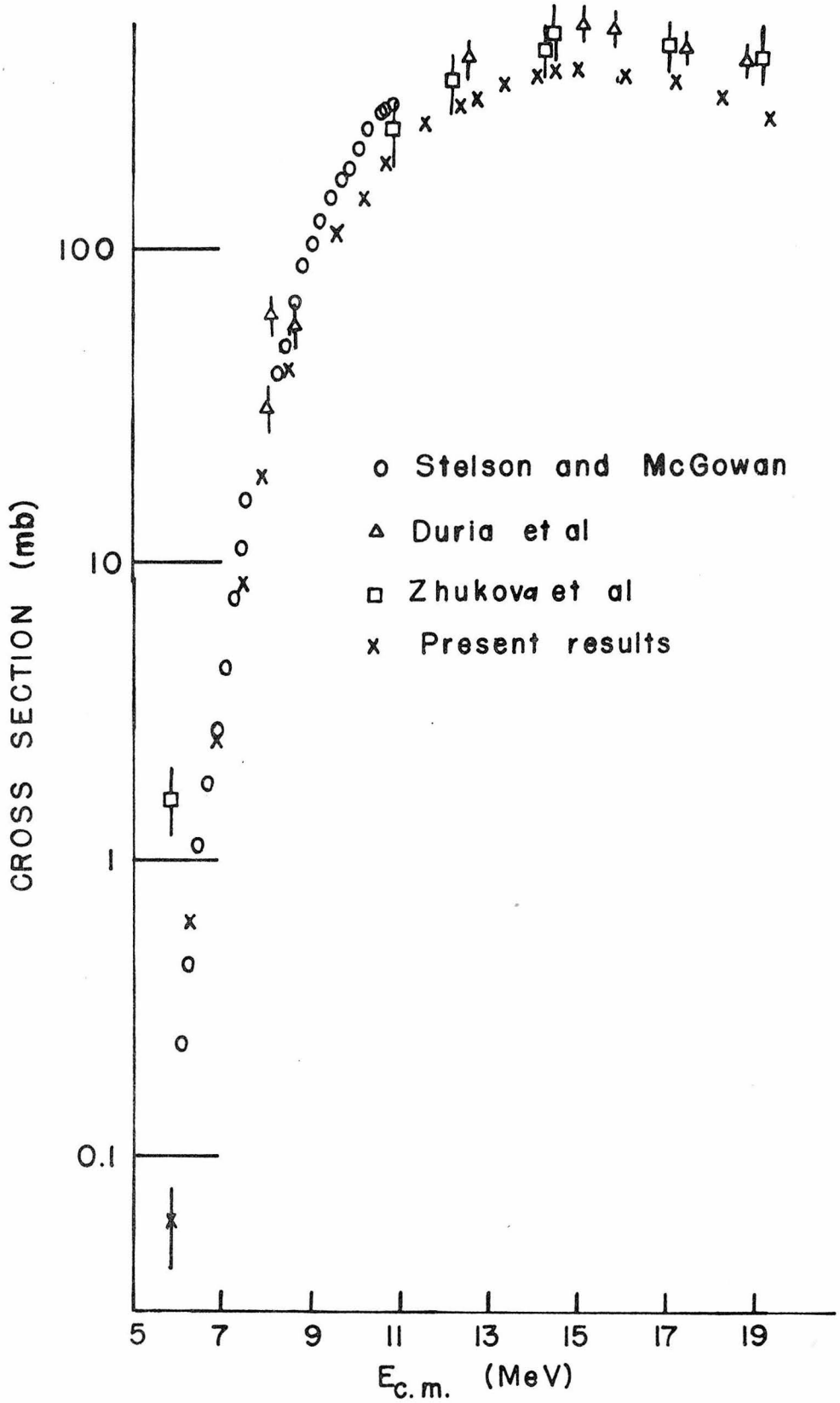
100
10
1
0.1
CROSS SECTION (mb)
o Stelson and McGowan
△ Duria et al
□ Zhukova et al
x Present results
5
7
9
11
13
15
17
19
E c. m. (MeV)

Figure 16

Typical delayed gamma spectrum following alpha bombardment of Cu. The spectrum shown is for $E_{cm} \sim 14.5$ MeV. The gamma rays seen are from the decays of ^{66}Ga and ^{68}Ga. The gamma ray at 1039 keV was used to infer the $^{63}Cu(\alpha,n)^{66}Ga$ cross section, the line at 833 keV providing a check that the yield was due to ^{66}Ga decay. The 1078-keV gamma ray was used to infer the $^{65}Cu(\alpha,n)^{68}Ga$ cross section.

(See page 233.)

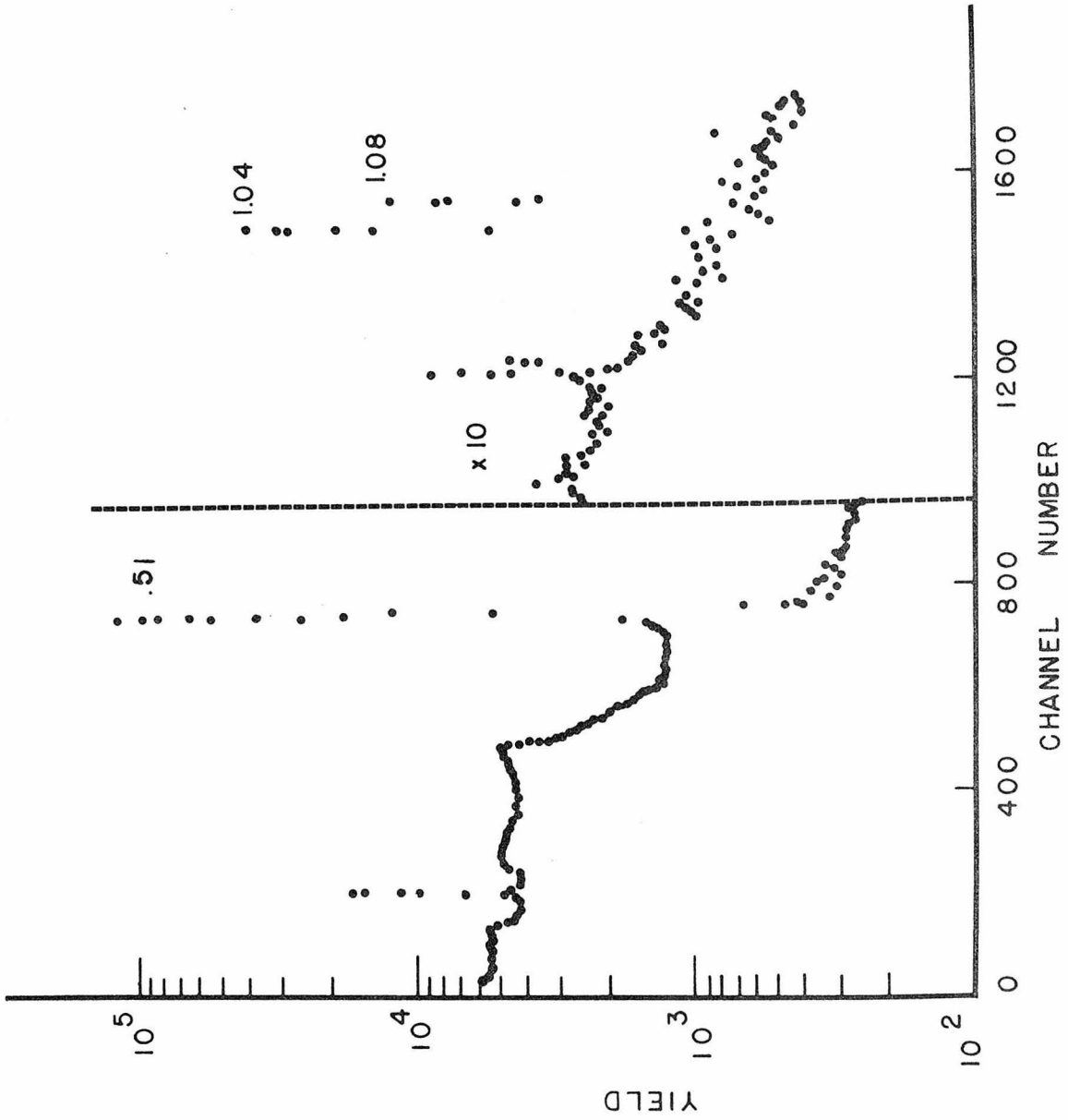
YIELD
10^5
10^4
10^3
10^2
0
400
800
1200
1600
CHANNEL NUMBER
.51
1.04
1.08
x 10

Figure 17

Cross section for $^{63}Cu(\alpha,n)^{66}Ga$ for E_{cm} = 7.9 to 17.4 MeV. The Q value for this reaction is -7.5 MeV. The cross sections are also listed in Table XII.

The Q values for sequential particle emission from ^{66}Ga are shown at the appropriate energies. Sequential particle emission competes with gamma decay of excited ^{66}Ga levels and causes the cross section to turn over at the higher energies.

The work of previous investigators (Stelson and McGowan 1964, Porile and Morrison 1959, and Hille et al 1972) is also presented. The agreement is good except for the work of Porile and Morrison.

(See page 233.)

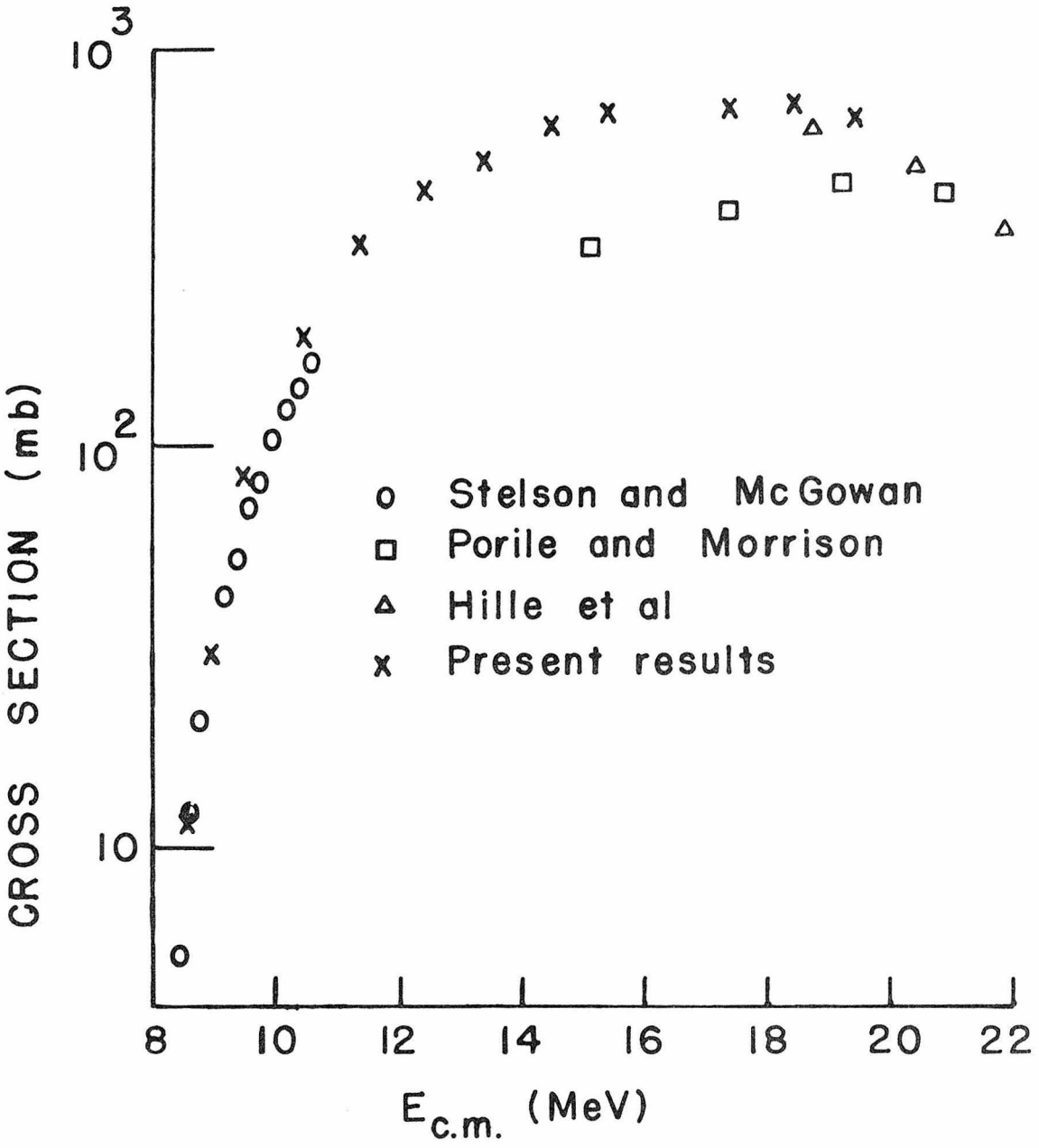
CROSS SECTION (mb)
10^3
10^2
10
o Stelson and McGowan
□ Porile and Morrison
△ Hille et al
x Present results
8
10
12
14
16
18
20
22
E c.m. (MeV)

Figure 18

Cross section for $^{65}Cu(\alpha,n)^{68}Ga$ for E_{cm} = 6.0 to 17.4 MeV. The Q value for this reaction is -5.8 MeV. The cross sections are also listed in Table XIII.

The Q values for sequential particle emission from ^{68}Ga are shown at the appropriate energies. Sequential particle emission takes strength away from the ^{68}Ga + n channels, causing the cross sections to turn over at higher energies.

The work of previous investigators (Stelson and McGowan 1964, Porile and Morrison 1959, and Hille et al 1972) is also presented. The agreement among the groups is good except for the work of Porile and Morrison.

(See page 233.)

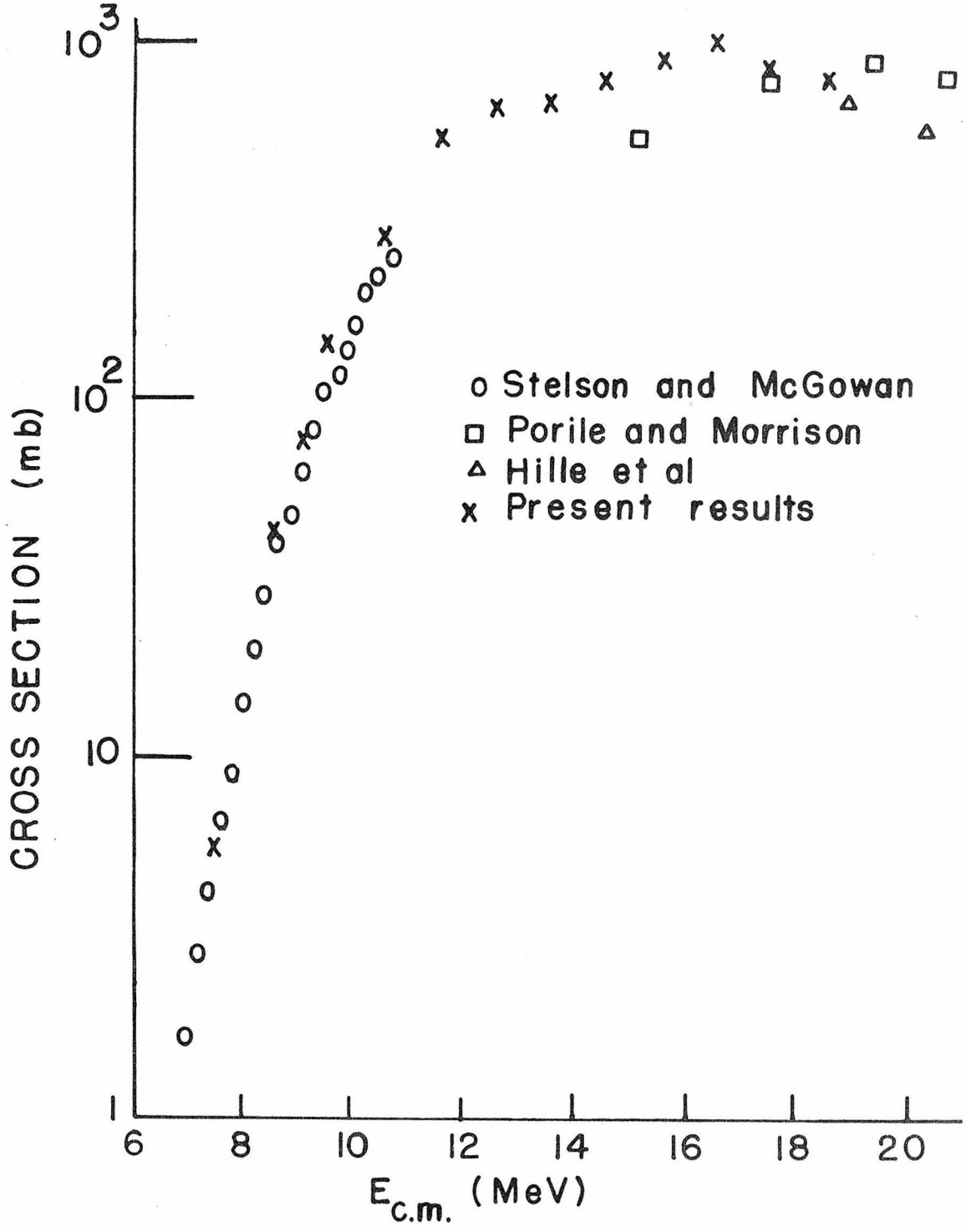
CROSS SECTION (mb)
10^3
10^2
10
1
6
8
10
12
14
16
18
20
E c.m. (MeV)
o Stelson and McGowan
□ Porile and Morrison
△ Hille et al
x Present results

Figure 19

Typical delayed gamma spectrum following proton bombardment of Cu. The spectrum shown is for E_{cm} = 8 MeV. The strongest lines (at 0.51, 0.67, and 0.96 MeV) are due to the decays of ^{63}Zn. As the yield ratios of these three gamma rays were constant as the bombarding energy was increased, all three gamma rays were used to determine the relative cross section. The non-annihilation gamma rays were then used to find the proper normalization.

(See page 234.)

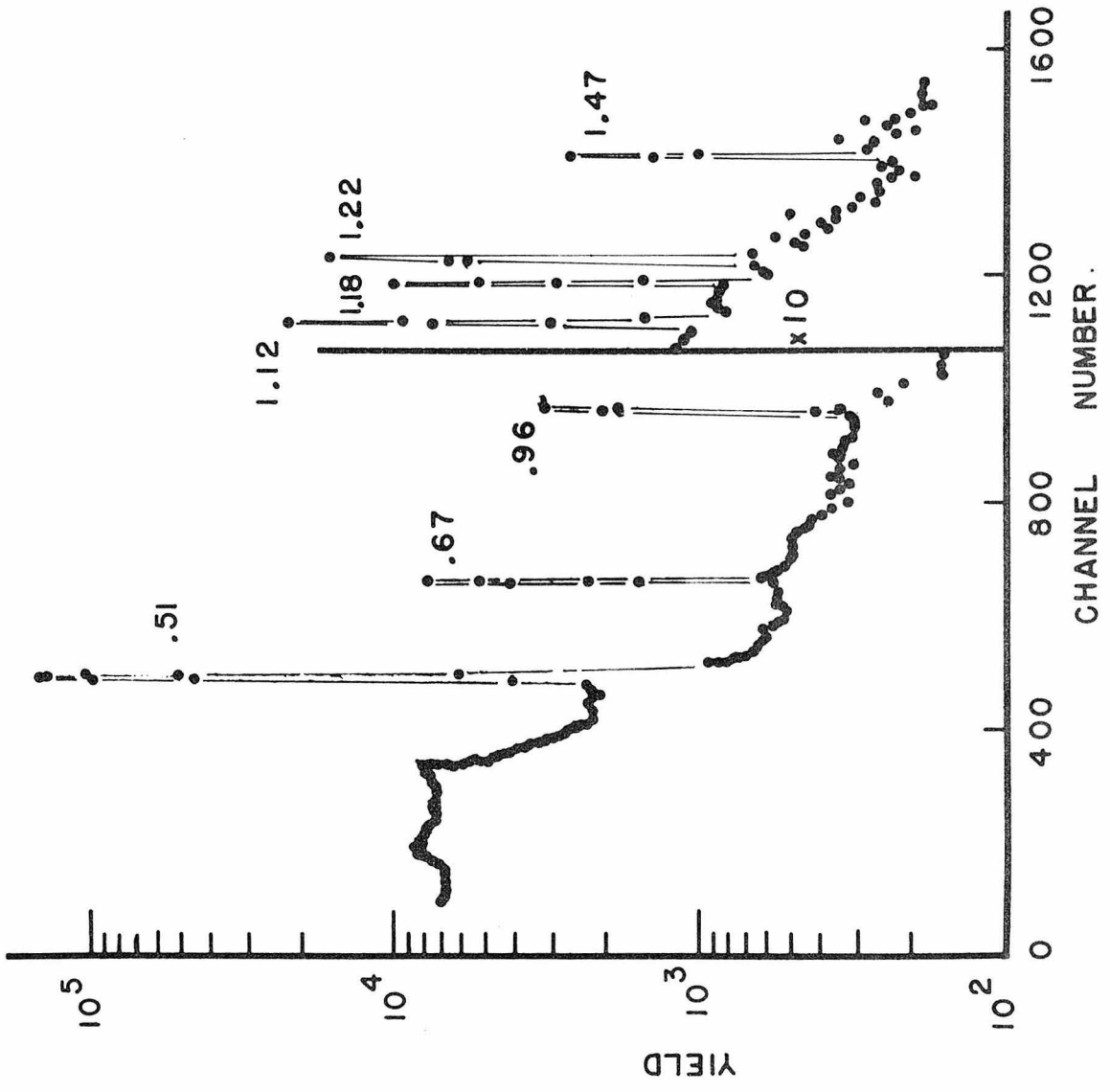
YIELD
10^5
10^4
10^3
10^2
0
400
800
1200
1600
CHANNEL NUMBER.
.51
.67
.96
1.12
1.18
1.22
1.47
x10

Figure 20

Cross section for $^{63}Cu(p,n)^{63}Zn$ for E_{cm} = 4.17 to 12 MeV. The Q value for this reaction is -4.15 MeV. The cross sections are also listed in Table XIV.

Much previous effort has been expended on the measurement of this cross section. See Collé et al (1974) for a review. Plotted along with the present results are the results of Collé et al. The various groups are in good agreement.

(See page 234.)

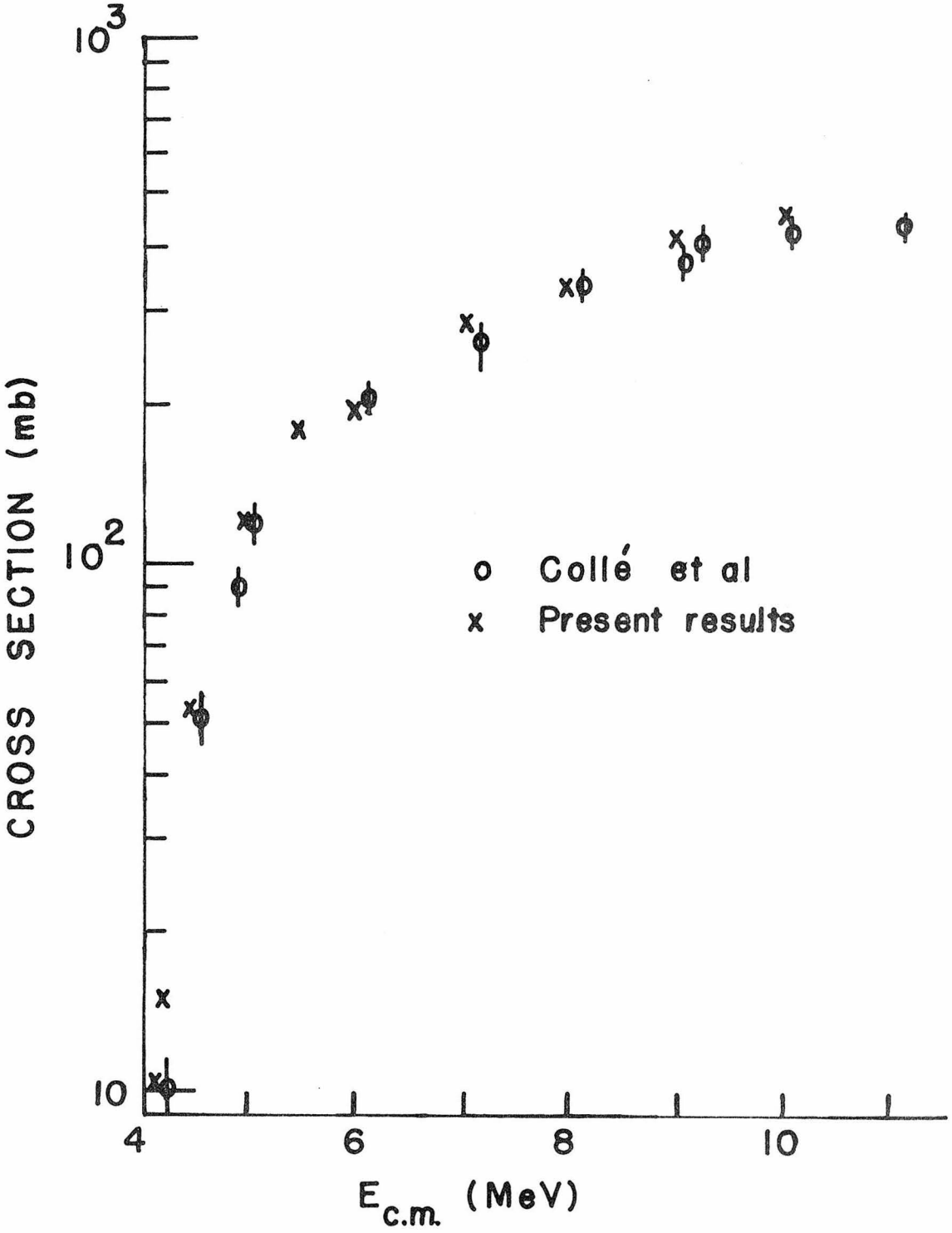
CROSS SECTION (mb)
10^3
10^2
10
4
6
8
10
$E_{c.m.}$ (MeV)
o Collé et al
x Present results

Figure 21

Ladder diagram for $^{23}Na + p$, only the most important channels being shown. Other channels not shown (with Q values relative to $^{23}Na + p$) include $d + {}^{22}Na$ (-10.2 MeV), $2\alpha + {}^{16}O$ (-2.35 MeV), and $^{12}C + {}^{12}C$ (-2.24 MeV).

The discrete states shown were included in the statistical model calculations. The levels characterized by the slashed region were included by means of a level density formula (the constant temperature formula using parameters which predicted the known level density of the nuclei). Only the n,p and α channels were considered in the calculations, since the presence of other channels has negligible effect for the energies studied.

(See page 236.)

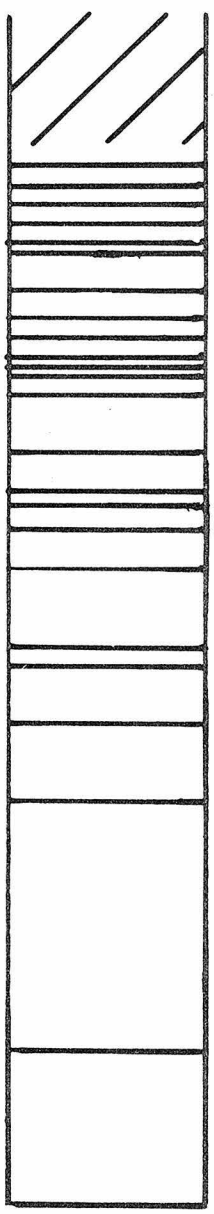

2.38

$^{20}Ne + \alpha$

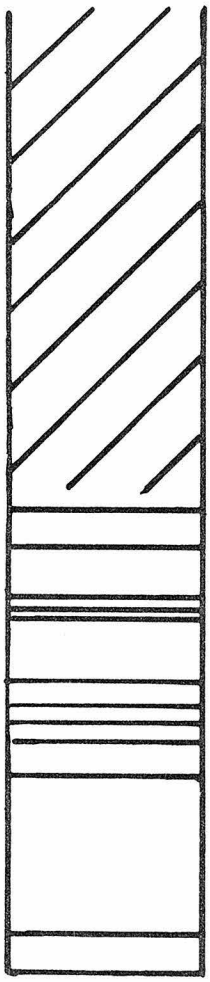

0.0

$^{23}Na + p$

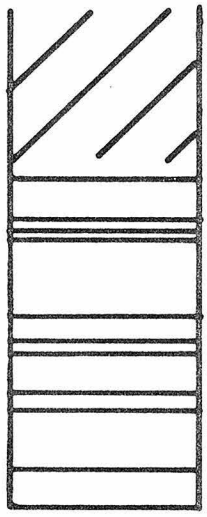

-4.84

$^{23}Mg + n$

11.69

^{24}Mg

Figure 22.

Theoretical reaction cross sections for $^{23}Na(p,n)^{23}Mg$ divided by the measured values. The points plotted are the averages of values in 250 keV energy interval around the point. Two potential sets are shown: 1) proton potential from Perey (1963) neutron potential from Wilmore and Hodgson (1964), and the alpha potential from Igo (1959a and 1959b); and 2) proton, neutron and alpha potentials from Michaud and Fowler (1970a). The results from other potential sets lie in between the results shown.

The theoretical values overpredict the measured cross sections. This overprediction is understandable as it is known from previous work (see page 236) that $^{23}Na(p,p')$ goes strongly by direct reactions, thus robbing the (p,n) channels of strength.

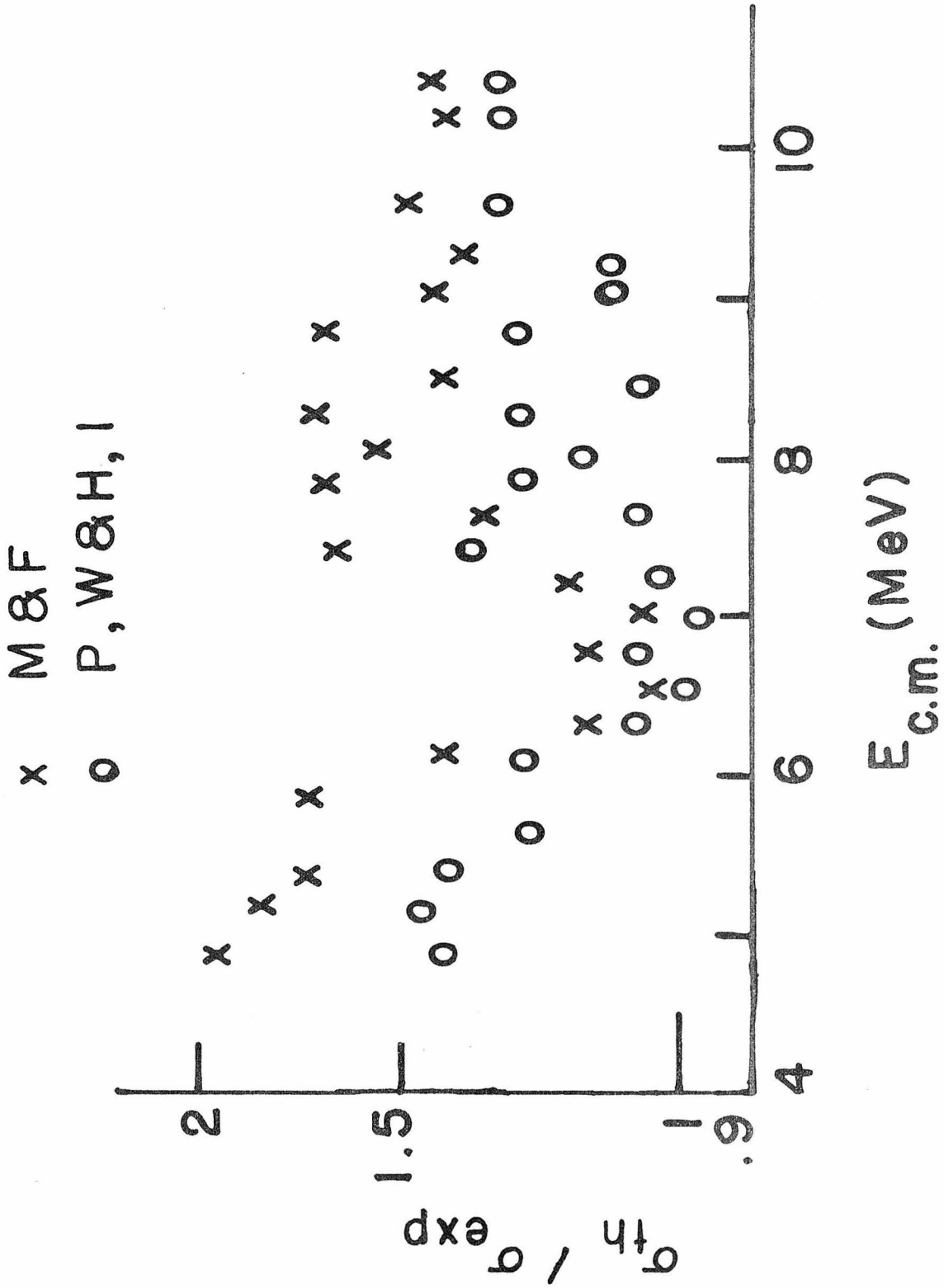
x M&F
o P,W&H,I
σ_{th} / σ_{exp}
2
1.5
1
.6
4
6
8
10
$E_{c.m.}$ (MeV)

Figure 23

Ladder diagram for $^{35}Cl + \alpha$, only the most important channels being shown. Other channels not shown (with Q values relative to $^{35}Cl + \alpha$) include $d + {}^{37}Ar$ (-8.77 MeV), $p + \alpha + {}^{34}S$ (-6.37 MeV), and $2\alpha + {}^{31}P$ (-7.00 MeV).

The discrete states shown were included in the statistical model calculations. The levels characterized by the slashed region were included by means of a level density formula (the parameters being from Gilbert and Cameron 1965a). Only n, p, and α channels were included in the calculations since the presence of other channels has negligible effect for the energies studied.

(See page 238.)

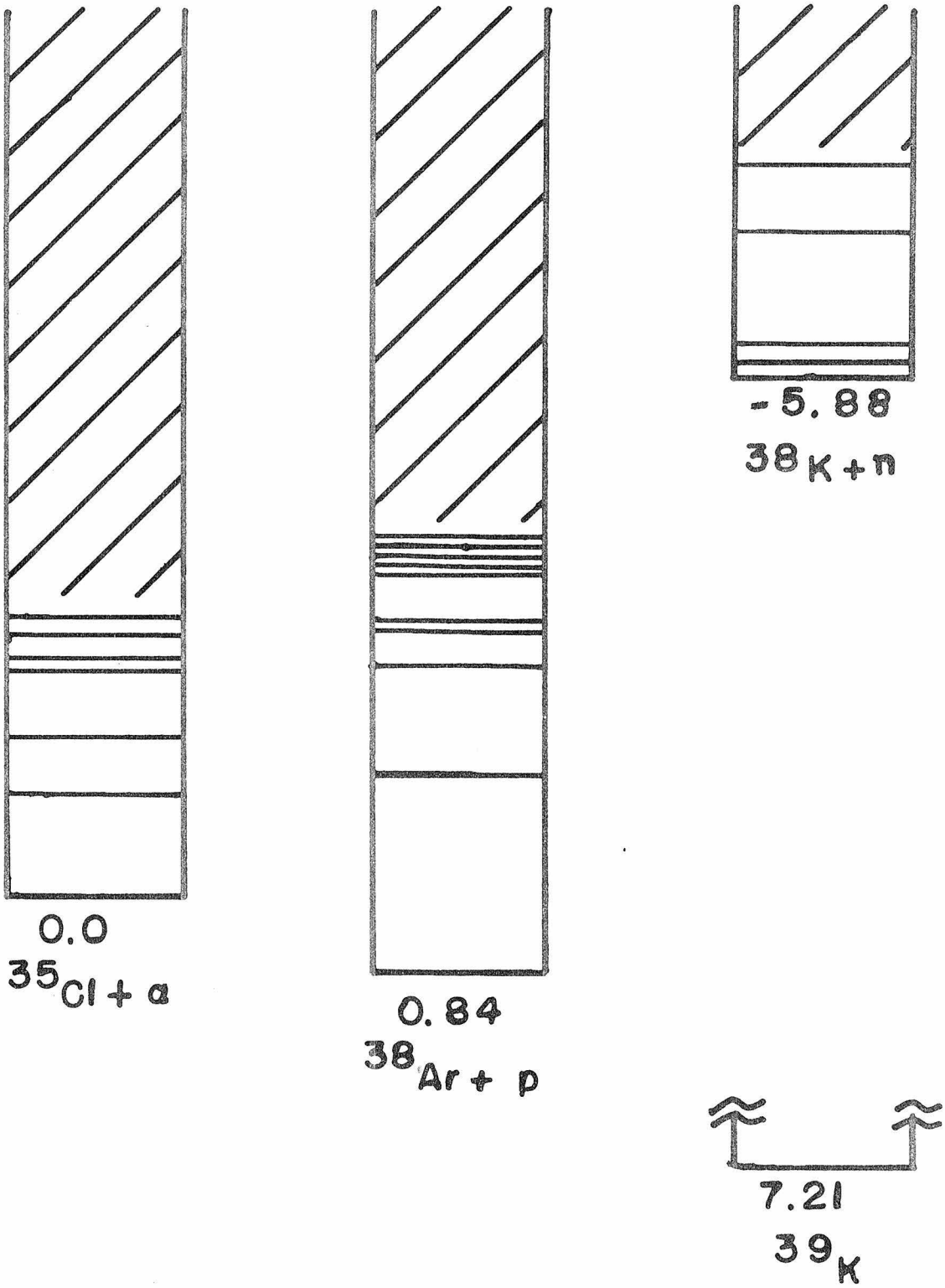
0.0
35Cl + a
0.84
38Ar + p
-5.88
38K + n
7.21
39K

Figure 24

Theoretical reaction cross sections for $^{35}Cl(\alpha,n)^{38}K$ divided by measured values. Four potential sets are shown: 1) proton potential from Perey (1963), neutron potential from Wilmore and Hodgson (1964), and alpha potential from Igo (1959a and 1959b); 2) proton potential from Perey, neutron potential from Wilmore and Hodgson, and alpha potential from Michaud and Fowler (1970a); 3) proton and neutron potentials from Michaud and Fowler and alpha potential from Igo; and 4) proton, neutron, and alpha potentials from Michaud and Fowler. See text (page 234) for a discussion of other potential sets.

Potential set 4 predicts values in excellent agreement with experiment.

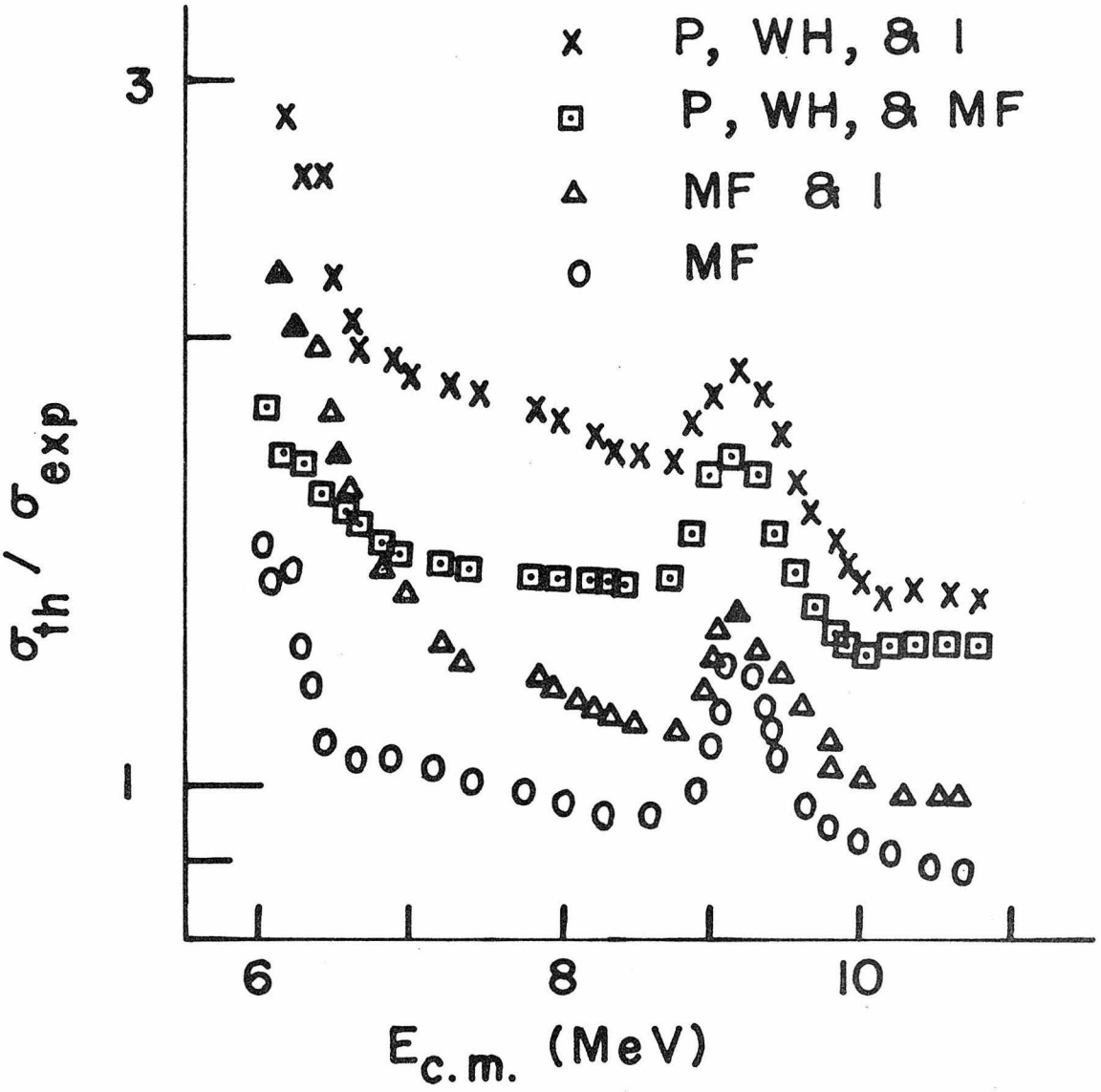
P, WH, & I
P, WH, & MF
MF & I
MF
3
1
6
8
10
$\sigma_{th} / \sigma_{exp}$
$E_{c.m.}$ (MeV)

Figure 25

Theoretical reaction cross section predictions (divided by measured values) for $^{35}Cl(\alpha,n)^{38}K(g.s.)$ and for $^{35}Cl(\alpha,n)^{38}K(i.s.)$. The potentials used were from Michaud and Fowler (1970a) for protons, neutrons, and alphas.

The theoretical values end at E_{cm} = 8.5 MeV, since above this energy, states in ^{38}K are populated whose spin is not known. Therefore a unique division between states which eventually decay to the ground state and states which decay to the isomeric level cannot be made above this energy.

The agreement is very good, especially considering that a "global" potential was used to describe two quite different types of states in ^{38}K.

(See page 239.)

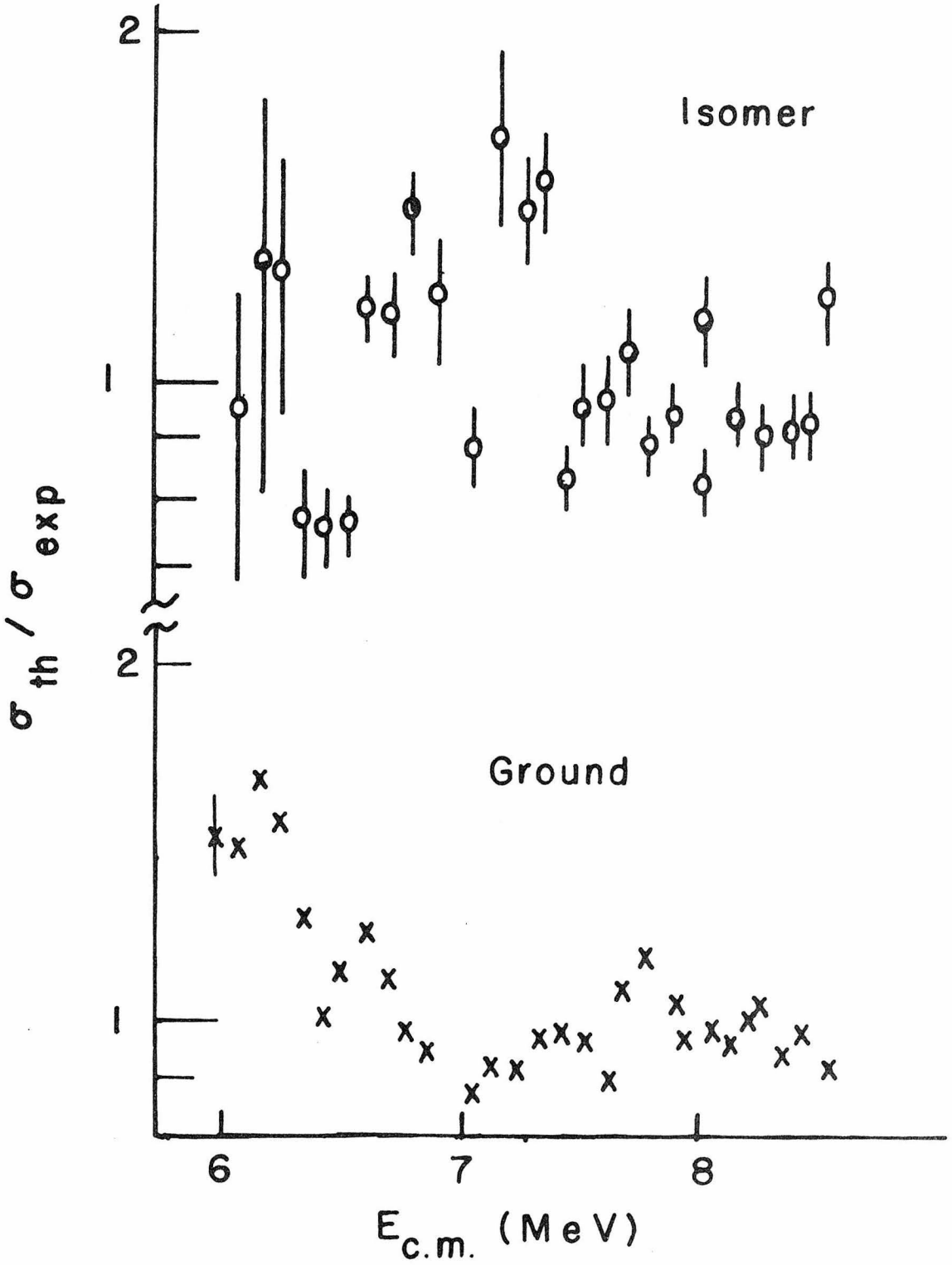
2
1
2
1
Isomer
Ground
$\sigma_{th} / \sigma_{exp}$
6
7
8
$E_{c.m.}$ (MeV)

Figure 26

Ladder diagram for $^{59}Co + \alpha$, only the most important channels being shown. The sequential particle breakups of ^{62}Cu are shown at the appropriate energies. Other channels not shown (with Q values relative to $^{59}Co + \alpha$) include $d + {}^{61}Ni$ (-8.72 MeV), $p + \alpha + {}^{58}Fe$ (-7.38 MeV), and $2\alpha + {}^{55}Mn$ (-6.95 MeV).

The discrete states shown were included in the statistical model calculations. The discrete states for ^{62}Cu used in the calculations are not explicitly shown as they are so dense; only the first and last levels used are shown. The levels characterized by the slashed region were included by means of a level-density formula (the parameters being from Dilg et al 1973). Only n, p, and α channels were included in the calculations since the presence of other channels has negligible effect for the energies studied.

(See page 240.)

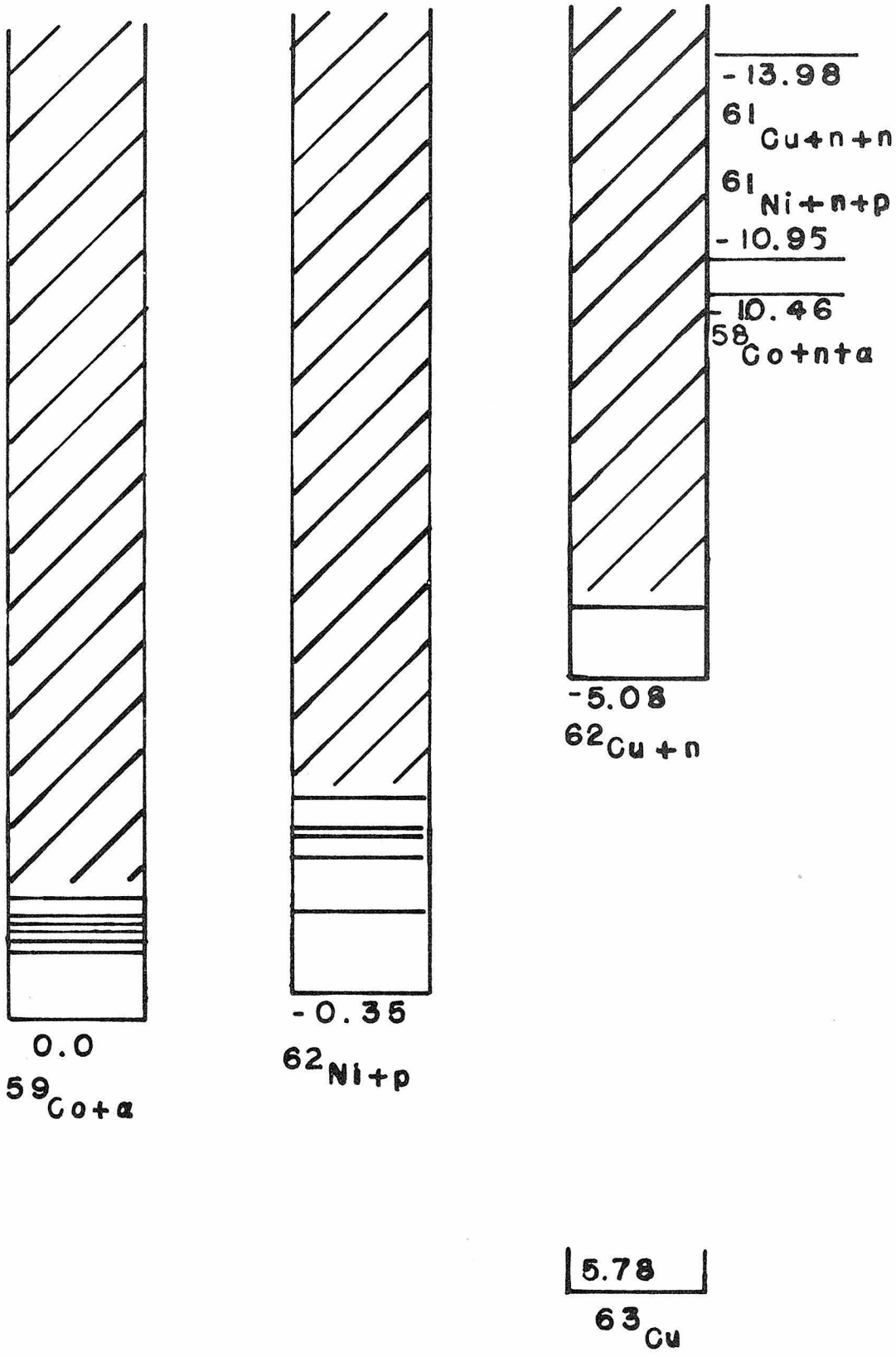
-13.98
61 Cu+n+n
61 Ni+n+p
-10.95
-10.46
58 Co+n+α
-5.08
62 Cu + n
-0.35
62 Ni+p
0.0
59 Co+α
5.78
63 Cu

Figure 27

Theoretical cross sections for $^{59}Co(\alpha,n)^{62}$ as a function of the "effective gamma-ray transmission coefficient". As thresholds for sequential particle emission are passed, new modes for the decay of the residual nucleus are opened. Thus the residual nucleus can be treated as a new compound nucleus and its decay can be predicted by the statistical model. For this calculation, gamma ray transmission coefficients are needed. In the calculations presented here, only one coefficient was used which approximates the effect of using the complete set. This approximation is valid, since the transmission coefficients for the particles increase quickly as a function of energy and small errors in the gamma ray channels make only small errors in the predictions in the leakage from the residual nucleus.

That such a leakage occurs is evident from comparing this figure and the figure showing the measured values of the cross section (Figure 15). From single particle estimates, the "effective gamma ray transmission coefficient" should be about 0.001.

(See page 240.)

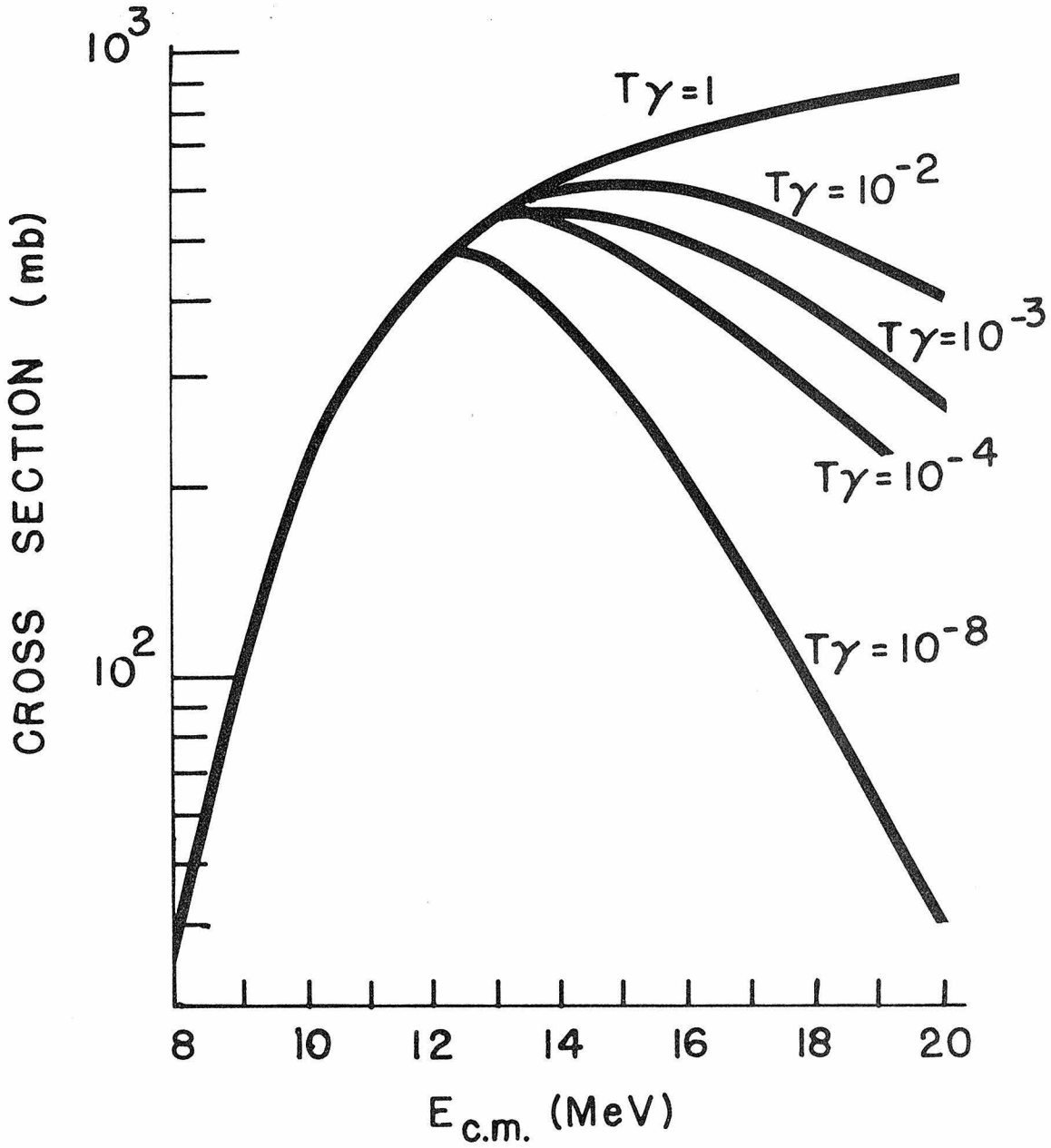
10^3
10^2
CROSS SECTION (mb)
$T\gamma = 1$
$T\gamma = 10^{-2}$
$T\gamma = 10^{-3}$
$T\gamma = 10^{-4}$
$T\gamma = 10^{-8}$
8
10
12
14
16
18
20
$E_{c.m.}$ (MeV)

Figure 28

Theoretical cross sections for $^{59}Co(\alpha,n)^{62}Cu$ divided by measured values. Three potential sets are shown: the proton and neutron potentials of Becchetti and Greenless (1969a), and 1) the alpha potential of Igo (1959a and 1959b), 2) the alpha potential of McFadden and Satchler (1966), and 3) the alpha potential of Michaud and Fowler (1970a). The choice of the nucleon potential makes little difference in the calculated values.

Potential set 2, the alpha potential of McFadden and Satchler, seems to agree with the measurements better than the other two potential sets.

(See page 240.)

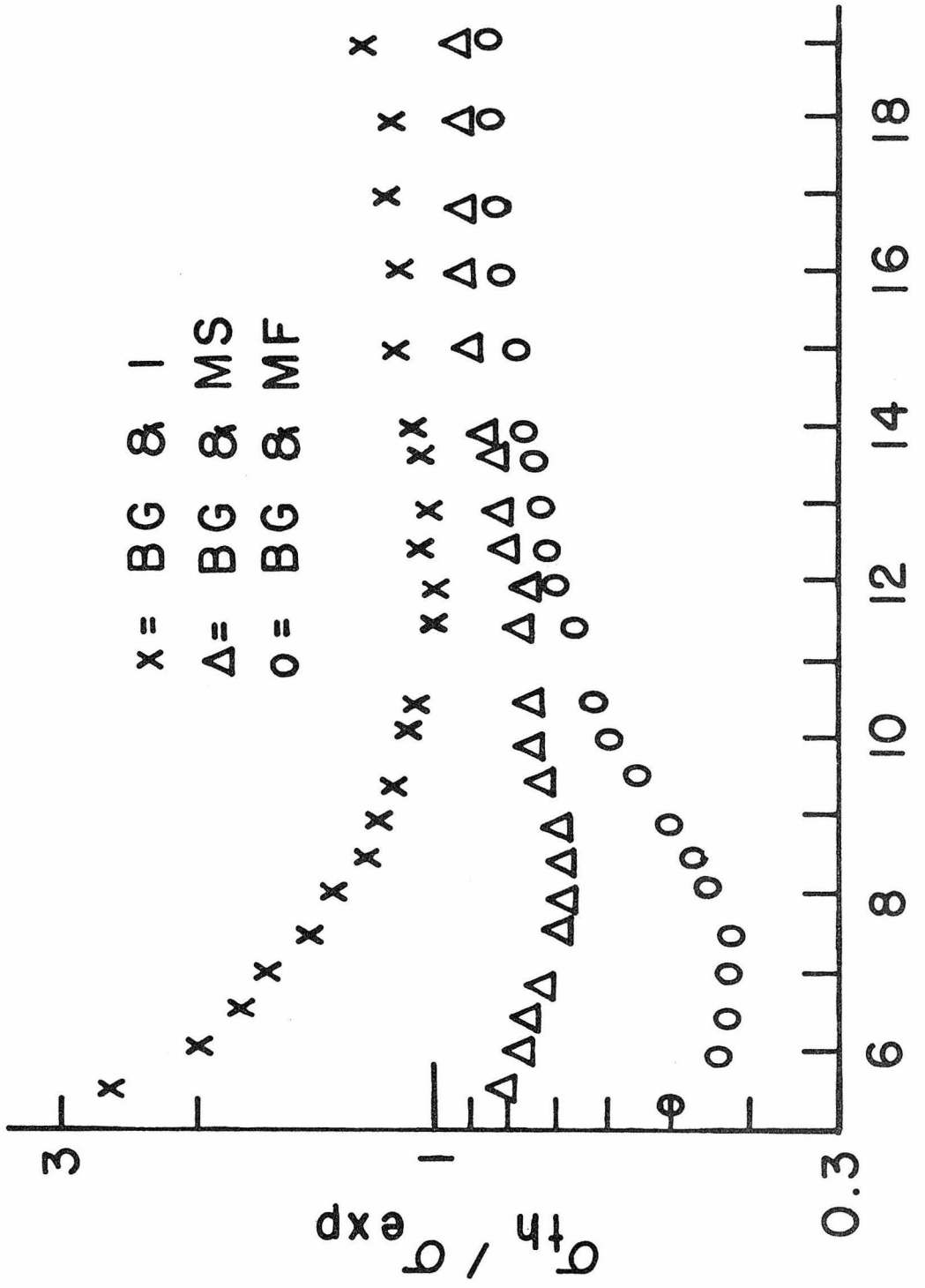
x= BG & I
Δ= BG & MS
o= BG & MF
3
1
0.3
$\sigma_{th} / \sigma_{exp}$
6
8
10
12
14
16
18
$E_{c.m.}$ (MeV)

Figure 29

Ladder diagram for $^{63}Cu + \alpha$, only the most important channels being shown. The sequential particle breakups of ^{66}Ga are shown at the appropriate energies. Other channels not shown (with Q values relative to $^{63}Cu + \alpha$) include $d + {}^{65}Zn$ (-10.38 MeV), $p + \alpha + {}^{62}Cu$ (-10.84), and $2\alpha + {}^{59}Co$ (-5.78 MeV).

The discrete states shown were included in the statistical model calculations. The discrete states for ^{66}Ga used in the calculations are not explicitly shown as they are so dense; only the first and last levels are shown. The levels characterized by the slashed region were included by means of a level density formula (parameters from Dilg et al 1973). Only n, p, and α channels were included in the calculations since the presence of other channels has negligible effect.

(See page 242.)

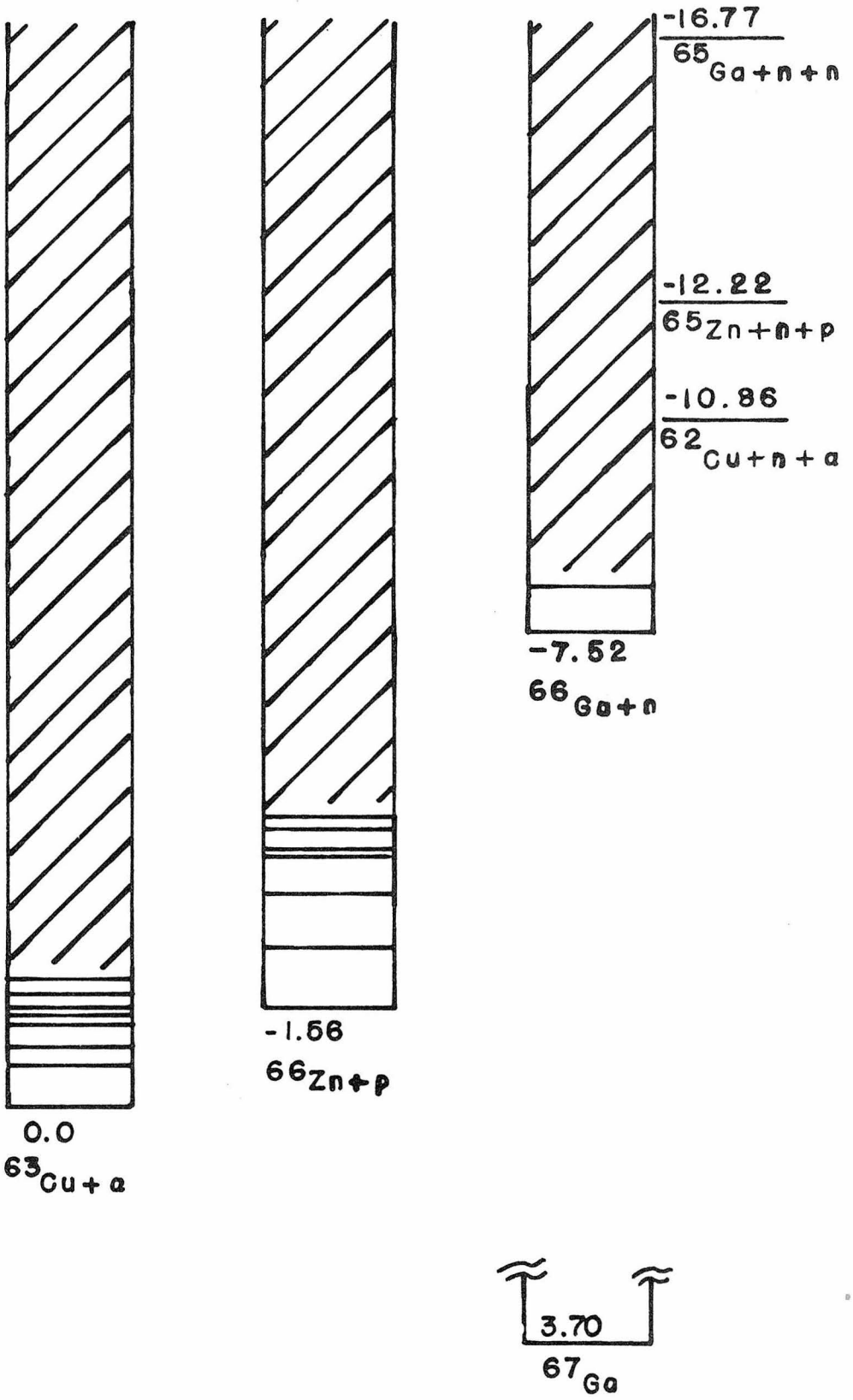
-16.77
65Ga+n+n
-12.22
65Zn+n+p
-10.86
62Cu+n+a
-7.52
66Ga+n
-1.56
66Zn+p
0.0
63Cu+a
3.70
67Ga

Figure 30

Theoretical cross sections for $^{63}Cu(\alpha,n)^{66}Ga$ divided by measured values. Two potential sets are shown: 1) the proton and neutron potentials of Becchetti and Greenlees (1969a) and the alpha potential of Igo (1959a and 1959b), and 2) the proton and neutron potentials of Becchetti and Greenlees and the alpha potential of Michaud and Fowler (1970a). If the alpha potential of McFadden and Satchler (1966) is used with the nucleon potential of Becchetti and Greenlees, the calculated values fall between the results of potential sets 1 and 2. The choice of the nucleon potential makes little difference in the calculated results.

Also shown on this figure are the theoretical cross sections for $^{63}Cu(\alpha,n)^{66}Zn$ divided by the measured values of Lassen and Sidorov (1960).

(See page 242.)

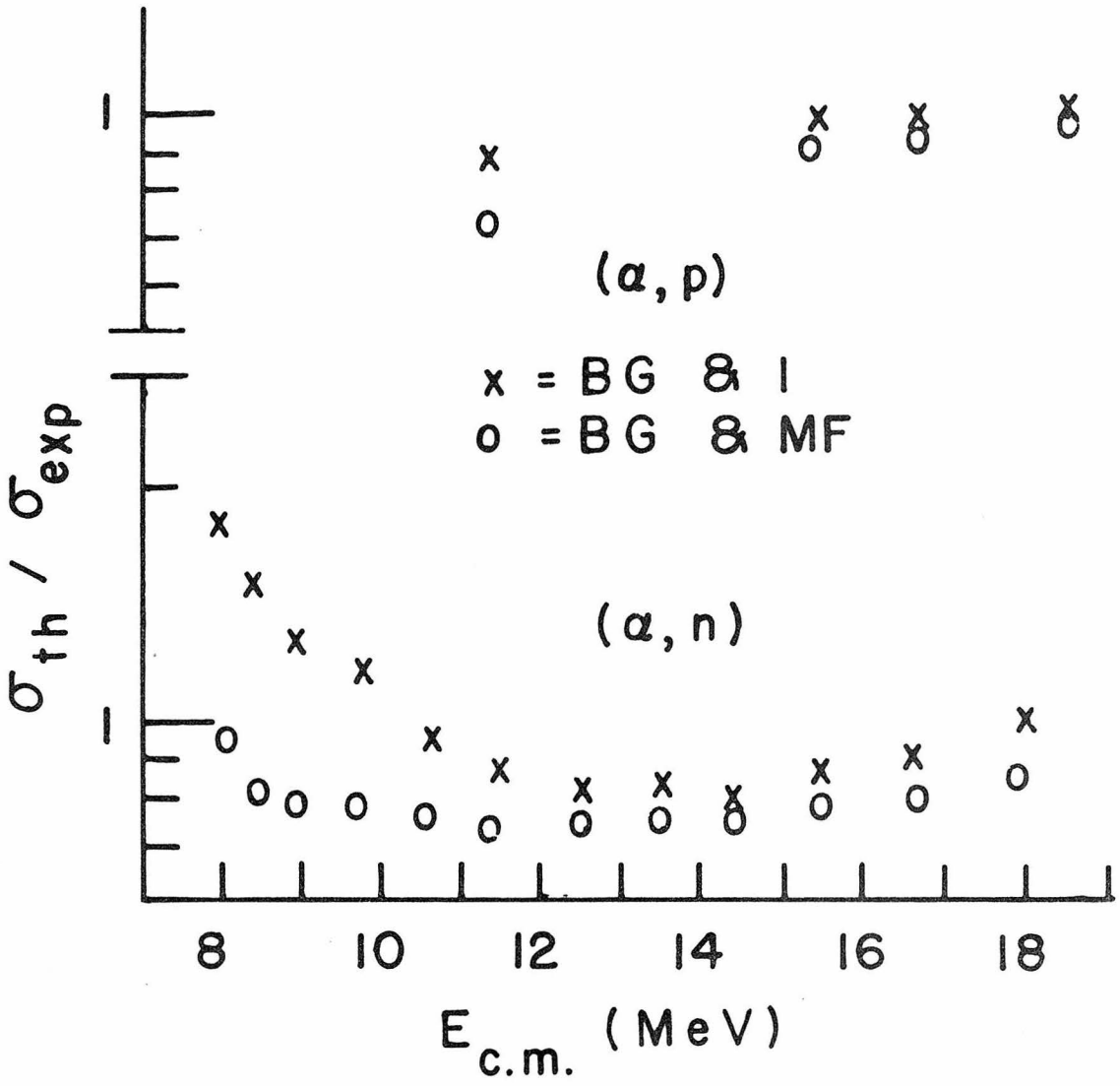
1
1
$\sigma_{th} / \sigma_{exp}$
(α, p)
x = BG & I
o = BG & MF
(α, n)
8
10
12
14
16
18
$E_{c.m.}$ (MeV)

Figure 31

Ladder diagram for $^{65}Cu + \alpha$, only the most important channels being shown. The sequential particle breakups of ^{68}Ga are shown at the appropriate energies. Other channels not shown (with Q values relative to $^{65}Cu + \alpha$) include $d + {}^{67}Zn$ (-10.11 MeV), $t + {}^{66}Zn$ (-10.91), $p + \alpha + {}^{64}Ni$ (-7.45 MeV), and $2\alpha + {}^{61}Co$ (-6.76 MeV).

The discrete states shown were included in the statistical-model calculations. The discrete states for ^{68}Ga used in the calculations are not explicitly shown as they are so dense; only the first and last levels are shown. The levels characterized by the slashed region were included by means of a level-density formula (parameters from Dilg et al 1973). Only p, n, and α channels were included in the calculations since the presence of other channels has negligible effect.

(See page 242.)

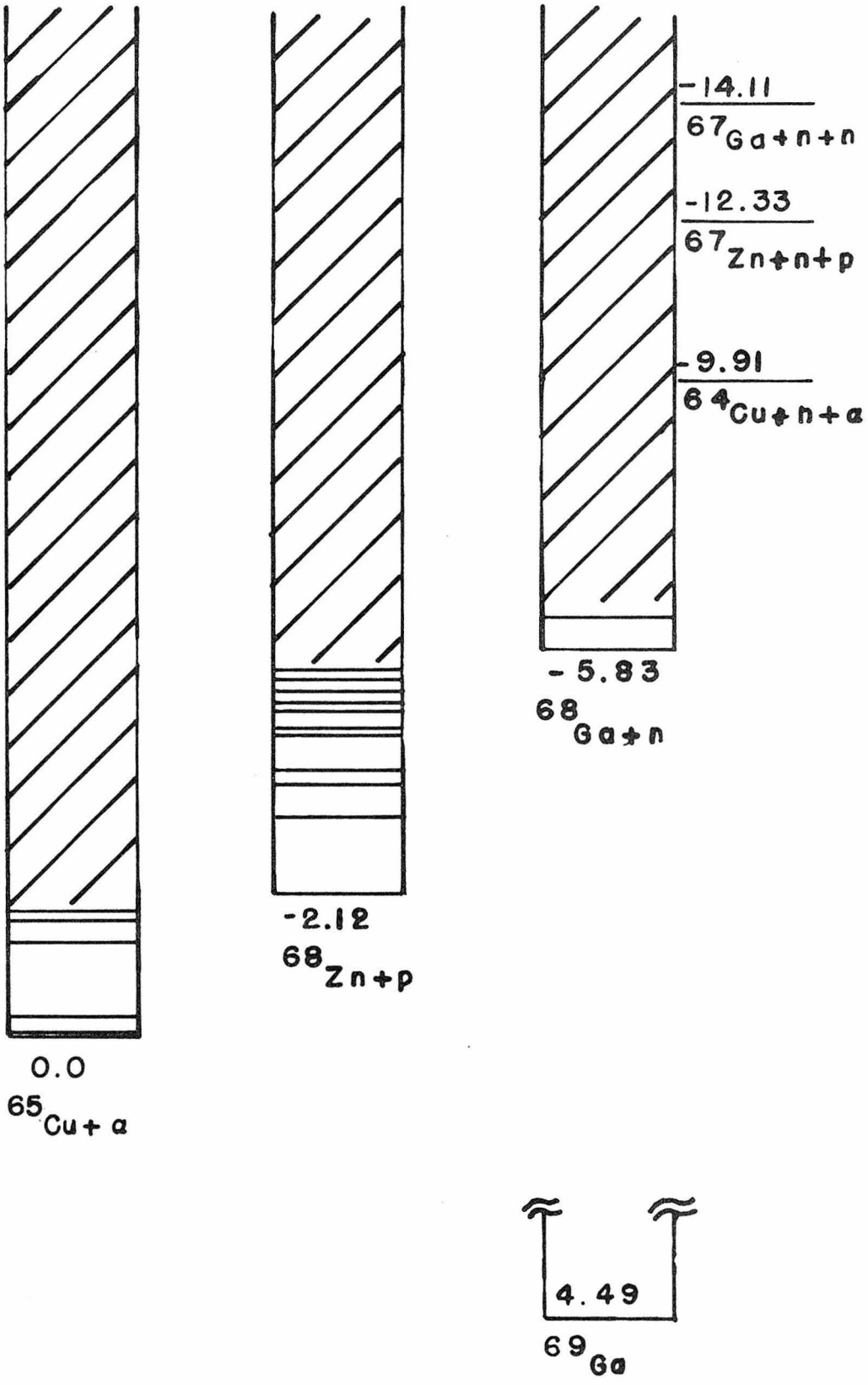
-14.11
67Ga+n+n
-12.33
67Zn+n+p
-9.91
64Cu+n+α
-5.83
68Ga+n
-2.12
68Zn+p
0.0
65Cu+α
4.49
69Ga

Figure 32

Theoretical cross section for $^{65}Cu(\alpha,n)^{68}Ga$ divided by the measured values. Two potential sets are shown: the proton and neutron potentials of Becchetti and Greenlees (1969a) and the alpha potential of Igo (1959a and 1959b) and of Michaud and Fowler (1970a). The choice of the nucleon potential makes little in the results of the calculation. The use of the alpha potential of McFadden and Satchler lies between the two results shown.

(See page 242.)

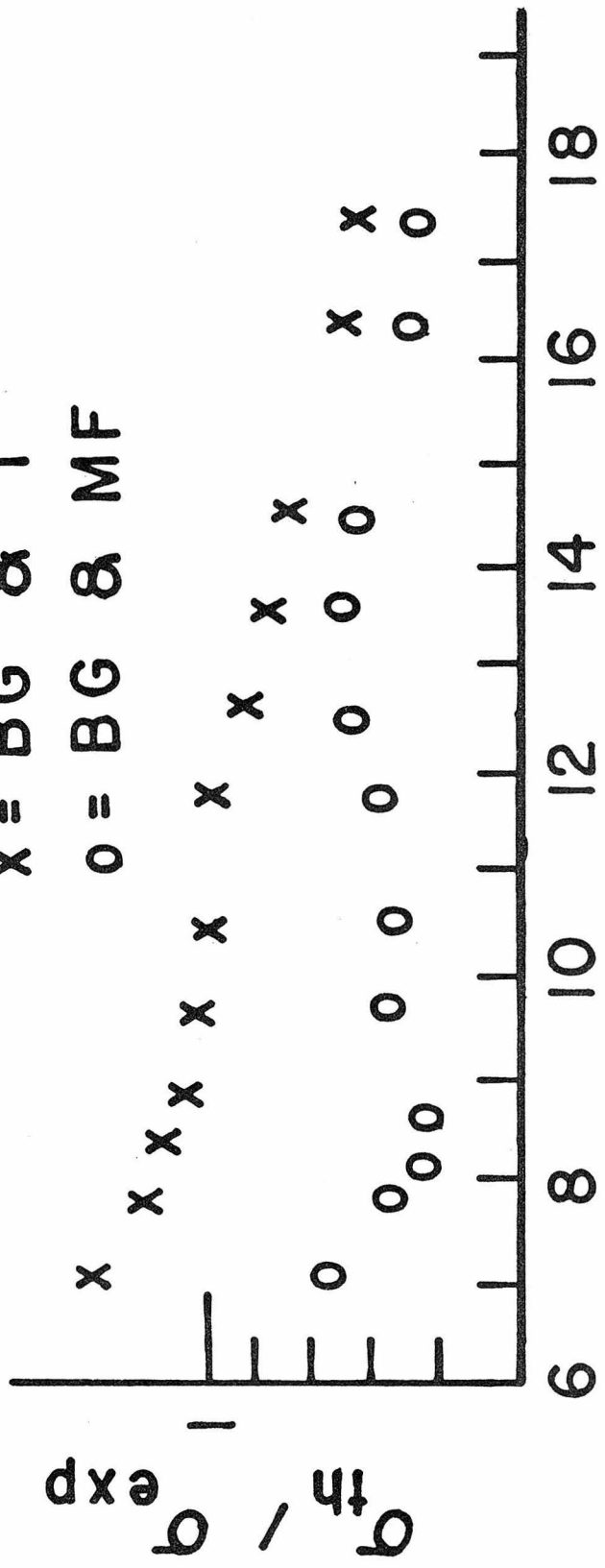
x = BG & I
o = BG & MF
$\sigma_{th} / \sigma_{exp}$
1
6
8
10
12
14
16
18
$E_{c.m.}$ (MeV)

Figure 33

Ladder diagram for $^{63}Cu + p$, only the most important channels are shown. Other channels not shown (with Q values relative to $^{63}Cu + p$) include $2p + {}^{62}Ni$ (-6.12 MeV), $p + \alpha + {}^{59}Co$ (-5.78 MeV), and $2\alpha + {}^{56}Fe$ (-3.97).

The discrete states shown were included in the statistical-model calculations. Only two states in ^{63}Zn (the ground and first excited states) have known spin and parity. The levels characterized by the slashed region were included by means of a level density formula (the parameters for ^{63}Cu and ^{60}Ni from Dilg et al 1973). The level-density parameters for ^{63}Zn were changed from that of Dilg et al to obtain better agreement with experiment (see text, page 244, and Figure 34). Only n, p, and α channels were included in the calculations, since the presence of other channels has negligible effect.

(See page 244.)

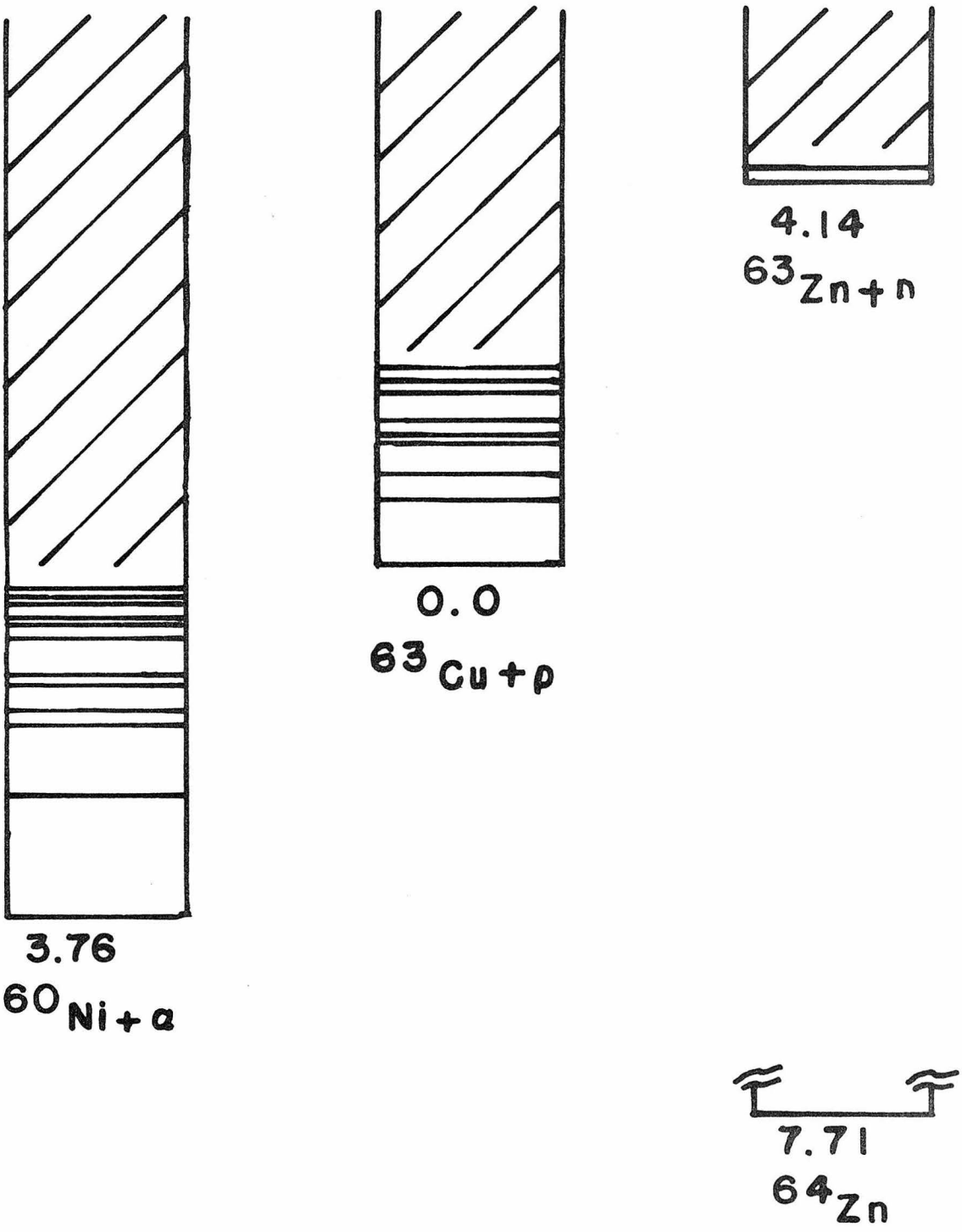
4.14
63Zn+n
0.0
63Cu+p
3.76
60Ni+α
7.71
64Zn

Figure 34

Theoretical predictions of the $^{63}Cu(p,n)^{63}Zn$ as a function of the "level density parameter" (a of equation 47). The value from Dilg et al (1973) is from their default equation (equation 61 of this thesis), as there is no experimental evidence concerning the level density of ^{63}Zn.

As the curves show, there is a very strong dependence of the predicted cross section on the value taken for the level-density parameter a .

By comparing the measured cross section (Figure 20), a value for the parameter a of about 20 to 25% higher than suggested by Dilg et al is required if the theoretical and experimental results are to agree.

(See page 244.)

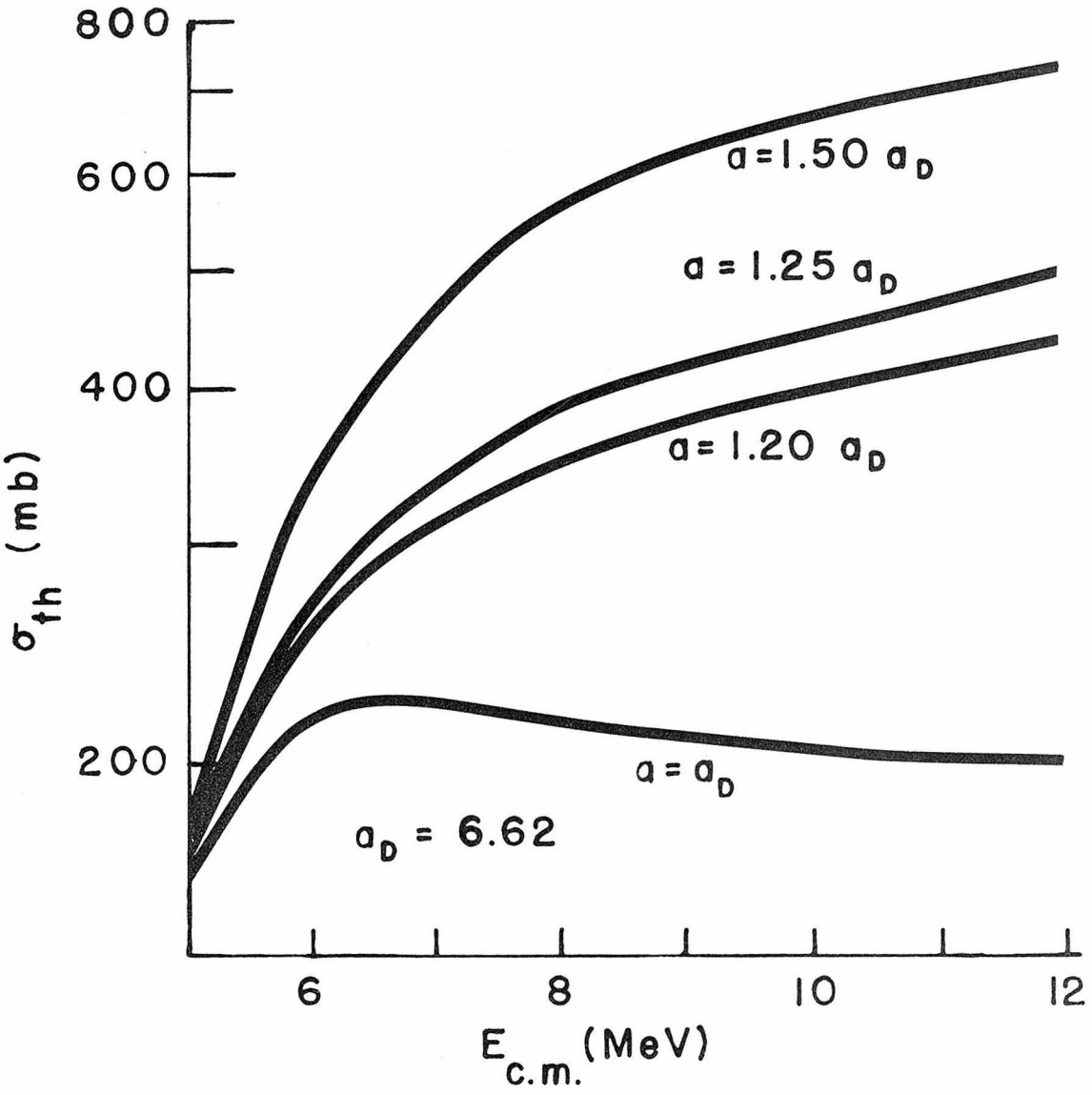
800
600
400
200
σ_{th} (mb)
a = 1.50 a_D
a = 1.25 a_D
a = 1.20 a_D
a = a_D
a_D = 6.62
6
8
10
12
$E_{c.m.}$ (MeV)

Figure 35

Theoretical cross section for $^{63}Cu(p,n)^{63}Zn$ divided by measured values. Also presented are the theoretical cross sections for $^{63}Cu(p,p')$ and $^{63}Cu(p,\alpha)^{60}Ni$ divided by the measured values of Benveniste et al (1961). Various potential sets were used as indicated in the figure.

Because the level-density parameter a (of equation 47) was treated as a free parameter, little comment can be made concerning the potentials which provide the best fits, since all potential sets can give excellent fits if the level-density parameter is slightly varied. However, the agreement for all three reaction pairs ($^{63}Cu + p$, $^{63}Zn + n$, and $^{60}Ni + \alpha$) is very good if the level density parameter a is increased by 20 to 25% over the value recommended by Dilg et al (1973).

(See page 244.)

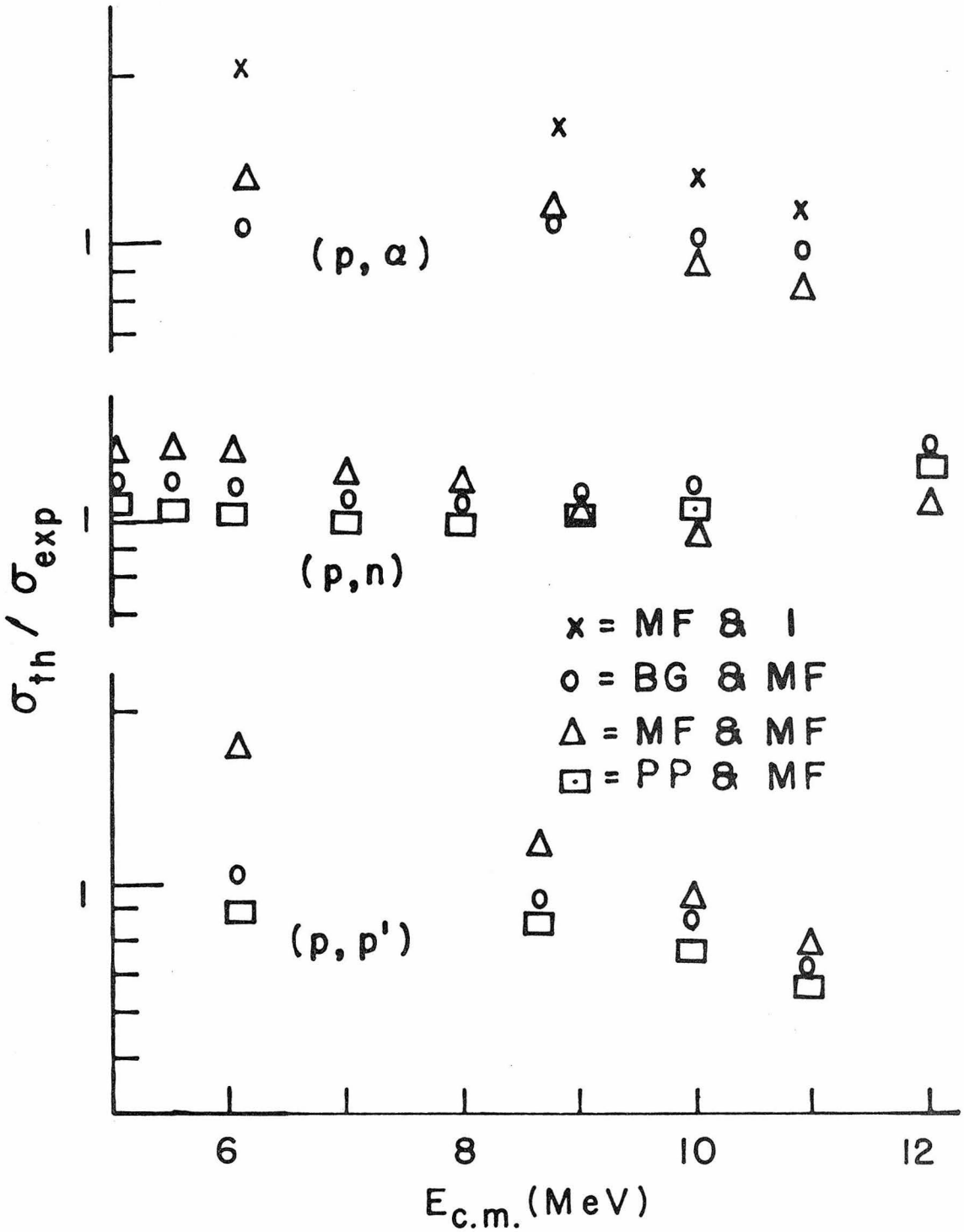
(p, α)
(p, n)
(p, p')
1
1
1
x = MF & I
o = BG & MF
Δ = MF & MF
⊡ = PP & MF
6
8
10
12
$E_{c.m.}$ (MeV)
$\sigma_{th} / \sigma_{exp}$